Globular Clusters in the Andromeda Galaxy

A thesis presented

by

Pauline Margaret Barmby

to

The Department of Astronomy

in partial fulfillment of the requirements
for the degree of
Doctor of Philosophy
in the subject of
Astronomy

Harvard University
Cambridge, Massachusetts

April 2001

Globular Clusters in the Andromeda Galaxy

Advisor: Prof. John P. Huchra Pauline Margaret Barmby

Abstract

Globular clusters are among the oldest stellar systems, and the properties of their simple stellar populations provide valuable clues about galaxy formation. Local Group globular clusters form a bridge between Galactic and extragalactic globular clusters. The globular clusters of the Andromeda galaxy (Messier 31, or M31), the largest population in the Local Group, are the topic of this thesis.

I present a catalog of integrated photometric and spectroscopic data on M31 globular clusters, including substantial new observational data. With it, I perform several studies of M31 globular clusters: (1) I determine the reddening and intrinsic colors of individual clusters, and find that the extinction laws in the Galaxy and M31 are not significantly different. (2) I measure the distributions of M31 clusters' metallicities and metallicity-sensitive colors; both are bimodal with peaks at [Fe/H] ≈ -1.4 and -0.6. The radial distribution and kinematics of the two M31 metallicity groups imply that they are analogs of the Galactic 'halo' and 'disk/bulge' cluster systems. (3) I compare colors for M31 and Milky Way globular clusters to the predicted simple stellar population colors of three population synthesis models. The best-fitting models fit the cluster colors very well; offsets between model and data in the U and B passbands are likely due to problems with the spectral libraries used by the models. The best-fit models for the metal-rich clusters are younger than those for the metal-poor ones. (4) I determine the globular cluster luminosity function (GCLF) parameters for several subsamples of the M31 globular cluster population. The inner third of the clusters have a brighter GCLF peak than the outer clusters, and the metal-poor clusters are fainter than the metal-rich clusters. The results in (3) and (4) imply the globular cluster populations in M31 may have substantially different ages, which has important consequences for models of galaxy and cluster formation. I also use WFPC2 images from the Hubble Space Telescope Archive to model the selection effects in existing M31 cluster catalogs and measure structural parameters for globular clusters in M31. The M31 clusters have very similar structural parameters to the Galactic globulars, and are located on the same 'fundamental plane'.

Contents

List of Figures

List of Tables

Acknowledgements

The road to a PhD is like the mountain road at an observatory: long, winding, and sometimes muddy, with a giddy feeling at the end. Fortunately the PhD road is not traveled alone; I am grateful to the many people who helped me out along the way. My advisor John Huchra helped me plot my course, and my thesis advisory and defense committee members, Josh Grindlay, Dimitar Sasselov, Paul Schechter, Pat Thaddeus and Steve Zepf, pointed out interesting scenic viewpoints along the way. All resisted any temptation to backseat driving, and I am grateful for their sage advice and counsel.

I have learned a lot from other travelers on the PhD road, my fellow graduate students. My classmates Héctor Arce, Warren Brown, Lucas Macri, and Greg Sobczak were sources of friendship, inspiration, and (occasionally) amusement, as were older and younger people like Lorraine Allen, Betsy Barton, Peter Bloser, Dave Charbonneau, John Girash, Norm Grogin, Paul Janzen, Saurabh Jha, Dan Koranyi, and Sara Seager. I also learned a lot from the Harvard undergrads I "TFed" over the years, and from the professors whose courses I worked in: Margaret Geller, Owen Gingerich and Dave Latham, and Bob Kirshner. No mention of Harvard would be complete without the people who kept the Astronomy Department running: Jean Collins, Christina Doyle, and Peggy Herlihy. Jean in particular has become a good friend, and I will miss her.

Many people in the Optical and Infrared Division of the CfA have patiently endured my pestering over the years. In particular I would like to thank Nelson Caldwell, Leslie Feldman, Peter Garnavich, Katie Lynn, Jeff Mader, Doug Mink, Krzysztof Stanek, Andy Szentgyorgyi, Eric Tollestrup, and Bill Wyatt for their help with various aspects of observing and research. The observatory staffs at Whipple and Lick Observatories provided productive observing runs (when the weather cooperated!) and patient post-observing support. Other CfA staff including Jonathan McDowell, Irwin Shapiro, and Rosanne di Stefano provided scientific interest and friendship; honorary CfAer Kim McLeod provided advice and encouragement at a critical moment. The Smithsonian Astrophysical Observatory also provided financial support for which I am grateful.

My scientific collaborators, including Jean Brodie, Duncan Forbes, Carl Grillmair, Markus Kissler-Patig, Claudia Maraston, Linda Schroder, and Graeme Smith have been invaluable sources of advice, ideas, and encouragement. I look forward to continuing to work with them in the future. Several people whom I have never met also helped my work by making their software packages publicly

available: P. Hall (PHIIRS), M. Akritas & M. Bershady (BCES), C. Bird (KMM), and J. Secker (MAXIMUM). The anonymous referees of the papers corresponding to Chapters 2, 3 and 4 made comments which helped to substantially improve the work.

I would never have finished my PhD without the love and support of the Barmby and McKenzie clans. My parents Bev and John Barmby and my brother Greg provided encouragement and unstinting optimism even in my darker days, and I can't thank them enough. Waiting patiently for me at the end of the PhD road is my husband, Dr. Charles McKenzie. His love and encouragement sustained me through graduate school, and will continue to do so in the many years of our partnership which lie ahead. Thank you, sweetheart.

Chapter 1

Introduction

1.1 Historical Background

"No one can behold this magnificent object for the first time without exclamations of wonder and excitement"; thus was the brightest globular cluster in the northern sky described by Mitchel (1869). Globular clusters (GCs) are still a source of wonder and excitement, and they occupy a unique niche in the study of stars and stellar systems. These bright, compact objects, composed of thousands to millions of stars, have been beacons for the study of Galactic structure, stellar evolution, and more recently, galaxy formation and evolution. The identification of globular clusters in other galaxies came very soon after the demonstration that the 'spiral nebulae' were indeed external stellar systems (Hubble 1929, 1932). The globular cluster system (GCS) of the Andromeda Galaxy (the 31^{st} object in Messier's catalog of nebulous objects, = M31) was the first example of such a system comparable in size and scale to that of the Milky Way. Studies of the M31 and Milky Way GCSs over the past seventy years have progressed at different rates and with different emphases, but both have yielded much useful information about these two dominant galaxies in the Local Group and about the universe in general.

The recognizability of globular clusters allowed most of the Milky Way population to be identified by the early 1900s. Shapley (1918) used globular clusters as markers to map out the shape and size of the Milky Way. Baade's (1944) recognition of different stellar populations in M31 and its companions M32 and NGC 205 led to a realization that globular clusters were extremely old stellar systems whose ages could constrain the age of the universe. Shortly after his pioneering study of M31 in 1929, Hubble (1932) identified the first globular

cluster candidates in M31 and began the comparison of their properties to those of Milky Way clusters. True 'astrophysical' studies of the M31 clusters began in the late 1950s, about the same time that the first stellar evolution models were being computed and compared to color-magnitude diagrams of Milky Way GCs (Sandage & Schwarzschild 1952; Arp, Baum, & Sandage 1952). The early studies of the M31 GCS (Kron & Mayall 1960; Kinman 1963) employed the most advanced technology of the time—photoelectric photometers on the largest telescopes—and focused on the luminosity and color distributions of the clusters. At about the same time, the first spectra of individual stars in Milky Way clusters became available (Helfer, Wallerstein, & Greenstein 1959), eventually leading to detailed investigations of chemical abundance patterns and cluster internal kinematics.

There was a revival of interest in the M31 GCS late 1960s and early 1970s as the study of globular cluster systems in non-Local Group galaxies (e.g. M87; Racine 1968) began. The first spectra of M31 GCs (van den Bergh 1969) revealed important differences and similarities between M31 and Milky Way GCs, and allowed the first extragalactic use of GCs as 'test masses' for determining a galaxy's mass. At the same time, interest in theoretical studies of cluster formation and destruction began to increase (e.g., Peebles & Dicke 1968), and Tinsley (1968) made the first attempt to model the integrated light of stellar populations. Milky Way GC X-ray sources were first identified soon after the first X-ray astronomy satellites (Giacconi et al. 1974). The first infrared observations of globular clusters in the Milky Way (Glass & Feast 1973) and M31 (Frogel, Persson, & Cohen 1980) allowed the exploration of GC properties in a new wavelength regime. The early 1980s saw the first examination of the M31 GCS kinematics (Huchra et al. 1982) and the publication of an atlas of M31 (Hodge 1982), which included the results of a comprehensive photographic survey for GCs (Sargent et al. 1977).

In the mid-1980s, the first population synthesis models using modern techniques and input data appeared (e.g., Arimoto & Yoshii 1986). The advent of CCD detectors greatly improved the photometric study of Milky Way GCs and allowed the rigorous study of many more extragalactic GCSs. The discovery of blue cluster-like objects in merging and interacting galaxies (Lutz 1991; Holtzman et al. 1992) spurred debate on whether these objects might be young globular clusters. The Hubble Space Telescope's high spatial resolution provided a wealth of information on Milky Way globulars and the first usable color-magnitude diagrams of M31 clusters (Couture et al. 1995; Rich et al. 1996). Large ground-based telescopes extended GC spectroscopy to the distance of the Virgo and Fornax clusters (Cohen et al. 1998; Kissler-Patig et al. 1998). The study of globular clusters is perhaps not as fashionable as that of more recently-discovered phenomena,

but is an excellent example of the gains made by astrophysics as technology and fundamental understanding improve. Each new generation of astronomers has gained fresh insights from the study of globular clusters. This thesis, an observational study of the M31 globular cluster system, continues in the tradition of using new technologies to address fundamental questions with globular clusters.

1.2 Context of globular cluster research

Globular clusters are fascinating objects in their own right. The combination of great age, chemical homogeneity, and high density is unique among stellar systems. These properties result in consequences of stellar evolution and dynamics that occur nowhere else in the universe. The most important contribution of globular cluster research, however, is to provide a bridge between the worlds of stellar astronomy, where stars are studied individually, and extragalactic astronomy, where usually only the combined light of populations of stars is observable. The fundamental questions we wish to answer are 1) how and when did galaxies and stars form and evolve? and 2) how do star and galaxy formation formation and evolution affect each other? Part of the answer to question (2) seems obvious: stars are a major component of galaxies, so star formation must affect a galaxy's evolution. But there are more subtle interplays as well: for example, the stellar initial mass function (IMF) of stars affects chemical enrichment in galaxies, which in turn affects future star formation. Galaxy interactions can trigger star formation (Larson & Tinsley 1978), which again changes galaxy content.

The long timescales of star and galaxy formation and evolution require the use of many approaches to answer the very broad questions raised above. Observing galaxies and stars in the process of formation is the most obvious way to learn about such processes, but this method allows the study of star formation only at the present epoch, and galaxy formation only in the distant past. Forming galaxies at high redshifts are small and faint, and their study requires heroic efforts with advanced technology. The 'lazy way' (Kissler-Patig 2000) to study galaxy and star formation and evolution is to observe nearby objects, both evolved star clusters and objects which appear to be in earlier stages of evolution. The current properties of old clusters constrain models which can then be used to infer their history. Determination of the ages of globular clusters by comparison with stellar evolution models is an example of this approach. This thesis concentrates on the second approach since it is most relevant for globular clusters.

Globular clusters have many properties which make them useful probes of

galaxy and stellar history. With a few exceptions (ω Cen, Woolley 1966; M22, Lloyd Evans 1978), the stars in individual globular clusters in the Milky Way are found to be homogeneous in both age and chemical composition (Suntzeff 1993). This has generally been assumed to be true for extragalactic globular clusters as well. (The assumption is reasonable since many other properties of Milky Way globulars are shared by extragalactic ones, and unavoidable since there is at present no way to test it.) As shown below, the homogeneity of globular clusters strongly constrains models of their formation, and simplifies understanding of their present-day properties. GCs' high surface brightness makes them visible at much larger distances than any individual stars except supernovae. Their small physical size means that, to first order, all stars feel the same potential from the parent galaxy, so that the globular clusters can be considered a single object for investigating the properties of the host galaxy. The globular cluster populations of large galaxies typically number in the hundreds, so their average properties can be quite well determined. Lastly, the great age of globular clusters means that they have been witnesses to most of the universe's 'stelliferous era' (Adams & Laughlin 1999) and to the important processes in the history of their parent galaxy.

1.3 Specific questions and models

Globular cluster formation is, of course, intimately connected to star formation. Most star formation is clustered (Lada et al. 1991), although the fraction of star formation that occurs in massive clusters varies widely (Larsen & Richtler 1999, 2000). A natural question is how globular cluster formation is related to other types of star cluster formation. The properties of globular clusters have led to suggestions that their formation required special circumstances. Other modelers claim that globular cluster formation is only the extreme (age, mass, or density) tail of a much more general process. Another important question in globular cluster formation is the timing: did globular cluster formation occur before, during, or after the bulk of star formation in galaxies? Fall & Rees (1988) categorize these three scenarios as 'primary', 'secondary' and 'tertiary' models. Many authors have pointed out that the distinction between the three modes is somewhat blurry, since galaxy formation is not likely an instantaneous process; Burgarella, Kissler-Patig, & Buat (2000) propose that models be divided into 'external' (formation not related to the final parent galaxy) and 'internal' (formation occurred inside or near the final parent galaxy) classifications. Many galaxies have multiple populations of GCs, which might not have the same origin. We review some of the models for GC formation below.

One property of globular cluster systems is the luminosity function (GCLF): the distribution, in magnitudes, of the integrated cluster luminosities. In all large galaxies, the GCLF is observed to be unimodal and symmetric, with peak magnitude at about $M_V = -7.3$ (Harris 2000). Assuming that all globular clusters have similar mass-to-light ratios ($M/L_V \sim 2$ is typical for Milky Way globular clusters; Pryor & Meylan 1993), this peak luminosity has been interpreted as indicative of a characteristic mass scale for globular clusters, approximately 10^5 $M_\odot$. Peebles & Dicke (1968) noted that this mass is equivalent to the Jeans mass at the temperature of the universe just after recombination, and suggested that globular cluster formation occurred at this time, before galaxy formation. Carr & Rees (1984) showed that the mass scale can vary somewhat with cosmological factors, but it is still comparable to typical masses of globular clusters.

The strongest objection to the 'primordial' formation model is the lack of dark matter halos around globular clusters. For this model to be consistent with cosmological constraints, globular clusters must have such halos (Peebles 1984). However, detailed modeling of Milky Way GCs' tidal streams has shown that global mass-to-light ratios are near the values observed for the stars alone (Moore 1996). A second objection is that the characteristic mass might not be determined by formation conditions, but by subsequent dynamical evolution. Okazaki & Tosa (1995) showed that an initial power-law mass distribution (typical of young star clusters; van den Bergh & Lafontaine 1984) can evolve into a log-normal mass distribution (implied by the Gaussian magnitude distribution) as low-mass clusters are destroyed by evaporation and disk shocking. The characteristic mass is therefore indicative of the age of the GCS and not its initial mass distribution. Vesperini (1998, 2000, 2001) found similar results for the evolution of initial power-law mass distributions but also showed that there was a particular initial log-normal mass distribution which stayed essentially constant in time. Dynamical evolution as the source of the characteristic GC mass has a problem in explaining why all galaxy masses, types, and environments should have such a similar effect on the globular cluster mass function.

A final problem with primary formation models is that some properties (number, metallicity, spatial distribution) of globular cluster systems are correlated with those of their parent galaxies. Ashman & Zepf (1998) point out that "it is difficult to imagine how this could be set up if the globular clusters formed before and independently of galaxies", but there are a few possibilities. Biased globular cluster formation (Rosenblatt, Faber, & Blumenthal 1988; West 1993), in which GCs form more efficiently in overdense regions, could account for the number and spatial correlations. The metallicity correlation can be accounted for by noting that

many galaxies have two populations of globular clusters, and only the metal-rich clusters' properties correlate with the parent galaxies' (Forbes, Brodie, & Grillmair 1997a; Forbes & Forte 2001). Forbes et al. use this result to argue that there are two epochs of GC formation: one before galaxy formation and one after. So a 'secondary' formation scenario is still required for at least some GCs.

A secondary formation model motivated by the GC mass distribution is that of Fall & Rees (1985). They propose that GCs formed in cool clouds in pressure equilibrium with surrounding hotter gas. In low-metallicity clouds, cooling becomes inefficient at temperatures of about 10^4 K, so the clouds stop cooling and fragment into stars. Fall & Rees claim that cooling must stop for the characteristic mass scale to be imprinted on the clouds and the resulting globular clusters. On the other hand, the model of Gunn (1980), in which GCs form in strong shocks in proto-galactic gas, requires that cloud cooling time be *short*, in order for the cloud to fragment and form stars. The Fall & Rees and Gunn models both require the gas to have low metallicity, and obviously cannot account for the formation of metal-rich globular clusters found in the disk of the Milky Way and around many ellipticals. The metallicities of these clusters are likely too high for self-enrichment to have produced all the metals (Ashman & Zepf 1998), implying that the gas must have been pre-enriched. In high-metallicity gas, the characteristic mass would be different if it existed at all, yet the luminosity (and by inference, mass) distributions of the metal-rich and metal-poor Milky Way clusters are indistinguishable (Armandroff 1989).[1] There are two minor problems with the Fall & Rees and Gunn models which could be remedied by the effects of dynamical evolution: the predicted minimum mass of the clusters is larger than the mass of most Milky Way clusters, and the minimum mass is expected to increase with galactocentric distance. An increase in GC mass with R is not seen in Milky Way clusters, although an increase in cluster size has been found (van den Bergh 1994, and see Chapter 5). The first problem can be explained by noting that GCs lose mass with time (through stellar evolution and dynamical effects), and the second problem can be explained if more low-mass GCs are destroyed at low galactocentric distances.

The most well-known property of globular clusters is their great age. If all globular clusters were formed in the early universe, perhaps globular cluster formation could *only* have happened then. This is implicit in the Peebles & Dicke (1968) model, and also in the model of Burgarella et al. (2000), who suggest that metal-poor GCs form in damped Lyα systems. While all Milky Way globular

[1]While there is some evidence for different masses between metal-rich and metal-poor clusters in M31 (see Chapter 4), this is still tentative.

clusters are old (Chaboyer et al. 1996a), there is evidence for an age spread among Milky Way globulars (Sarajedini, Chaboyer, & Demarque 1997; Rosenberg et al. 1999) and more tentative evidence (see Chapters 3 & 4) for larger differences in the ages of M31 clusters. The presence of apparently bound young star clusters in nearby merging and interacting galaxies is another reason to doubt that globular cluster formation could only have occurred in the early universe.

The chemical homogeneity of globular clusters can also be taken as an indicator that globular cluster formation had to occur at high redshift, before numerous supernovae produced spatially varying abundance patterns in the progenitor gas. This is not necessarily an indicator that the enrichment had to occur at early times, however: it just means that enriching generation of stars had to form quickly (so that it disappeared before the globular cluster stars formed), and that the mixing of metals also had to proceed quickly to destroy any spatial variations. As noted above, the high metallicities of some clusters imply that at least some pre-enrichment took place. The effect of self-enrichment is more difficult to constrain: it has generally been argued (e.g., by Murray & Lin 1992) that most globular clusters could not survive the supernova explosions that produced their metals, and that the mixing timescales were too long for the second generation of stars to be chemically homogeneous. However, recent work by Parmentier et al. (1999) claims that the formation time for the second generation of stars is longer than the mixing timescale, and that self-enrichment (from [Fe/H] $= -2$ to [Fe/H] $= -1$) is a realistic possibility. One would expect that more massive clusters would be able to hold on to more of their metals and thus be more metal-rich, and there is some evidence for this in M31 (see Chapter 4).

The special properties of globular clusters are one starting point for constructing models of GC formation. Another starting point comes from noting the similarities between globular clusters and other types of star clusters. Larson (1993) notes that globular clusters differ from open clusters largely in that they remain bound for their much longer lifetimes, and that bound clusters form only in dense cores of much larger objects. This implies that proto-globular cluster clouds had masses much larger than the final cluster masses, in contrast to the models described above. The special properties of globular clusters then cease to be the motivation for formation models; rather the motivation is to understand the formation of the massive gas clouds needed to form the clusters. Most of these models are 'secondary'/'internal' models, since they require the clusters to form inside the parent galaxy, during or after galaxy formation.

A major motivation for this type of model is the observation that the globular cluster mass function above $10^5 M_\odot$ can be fitted as a power law, $N \propto M^{-\alpha}$,

$\alpha \approx$1.5–2 (Richtler 1992; Harris & Pudritz 1994). Similar power-law exponents are found for the mass spectra of open clusters (van den Bergh & Lafontaine 1984), young star clusters (Whitmore & Schweizer 1995) and giant molecular clouds (Solomon et al. 1987). Harris & Pudritz (1994) and McLaughlin & Pudritz (1996) use this to argue that globular clusters form in super giant molecular clouds (SGMCs) with masses in the range $10^7 - 10^9$ $M_\odot$. These clouds would be supported by turbulence and internal magnetic fields, so their lifetimes would be much longer than that expected from radiative cooling alone, as in the Fall & Rees (1985) and Murray & Lin (1992) models. McLaughlin & Pudritz (1996) suggest that dense clumps within the SGMCs will collide and agglomerate to form protoclusters. They reproduce the observed GCMF by tuning the ratio of collision and star formation timescales. Elmegreen & Efremov (1997) also use the 'universal' power-law mass distribution to argue for a universal star cluster formation process. In their model, the mass spectrum is due to the turbulent nature of the gas, and the different cluster masses arise from pressure differences. Globular clusters preferentially form in high-pressure regions, which are found in high-density environments (galactic nuclei, nuclear rings), regions of turbulent compression (galaxy halos), or large-scale shocks (interacting galaxies). Elmegreen & Efremov (1997) suggest that the location of the peak of the present-day GCMF is due to dynamical destruction over the lifetime of the GCS.

Both of these generic cluster formation scenarios have problems. The Harris & Pudritz (1994) model has been criticized for requiring the existence of gas clouds much larger than those found in present-day galaxies, but Harris (2000) argues that such clouds must have existed in the pre-galactic era in order to produce the merging objects observed at high redshift. The merger NGC 4038/4039 is known to have a large population of young star clusters (Whitmore & Schweizer 1995): Wilson et al. (2000) present evidence for the existence of SGMCs in this galaxy, but this may be an effect of their observations' spatial resolution. Possible identifications of the SGMCs are DLA systems at high redshift (Burgarella et al. 2000), or the pre-galactic fragments of Searle & Zinn (1978). Although Elmegreen & Efremov (1997) point out that "mass dependence of the cluster destruction rate does not vary with galactocentric radius much", the dynamical destruction mechanisms do vary with galaxy type (e.g., elliptical galaxies have no disk shocking) and it is difficult to understand how the cluster destruction timescales (and therefore the GCMF) can be the same for all galaxies .

A factor not often addressed in models of globular cluster formation is the *stellar* initial mass function (IMF), which can have a significant effect on many of the processes discussed in this section. Vesperini & Heggie (1997) show that

the loss of low-mass stars due to relaxation and disk shocking flattens the stellar mass function with time, and Takahashi (2000) finds that the lifetime of clusters against dynamical destruction is fairly sensitive to the form of the IMF. The stellar mass function also strongly affects the total luminosity of GCs (see Chapter 4). Derivations of the IMF from observations of the stellar luminosity function in Milky Way GCs have found that the exponent x of the IMF $n(M) \propto M^{(-1+x)}$ increases with GC Galactocentric radius R and height above the plane Z (Capaccioli et al. 1991), and decreases slightly with metallicity (Djorgovski et al. 1993). The distance dependence is likely due to evolutionary effects, as discussed above, while the metallicity dependence seems more likely to be primordial. Either the metallicity affects the IMF (Silk 1977), or clusters with more high-mass stars naturally have more self-enrichment and thus higher-metallicity (Smith & McClure 1987). If self-enrichment occurs, the IMF also plays a role: the enriching stars should have a different IMF from the 'true' GC stars (so that they disappear before the GC stars form), but there cannot be so many high-mass stars that the cluster destroys itself before the second generation forms. Parmentier et al. (1999) construct an IMF for the enriching stars that satisfies both of these conditions.

The formation and evolution of globular clusters are clearly affected by both the stars that make up clusters and the galaxies where they are located. Correlations between galaxy and GCS properties are key observables for determining whether GC formation occurred before, during or after galaxy formation. While characteristic properties of globular clusters (age, mass, metallicity, density) may provide clues to their formation, they may also reflect the the subsequent effects of both stellar and dynamical evolution. At present, there are few observational tests which can determine whether globular cluster formation is special, or just part of a continuum of star cluster formation processes.

1.4 Globular clusters and galaxy formation

Globular clusters are made up of stars, and both stars and GCs are constituents of galaxies. After relating globular cluster formation to star formation, we also need to see how it fits into the big picture of galaxy formation. Some of the 'big questions' in galaxy formation relevant to GCs are these: 1) what accounts for the range of galaxy morphologies? There are large differences between spiral and elliptical galaxies (dynamics, stellar populations, surface brightness). Clearly environment is important (e.g., the morphology-density relation; Dressler 1980), but it is not the only factor. How did these two very different types of galaxies form and evolve? 2)

What was the timescale for galaxy formation? Was galaxy formation a relatively recent phenomenon or did it take place long ago? Observations of apparently 'normal' galaxies at $z \sim 1$ (Abraham et al. 1996) imply that at least some galaxy formation took place at high redshift. But the question of whether recent events, e.g. mergers, are important for the majority of galaxies remains open. van den Bergh (2000) points out that an interesting contrast in globular cluster properties is provided by M33 and the Large Magellanic Cloud (LMC), two galaxies with similar total luminosities. The M33 cluster have halo kinematics as would be expected for an old population (Schommer et al. 1991), but show evidence of being intermediate-aged (Sarajedini et al. 2000). The LMC clusters show disk-like kinematics (Schommer et al. 1992), and a wide range of ages (Girardi et al. 1995).

Two extreme possibilities are often used to illustrate scenarios for galaxy formation. One is the idea of dissipational collapse, often associated with the classic paper of Eggen, Lynden-Bell, & Sandage (1962). In this picture, star formation proceeds rapidly at an early epoch, violent relaxation occurs, and the galaxy collapses on a free-fall timescale. In spirals, the collapse phase includes the gas left over from star formation and produces the disk, while in ellipticals little gas remains after star formation and no disk is produced. The reasons for the differences between spirals and ellipticals are not well-understood, but may be related to initial conditions or angular momentum. In the other picture of galaxy formation, often associated with the work of Searle & Zinn (1978), star formation occurs in isolated proto-galactic fragments, which then coalesce into a galaxy. This is the same galaxy formation scenario predicted by cold dark matter cosmological models (Peebles 1984; Blumenthal et al. 1984), where structure formation occurs through hierarchical clustering. It is also related to the hypothesis that elliptical galaxies are formed by mergers of spirals (Toomre 1977), which has come to play a prominent role in theories of GCS formation.

If globular clusters formed before galaxies, then there should be little correlation between galaxy and GCS properties, except for possibly a general environmental effect (perhaps from biased GC formation; see the previous section). If globular cluster formation occurs before galaxy formation then the only information on galaxy formation provided by GCs is an upper age limit. However, since there is evidence for correlations between GCS and galaxy properties, it is important to know how GCS properties might be influenced by parent galaxy formation and evolution.

One GCS property relevant to galaxy formation is the contrast between the properties of globular clusters in ellipticals and the surrounding galaxy halos. The integrated colors of old stellar populations are primarily determined by metallicity,

which affects the temperature (and therefore the color) of the stars on the red giant branch. The bluer colors of GCs compared to the halo stars can be used to argue that the GCs are more metal-poor than the surrounding halo; Holland, Fahlman, & Richer (1996) derive the metallicity difference directly from color-magnitude diagrams of M31 GCs and the M31 halo. Globular cluster systems are more spatially extended than halo stars, which is often used to argue that the GCs are older than the stars. McLaughlin (1999) argues against this interpretation, pointing out that, in several of the best-studied cases, the shallower GCS profiles do not occur when the GC distribution is compared to the galaxy mass (rather than luminosity) distribution. Both galaxy halos and GCSs show color gradients, in that colors become bluer at greater galactocentric distances (Ashman & Zepf 1998). The color gradients (usually assumed to correspond to metallicity gradients) are interpreted as supporting the dissipational collapse picture, in which such gradients are natural. However, the galaxy and GCS color gradients are generally not the same, and are smaller than model predictions, so their relevance to galaxy formation is unclear. GCS color gradients may also be due to radial differences in the relative proportions of red and blue clusters (Ashman & Zepf 1992; Geisler, Lee, & Kim 1996) rather than a true gradient within individual populations.

The total number of globular clusters in a galaxy, or that number normalized by the galaxy luminosity (the specific frequency, $S_N = N_{gc} \times 10^{-0.4(M_V^T+15)}$), is another key observable of GCSs. Most galaxies have values of S_N between 0.5 and 20, so the number of GCs scales roughly, but not exactly, with galaxy luminosity. Typical values of S_N in ellipticals are about 3–5; spirals typically have lower values in the range 0.5–1.5, while dwarf ellipticals and some giant ellipticals have much higher values, up to $S_N \sim 20$. The reasons for the differences in S_N are not well understood, although spiral galaxies' S_N values become similar to those of ellipticals if only the spiral bulge luminosity (more similar to ellipticals' stellar populations) is used to calculate S_N (Kissler-Patig 1997a). Attempts to explain the very large values of S_N seen in gE galaxies (which are preferentially located in galaxy clusters) have produced a number of important ideas about galaxy and globular cluster formation. One idea is to invoke the effects of environment by postulating that galaxies in denser environments somehow make globular clusters more efficiently (West 1993; Blakeslee, Tonry, & Metzger 1997). The notion that globular cluster formation is related to galaxy environment has been expanded upon by Harris, Harris, & McLaughlin (1998), who propose that the environment of these galaxies causes them to be underluminous, rather than over-endowed with GCs. McLaughlin (1999) develops this idea further, and shows that, for ellipticals, the number of GCs per unit (stellar+gas) mass is nearly constant: galaxies with high S_N have more gas and fewer stars. However, van den Bergh (2000) points out

that this analysis ignores an important component of galaxy mass, dark matter.

Another important class of models for explaining galaxy-type variations in S_N requires the presence of additional galaxies. Several authors (Richtler 1994; Côté et al. 1998) have suggested accretion of globular clusters, tidally stripped from or along with dwarf galaxies, as a cause of the high S_N of some galaxies. Côté et al. (1998) use the fact that GC systems are more spatially extended than their parent galaxies to show that tidal stripping of dwarf ellipticals results in a different distribution of GCs and stars in the final galaxy, answering earlier objections that tidal stripping would conserve specific frequency. The other important model involving galaxies other than the final, high-S_N elliptical is the merger model (Ashman & Zepf 1992; Zepf & Ashman 1993). Inspired by earlier work by Toomre (1977) and Schweizer (1982), Ashman & Zepf conjectured that elliptical galaxies result from mergers of spirals, and that the 'extra' GCs in ellipticals are formed during the merger. This is compatible with observations of young star clusters (possible 'proto-GCs') in present-day mergers and interactions, but has several major problems. One is explaining the variation in S_N between large ellipticals (e.g. NGC 4486 and NGC 4472 in Virgo; Côté et al. 1998), and another is the lack of an observed correlation between S_N and GCS average [Fe/H].

West et al. (1995) proposed that high-S_N galaxies in clusters could accrete their extra clusters from an 'intracluster' population of GCs. The intracluster GC model has received little attention, presumably because there is as yet no evidence that such objects exist. However, since intracluster stars are known to exist in the Virgo Cluster (Ciardullo et al. 1998), the existence of intracluster GCs is not completely unreasonable. Finding such objects would either imply that (at least some) globular cluster formation need not be associated with galaxies, or provide new information on GC stripping from cluster galaxies.

The metallicity distribution of GCSs has recently emerged as perhaps *the* key property in explaining their formation.[2] The mean metallicity of globular cluster systems increases with galaxy luminosity (Forbes et al. 1997a; Forbes & Forte 2001). This has been taken as support for the monolithic collapse model, where more luminous galaxies naturally have deeper potential wells and can retain more of the metals produced in the collapse-enrichment phase. However, another property of GCS metallicity distributions is that they are often multi-modal. The

[2]GCS metallicity distributions in ellipticals are usually inferred from color distributions, as this is much easier than object-by-object spectroscopy. Using color to infer metallicity is reasonable since, at the old ages expected for GCs, color is much more dependent on metallicity than on age. In the few galaxies where both colors and spectroscopic metallicities are available (Kissler-Patig et al. 1998; Cohen et al. 1998), the resulting distributions show good agreement.

presence of two metallicity populations in the Milky Way GCS was first established by Zinn (1985), who associated the two populations with the Galactic disk and halo. The relevance of GC populations to galaxy/GCS formation was not generally appreciated until multiple metallicity populations were also discovered in ellipticals (Zepf & Ashman 1993; Ostrov et al. 1993). The metallicity of the metal-poor GCS population does not correlate with galaxy luminosity, so the luminosity-metallicity correspondence is due mostly to an increasing number of metal-rich clusters with galaxy luminosity (Burgarella et al. 2000; Forbes et al. 1997a). This is used as an argument in favor of the ideas that galaxies and GCs formed in two distinct collapse phases (Berman & Suchkov 1991) , with the metal-poor clusters either completely pre-galactic (Burgarella et al. 2000) or somehow related to the final galaxy (Forbes et al. 1997a). Forbes et al. suggest that the disk clusters in spirals may represent a third collapse phase. While these models qualitatively explain the existence of two metallicity populations, they do not account for the populations' relative sizes or predict an expected age difference. These models also lack a physical motivation for the length or separation of the two star formation phases.

The GCS formation models that involve other galaxies seem to explain the multi-modal metallicity distributions more naturally. A multi-modal metallicity distribution for ellipticals was *predicted* by the merger model of Ashman & Zepf and is one of its major successes. The metal-poor clusters are supposed to have been associated with the progenitor spirals, with the metal-rich clusters formed during the merger. To explain the S_N problem, this model requires the metal-rich clusters to be more numerous than the metal-poor clusters; this is not observed in most galaxies (Gebhardt & Kissler-Patig 1999). The merger/tidal stripping model of Côté et al. (1998) assumes that the metal-rich clusters belong to the original 'seed' galaxy, and the metal-poor clusters come from the accreted dwarfs. This scenario has more success in reproducing the observed metallicity distribution, and it is reasonable in that dwarf galaxies are known to be accreted by larger galaxies (e.g. the Sagittarius dwarf by the Milky Way; Ibata et al. 1994). However, Hilker et al. (1999) point out that the accretion scenario requires the original galaxy luminosity function to be quite steep (to produce the large number of accreted dwarfs), and the feasibility of the accretion process must be confirmed with dynamical studies.

The age distribution of GCSs is the final property relevant to the GCS/galaxy formation models. Absolute ages of GCs are notoriously difficult to determine, being subject to a host of systematic uncertainties (Chaboyer et al. 1996a), but there is hope for a determination of the relative age distribution, which is still an important constraint on models. The two-phase models and the merger model clearly require that the metal-rich clusters be younger on average than the

metal-poor clusters, although none of the models predicts a specific age difference. In the accretion scenario, the globular clusters are assumed to form with their parent galaxies, so any age difference between metal-rich and metal-poor clusters depends on the age difference between large and small elliptical galaxies. The hierarchical galaxy formation picture would then suggest that the smaller galaxies finish forming first, so their metal-poor clusters could be older. But if galaxies formed by collapse, the smaller galaxies (and their metal-poor globular clusters) could be the last to form and therefore younger.

Testing predictions about relative ages is difficult. The integrated colors and spectral features of GCs suffer from age-metallicity degeneracy, and cannot easily distinguish between an old, metal-rich population, and a young, metal-poor one (Worthey 1994). Only the relative ages of some Milky Way globular clusters are reasonably well-established. Sarajedini et al. (1997) found that there is an age spread for the Milky Way halo clusters at $R > 8$ kpc, lending some support to the collapse picture, at least for the outer halo. Rosenberg et al. (1999) also studied the age distribution of the Milky Way GCs. They found no age spread for metal-poor Milky Way GCs, a large age dispersion for intermediate-metallicity GCs, and a systematically younger age for metal-rich GCs. This seems to support the collapse picture, although it is also consistent with the merger scenario. Chapters 3 and 4 discuss the age distributions of Milky Way and M31 GCs in more detail.

All known globular clusters are associated with galaxies, because galaxies are where we look for GCs. There is clearly an association between globular clusters and galaxies, and globular clusters have much to contribute towards the understanding of galaxy formation. Key observables include the total number of globular clusters and its relation to galaxy luminosity/mass, and the distribution of GC properties such as age, mass, and metallicity. These parameters are likely not independent of each other, and it may seem hopeless to use them to find out anything about their parent galaxies. However, the integrated properties of the field stellar populations in galaxies are even more difficult to disentangle, so GCs are still some of the best tools for understanding galaxy histories.

1.5 Relevance of M31 and this thesis

The study of the M31 globular cluster system has much to contribute to the questions discussed in the previous sections. After the Milky Way GCS, the M31 GCS is the nearest large globular cluster system. The Magellanic Cloud clusters are much nearer, but only a small number are old, 'globular' clusters. M31 is,

of course, also the nearest large galaxy, and its properties have been extensively studied (Hodge 1992). The M31 GCS provides an important bridge between the study of Milky Way GCs as objects made up of individual stars (e.g., with color-magnitude diagrams) and as populations for which only integrated properties are available. The inclination of the M31 disk to the line of sight (77°) is large enough to allow detailed kinematical studies, but small enough that few clusters are completely hidden by the M31 disk.

M31's other relevant characteristic for the study of globular clusters is its morphology. Most studies of extragalactic globular cluster systems have been of elliptical galaxies for two simple reasons: ellipticals have more clusters, and their clusters are more easily found. It is much simpler to subtract the smooth background of an elliptical galaxy than the irregular background of a spiral. Although globular clusters have been detected in ~ 20 spiral and irregular galaxies (Ashman & Zepf 1998), M31 and the Milky Way are the only spirals whose GCSs have been examined in detail. Understanding the properties of spiral galaxies' GCSs is critical to ensure that conclusions about galaxy and cluster formation do not apply only to ellipticals. It is also critical for understanding the differences between spirals and ellipticals' GCSs, especially in the light of the (spiral+spiral→elliptical) merger hypothesis.

The M31 GCS has been studied for many years (over 70 papers referenced in this thesis have M31 GCs as their primary subject), so why another study? Advances in both observation and theory drove this research. Large-format CCD detectors made possible precise optical photometry of all M31 globular clusters; such photometry allows observations to be made at longer wavelengths and with better background subtraction than with photoelectric photometers. This is critical for clusters projected onto the disk of M31. Availability of an infrared array camera allowed me to double the number of M31 GCs with near-IR photometry, which is important in estimating reddening and metallicities. The advance of theoretical work on stellar populations provided a new generation of models to be compared to the globular clusters' photometric properties. Interest in globular cluster systems has been spurred by the success of the Hubble Space Telescope and 10-m class telescopes in detecting and studying globular cluster around galaxies as far away as the Coma cluster (Baum et al. 1995) and possible young cluster systems in interacting galaxies (Holtzman et al. 1992). It is important to have modern, reliable data on the M31 cluster system since it serves as a comparison for these more distant cluster systems. The renewed interest in globular clusters has produced a number of new ideas about the relationships between globular clusters and their parent galaxies (e.g., McLaughlin 1999; Burgarella et al. 2000; Forbes &

Forte 2001). Although these works have mainly focussed on elliptical galaxies, the broad similarity of spiral and elliptical GCSs mean that they should be applicable to spirals as well; M31 provides some of the detailed observational data required to test these theories.

In Chapter 2 I lay the groundwork for the study of the M31 GCS, compiling a new catalog of the best available photometry and spectroscopy for confirmed clusters and plausible cluster candidates. This catalog includes a substantial amount of new observational data, mostly obtained with the 1.2m telescope of the Fred L. Whipple Observatory. Using this data, I estimate the individual reddening of 212 M31 globular clusters and define the relationship between intrinsic color and metallicity. I determine the metallicity distribution for the M31 clusters, and investigate relationships between galactocentric distance, luminosity, and metallicity. In Chapter 3, I compare the intrinsic colors of M31 and Milky Way clusters of known metallicity to the predictions of population synthesis models. In Chapter 4, I examine variations in the M31 globular cluster luminosity function with galactocentric distance and metallicity. In Chapter 5, I use images from the Hubble Space Telescope Archive to search for new globular cluster candidates in M31 and to measure the structural properties of over 70 detected clusters. Chapter 6 contains a summary of the important results and their implications and prospects for future work.

Chapters 2, 3 and 4 have been previously published as Barmby, P., Huchra, J.P., Brodie, J.P., Forbes, D.A., Schroder, L.L., & Grillmair, C.J. 2000, AJ, 119, 727; Barmby, P. & Huchra, J.P. 2000, ApJ, 531, L29; and Barmby, P., Huchra, J.P. & Brodie, J.P. 2001, AJ, 121, 1482, respectively. They appear here by permission of the American Astronomical Society.

Chapter 2

M31 Globular Clusters: Colors and Metallicities

2.1 Introduction

M31's globular clusters were first recognized by Hubble (1932). The M31 globular cluster system has a unique place in the study of globular cluster systems: it is the most populous GCS in the Local Group, with about 800 proposed cluster candidates. Over 200 of these objects have been confirmed as clusters, 200 have been shown not to be clusters, and the nature of the remaining objects is unknown. The study of the M31 GCS provides a bridge between the study of the Galactic globular clusters, where most observations are of individual stellar properties, and the study of most extragalactic clusters, where integrated properties are the only observables. In M31, most data are on integrated properties, but the advent of HST has made individual stellar properties available in the form of color-magnitude diagrams (e.g. Ajhar et al. 1996), and ground-based adaptive optics systems will continue this trend. The same technological advances also extend the distance to which individual GCs can be observed: for example, Baum et al. (1997) detected

*Work reported here is based on observations made with the Multiple Mirror Telescope, a joint facility of the Smithsonian Institution and the University of Arizona. Some of the data presented herein were obtained at the W.M. Keck Observatory, which is operated as a scientific partnership among the California Institute of Technology, the University of California, and the National Aeronautics and Space Administration. The Observatory was made possible by the generous support of the W.M. Keck Foundation. This publication makes use of data products from the Two Micron All Sky Survey, which is a joint project of the University of Massachusetts and the Infrared Processing and Analysis Center, funded by the National Aeronautics and Space Administration and the National Science Foundation.

globular clusters around the Coma cluster galaxy IC 4051. The M31 GCS will be important as a comparison in the study of the integrated properties of these distant cluster systems.

Studies of the M31 globular cluster system are numerous: some of the major attempts to catalog the system include Vetešnik (1962a), Sargent et al. (1977), Battistini et al. (1980, 1987, 1993) and Crampton et al. (1985). We attempt to combine the existing catalogs of M31 GCs to make a comprehensive catalog of confirmed clusters and good cluster candidates, and a complete list of definitive *non*-clusters. We bring together the published spectroscopic and photometric information along with substantial amount of new photometry in the optical and near-infrared, made possible by large-area mosaic CCD cameras and IR array detectors. We determine the reddening for individual clusters, and use these data to examine the extinction in M31 as a whole and the intrinsic colors of the clusters. We use the information to examine the use of colors both to identify clusters and as metallicity indicators. This is an important issue for distant GCSs, where obtaining spectroscopic information is not feasible. The combination of spectroscopic and photometric information allows us to search for multiple populations of globular clusters in M31 and determine those populations' characteristics.

2.2 Catalog preparation

A study of the M31 cluster system requires a catalog that is as complete and uncontaminated as possible, to avoid selection biases and interlopers. Our catalog is based on the work of several previous authors, of which the catalog of Battistini et al. (1987) is the most comprehensive. To this we added the DAO catalog (Crampton et al. 1985) and a list of cluster candidates near the nucleus by Battistini et al. (1993). The Battistini et al. (1987) and DAO catalogs cover the entire galaxy in a fairly uniform manner. To avoid introducing biases in the azimuthal distribution of clusters, we did not include the new cluster candidates of Mochejska et al. (1998) in our catalog since their fields cover only a small portion of the galaxy. We pruned our catalog by removing objects which the Bologna group classified as class 'C', 'D', or 'E' (unlikely to be clusters), unless they had been observed by another group. We also compiled a complete list of candidates shown not to be clusters by high-resolution imaging or spectroscopy, and removed these objects from our 'cluster' catalog.

Naming the M31 globular clusters is complicated by the number of works that have attempted to catalog the system. The Bologna group's catalogs are

the most extensive, so we retained their numbering system. Following Huchra, Brodie, & Kent (1991) (hereafter HBK), we added the number of the object in the "next most significant" catalogs to the Bologna numbers. These catalogs are the catalog of Sargent et al. (1977) (indicated without a letter after the dash), the 'DAO' objects of Crampton et al. (1985) (indicated with a D after the dash), and the catalog of Vetešnik (1962a) (his Hubble or Baade numbers indicated with H or B). Objects not in the Bologna catalog have numbers beginning with '000–' and objects appearing only in their catalog have numbers ending in '–000'. Of course, many objects appear in more than two catalogs, but we refer the reader to the original papers (Sargent et al. 1977; Battistini et al. 1987; Vetešnik 1962a) for further cross-identifications. Note that the Bologna group maintained a separate numbering system for their D-class objects, so 150D–000 is object #150 in the Battistini et al. (1987) list of D-class objects and 279–D068 is #279 in Battistini et al. (1987) and #68 in Crampton et al. (1985).

The finding charts in the Bologna group's papers were extremely useful in correctly identifying the clusters and cluster candidates in the crowded M31 fields. However, we found several cases where the object identified on the finding charts did not match the coordinates in the table, considered relative to nearby objects. The coordinates in the Battistini et al. (1987) table are the same as those given in Sargent et al. (1977), so we take those to be the correct positions. The objects incorrectly shown on the finding charts and their correct positions are: 064–125 (about $1'$ east of indication), 208–259 ($1'$ south and $20''$ east), and 375–307 ($15''$ east, $25''$ south). The object identified on the finding chart as 375–307 is actually 268D–D082.

The next step after constructing the object catalog was the construction of a photometry catalog; analyzing the color and color-metallicity distributions and determining the reddening required that we compile as much photometric information as possible, and that it be as accurate as possible. For our catalog, we attempted to find the "best" photometry for each object by searching the literature, in the following order of priority: (1) CCD photometry (Reed et al. 1992, 1994; Battistini et al. 1993; Mochejska et al. 1998), (2) photoelectric photometry (the series of papers by Sharov, Lyutyi, and collaborators, some of which are compilations of earlier photoelectric measurements), and (3) photometry from photographic plates (Buonanno et al. 1982; Crampton et al. 1985; Battistini et al. 1987). We did not include the photographic r-band data of Battistini et al. (1987) since these have a large zero-point offset from the standard Cousins R-band (Reed et al. 1992); we also did not include photometric data marked as uncertain (although we did compare these data with our photometry) or with given

photometric errors > 0.1 mag. There is no overlap between the CCD photometry datasets (they cover different parts of the galaxy), so we did not need to choose between different observations of the same object. For duplicate observations in the photoelectric data, we used the most recent "average" value, which includes all of the observations by Sharov, Lyutyi, and collaborators of a given object. For duplicate instances of plate photometry, we used the most recent value. Because the photoelectric and photographic data are in UBV or $B-V$ and the CCD data in subsets of $BVRI$, compiling data for each object in as many filters as possible resulted in many of the objects having photometry from multiple sources. Part of the motivation for our new observations was to produce a set of consistent photometry using the same identifications and aperture sizes for all objects.

In the near-infrared, there are fewer sources of photometry (Frogel, Persson, & Cohen 1980; Sitko 1984; Bònoli et al. 1987, 1992; Cohen & Matthews 1994) and there is less overlap between them. We used the list of observations in Bònoli et al. (1992), which includes the earlier IR papers, and added the data reported in Cohen & Matthews (1994). Most observations of the same object by different groups agreed very well, and we used the Frogel et al. (1980) observations when these duplications occurred. There were a few cases where duplicate observations did not agree (317–041, 029–090, 403–348, 373–305), and for these we used the photometry with the smaller reported error. Table 2.1 contains the "best" photometry, with references, for all of the objects in our catalog. Where an object has multiple sources for optical photometry, the references are given in order for the individual filters or colors. The comments section in this table indicates the existence of additional observational data not used in this study. These include high-resolution imaging to confirm that objects are clusters (HRI), from Racine (1991) and Racine & Harris (1992); color-magnitude diagrams (CMD), from various authors; and high resolution spectroscopy (HRS), from Dubath & Grillmair (1997) or Djorgovski et al. (1997).

Table 2.1. Catalog of photometric data for M31 globular clusters

name	V	$B-V$	$U-B$	$V-R$	$V-I$	J	H	K	opt source[a]	IR source[a]	comments
000–001	13.75	0.83	0.29	0.56	···	11.84	11.20	11.04	(1,1,2,1)	(3)	CMD4,HRI1,HRS1
000–002	15.81	0.68	0.26	0.48	···	13.97	13.53	13.43	(1,1,4,1)	(5)	HRS1
000–260	17.01	0.80	0.06	0.48	···	15.33	14.55	14.52	(6,6,2,6)	(7)	HRI1
000–268	16.63	0.96	0.54	0.62	···	14.43	13.82	13.54	(6,6,6,6)	(7)	···
000–327	15.94	0.73	0.20	0.54	···	14.20	13.69	13.52	(6,6,8,6)	(3)	CMD2,HRI1
000–353	17.15	0.65	0.32	0.42	···	15.52	14.97	14.83	(6,6,2,6)	(7)	HRI1
001–039	17.06	1.27	0.49	···	···	14.78	···	14.10	(2)	(9)	···
002–043	17.59	0.72	0.12	···	···	···	···	···	(2)	···	···
003–045	17.63	0.74	0.26	···	···	···	···	···	(2)	···	···
004–050	16.97	0.90	0.50	0.61	···	···	···	···	(1,1,8,1)	···	···
005–052	15.71	0.97	0.36	···	···	···	···	···	(10)	···	···
006–058	15.57	0.94	0.49	0.57	···	13.33	12.68	12.54	(1,1,2,1)	(3)	CMD1,HRS1,HRS2
008–060	16.52	1.03	0.59	···	···	···	···	···	(8)	···	···
009–061	17.10	0.62	0.26	···	···	15.13	14.66	14.64	(10)	(11)	N205?
010–062	16.65	0.58	0.19	···	···	···	···	···	(12,12,2)	···	···
011–063	16.79	0.74	0.08	···	···	14.84	14.15	14.19	(8)	(5)	N205
012–064	15.14	0.67	0.10	···	···	13.31	12.82	12.69	(12,12,2)	(3)	HRS1
013–065	17.05	0.72	0.46	···	···	···	···	···	(12,12,2)	···	···
014–B222	17.88	1.50	0.29	···	···	···	···	···	(2)	···	···
015–B204	17.95	1.05	···	···	···	···	···	···	(13)	···	···
016–066	17.45	1.09	0.32	···	···	···	···	···	(2)	···	···
017–070	15.87	1.16	0.39	···	···	···	···	···	(12,12,2)	···	···
018–071	17.51	0.74	0.22	···	···	···	···	···	(2)	···	···
019–072	14.99	0.96	0.41	···	···	12.80	12.14	11.98	(2)	(3)	···
020–073	14.91	0.83	0.22	0.54	···	12.89	12.28	12.15	(1,1,14,1)	(3)	HRS1,HRS2
021–075	17.34	0.96	0.36	···	···	···	···	···	(2)	···	···

Table 2.1—Continued

name	V	$B-V$	$U-B$	$V-R$	$V-I$	J	H	K	opt source[a]	IR source[a]	comments
022–074	17.41	0.76	0.10	···	···	···	···	···	(2)	···	···
023–078	14.26	1.13	0.52	···	···	11.62	10.90	10.72	(2)	(3)	HRS1
024–082	16.85	0.88	0.58	0.60	···	···	···	14.20	(1,1,10,1)	(9)	···
025–084	16.81	0.91	0.50	···	···	···	···	···	(4)	···	···
026–086	17.47	1.09	0.66	···	···	···	···	···	(2)	···	···
027–087	15.63	0.84	0.26	···	···	13.71	13.20	13.15	(2)	(3)	···
028–088	16.81	0.93	0.09	···	···	···	···	···	(4)	···	···
029–090	16.64	1.01	0.66	···	···	14.42	···	13.64	(4)	(9)	···
030–091	17.89	1.89	1.27	···	···	···	···	···	(15,15,12)	···	···
031–092	17.85	1.20	0.49	···	···	···	···	···	(15)	···	···
032–093	17.66	1.22	1.01	···	···	···	···	···	(15)	···	···
033–095	17.89	0.99	0.47	···	···	···	···	···	(2)	···	···
034–096	15.53	0.90	0.41	···	···	13.33	12.70	12.59	(2)	(3)	···
035–000	17.58	0.92	0.26	···	···	···	···	···	(12)	···	···
036–000	17.38	0.98	0.36	···	···	···	···	···	(4)	···	···
037–B327	16.71	2.14	···	···	···	12.20	11.23	10.95	(13)	(5)	···
038–098	16.48	0.89	0.31	···	···	···	···	···	(4)	···	···
039–101	16.13	1.25	0.64	···	···	···	···	···	(14)	···	···
040–102	17.46	0.38	0.05	···	···	···	···	···	(15)	···	···
041–103	···	···	···	···	···	···	···	···	···	···	···
042–104	16.16	1.62	0.71	···	···	···	···	···	(10)	···	···
043–106	16.96	0.26	−0.02	···	···	···	···	···	(2)	···	young?
044–107	16.62	1.30	0.44	···	···	···	···	···	(10)	···	···
045–108	15.83	0.97	0.36	···	···	13.65	13.09	12.88	(2)	(3)	CMD1,HRS1,HRS2
046–109	17.83	0.90	0.20	···	···	15.97	15.46	15.44	(2)	(11)	···
047–111	17.45	0.89	0.24	···	···	···	···	···	(2)	···	···

Table 2.1—Continued

name	V	$B-V$	$U-B$	$V-R$	$V-I$	J	H	K	opt source[a]	IR source[a]	comments
048–110	16.64	1.16	0.72	···	···	···	···	···	(2)	···	···
049–112	17.82	0.51	0.85	···	···	···	···	···	(15)	···	···
050–113	16.85	0.99	0.29	···	···	···	···	···	(2)	···	···
051–114	16.14	1.11	0.66	···	···	13.62	12.94	12.77	(4)	(3)	···
052–B266	17.37	1.51	0.58	···	···	···	···	···	(2)	···	···
053–000	17.85	1.20	···	···	···	···	···	···	(13)	···	···
054–115	18.21	0.89	0.52	···	···	···	···	···	(15)	···	···
056–117	17.14	0.91	0.59	···	···	···	···	···	(4)	···	···
057–118	17.66	0.78	−0.03	···	···	···	···	···	(15)	···	···
058–119	15.04	0.82	0.22	···	···	13.09	12.52	12.38	(2)	(3)	···
059–120	17.17	1.17	···	···	···	···	···	···	(13)	···	···
060–121	16.64	0.40	0.30	···	···	···	···	···	(2)	···	···
061–122	16.73	1.16	0.53	···	···	···	···	···	(10)	···	···
062–123	17.32	1.44	0.50	···	···	···	···	···	(2)	···	···
063–124	15.74	1.21	0.60	···	···	···	···	···	(4)	···	···
064–125	16.44	0.85	0.31	···	···	···	···	···	(2)	···	···
065–126	16.93	0.86	0.37	···	···	···	···	···	(4)	···	···
066–128	17.42	0.36	−0.27	···	···	···	···	···	(2)	···	···
067–129	17.24	0.87	0.46	···	···	···	···	···	(15)	···	···
068–130	16.42	1.34	0.63	···	···	13.77	···	12.94	(4)	(9)	···
069–132	18.64	0.25	0.60	···	···	···	···	···	(2)	···	···
070–133	16.77	0.76	···	···	···	···	···	···	(13)	···	···
071–000	18.18	1.23	···	···	···	···	···	···	(15)	···	···
072–000	17.26	1.28	1.37	···	···	···	···	···	(15)	···	···
073–134	15.99	0.92	0.49	···	···	13.91	13.10	13.16	(2)	(5)	···
074–135	17.25	0.90	−0.14	···	···	···	···	···	(2)	···	···

Table 2.1—Continued

name	V	$B-V$	$U-B$	$V-R$	$V-I$	J	H	K	opt source[a]	IR source[a]	comments
075–136	17.17	0.97	0.44	···	···	···	···	···	(15)	···	···
076–138	16.88	0.84	0.11	···	···	···	···	···	(4)	···	···
077–139	17.32	1.19	···	···	···	···	···	···	(13)	···	···
078–140	18.71	1.86	···	···	···	···	···	···	(15)	···	···
079–000	17.67	1.33	0.97	···	···	···	···	···	(15)	···	···
080–141	17.59	1.38	1.20	···	···	···	···	···	(4)	···	···
081–142	16.72	0.63	0.43	···	···	···	···	···	(4)	···	···
082–144	15.59	1.67	1.40	···	···	···	···	···	(10)	···	···
083–146	17.09	0.86	0.54	···	···	···	···	···	(2)	···	···
084–000	17.62	1.08	0.58	···	···	···	···	···	(15)	···	···
085–147	16.84	0.71	0.37	···	···	···	···	···	(2)	···	···
086–148	15.04	0.75	0.08	···	···	13.44	12.99	12.96	(2)	(3)	···
088–150	15.44	1.10	0.43	···	···	12.98	12.37	12.22	(2)	(3)	···
089–000	18.28	0.40	0.43	···	···	···	···	···	(15)	···	···
090–000	···	···	···	···	···	···	···	···	···	···	···
091–151	17.59	0.54	0.42	···	···	···	···	···	(15)	···	···
092–152	17.02	0.71	···	···	···	···	···	···	(13)	···	···
093–155	16.89	1.00	0.57	···	···	···	···	···	(2)	···	···
094–156	15.60	0.90	0.52	···	···	···	···	···	(2)	···	···
095–157	15.95	1.35	0.64	···	···	···	···	···	(2)	···	···
096–158	16.54	1.47	1.13	0.36	1.49	···	···	···	(16,16,2,16,16)	···	···
097–159	16.85	1.26	0.21	···	···	···	···	···	(2)	···	···
098–000	16.32	0.87	0.33	···	···	···	···	···	(10)	···	···
099–161	16.82	0.94	···	···	···	···	···	···	(13)	···	···
100–163	17.91	0.88	0.15	···	···	···	···	···	(2)	···	···
101–164	16.91	0.79	0.16	···	···	···	···	···	(15)	···	···

Table 2.1—Continued

name	V	$B-V$	$U-B$	$V-R$	$V-I$	J	H	K	opt source[a]	IR source[a]	comments
102–000	16.69	0.55	−0.15	···	···	···	···	···	(10)	···	···
103–165	15.20	1.25	0.61	0.26	1.29	12.98	···	12.10	(16,16,14,16,16)	(9)	···
104–NB5	17.40	1.06	···	0.15	0.95	···	···	···	(16)	···	···
105–166	17.25	0.97	0.57	···	···	···	···	···	(2)	···	···
106–168	16.14	1.19	0.47	0.17	1.07	14.10	···	13.32	(16,16,2,16,16)	(9)	···
107–169	15.79	1.20	0.41	0.25	1.20	13.75	···	13.04	(16,16,14,16,16)	(9)	···
108–167	18.03	0.50	0.84	···	···	···	···	···	(15)	···	···
109–170	16.02	0.93	0.69	···	···	···	···	···	(4)	···	···
110–172	15.22	0.89	0.33	···	···	13.09	12.42	12.29	(2)	(3)	···
111–173	16.82	0.69	0.21	···	···	···	···	···	(2)	···	···
112–174	16.33	1.42	0.70	0.27	1.37	13.84	···	12.84	(16,16,2,16,16)	(9)	···
114–175	17.13	0.98	···	0.10	0.95	15.06	···	14.28	(16)	(9)	···
115–177	16.05	1.27	···	0.22	1.21	13.42	···	12.50	(16)	(9)	···
116–178	16.85	1.47	0.50	···	···	···	···	···	(2)	···	···
117–176	16.36	0.76	0.29	···	···	···	···	···	(2)	···	young?
118–NB6	16.38	1.09	···	0.10	0.92	···	···	···	(16)	···	···
119–NB14	17.27	1.47	···	0.16	1.44	···	···	···	(16)	···	···
122–181	17.91	1.40	0.84	···	···	···	···	···	(4)	···	···
123–182	17.45	1.04	···	···	···	···	···	···	(13)	···	···
124–NB10	14.71	1.16	···	0.23	0.84	···	···	···	(16)	···	···
125–183	16.53	0.77	0.14	···	···	···	···	···	(14)	···	···
126–184	17.09	0.99	···	0.15	0.56	15.18	···	14.30	(16)	(9)	···
127–185	14.47	1.10	0.40	0.25	0.85	12.43	···	11.66	(16,16,2,16,16)	(9)	···
128–187	17.08	1.07	···	···	···	···	···	···	(13)	···	···
129–000	17.40	2.16	···	···	···	···	···	···	(15)	···	···
130–188	16.90	1.18	0.45	···	···	···	···	···	(2)	···	···

Table 2.1—Continued

name	V	$B-V$	$U-B$	$V-R$	$V-I$	J	H	K	opt source[a]	IR source[a]	comments
131–189	15.07	0.86	0.38	···	···	13.37	···	12.62	(2)	(9)	···
133–191	17.51	0.66	···	···	···	···	···	···	(13)	···	···
134–190	16.52	1.07	0.18	0.19	0.73	14.62	···	14.11	(16,16,4,16,16)	(9)	···
135–192	16.07	0.91	0.22	···	···	···	···	···	(2)	···	···
136–194	16.88	1.16	···	···	···	15.31	···	14.45	(13)	(9)	···
137–195	17.73	1.55	0.14	···	···	···	···	···	(2)	···	···
138–000	16.84	1.32	···	···	···	···	···	···	(13)	···	···
141–197	16.90	1.00	0.33	···	···	···	···	···	(4)	···	···
143–198	15.94	1.08	1.20	···	···	13.71	···	12.80	(8)	(9)	···
144–000	16.71	1.34	···	···	···	···	···	···	(13)	···	···
145–000	18.1	···	···	···	···	···	···	···	(17)	···	···
146–000	16.85	1.12	···	···	···	···	···	···	(13)	···	···
148–200	16.00	0.80	0.12	···	···	13.95	···	13.31	(8)	(9)	···
149–201	17.10	1.02	0.43	···	···	···	···	···	(2)	···	···
150–203	16.86	0.82	0.75	···	···	···	···	···	(8)	···	···
150D–000	17.67	0.50	0.04	···	···	···	···	···	(12)	···	HRI2
151–205	14.83	1.27	0.73	···	···	12.33	11.64	11.47	(2)	(3)	···
152–207	16.08	0.94	0.48	···	···	14.12	···	13.24	(2)	(9)	···
153–000	16.36	0.95	0.62	···	···	···	···	···	(8)	···	···
154–208	17.02	1.12	0.45	···	···	14.68	13.90	13.72	(8)	(3)	···
155–210	18.03	1.49	···	···	···	···	···	···	(15)	···	···
156–211	17.94	0.83	−0.48	···	···	···	···	···	(15)	···	···
157–212	17.80	0.34	0.13	···	···	···	···	···	(15)	···	···
158–213	14.68	0.90	0.32	···	···	12.63	11.97	11.83	(2)	(3)	HRS1,HRS2
159–000	17.42	0.78	···	···	···	···	···	···	(13)	···	···
160–214	18.12	0.66	0.22	···	···	···	···	···	(15)	···	···

Table 2.1—Continued

name	V	$B-V$	$U-B$	$V-R$	$V-I$	J	H	K	opt source[a]	IR source[a]	comments
161–215	16.19	0.82	0.42	···	···	···	···	···	(10)	···	···
162–216	17.60	0.82	···	···	···	···	···	···	(13)	···	···
163–217	15.05	1.04	0.64	···	···	12.57	11.83	11.62	(2)	(3)	···
164–B253	17.80	1.17	···	···	···	···	···	···	(13)	···	···
165–218	16.39	0.74	0.37	···	···	···	···	···	(8)	···	···
166–000	16.85	0.65	···	···	···	···	···	···	(13)	···	···
167–000	17.24	1.21	···	···	···	···	···	···	(13)	···	···
167D–000	17.95	0.77	−0.11	···	···	···	···	···	(12)	···	HRI2
168–000	17.97	1.47	1.38	···	···	···	···	···	(15)	···	···
169–000	17.04	1.09	0.37	···	···	···	···	···	(2)	···	···
170–221	17.50	0.91	0.48	···	···	···	···	···	(2)	···	···
171–222	15.24	0.98	0.57	···	···	12.96	12.28	12.08	(8)	(3)	···
172–223	16.65	0.98	0.54	···	···	···	···	···	(8)	···	···
173–224	17.51	0.85	···	···	···	···	···	···	(13)	···	···
174–226	15.48	0.98	0.35	···	···	···	···	···	(2)	···	···
176–227	16.52	0.75	0.09	···	···	···	···	···	(14)	···	···
177–228	···	···	···	···	···	···	···	···	···	···	···
178–229	15.04	0.79	0.11	···	···	···	···	···	(2)	···	···
179–230	15.24	0.84	0.26	···	···	13.52	12.84	12.73	(2)	(3)	···
180–231	16.04	0.90	0.38	···	···	···	···	···	(2)	···	···
181–232	16.81	1.00	0.05	···	···	···	···	···	(2)	···	···
182–233	15.38	0.96	0.32	···	···	13.12	12.43	12.28	(2)	(3)	···
183–234	15.97	0.97	0.51	···	···	13.79	13.13	13.00	(2)	(3)	···
184–236	17.53	1.38	0.96	···	···	···	···	···	(2)	···	···
185–235	15.56	0.90	0.47	···	···	···	···	···	(2)	···	···
186–000	18.13	1.26	1.29	···	···	···	···	···	(15)	···	···

Table 2.1—Continued

name	V	$B-V$	$U-B$	$V-R$	$V-I$	J	H	K	opt source[a]	IR source[a]	comments
187–237	17.19	1.14	0.46	···	···	···	···	···	(2)	···	···
188–239	17.06	0.66	···	···	···	···	···	···	(13)	···	···
189–240	17.18	1.10	0.88	···	···	···	···	···	(2)	···	···
190–241	16.81	0.84	0.58	···	···	···	···	···	(2)	···	···
192–242	18.28	0.20	0.32	···	···	···	···	···	(2)	···	···
193–244	15.37	1.00	0.64	···	···	13.03	12.35	12.15	(2)	(3)	HRS1
194–243	17.14	0.77	0.57	···	···	···	···	···	(2)	···	···
195–000	18.80	0.53	0.61	···	···	···	···	···	(15)	···	···
196–246	17.40	0.65	0.13	0.65	···	···	···	···	(1,1,2,1)	···	···
197–247	17.98	1.85	−0.55	···	···	···	···	···	(12)	···	···
198–249	17.56	1.22	···	···	···	···	···	···	(13)	···	···
199–248	17.60	0.77	0.08	···	···	···	···	···	(2)	···	···
200–000	···	···	···	···	···	···	···	···	···	···	···
201–250	16.20	0.85	0.31	···	···	···	···	···	(14)	···	···
202–251	17.66	0.98	0.24	···	···	···	···	···	(2)	···	···
203–252	16.88	0.85	0.28	···	···	···	···	···	(2)	···	···
204–254	15.74	0.96	0.49	···	···	···	···	···	(2)	···	···
205–256	15.43	0.82	0.28	···	1.09	13.42	12.74	12.64	(18,2,2,18)	(3)	···
206–257	15.06	0.87	0.22	···	1.07	···	···	···	(18,2,2,18)	···	···
207–258	17.47	1.06	−0.30	···	···	···	···	···	(15)	···	···
208–259	17.78	1.33	0.36	···	1.22	···	···	···	(18,12,12,18)	···	···
209–261	16.64	0.81	0.27	···	1.01	···	···	···	(18,2,2,18)	···	···
210–000	17.81	0.60	0.09	···	0.41	···	···	···	(18,15,15,18)	···	···
211–262	16.67	0.79	0.09	···	1.00	···	···	···	(18,14,14,18)	···	···
212–263	15.58	0.70	0.05	···	···	13.79	13.21	13.10	(2)	(3)	···
213–264	16.92	0.92	0.23	···	1.19	···	···	···	(18,2,2,18)	···	···

Table 2.1—Continued

name	V	$B-V$	$U-B$	$V-R$	$V-I$	J	H	K	opt source[a]	IR source[a]	comments
214–265	17.61	0.23	0.21	···	0.95	···	···	···	(18,15,15,18)	···	···
215–266	17.16	0.95	0.55	···	···	···	···	···	(15)	···	···
216–267	17.25	0.35	0.15	···	···	···	···	···	(2)	···	young?
217–269	16.49	1.00	0.30	···	1.12	···	···	···	(18,4,4,18)	···	···
218–272	14.77	0.86	0.30	···	1.14	12.70	12.06	11.88	(18,2,2,18)	(3)	HRS1,HRS2
219–271	16.39	0.94	0.52	0.57	···	···	···	···	(6,6,10,14)	···	···
220–275	16.62	0.86	0.12	···	1.06	···	···	···	(18,2,4,18)	···	···
220D–000	16.97	0.58	−0.04	···	···	···	···	···	(12)	···	HRI1
221–276	16.80	1.04	0.29	···	1.12	14.80	14.04	13.87	(18,2,2,18)	(3)	···
222–277	17.65	1.08	−0.17	1.02	···	···	···	···	(18,15,2,18)	···	···
223–278	17.81	0.38	0.14	···	0.14	···	···	···	(18,2,2,18)	···	···
224–279	15.45	0.74	0.11	···	1.03	13.73	13.20	13.11	(18,2,2,18)	(3)	···
225–280	14.15	0.95	0.52	···	···	11.94	11.21	11.06	(18,2,2)	(3)	CMD5,HRS1,HRS2
225D–000	18.36	0.53	−0.22	···	···	···	···	···	(12)	···	HRI2
226–000	17.65	1.05	0.04	···	1.34	···	···	···	(18,15,15,18)	···	···
227–000	17.79	1.00	−0.12	0.63	···	···	···	···	(6,6,15,6)	···	···
228–281	16.82	1.03	0.32	···	···	···	···	···	(8)	···	···
229–282	16.56	0.76	0.03	···	1.04	···	···	···	(18,10,10,18)	···	···
230–283	16.01	0.69	0.07	0.47	···	···	···	···	(6,6,14,6)	···	···
231–285	17.23	0.74	0.24	···	1.08	···	···	···	(18,15,15,18)	···	···
232–286	15.66	0.78	0.12	···	···	···	···	···	(2)	···	···
233–287	15.82	0.84	0.33	···	···	···	···	···	(2)	···	···
234–290	16.82	0.92	−0.04	···	···	···	···	···	(2)	···	···
235–297	16.36	0.86	0.45	···	···	···	···	···	(14)	···	···
236–298	17.33	0.72	0.15	0.68	···	···	···	···	(6,6,15,6)	···	HRI1
237–299	17.13	0.78	0.33	···	···	···	···	···	(2)	···	···

Table 2.1—Continued

name	V	$B-V$	$U-B$	$V-R$	$V-I$	J	H	K	opt source[a]	IR source[a]	comments
238–301	16.54	0.91	0.31	···	···	14.48	13.79	13.68	(4)	(3)	···
239–000	17.15	0.64	0.32	···	1.05	···	···	···	(18,15,15,18)	···	···
240–302	15.19	0.73	0.08	0.51	···	13.54	12.94	12.83	(6,6,2,6)	(3)	CMD3,HRI1,HRS1
242D–000	17.81	0.76	0.42	···	···	···	···	···	(12)	···	HRI2
244–000	18.40	0.79	0.46	···	···	···	···	···	(12)	···	···
260–000	18.50	···	···	···	···	···	···	···	(12)	···	···
268–000	18.20	···	···	···	···	···	···	···	(12)	···	···
272–B294	18.16	1.15	0.63	···	···	···	···	···	(2)	···	···
277–000	18.74	···	···	···	1.28	···	···	···	(18)	···	···
278–000	18.83	···	···	···	0.23	···	···	···	(18)	···	···
279–D068	18.40	···	···	···	···	···	···	···	(12)	···	···
281–288	18.08	0.74	0.12	···	···	···	···	···	(2)	···	···
282–000	18.20	···	···	···	···	···	···	···	(12)	···	HRI2
283–296	17.78	0.91	0.94	···	···	···	···	···	(2)	···	···
284–000	18.40	···	···	···	···	···	···	···	(12)	···	HRI2
289–000	16.09	0.67	0.18	0.47	···	14.28	13.68	13.64	(1,1,10,1)	(5)	HRI1,HRS1
290–000	17.14	0.91	0.97	0.57	···	15.23	14.48	14.27	(1,1,12,1)	(7)	HRI1
291–009	16.59	0.75	0.24	0.51	···	14.74	14.18	14.16	(1,1,2,1)	(11)	HRI1
292–010	17.00	0.90	−0.19	0.37	···	15.54	14.89	14.91	(6,6,10,6)	(7)	HRI1
293–011	16.30	0.74	0.14	0.51	···	14.60	14.00	13.99	(6,6,4,6)	(5)	CMD2
295–014	16.72	0.69	0.26	···	···	15.04	14.41	14.30	(10)	(7)	young?
298–021	16.59	0.64	0.10	0.56	···	15.25	14.53	14.24	(6,6,10,6)	(5)	···
299–000	16.83	1.20	0.86	0.50	···	···	···	···	(6,6,12,6)	···	···
301–022	17.12	1.01	0.35	···	···	15.08	14.26	14.08	(2)	(7)	···
302–023	16.68	0.78	0.17	0.50	···	···	···	···	(1,1,2,1)	···	HRI1
303–026	18.22	0.24	0.46	···	···	···	···	···	(2)	···	···

Table 2.1—Continued

name	V	$B-V$	$U-B$	$V-R$	$V-I$	J	H	K	opt source[a]	IR source[a]	comments
304–028	16.83	0.71	0.09	0.51	···	···	···	···	(1,1,2,1)	···	HRI1
305–D024	18.11	1.02	−0.15	···	···	···	···	···	(12)	···	···
306–029	16.30	1.21	0.64	···	···	13.41	12.71	12.51	(14)	(7)	···
307–030	17.41	0.78	1.01	···	···	···	···	···	(2)	···	···
309–031	17.50	0.97	0.16	···	···	···	···	···	(2)	···	···
310–032	17.04	0.76	0.15	0.50	···	···	···	···	(1,1,2,1)	···	HRI1
311–033	15.48	0.90	0.12	···	···	13.46	12.89	12.75	(2)	(3)	···
312–035	15.58	0.87	0.33	···	···	13.27	13.71	12.60	(4)	(5)	···
313–036	16.36	1.05	0.19	···	···	···	···	···	(10)	···	···
314–037	17.63	0.59	0.34	···	···	···	···	···	(2)	···	young?
315–038	16.32	0.35	−0.08	···	···	14.88	14.41	14.26	(2)	(7)	young?
316–040	16.82	0.84	−0.01	···	···	···	···	···	(2)	···	···
317–041	16.55	0.76	0.20	0.42	···	15.06	14.66	14.58	(1,1,10,1)	(3)	N205?
318–042	16.89	0.40	−0.40	···	···	15.99	15.42	15.34	(2)	(7)	young?
319–044	17.49	0.21	−0.01	···	···	···	···	···	(2)	···	···
320–000	18.2	···	···	···	···	···	···	···	(12)	···	N205?
321–046	17.78	0.23	0.10	···	···	···	···	···	(2)	···	young?
322–049	17.92	−0.08	−0.31	···	···	···	···	···	(12)	···	young?
323–000	17.74	0.93	0.42	···	···	···	···	···	(12)	···	···
324–051	16.91	0.66	0.79	···	···	···	···	···	(10)	···	young?,N205?
325–000	···	···	···	···	···	15.21	14.56	14.40	···	(7)	···
326–000	···	···	···	···	···	···	···	···	···	···	N205?
327–053	16.58	0.31	−0.35	···	···	···	···	···	(10)	···	young?
328–054	18.52	0.51	0.70	···	···	···	···	···	(2)	···	N205?
329–000	18.5	···	···	···	···	···	···	···	(12)	···	N205?
330–056	17.24	0.76	0.1	···	···	···	···	···	(2)	···	N205

Table 2.1—Continued

name	V	$B-V$	$U-B$	$V-R$	$V-I$	J	H	K	opt source[a]	IR source[a]	comments
331–057	17.86	0.72	0.80	···	···	···	···	···	(2)	···	N205
333–000	19.0	···	···	···	···	···	···	···	(12)	···	N205?
335–H13	18.04	1.78	0.17	···	···	···	···	···	(2)	···	···
336–067	17.81	0.71	0.14	0.41	···	···	···	···	(1,1,2,1)	···	HRI1
337–068	16.73	0.79	0.18	0.49	···	15.00	14.39	14.16	(1,1,8,1)	(7)	HRI1
337D–000	18.23	0.87	0.52	···	···	···	···	···	(12)	···	HRI2
338–076	14.26	0.84	0.23	···	···	12.35	11.75	11.61	(2)	(3)	···
339–077	16.87	0.89	···	0.60	···	14.70	14.00	13.75	(6)	(7)	HRI1
342–094	18.35	0.06	0.29	···	···	···	···	···	(2)	···	···
343–105	16.34	0.73	0.14	···	···	14.46	14.07	13.65	(2)	(5)	CMD1,HRS1,HRS2
344–127	15.94	0.84	0.25	···	···	14.02	13.40	13.29	(8)	(3)	···
344D–000	17.05	0.58	0.25	···	···	···	···	···	(12)	···	HRI2
345–143	16.84	0.76	0.12	···	···	14.64	14.16	14.15	(2)	(7)	···
346–149	17.48	1.67	0.56	···	···	···	···	···	(2)	···	···
347–154	16.54	0.68	0.14	···	···	···	···	···	(14)	···	young?
348–153	17.08	0.90	0.35	···	···	···	···	···	(2)	···	···
349–000	18.28	0.81	0.58	···	···	···	···	···	(12)	···	···
350–162	16.61	0.72	0.08	···	···	···	···	···	(2)	···	···
351–179	17.55	0.84	0.15	0.48	···	···	···	···	(1,1,2,1)	···	HRI1
352–180	16.53	0.70	0.09	···	···	···	···	···	(10)	···	···
353–CFA	···	···	···	···	···	···	···	···	···	···	···
354–186	17.80	0.70	0.25	···	···	···	···	···	(12)	···	···
355–193	17.63	0.66	0.02	···	···	···	···	···	(2)	···	···
356–206	17.34	0.78	0.30	···	···	···	···	···	(2)	···	···
357–209	16.61	0.88	0.35	0.64	···	14.51	13.80	13.57	(6,6,2,6)	(7)	···
358–219	15.12	0.59	0.05	0.48	···	13.57	13.05	12.91	(6,6,2,6)	(3)	CMD1,HRI1,HRS1,HRS2

Table 2.1—Continued

name	V	$B-V$	$U-B$	$V-R$	$V-I$	J	H	K	opt source[a]	IR source[a]	comments
361–255	17.10	0.74	0.14	···	···	15.31	14.64	14.64	(2)	(7)	HRI1
362–000	17.82	1.05	−0.25	···	···	···	···	···	(12)	···	···
363–274	17.86	0.65	0.14	0.48	···	···	···	···	(6,6,2,6)	···	HRI1
365–284	16.73	0.79	0.21	···	···	14.85	14.21	13.97	(10)	(7)	···
366–291	16.23	0.78	0.14	···	···	14.25	13.56	13.55	(14)	(7)	···
367–292	18.45	0.32	−0.17	···	···	···	···	···	(2)	···	···
368–293	18.04	0.23	−0.44	···	···	···	···	···	(2)	···	···
370–300	16.24	0.92	0.24	···	···	14.08	13.44	13.14	(2)	(5)	···
371–303	17.76	0.55	0.63	···	0.56	···	···	···	(18,2,2,18)	···	···
372–304	16.60	0.84	0.23	···	···	14.78	14.10	13.93	(2)	(7)	···
373–305	15.58	0.98	0.55	···	1.16	13.48	···	12.67	(18,2,2,18)	(9)	HRS1
374–306	18.08	0.24	0.45	···	0.61	···	···	···	(18,2,2,18)	···	···
375–307	17.47	1.62	0.30	···	1.03	···	···	···	(18,2,2,18)	···	···
376–309	17.91	0.29	0.23	···	0.64	···	···	···	(18,2,2,18)	···	young?
377–308	17.14	0.64	0.00	0.50	···	15.38	14.85	14.77	(1,1,2,1)	(11)	HRI1
378–311	17.83	0.69	0.33	···	···	···	···	···	(2)	···	···
379–312	16.13	0.90	0.35	0.57	···	14.02	13.37	13.22	(1,1,8,1)	(11)	CMD3,HRI1,HRS1
380–313	16.95	0.47	0.32	···	···	15.77	15.01	14.75	(10)	(7)	young?
381–315	15.76	0.85	0.30	0.61	···	13.76	13.16	12.96	(6,6,2,6)	(3)	···
382–317	17.36	0.79	0.13	···	···	···	···	···	(2)	···	···
383–318	15.33	0.83	0.48	0.46	···	13.59	12.83	12.66	(6,6,14,6)	(7)	···
384–319	15.79	0.95	0.57	0.53	···	13.91	13.29	13.31	(6,6,8,6)	(5)	CMD2,HRI1,HRS1,HRS
385–321	17.65	0.83	0.07	···	···	···	···	···	(2)	···	···
386–322	15.64	0.75	0.20	···	···	13.47	12.81	12.60	(2)	(5)	HRS1
387–323	16.98	0.68	0.15	0.50	···	15.43	14.82	14.70	(6,6,2,6)	(7)	CMD2,HRI1
389–326	17.54	1.44	0.36	···	···	···	···	···	(2)	···	···

Table 2.1—Continued

name	V	$B-V$	$U-B$	$V-R$	$V-I$	J	H	K	opt source[a]	IR source[a]	comments
391–328	17.18	0.86	0.28	···	···	···	···	···	(2)	···	···
393–330	16.93	0.79	0.19	0.53	···	···	···	···	(6,6,2,6)	···	HRI1
396–335	17.38	0.56	0.23	0.47	···	15.54	15.15	15.15	(6,6,2,6)	(11)	HRI1
397–336	16.53	0.63	0.40	0.65	···	14.54	13.79	13.79	(1,1,14,6)	(7)	HRI1
398–341	17.46	0.92	1.10	0.79	···	···	···	···	(6,6,8,6)	···	···
399–342	17.28	0.77	0.12	0.43	···	···	···	···	(6,6,2,6)	···	HRI1
400–343	16.46	0.81	0.32	0.48	···	14.58	13.76	13.76	(6,6,8,6)	(5)	···
401–344	16.83	0.69	0.27	0.32	···	15.20	14.60	14.57	(6,6,2,6)	(7)	HRI1
402–346	17.27	0.88	0.16	0.48	···	15.23	14.52	14.35	(6,6,2,6)	(7)	HRI1
403–348	16.22	0.98	0.54	0.59	···	13.89	13.31	13.05	(6,6,8,6)	(5)	···
405–351	15.20	0.74	0.18	0.54	···	13.58	12.91	12.80	(1,1,8,1)	(5)	CMD5,HRI1,HRS1
407–352	16.09	0.93	0.48	0.61	···	13.96	13.18	13.17	(1,1,2,1)	(5)	CMD2,HRI1,HRS1
416–D007	18.07	1.67	0.63	···	···	···	···	···	(12)	···	···
418–000	18.43	0.73	0.67	···	···	···	···	···	(12)	···	···
419–D010	18.4	···	···	···	···	···	···	···	(17)	···	···
422–000	18.11	0.60	0.48	···	···	···	···	···	(12)	···	HRI2
423–000	17.87	0.53	0.22	···	···	···	···	···	(12)	···	HRI2
424–D017	18.38	1.12	0.47	···	···	···	···	···	(12)	···	···
427–D019	18.18	1.18	0.62	···	···	···	···	···	(12)	···	···
430–025	18.52	0.50	−0.01	0.54	···	···	···	···	(1,1,2,1)	···	HRI1
431–027	17.73	0.49	0.29	···	···	···	···	···	(2)	···	···
432–000	18.33	0.59	···	0.27	···	···	···	···	(1)	···	···
433–000	18.28	0.90	−0.38	···	···	···	···	···	(12)	···	···
435–D028	18.61	1.52	0.42	···	···	···	···	···	(12)	···	···
436–000	18.41	0.96	···	···	···	···	···	···	(12)	···	···
442–D033	18.62	0.19	−0.09	···	···	···	···	···	(12)	···	···

Table 2.1—Continued

name	V	$B-V$	$U-B$	$V-R$	$V-I$	J	H	K	opt source[a]	IR source[a]	comments
443–D034	18.43	0.97	−0.70	···	···	···	···	···	(12)	···	···
448–D035	18.41	0.42	−0.13	···	···	···	···	···	(12)	···	···
449–H11	18.84	1.30	0.11	···	···	···	···	···	(2)	···	···
450–000	19.5	···	···	···	···	···	···	···	(12)	···	N205?,HRI2
451–D037	18.95	0.23	···	···	···	···	···	···	(12)	···	···
452–069	17.87	0.22	−0.09	···	···	···	···	···	(2)	···	···
453–D042	18.0	···	···	···	···	···	···	···	(17)	···	···
456–D045	18.09	0.66	−0.12	···	···	···	···	···	(12)	···	···
457–097	16.91	0.82	···	0.53	···	···	···	···	(1)	···	HRI1
458–D049	18.17	0.57	1.00	···	···	···	···	···	(12)	···	···
461–131	17.52	1.24	0.38	0.64	···	···	···	···	(1,1,2,1)	···	HRI1
462–000	18.17	0.98	0.02	···	···	···	···	···	(12)	···	HRI2
463–160	18.16	0.71	0.39	···	···	···	···	···	(2)	···	···
465–D057	16.5	···	···	···	···	···	···	···	(17)	···	···
467–202	17.43	0.88	0.05	···	···	···	···	···	(2)	···	···
468–000	18.12	0.53	0.06	···	···	···	···	···	(12)	···	CMD5,HRI2
469–220	17.58	0.53	−0.04	···	···	···	···	···	(2)	···	···
470–D063	17.89	0.99	−0.54	···	···	···	···	···	(12)	···	···
471–238	17.12	1.22	0.37	···	···	···	···	···	(2)	···	···
472–D064	16.00	···	···	···	···	···	···	···	(12)	···	···
473–000	17.46	1.05	0.35	···	0.90	···	···	···	(18,12,12,18)	···	···
475–H128	17.67	0.49	0.37	···	···	···	···	···	(12)	···	···
476–D074	18.25	···	···	···	1.03	···	···	···	(18)	···	···
477–D075	18.12	···	···	···	0.50	···	···	···	(18)	···	···
478–D076	17.50	1.09	0.15	···	···	···	···	···	(12)	···	···
479–D080	17.35	2.19	···	···	···	···	···	···	(12)	···	···

Table 2.1—Continued

name	V	$B-V$	$U-B$	$V-R$	$V-I$	J	H	K	opt source[a]	IR source[a]	comments
480–H127	17.91	···	···	···	0.72	···	···	···	(18)	···	···
483–D085	18.71	0.29	0.16	···	···	···	···	···	(12)	···	···
484–310	18.34	0.65	0.21	···	···	···	···	···	(2)	···	···
486–316	17.52	0.35	0.36	0.49	···	15.84	15.36	15.36	(6,6,15,6)	(11)	···
493–D090	18.11	1.49	1.98	···	···	···	···	···	(12)	···	···
495–333	17.39	1.33	0.38	···	···	···	···	···	(2)	···	···
BA11	17.66	0.59	0.14	···	···	···	···	···	(2)	···	···
DAO011	19.7	···	···	···	···	···	···	···	(17)	···	···
DAO016	18.5	···	···	···	···	···	···	···	(17)	···	···
DAO023	18.4	···	···	···	···	···	···	···	(17)	···	···
DAO025	18.8	···	···	···	···	···	···	···	(17)	···	···
DAO027	18.0	···	···	···	···	···	···	···	(17)	···	···
DAO030	18.4	···	···	···	···	···	···	···	(17)	···	···
DAO032	18.3	···	···	···	···	···	···	···	(17)	···	···
DAO040	18.0	···	···	···	···	···	···	···	(17)	···	···
DAO046	18.4	···	···	···	···	···	···	···	(17)	···	···
DAO047	19.0	···	···	···	···	···	···	···	(17)	···	···
DAO052	19.0	···	···	···	···	···	···	···	(17)	···	···
DAO053	18.8	···	···	···	···	···	···	···	(17)	···	···
DAO054	18.7	···	···	···	···	···	···	···	(17)	···	···
DAO055	18.7	···	···	···	···	···	···	···	(17)	···	···
DAO060	17.2	···	···	···	···	···	···	···	(17)	···	···
DAO062	18.3	···	···	···	···	···	···	···	(17)	···	···
DAO069	16.6	···	···	···	···	···	···	···	(17)	···	···
DAO083	19.8	···	···	···	···	···	···	···	(17)	···	···
DAO084	18.7	···	···	···	···	···	···	···	(17)	···	···

Table 2.1—Continued

name	V	$B-V$	$U-B$	$V-R$	$V-I$	J	H	K	opt source[a]	IR source[a]	comments
DAO094	18.58	0.70	···	0.28	···	···	···	···	(6)	···	···
DAO099	19.03	0.96	···	−0.02	···	···	···	···	(6)	···	···
DAO104	18.79	0.87	···	0.18	···	···	···	···	(6)	···	HRI1
EX8	···	···	···	···	···	14.03	13.51	13.41	···	(7)	···
NB16	18.17	1.33	···	0.51	1.55	···	···	···	(16)	···	young?
NB17	18.26	1.09	···	0.08	1.30	···	···	···	(16)	···	···
NB18	18.43	1.14	···	0.16	0.27	···	···	···	(16)	···	···
NB21	17.69	0.86	···	0.28	0.67	···	···	···	(16)	···	···
NB23	18.00	1.52	···	0.37	1.51	···	···	···	(16)	···	···
NB25	18.21	1.71	···	0.74	2.06	···	···	···	(16)	···	···
NB29	18.43	1.48	···	0.33	1.42	···	···	···	(16)	···	···
NB42	18.49	0.89	···	0.22	0.72	···	···	···	(16)	···	···
NB61	> 19	···	···	···	···	···	···	···	(16)	···	···
NB67	15.91	0.86	···	0.00	0.66	···	···	···	(16)	···	···
NB68	15.48	0.99	···	0.08	0.85	···	···	···	(16)	···	···
NB74	15.55	1.00	···	0.59	−0.05	···	···	···	(16)	···	···
NB81	16.14	1.00	···	−0.04	0.65	···	···	···	(16)	···	···
NB83	16.68	0.89	···	−0.03	0.66	···	···	···	(16)	···	···
NB87	15.58	1.04	···	0.17	0.64	···	···	···	(16)	···	···
NB89	> 19	···	···	···	···	···	···	···	(16)	···	···
NB91	15.65	0.92	···	0.08	0.47	···	···	···	(16)	···	···

[a]Key to references is in Table 2.2.

Table 2.2. References for Table 2.1

Code	Reference
(1)	Reed et al. (1994)
(2)	Sharov & Lyutyi (1983)
(3)	Frogel et al. (1980)
(4)	Sharov et al. (1987)
(5)	Bònoli et al. (1987)
(6)	Reed et al. (1992)
(7)	Bònoli et al. (1992)
(8)	Sharov et al. (1996)
(9)	Cohen & Matthews (1994)
(10)	Sharov et al. (1995)
(11)	Sitko (1984)
(12)	Battistini et al. (1987)
(13)	Buonanno et al. (1982)
(14)	Sharov et al. (1992)
(15)	Sharov & Lyutyi (1985)
(16)	Battistini et al. (1993)
(17)	Crampton et al. (1985)
(18)	Mochejska et al. (1998)
HRI1	Racine (1991)
HRI2	Racine & Harris (1992)
HRS1	Djorgovski et al. (1997)
HRS2	Dubath & Grillmair (1997)
CMD1	Ajhar et al. (1996)
CMD2	Couture et al. (1995)
CMD3	Holland et al. (1997)
CMD4	Rich et al. (1996)
CMD5	Fusi Pecci et al. (1996)

Our resulting catalog has a total of 435 objects. Prior to our new observations, all but 8 had at least estimated V magnitudes, and 330 had at least UBV photometry. 158 had been observed spectroscopically, and 106 had infrared photometry. Our catalog contains all the objects in the Battistini et al. (1993) "current best" and "extended" samples, except for a few objects shown to be non-clusters after 1993. About a dozen objects are possibly associated with NGC 205. Because this galaxy is located well within the M31 globular cluster halo, in both position and radial velocity, it is not obvious how to determine which clusters are actually associated with NGC 205 and which belong to the M31 halo; different authors have come to different conclusions on this subject (see Da Costa

& Mould 1988; Reed et al. 1992). We have flagged these possible NGC 205 clusters in Table 2.1. We retain them in our analysis of colors and color-metallicity relations, but omit them in studies of radial gradients and metallicity distribution. We note that no globular clusters are usually associated with M31's other close-in companion, M32 (Harris & Racine 1979).

We did not attempt to collect observational data for objects declared to be non-clusters, but we did retain a list of the classifications (star, galaxy, H II region) of the objects and the reference for this classification, given in Table 2.3.

Table 2.3. M31 cluster candidates shown not to be clusters

name	classification	reference
000-003	gal+star	(1)
000-004	gal	(1)
000-005	gal	(1)
000-006	gal	(1)
000-007	gal	(1)
000-008	gal	(1)
000-013	star	(1)
000-017	star	(1)
000-018	star	(2)
000-034	gal	(3)
000-079	gal	(4)
000-099	gal	(5)
000-100	star	(5)
000-145	QSO/Sy1	(1)
000-171	gal	(4)
000-225	Sy2	(1)
000-245	star	(1)
000-273	gal	(1,4)
000-294	gal	(1)
000-314	star	(2,3)
000-324	HIIR	(1)
000-338	gal	(4)
000-339	noncl	(6)
000-340	gal	(3)
000-347	gal	(1)
000-349	gal	(1)
000-355	gal+star	(1,4)
007-059	gal	(3)
053D-NB20	star	(3)
055-116	star	(3)
080D-NB93	star	(3)
087-000	star	(5)
113-000	star	(3)
120-000	star	(7)
121-000	star	(5)
132-000	star	(3)
133D-000	noncl	(8)
135D-000	noncl	(8)
137D-000	noncl	(8)

Table 2.3—Continued

name	classification	reference
140-196	gal	(4)
146D-000	noncl	(8)
147-199	star	(9)
175-000	star	(3,5)
179D-000	noncl	(8)
182D-000	noncl	(8)
184D-000	noncl	(8)
191-000	gal	(10)
191D-000	noncl	(8)
208D-000	noncl	(8)
209D-000	noncl	(8)
210D-000	noncl	(8)
211D-000	noncl	(8)
212D-000	noncl	(8)
213D-000	noncl	(8)
214D-000	noncl	(8)
222D-000	noncl	(8)
224D-000	noncl	(8)
229D-000	noncl	(8)
234D-000	noncl	(8)
236D-000	noncl	(8)
249D-000	noncl	(8)
251D-000	noncl	(8)
253D-000	noncl	(8)
259D-000	noncl	(8)
264-000	star	(3)
264D-000	noncl	(8)
267D-000	noncl	(8)
271D-000	noncl	(8)
272D-000	noncl	(8)
279D-000	noncl	(8)
280-000	noncl	(8)
281D-000	noncl	(8)
282D-000	noncl	(8)
284D-000	noncl	(8)
285-000	noncl	(8)
285D-000	noncl	(8)
287D-000	noncl	(8)
290D-000	noncl	(8)

Table 2.3—Continued

name	classification	reference
291D-000	noncl	(8)
293-000	noncl	(8)
294-012	gal	(4)
294D-000	noncl	(8)
296-015	gal	(1)
297-016	gal	(1)
299-000	gal	(6)
300-000	gal	(4)
301D-000	noncl	(8)
305D-000	noncl	(8)
306D-000	noncl	(8)
308-000	gal	(3)
309D-000	noncl	(8)
311D-337	gal	(11)
312D-000	noncl	(8)
316D-000	noncl	(8)
318D-000	noncl	(8)
321D-000	noncl	(8)
323D-000	noncl	(8)
333D-000	noncl	(8)
340-000	gal	(4)
341-081	star	(3)
345-143	gal	(4)
360-000	gal	(4)
364-000	gal	(4,11)
369-000	gal	(4,11)
390-000	gal	(4)
392-329	star	(3)
394-331	gal	(1)
395-332	gal	(3,4)
398-341	gal	(11)
404-350	gal	(4)
406-000	gal	(4)
408-354	gal	(1)
409-000	gal	(4)
410-000	gal	(4,11)
414-000	noncl	(8)
415-000	gal	(8)
417-000	gal	(8)

Table 2.3—Continued

name	classification	reference
421-019	gal	(4)
425-000	gal	(8)
426-000	star,gal	(2,10)
429-024	gal	(4)
432-000	noncl	(8)
434-000	gal	(4)
437-000	gal	(8)
441-000	noncl	(8)
444-000	noncl	(8)
445-000	noncl	(8)
446-000	noncl	(8)
455-080	gal	(4)
459-000	noncl	(8)
460-000	noncl	(8)
466-000	st	(4)
485-000	noncl	(8)
487-320	star,star+gal	(1,12)
491-000	noncl	(8)
496-000	noncl	(8)
496-334	gal	(8)
499-000	noncl	(8)
500-000	noncl	(8)
501-345	gal	(1)
502-000	noncl	(8)
504-000	noncl	(8)
505-D103	gal	(11)
507-000	noncl	(8)
509-000	gal	(4)
510-000	noncl	(8)
511-000	noncl	(8)
512-000	noncl	(8)
000-B285	noncl	(2)
DAO001	gal	(4)
DAO002	gal	(4)
DAO003	gal	(4)
DAO004	gal	(4)
DAO005	gal	(4)
DAO006	noncl	(2)
DAO009	gal	(2)

Table 2.3—Continued

name	classification	reference
DAO012	gal	(2)
DAO013	gal	(2)
DAO014	gal	(2)
DAO015	gal	(2)
DAO018	star	(3)
DAO022	gal	(4)
DAO029	gal	(4)
DAO031	gal	(4)
DAO031	gal	(10)
DAO038	gal	(2)
DAO051	gal	(2)
DAO061	gal	(4)
DAO061	gal	(10)
DAO067	HIIR	(2)
DAO071	gal	(2)
DAO081	gal	(2)
DAO086	gal	(2)
DAO087	gal	(2)
DAO088	HIIR	(2)
DAO089	gal	(11)
DAO091	gal	(11)
DAO092	gal	(11)
DAO093	gal	(11)
DAO095	gal	(4)
DAO095	gal	(11)
DAO096	gal	(11)
DAO097	gal	(4)
DAO098	gal	(11)
DAO100	gal	(4)
DAO100	gal	(11)
DAO101	gal	(11)
DAO102	gal	(4)
DAO102	gal	(11)
DAO105	gal	(4)
DAO106	gal	(4)
DAO106	gal	(11)
DAO107	gal	(4)
DAO107	gal	(11)
GS-1	star	(1)

Table 2.3—Continued

name	classification	reference
GS-SET	star	(1)
000-H129	HIIR	(13)
NB22	star	(14)
NB32	star	(14)
NB34	HIIR	(7)
NB38	gal	(14)
NB45	star	(7)
NB49	star	(7)
NB57	open cl.	(7)
NB94	star	(3)
NB95	star	(3)
NB96	star	(3)

References. — (1) Huchra et al. 1991;(2) Battistini et al. 1987; (3) this work (4) Racine 1991; (5) Crampton et al. 1985; (6) Federici et al. 1993; (7) Battistini et al. 1993; (8) Racine & Harris 1992; (9) Dubath & Grillmair 1997; (10) Reed et al. 1994; (11) Reed et al. 1992; (12) Cohen & Freeman 1991; (13) Sargent et al. 1977; (14) Jablonka et al. 1998

2.3 Observations and Data Reduction

2.3.1 Optical photometry

All of the new optical photometry reported here was collected using the 4-Shooter CCD mosaic camera (Szentgyorgyi et al. 1999) on the 1.2 meter telescope of the Fred L. Whipple Observatory. Most of the observations were made in June 1998, with additional data taken in October 1998 and January 1999. The new data comprise 13 fields 22-arcmin square in a grid centered on M31, with a pixel scale of $0.67''$ per pixel. Data reduction, beginning with the usual CCD processing steps of bias subtraction and flat-fielding with dome flats, was performed in IRAF[1] using the MSCRED, APPHOT, and PHOTCAL packages.

We performed photometric calibration of the M31 images using observations of Landolt (1992) standard fields. We chose positions for the fields to get standard stars on all four chips, and also observed some smaller fields sequentially on all chips in all five filters. We measured instrumental magnitudes of the standard stars in large apertures using APPHOT. To determine a photometric solution we fit data from all four chips simultaneously, with separate zeropoints and color terms for each chip, but only one airmass coefficient for each color. For our June 1998 observing run we averaged the color terms from the above procedure over all five nights, and redid the photometric solutions. The airmass coefficients varied by $\lesssim 0.02$ mag over the five nights (except in U where the photometric solution was poorer and the variation was ~ 0.2 mag), and the zeropoint difference between chips was $\lesssim 0.10$ mag. We expected a small zeropoint difference since the dome flats remove most, but not all, of the overall quantum efficiency differences between the chips. The color term differences between chips were on the order of 0.05 mag; again, these differences were expected since the chips do not have exactly the same response curves. A few of our fields also had deeper observations taken in non-photometric conditions. We calibrated the photometry on the deeper images by comparing stellar magnitudes to determine a mean magnitude offset to the photometric images.

We identified the clusters and candidates by comparing our images with the finding charts in the Bologna group's papers (Battistini et al. 1980, 1987, 1993). Clusters not on the finding charts (DAO clusters, etc.) were located by offsetting from the nearest cluster marked on the chart. Some clusters were difficult to

[1]IRAF is distributed by the National Optical Astronomy Observatories, which are operated by the Association of Universities for Research in Astronomy, Inc., under cooperative agreement with the National Science Foundation.

identify, either because of high local background or confusion between nearby objects. These are marked with 'ID' in the comments to Table 2.4.

We did simple aperture photometry of the clusters using APPHOT; the results are in Table 2.4. To match the aperture sizes of previous photometry, we used an aperture of radius 12 pixels (8.0 arcsec) for most clusters. For the few clusters near bright stars, we measured the magnitude in a smaller aperture and corrected it to the larger aperture size, using average growth curves derived from other clusters in the same field. These growth curves also showed that the choice of aperture size was reasonable, as $\sim 94\%$ of the light from the clusters was contained within the 12 pixel radius. Clusters with aperture-corrected magnitudes are marked in the comments to Table 2.4 as 'ac'.

Steep gradients in the galaxy light near the nucleus cause two problems in aperture photometry of clusters: inaccurate centering of the cluster in the aperture, and systematic errors in the background subtraction caused by steep gradients in the galaxy light. For fields near the nucleus of the galaxy we performed additional galaxy background removal. For each field, we subtracted an image of the smooth galaxy background produced using a ring median filter (Secker 1995) and rescaled the resulting image to have the same mode as the original image. This produced very good galaxy subtraction to within $\sim 5'$ of the nucleus. Comparison of photometry on subtracted and non-subtracted images showed no changes in photometric scale or zeropoint, but (as hoped) the photometric errors were lower on the subtracted images because of lower sky background uncertainties.

Our 4-shooter fields in M31 overlap slightly. This provides an opportunity to determine the precision of our photometry and photometric calibration by comparing photometry of clusters that appear (always on different chips) in more than one field. The overlap regions are at the edges of the chips, where accurate flat-fielding is more difficult and the photometric precision is slightly lower. The RMS differences between measurements of the same objects near the edges of different chips should therefore provide an upper limit to our actual internal photometric uncertainties. There are about 45 objects in the overlap regions; comparison of their magnitudes and colors shows that the scatter in the V magnitudes is approximately 0.05 mag, and the scatter in $B-V$, $V-R$, and $V-I$ colors is ~ 0.08 mag. Our U observations were not deep enough to produce reliable U magnitudes for many clusters, so there are not enough duplicate observations to determine the scatter in $U-B$. However, the scatter in $U-B$ is likely larger than that in the other colors and we estimate it to be ~ 0.15 mag.

Table 2.4. New photometric data for M31 globular clusters

name	V	$B-V$	$U-B$	$V-R$	$V-I$	J	K	notes
002–043	17.55(1)	0.63(2)	−0.04(3)	0.43(3)	0.97(2)	···	···	···
003–045	17.57(1)	0.78(2)	0.05(4)	0.50(3)	1.16(2)	···	···	···
004–050	16.95(1)	0.92(1)	0.42(3)	0.59(2)	1.22(1)	14.91(2)	14.19(5)	···
005–052	15.44(1)	0.60(1)	0.08(2)	0.45(1)	0.78(1)	14.16(2)	13.81(6)	ID
006–058	15.53(1)	0.96(1)	0.45(2)	0.56(1)	1.22(1)	···	···	···
008–060	···	···	···	···	···	14.68(5)	13.98(6)	···
009–061	16.92(1)	0.71(2)	−0.09(7)	0.50(2)	0.99(2)	···	···	···
010–062	16.66(1)	0.84(1)	0.15(2)	0.54(1)	1.18(1)	14.76(3)	14.07(6)	···
012–064	15.13(1)	0.73(1)	0.13(1)	0.51(1)	1.05(1)	···	···	···
013–065	17.19(1)	0.87(2)	0.50(5)	0.59(2)	1.23(2)	15.18(3)	14.34(5)	···
014–B222	18.09(1)	1.57(5)	···	0.70(4)	1.54(3)	15.19(4)	14.11(6)	···
015–B204	17.79(1)	1.41(6)	···	0.86(4)	1.89(3)	···	···	···
016–066	17.58(1)	1.00(4)	···	0.73(3)	1.43(2)	···	···	···
017–070	15.95(1)	1.09(1)	0.51(2)	0.72(1)	1.44(1)	13.43(1)	12.60(2)	···
019–072	14.93(1)	1.01(1)	0.42(1)	···	1.19(1)	···	···	···
021–075	17.54(1)	0.79(4)	···	0.66(3)	1.60(2)	···	···	···
022–074	17.36(1)	0.73(2)	0.05(8)	0.39(2)	1.01(2)	···	···	···
023–078	14.22(1)	1.18(1)	···	0.66(1)	···	···	···	···
024–082	16.80(1)	0.95(2)	0.65(8)	0.53(1)	1.15(1)	···	···	···
025–084	16.86(1)	0.95(2)	0.00(6)	0.57(2)	1.18(2)	14.81(5)	14.27(9)	···
026–086	17.53(1)	1.07(2)	0.54(6)	0.65(3)	1.31(2)	···	···	···
028–088	16.86(1)	0.88(2)	−0.05(5)	0.50(2)	···	14.89(4)	14.29(7)	···
029–090	16.58(1)	1.04(2)	0.42(8)	0.54(2)	···	···	···	···
030–091	17.40(1)	1.92(6)	···	0.78(3)	1.64(3)	14.36(2)	13.44(4)	···
031–092	17.71(1)	1.37(5)	···	0.72(4)	1.33(3)	···	···	···
032–093	17.61(1)	1.14(3)	0.58(8)	0.74(3)	1.63(2)	···	···	···
033–095	17.86(1)	···	···	0.33(5)	0.88(6)	···	···	···
034–096	15.47(1)	0.95(1)	0.35(3)	0.57(1)	1.25(1)	···	···	···
035–000	17.48(1)	0.89(3)	···	0.67(2)	1.24(2)	···	···	···
036–000	17.31(1)	0.94(2)	0.07(3)	0.52(2)	1.18(2)	···	···	···
037–B327	16.82(1)	2.05(2)	···	1.28(1)	2.63(1)	···	···	···
038–098	16.49(1)	0.91(1)	0.12(2)	0.60(1)	1.25(1)	14.43(2)	13.81(5)	···
039–101	15.98(1)	1.31(1)	0.57(2)	0.72(1)	1.56(1)	13.33(1)	12.46(1)	···
040–102	17.30(1)	0.39(2)	−0.27(4)	0.38(2)	0.67(2)	···	···	···
041–103	17.65(1)	0.97(5)	···	0.52(5)	1.18(4)	···	···	···
042–104	16.29(1)	1.48(2)	···	0.92(1)	1.89(1)	13.08(1)	12.26(2)	···
043–106	16.96(1)	0.28(2)	−0.14(3)	0.28(2)	0.52(2)	···	···	···
044–107	16.70(1)	1.21(1)	0.45(3)	0.64(1)	1.37(1)	14.32(3)	13.52(5)	···
045–108	15.78(1)	0.94(1)	0.37(2)	0.59(1)	1.24(1)	···	···	···

Table 2.4—Continued

name	V	$B-V$	$U-B$	$V-R$	$V-I$	J	K	notes
046–109	17.81(1)	0.84(3)	0.05(9)	0.44(4)	0.94(3)	···	···	···
047–111	17.51(1)	0.72(2)	0.09(6)	0.63(3)	1.21(2)	···	···	···
048–110	16.51(1)	1.08(1)	0.45(3)	0.62(1)	1.28(1)	14.31(3)	13.40(5)	···
049–112	17.56(1)	0.52(4)	0.18(9)	0.45(4)	0.69(4)	···	···	···
050–113	16.84(1)	0.92(2)	0.33(5)	0.57(2)	1.18(1)	14.72(3)	13.96(5)	···
051–114	16.08(1)	1.16(1)	0.36(2)	0.69(1)	1.43(1)	···	···	···
052–B266	17.21(1)	1.41(2)	···	0.67(2)	1.44(2)	···	···	···
053–000	17.82(1)	0.91(5)	···	0.38(4)	1.01(4)	···	···	···
054–115	18.34(1)	0.73(8)	···	0.69(7)	1.39(6)	···	···	···
056–117	17.30(1)	1.06(3)	···	0.62(3)	1.34(2)	14.68(2)	13.80(4)	···
057–118	17.64(1)	0.69(3)	0.00(4)	0.44(4)	0.99(3)	···	···	···
058–119	15.01(1)	0.80(1)	0.24(1)	0.53(1)	1.10(1)	···	···	···
059–120	17.05(1)	0.94(3)	0.40(7)	0.64(3)	1.33(3)	14.80(5)	13.96(7)	···
060–121	16.75(1)	0.71(2)	0.08(3)	0.55(2)	1.17(2)	14.84(5)	14.11(9)	···
061–122	16.61(1)	1.12(1)	0.33(4)	0.72(1)	1.49(1)	13.96(2)	13.08(3)	···
062–123	17.24(1)	1.34(2)	···	0.63(2)	1.42(1)	···	···	···
063–124	15.66(1)	1.21(1)	0.62(2)	0.77(1)	1.58(1)	12.99(1)	12.11(1)	···
064–125	16.31(1)	0.74(1)	0.10(2)	0.53(2)	1.14(1)	14.39(5)	13.69(8)	···
065–126	···	···	···	···	···	15.23(4)	14.52(7)	···
067–129	17.25(1)	0.70(2)	0.12(4)	0.58(3)	1.10(3)	···	···	···
068–130	16.37(1)	1.25(1)	0.52(4)	0.78(1)	1.54(1)	···	···	···
069–132	18.16(1)	0.44(4)	0.02(7)	0.42(5)	0.65(6)	···	···	···
070–133	16.88(1)	0.73(2)	0.19(4)	0.38(2)	0.92(3)	···	···	···
071–000	17.79(1)	1.14(6)	···	0.38(7)	1.28(5)	···	···	···
072–000	17.23(1)	1.25(1)	1.97(7)	1.17(1)	1.78(1)	···	···	ac
073–134	15.99(1)	0.93(1)	0.45(2)	0.57(1)	1.22(1)	···	···	···
074–135	16.65(1)	0.75(1)	0.14(3)	0.51(1)	1.07(1)	14.83(2)	14.11(4)	···
075–136	17.33(1)	0.92(3)	0.20(8)	0.67(3)	1.38(2)	···	···	···
076–138	16.89(1)	0.87(2)	0.10(3)	0.57(2)	1.20(2)	···	···	···
077–139	17.26(1)	1.09(4)	0.16(9)	0.76(4)	1.41(3)	···	···	···
078–140	17.42(1)	1.67(7)	···	0.68(5)	1.62(4)	···	···	···
079–000	17.82(1)	1.42(4)	···	0.88(3)	1.82(2)	14.79(4)	13.48(4)	···
080–141	17.20(1)	···	···	0.67(7)	1.55(5)	14.53(4)	13.79(7)	···
081–142	16.80(1)	0.54(1)	0.26(2)	0.44(2)	1.07(2)	14.82(3)	13.96(5)	···
082–144	15.54(1)	1.56(1)	1.31(4)	0.99(1)	1.91(1)	12.39(1)	11.53(1)	···
083–146	17.09(1)	0.76(2)	0.06(4)	0.54(2)	1.16(1)	15.22(3)	14.48(6)	···
084–000	···	···	···	···	···	15.22(7)	14.08(9)	···
085–147	···	···	···	···	···	15.07(3)	14.44(6)	···
088–150	15.42(1)	1.12(1)	0.33(2)	0.69(1)	1.47(1)	···	···	···

Table 2.4—Continued

name	V	$B-V$	$U-B$	$V-R$	$V-I$	J	K	notes
089–000	18.18(3)	0.10(4)	−0.32(5)	−0.04(6)	0.48(6)	···	···	ID
090–000	18.80(1)	···	···	···	···	···	···	···
091–151	17.56(1)	0.41(5)	0.02(6)	0.56(6)	0.94(6)	···	···	···
092–152	16.92(1)	0.91(3)	0.28(8)	0.46(3)	1.18(2)	···	···	···
093–155	16.87(1)	0.97(4)	0.29(6)	0.69(3)	1.21(3)	14.50(3)	13.69(5)	···
094–156	15.55(1)	0.97(1)	0.49(4)	0.56(1)	1.26(1)	13.34(1)	12.54(2)	···
095–157	15.81(1)	0.95(1)	0.70(4)	···	···	13.05(1)	12.46(2)	ac
096–158	16.61(1)	1.11(3)	0.84(9)	0.76(3)	1.48(2)	13.93(2)	13.01(3)	···
097–159	16.85(1)	1.10(2)	0.20(5)	0.67(2)	1.37(2)	14.50(2)	13.90(6)	···
098–000	16.21(1)	0.98(1)	0.31(2)	0.52(1)	1.13(1)	14.25(2)	13.58(4)	···
099–161	16.74(1)	0.85(2)	0.30(5)	0.53(2)	1.32(2)	14.54(5)	13.59(5)	···
100–163	18.77(1)	0.28(7)	···	···	1.00(7)	···	···	ID
101–164	16.87(1)	0.81(2)	0.38(5)	0.59(2)	1.22(2)	14.58(3)	13.73(5)	···
102–000	16.58(1)	0.62(1)	−0.12(2)	0.39(2)	0.95(1)	···	···	···
103–165	15.23(1)	1.02(2)	0.38(3)	0.57(2)	1.31(1)	···	···	···
104–NB5	17.51(1)	···	···	···	0.65(11)	···	···	···
105–166	17.19(1)	0.89(2)	0.29(5)	0.54(2)	1.26(2)	15.08(3)	14.33(7)	···
106–168	16.03(1)	0.97(2)	0.60(4)	0.57(2)	1.26(2)	···	···	···
107–169	15.94(1)	1.02(2)	0.27(4)	0.65(2)	1.28(2)	···	···	···
108–167	17.47(1)	0.89(4)	···	0.70(4)	1.58(3)	15.06(6)	14.25(10)	···
109–170	16.25(1)	1.02(1)	0.98(4)	0.61(1)	1.38(1)	13.82(3)	12.84(4)	ac
110–172	15.20(1)	0.88(1)	0.30(1)	0.58(1)	1.20(1)	···	···	···
111–173	16.80(1)	0.75(2)	0.20(3)	0.47(2)	1.08(2)	15.01(4)	14.34(9)	···
112–174	16.26(1)	1.07(5)	0.74(9)	0.70(4)	1.29(3)	···	···	···
114–175	17.13(1)	0.57(4)	0.33(6)	0.56(5)	1.11(5)	···	···	···
115–177	16.06(1)	0.99(2)	0.83(5)	0.62(2)	1.48(2)	···	···	···
116–178	16.79(1)	1.39(2)	0.59(7)	0.87(1)	1.86(1)	13.63(1)	12.73(2)	···
117–176	16.34(1)	0.65(3)	···	0.44(2)	1.00(1)	14.66(3)	13.88(5)	···
118–NB6	16.51(1)	0.70(5)	0.33(8)	0.67(5)	1.37(5)	···	···	···
124–NB10	···	···	···	···	···	12.69(5)	11.93(6)	···
125–183	···	···	···	···	···	14.84(4)	14.32(1)	···
128–187	16.88(1)	1.01(5)	···	0.65(3)	1.13(3)	14.71(5)	13.78(8)	···
129–000	···	···	···	···	···	13.25(3)	12.19(4)	···
130–188	16.93(1)	1.15(3)	···	0.68(2)	1.41(2)	14.52(2)	13.83(5)	···
133–191	16.68(1)	0.93(3)	−0.68(3)	−0.37(4)	0.57(3)	···	···	ID
134–190	16.57(1)	0.91(4)	0.15(8)	0.50(4)	1.17(3)	···	···	···
135–192	16.04(1)	0.92(1)	0.26(4)	0.57(1)	1.22(1)	13.89(1)	13.17(2)	···
136–194	17.21(1)	0.77(5)	0.09(6)	0.69(5)	1.14(6)	···	···	···
137–195	17.64(1)	1.23(4)	···	0.67(3)	1.54(2)	15.00(3)	14.20(5)	···

Table 2.4—Continued

name	V	$B-V$	$U-B$	$V-R$	$V-I$	J	K	notes
141–197	···	···	···	···	···	14.69(2)	13.80(4)	···
143–198	16.05(1)	1.09(2)	0.61(4)	0.57(2)	1.20(2)	···	···	···
144–000	···	···	···	···	···	14.14(4)	13.13(7)	···
145–000	18.10(1)	0.32(7)	···	0.40(8)	···	···	···	···
146–000	16.95(1)	1.49(7)	···	···	1.09(5)	14.76(6)	13.95(9)	···
148–200	15.98(1)	0.84(2)	0.10(2)	0.58(2)	1.10(2)	···	···	···
149–201	17.04(1)	0.89(2)	0.07(3)	0.72(2)	1.29(2)	14.67(2)	13.90(5)	ac
150–203	16.80(1)	1.10(3)	0.39(6)	0.50(3)	1.28(3)	14.06(4)	13.13(5)	···
151–205	14.83(1)	1.23(1)	0.67(2)	0.70(1)	1.45(1)	···	···	···
152–207	16.16(1)	0.91(2)	0.19(2)	0.58(2)	1.24(2)	···	···	···
153–000	16.24(1)	1.00(2)	0.62(6)	0.55(2)	1.30(1)	13.90(2)	13.09(4)	···
155–210	17.93(1)	1.02(4)	···	0.57(4)	1.14(4)	···	···	···
156–211	16.84(1)	0.79(2)	0.26(2)	0.47(2)	···	···	···	···
157–212	17.73(1)	0.65(4)	···	0.31(5)	1.08(4)	···	···	···
158–213	14.70(1)	0.86(1)	0.34(1)	0.55(1)	1.15(1)	···	···	···
159–000	17.20(1)	0.88(3)	0.02(4)	0.67(3)	1.41(2)	···	···	ac
160–214	17.96(1)	0.61(4)	0.05(4)	0.41(5)	0.93(5)	···	···	···
161–215	16.33(1)	0.81(1)	0.27(4)	0.51(1)	1.10(1)	14.42(3)	13.69(5)	···
162–216	17.48(1)	1.05(4)	0.39(9)	0.62(4)	1.34(4)	···	···	···
163–217	15.05(1)	0.98(1)	0.68(2)	0.62(1)	1.34(1)	···	···	···
164–B253	17.94(1)	1.04(6)	···	0.65(6)	1.31(5)	···	···	···
165–218	16.47(1)	0.70(1)	−0.04(4)	0.42(1)	1.00(1)	14.78(3)	14.15(7)	···
166–000	16.76(1)	0.67(2)	−0.09(4)	0.36(2)	0.81(2)	···	···	···
167–000	17.41(1)	1.02(4)	···	0.50(4)	1.25(3)	15.18(5)	14.38(9)	···
168–000	17.63(1)	1.60(6)	···	0.94(3)	1.91(2)	14.52(6)	13.37(8)	···
169–000	17.08(1)	1.23(4)	···	···	1.31(3)	14.81(5)	13.96(7)	···
170–221	17.39(1)	0.98(2)	0.53(6)	0.59(2)	1.22(2)	···	···	···
172–223	16.69(1)	0.94(2)	0.49(5)	0.57(2)	1.29(2)	14.43(3)	13.48(5)	···
173–224	18.27(1)	···	···	0.80(10)	1.59(9)	···	···	···
174–226	15.47(1)	1.00(1)	0.34(1)	0.64(1)	1.29(1)	13.31(2)	12.42(4)	···
176–227	16.52(1)	0.73(1)	0.07(1)	0.43(1)	0.99(1)	14.83(2)	14.21(5)	ac
177–228	18.05(1)	0.95(4)	0.32(8)	0.53(5)	1.22(4)	···	···	···
178–229	15.03(1)	0.79(1)	0.09(1)	0.50(1)	1.02(1)	13.26(1)	12.57(2)	···
179–230	15.39(1)	0.83(1)	0.22(1)	0.55(1)	1.07(1)	···	···	···
180–231	16.02(1)	0.88(1)	0.36(3)	0.56(1)	1.20(1)	14.05(2)	13.25(2)	···
181–232	16.95(1)	0.91(3)	0.39(8)	0.62(3)	1.28(2)	14.68(4)	13.66(5)	···
182–233	15.43(1)	0.93(1)	0.26(2)	0.61(1)	1.29(1)	···	···	···
183–234	15.95(1)	1.01(1)	0.39(1)	0.60(1)	1.29(1)	···	···	···
184–236	17.24(1)	1.15(4)	···	0.75(3)	1.41(2)	···	···	···

Table 2.4—Continued

name	V	$B-V$	$U-B$	$V-R$	$V-I$	J	K	notes
185–235	15.54(1)	0.94(1)	0.55(1)	0.56(1)	1.18(1)	13.50(2)	12.72(3)	···
186–000	18.02(1)	1.08(6)	···	0.56(5)	1.38(4)	···	···	···
187–237	17.17(1)	1.04(4)	0.32(6)	0.65(4)	1.39(3)	···	···	···
188–239	17.04(1)	0.71(4)	0.20(5)	0.41(4)	1.12(3)	···	···	···
189–240	16.99(1)	1.05(2)	0.93(6)	0.60(2)	1.34(2)	14.58(3)	13.66(5)	···
190–241	16.82(1)	0.88(2)	0.38(8)	0.55(2)	1.14(2)	14.78(4)	14.13(8)	···
192–242	17.88(1)	0.34(5)	···	···	0.52(7)	···	···	···
193–244	15.33(1)	0.97(1)	0.61(6)	0.57(1)	1.28(1)	···	···	···
194–243	17.19(1)	0.76(2)	0.18(3)	0.46(2)	0.98(2)	15.43(4)	14.87(9)	···
195–000	18.57(1)	0.40(6)	···	0.55(7)	0.98(5)	···	···	···
197–247	17.63(1)	1.08(4)	···	0.71(4)	1.59(4)	···	···	···
198–249	17.55(1)	0.60(4)	−0.07(4)	0.40(5)	1.11(4)	···	···	···
199–248	17.60(1)	0.77(3)	···	0.57(3)	1.03(2)	···	···	···
200–000	18.55(1)	···	···	0.72(9)	1.53(7)	···	···	···
201–250	15.90(1)	0.88(1)	0.32(2)	0.58(1)	1.09(1)	14.23(2)	13.67(5)	···
202–251	17.79(1)	0.86(2)	···	0.61(2)	1.08(1)	···	···	ac
203–252	16.68(1)	0.93(1)	0.22(2)	0.52(2)	1.20(1)	14.58(3)	13.84(5)	···
204–254	15.75(1)	0.92(1)	0.44(1)	0.58(1)	1.17(1)	13.70(1)	12.87(2)	···
205–256	15.46(1)	0.83(1)	0.29(1)	0.53(1)	1.12(1)	···	···	···
206–257	15.06(1)	0.80(1)	0.21(1)	0.52(1)	1.03(1)	13.21(1)	12.52(2)	···
207–258	17.33(1)	0.74(2)	0.19(3)	0.52(2)	1.00(2)	15.67(5)	14.78(8)	···
208–259	17.81(1)	0.92(3)	0.63(8)	0.62(4)	1.40(3)	···	···	ac
209–261	16.64(1)	0.77(1)	0.30(2)	0.50(2)	1.07(2)	14.84(5)	14.23(9)	···
210–000	17.57(1)	0.52(3)	0.02(4)	···	1.37(3)	···	···	···
211–262	16.62(1)	0.67(1)	0.05(2)	0.49(2)	0.97(1)	14.87(4)	14.33(9)	···
212–263	15.48(1)	0.74(1)	0.01(2)	0.48(1)	1.00(1)	···	···	···
213–264	16.78(1)	1.05(2)	0.46(4)	0.56(2)	1.29(2)	14.71(4)	13.83(8)	···
214–265	17.65(1)	0.61(4)	0.28(5)	0.51(4)	1.12(4)	···	···	···
215–266	17.13(1)	1.02(2)	0.41(5)	0.47(3)	1.20(2)	15.00(5)	14.23(9)	···
216–267	17.25(1)	0.20(3)	0.02(2)	0.39(4)	0.63(3)	···	···	···
217–269	16.51(1)	0.92(1)	0.38(2)	0.56(1)	1.20(1)	14.56(3)	13.86(6)	···
218–272	14.79(1)	0.87(1)	0.40(1)	0.56(1)	1.16(1)	···	···	···
219–271	···	···	···	···	···	14.32(2)	13.51(4)	···
220–275	16.55(1)	0.78(1)	0.09(2)	0.45(2)	1.06(2)	14.89(4)	14.18(7)	···
221–276	16.86(1)	0.90(2)	0.31(3)	···	1.27(2)	···	···	···
222–277	17.43(1)	0.68(2)	0.47(4)	···	1.05(2)	···	···	···
228–281	16.78(1)	0.95(2)	0.39(7)	0.56(1)	1.17(1)	14.61(2)	13.84(5)	···
229–282	16.47(1)	0.67(2)	0.14(4)	0.52(1)	0.97(1)	14.87(4)	14.21(9)	···
230–283	16.05(1)	0.72(1)	0.01(2)	0.44(1)	0.92(1)	14.43(2)	13.85(5)	···

Table 2.4—Continued

name	V	$B-V$	$U-B$	$V-R$	$V-I$	J	K	notes
231–285	17.30(1)	0.69(3)	0.50(5)	0.46(3)	1.17(2)	15.26(5)	14.18(7)	···
232–286	15.70(1)	0.68(1)	0.15(1)	0.50(1)	1.05(1)	···	···	···
233–287	15.80(1)	0.81(1)	0.21(1)	0.53(1)	1.04(1)	13.90(2)	13.21(3)	···
234–290	···	···	···	···	···	14.69(3)	14.05(6)	···
235–297	16.27(1)	0.85(1)	0.30(2)	0.55(1)	1.32(1)	14.14(2)	13.22(4)	···
236–298	17.38(1)	0.82(2)	0.01(8)	0.41(2)	1.14(2)	···	···	···
237–299	17.10(1)	0.77(2)	0.16(2)	0.53(2)	1.05(2)	15.47(4)	14.91(9)	···
238–301	16.42(1)	0.97(1)	0.34(2)	0.56(1)	1.20(1)	···	···	···
239–000	17.08(1)	1.02(2)	0.39(4)	0.43(2)	0.99(2)	15.31(4)	14.55(8)	···
240–302	15.23(1)	0.70(1)	0.10(1)	0.50(1)	1.03(1)	···	···	···
244–000	18.27(1)	0.78(4)	0.08(8)	0.61(5)	1.05(4)	···	···	···
260–000	18.50(1)	···	···	0.98(10)	2.08(7)	14.72(3)	13.70(4)	···
272–B294	18.20(1)	1.32(6)	···	0.70(5)	1.59(5)	···	···	···
277–000	18.50(1)	0.62(5)	···	···	1.24(5)	···	···	···
281–288	17.67(1)	0.84(3)	0.50(6)	0.56(3)	1.16(3)	···	···	ac
283–296	17.64(1)	1.06(4)	···	0.44(3)	1.11(2)	···	···	···
284–000	19.23(1)	···	···	···	···	···	···	···
299–000	···	···	···	···	···	14.72(2)	13.73(4)	···
302–023	···	···	···	···	···	14.94(3)	14.31(7)	···
304–028	···	···	···	···	···	15.13(2)	14.58(6)	···
306–029	16.30(1)	···	···	···	1.67(1)	···	···	···
307–030	17.32(1)	···	···	···	1.22(1)	···	···	···
310–032	···	···	···	···	···	15.33(3)	14.81(8)	···
313–036	···	···	···	···	···	13.97(2)	13.11(3)	···
316–040	17.06(1)	0.71(2)	0.33(8)	0.67(2)	0.92(2)	···	···	···
318–042	16.98(1)	0.17(1)	−0.38(3)	0.32(2)	0.39(2)	···	···	···
321–046	17.67(1)	0.22(3)	−0.13(6)	0.29(4)	0.48(4)	···	···	···
322–049	17.75(1)	0.06(5)	···	0.58(5)	0.62(6)	···	···	···
323–000	17.59(1)	0.47(2)	0.17(7)	0.49(2)	1.35(2)	···	···	ac
325–000	16.94(1)	0.60(2)	···	0.52(2)	1.03(2)	···	···	···
327–053	···	···	···	···	···	15.15(3)	14.39(5)	···
333–000	17.10(1)	0.54(2)	−0.19(5)	0.44(3)	0.87(2)	···	···	ac
335–H13	17.89(1)	1.15(6)	···	0.98(4)	1.75(3)	···	···	···
338–076	14.30(1)	0.76(1)	0.15(1)	···	1.02(1)	···	···	···
342–094	18.00(1)	0.15(4)	−0.33(6)	0.25(5)	0.53(5)	···	···	···
344–127	15.95(1)	···	···	···	1.08(1)	···	···	···
346–149	17.51(1)	···	···	···	1.57(1)	14.76(2)	13.46(3)	···
347–154	16.50(1)	···	···	···	1.01(1)	14.85(2)	14.23(5)	···
348–153	16.79(1)	···	···	···	1.15(1)	14.88(2)	14.10(3)	···

Table 2.4—Continued

name	V	$B-V$	$U-B$	$V-R$	$V-I$	J	K	notes
349–000	18.01(1)	···	···	···	1.27(2)	15.89(4)	15.03(8)	···
350–162	16.74(1)	···	···	···	1.10(1)	14.88(3)	14.25(6)	···
352–180	···	···	···	···	···	14.88(1)	14.16(2)	···
354–186	17.81(1)	···	···	···	1.07(2)	16.09(4)	15.33(7)	···
355–193	17.76(1)	···	···	···	0.94(2)	···	···	···
362–000	17.61(1)	0.65(3)	0.08(2)	1.05(3)	0.87(3)	···	···	ac
366–291	15.99(1)	0.81(1)	0.26(3)	0.44(1)	1.01(1)	···	···	···
367–292	18.16(1)	0.27(4)	···	0.57(4)	1.01(4)	···	···	···
368–293	18.05(1)	0.16(4)	−0.52(8)	0.49(5)	0.56(5)	···	···	ID
370–300	16.30(1)	0.85(1)	0.13(3)	0.67(1)	1.16(1)	···	···	···
371–303	17.54(1)	0.48(3)	0.39(4)	···	0.53(5)	···	···	···
373–305	15.64(1)	0.94(1)	0.49(3)	0.51(1)	1.25(1)	···	···	···
374–306	18.31(1)	0.44(5)	···	0.41(6)	0.89(7)	···	···	···
375–307	17.61(1)	0.90(3)	···	0.54(3)	1.02(4)	···	···	···
376–309	18.06(1)	···	···	0.24(5)	0.97(5)	···	···	ac
385–321	17.67(1)	1.25(4)	···	0.43(3)	1.08(3)	···	···	···
389–326	17.38(1)	1.40(4)	···	0.60(2)	1.34(2)	···	···	···
391–328	···	···	···	···	···	15.41(2)	14.65(5)	···
393–330	···	···	···	···	···	15.09(2)	14.30(5)	···
442–D033	17.94(1)	0.39(6)	···	0.56(7)	0.78(6)	···	···	···
443–D034	18.20(1)	···	···	···	0.41(7)	···	···	···
448–D035	17.49(1)	0.61(4)	0.01(9)	0.43(4)	0.72(3)	···	···	···
450–000	19.05(1)	···	···	···	1.33(8)	···	···	···
452–069	17.78(1)	0.38(4)	−0.05(8)	···	0.55(5)	···	···	···
453–D042	17.30(1)	0.87(3)	0.16(8)	0.54(3)	1.26(2)	15.21(5)	14.38(9)	···
458–D049	17.84(1)	0.49(4)	···	0.20(5)	0.57(5)	···	···	···
462–000	18.06(1)	···	···	···	1.05(2)	···	···	···
463–160	18.30(1)	···	···	···	1.48(3)	15.96(5)	14.56(6)	···
470–D063	···	···	···	···	···	15.62(4)	14.46(6)	···
471–238	···	···	···	···	···	14.70(2)	13.63(3)	···
472–D064	15.19(1)	0.78(1)	0.19(1)	0.52(1)	1.07(1)	···	···	···
475–H128	17.56(1)	0.31(3)	0.10(10)	0.53(4)	0.65(4)	···	···	···
476–D074	18.12(1)	1.00(5)	0.40(9)	0.43(6)	1.12(5)	···	···	···
477–D075	18.46(1)	···	−0.07(7)	···	···	···	···	···
479–D080	17.46(1)	···	···	1.10(3)	2.00(2)	···	···	···
484–310	18.10(1)	0.52(6)	···	0.05(7)	1.14(6)	···	···	ID
DAO032	16.00(1)	1.41(1)	1.45(9)	1.22(1)	2.04(1)	···	···	ID,ac
DAO046	18.75(1)	0.53(7)	···	0.66(7)	0.90(7)	···	···	ID
DAO052	18.42(1)	0.14(5)	−0.50(4)	0.33(7)	1.31(6)	···	···	ID

Table 2.4—Continued

name	V	$B-V$	$U-B$	$V-R$	$V-I$	J	K	notes
DAO055	16.84(1)	···	···	···	0.82(1)	···	···	···
DAO060	16.65(1)	1.33(2)	1.41(10)	0.93(1)	1.83(1)	···	···	ID
DAO062	17.61(1)	1.60(3)	···	1.02(2)	2.45(2)	···	···	ID
DAO069	17.48(1)	0.26(4)	−0.65(8)	0.51(4)	1.05(3)	15.05(5)	14.05(7)	ID
NB16	17.55(1)	0.66(7)	···	0.81(7)	1.57(5)	···	···	···
NB23	17.17(1)	···	···	0.25(8)	1.33(5)	···	···	···
NB61	···	···	···	···	···	···	13.95(10)	···
NB67	16.14(1)	0.48(2)	−0.03(2)	0.32(3)	0.81(2)	···	···	···
NB68	15.59(1)	0.68(2)	0.18(3)	0.72(2)	0.67(2)	14.12(4)	13.78(10)	···
NB81	16.04(1)	0.66(2)	0.50(3)	0.45(3)	0.81(3)	···	···	···
NB83	16.68(1)	0.56(2)	−0.03(3)	0.33(3)	0.68(4)	···	···	···
NB87	···	···	···	···	···	14.03(5)	13.38(10)	···

We compared our optical photometry to published photometry, separating the previous work by method (photoelectric, photographic, or CCD). Figures 2.1, 2.2, and 2.3 and Table 2.5 show the comparisons, in the sense (previous photometry−this work), for the various colors and filters. As expected, the scatter increases with V magnitude, but there is no evidence of a zeropoint offset or a varying slope, with the exception noted below. In many objects where there is a large discrepancy between one type of published photometry and our new work, our work agrees much better with one of the other types of published photometry. These points are marked with bold symbols in the figures. These large disagreements between the various photometry sources are disappointing but unsurprising; Table 2.5 shows that, while the photographic and photometric zeropoints agree well, there is a large RMS scatter between the data sets. Overall, we find that the published photometry is consistent with our new data.

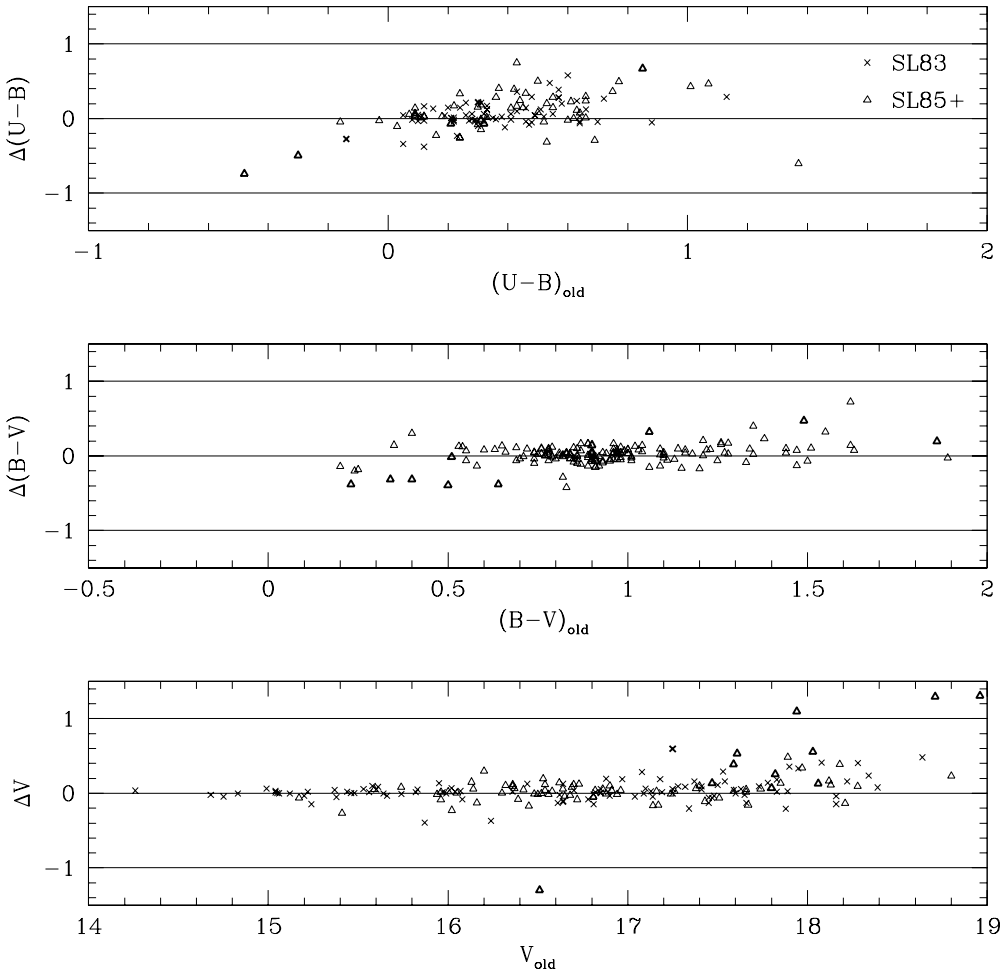

Fig. 2.1.— Comparison of new photometry to previous photoelectric results. Vertical axis in this and following figures is always (previous photometry)−(this work). SL83: Sharov & Lyutyi (1983); SL85+: Sharov & Lyutyi (1985) and succeeding papers. Bold symbols are objects for which another photometric method agrees better with our results.

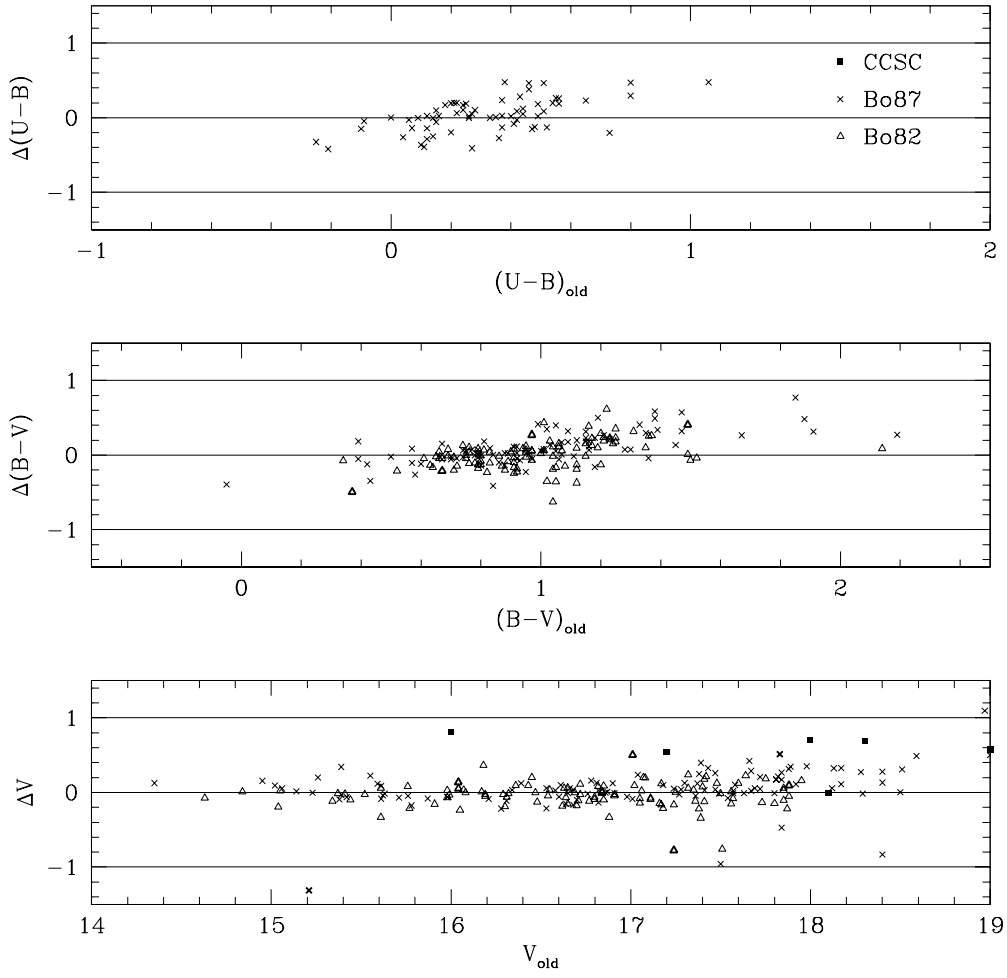

Fig. 2.2.— Comparison of new photometry to previous photographic results. CCSC: Crampton et al. (1985); Bo87: Battistini et al. (1987); Bo82: Buonanno et al. (1982). Bold symbols are objects for which another photometric method agrees better with our results.

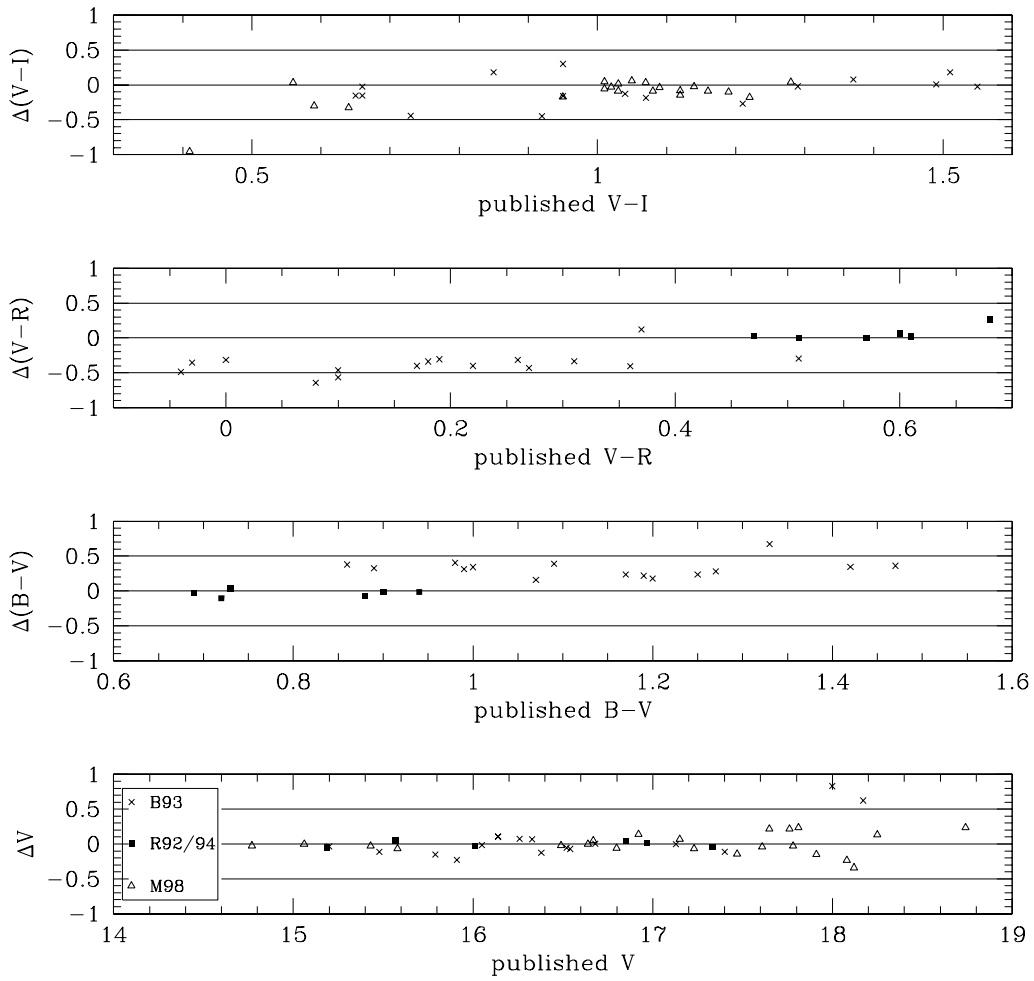

Fig. 2.3.— Comparison of new photometry to previous CCD results. B93: Battistini et al. (1993); R92/94: Reed et al. (1992, 1994); M98: Mochejska et al. (1998).

Table 2.5. Photometric offsets for new optical photometry

	ΔV			$\Delta(B-V)$			$\Delta(U-B)$					
	mean	σ	n	mean	σ	n	mean	σ	n			
PG												
all	0.058±0.020	0.287	203	0.050±0.015	0.205	173	···	···	···			
Bo87	0.029±0.029	0.297	104	0.098±0.023	0.215	85	0.035± 0.028	0.224	65			
Bo82	-0.032±0.015	0.150	92	-0.034±0.019	0.048	88	···	···	···			
CCSC	0.741±0.211	0.560	7	···	···	···	···	···	···			
PE												
all	0.037±0.010	0.134	188	0.024±0.010	0.120	157	0.082± 0.018	0.199	123			
SL83	0.037±0.014	0.137	98	0.032±0.014	0.132	91	0.066± 0.019	0.161	68			
SL85+	0.036±0.016	0.123	70	0.012±0.012	0.100	66	0.101± 0.032	0.238	55			
(previous photometry: PG-PE)												
all	0.018±0.018	0.240	175	0.005±0.016	0.215	175	0.003± 0.031	0.406	175			
CCD												
	ΔV			$\Delta(B-V)$			$\Delta(V-R)$			$\Delta(V-I)$		
	mean	σ	n	mean	σ	n	mean	σ	n	mean	σ	n
all	0.022± 0.029	0.197	45		···	···	···	···	···	-0.125± 0.042	0.259	38
B93	0.053± 0.066	0.272	17	0.322± 0.032	0.125	15	-0.371± 0.041	0.163	16	-0.135± 0.074	0.307	17
R92/94	-0.003± 0.019	0.046	6	-0.034± 0.019	0.048	6	0.065± 0.041	0.101	6	···	···	
M98	0.005± 0.032	0.151	22							-0.116± 0.048	0.220	21
internal scatter, this work												
···	···	0.053	41	···	0.076	41	···	0.082	41	···	0.082	41

There was one published data set with which our results show marked disagreement - the CCD photometry of bulge clusters from Battistini et al. (1993). Our $B-V$ colors are bluer and our $V-R$ colors redder than theirs, in each case by approximately 0.3 mag. An obvious explanation, that our V magnitudes were 0.3 mag fainter, was not the case – our V magnitudes agree well with theirs. The $V-R$ colors of Battistini et al. are bluer than those seen for most globulars in M31 or the Galaxy, so we suspect that there may be a systematic problem in their photometry. Their $B-V$ colors are redder than those of the average Galactic globular, but this is not unreasonable since these clusters are near the M31 bulge and hence are more likely to be metal-rich (and intrinsically red). Other clusters in the same fields, although further from the galaxy nucleus, show no large offsets against previous photometry, and a check of magnitudes on our "raw" and "galaxy subtracted" CCD frames shows that the galaxy subtraction procedure did not substantially change the $B-V$ colors.

There also appears to be a small offset in our $V-I$ colors: most of this is due to a few clusters with large offsets, and the median offset is consistent with zero. For the clusters where we disagree with Mochejska et al. (1998) they note that their I magnitudes are suspect due to nearby bad pixels. We have no explanation for the other large offsets, except to note that our galaxy subtraction procedure did not cause large changes in the $V-I$ colors. There is little comparison data for our $V-R$ and $V-I$ colors, so we made a second inspection of the photometric solutions in these colors. Our standard stars covered a wide range in colors, and we found no bias in the residuals as a function of color, so we are confident that any systematic errors affecting the R and I photometry are small.

2.3.2 Near-infrared photometry

Most of our new near-infrared data on the M31 clusters was taken with the SAO IR camera (Tollestrup & Willner 1998) on the 1.2m telescope at FLWO, on 1998 Oct 27 and 28; conditions on both nights were photometric. This two-channel camera has a $5'$ field of view, which required that we observe objects individually rather than attempting to map the entire galaxy. We observed the objects without published IR photometry in order of their V magnitudes, and obtained photometry for 122 new objects. We also obtained photometry of four objects from the 2MASS (Skrutskie et al. 1997) scans of M31; these scans covered most of the galaxy but the short integration time of 6 seconds meant that only the brightest objects had acceptable signal-to-noise.

Our near-IR observations of objects and standard stars consisted of 5 to 9

dithered frames in each of J and K per object. Total integration times ranged from 140 to 240 seconds. Data reduction for the IR data consisted of the following steps: application of a non-linearity correction, dark subtraction, flat-fielding, sky-subtraction, registration, and co-addition. We made use of P. Hall's PHIIRS package and a number of our own IRAF scripts.

Flat fields were constructed by median-combining about 100 M31 cluster frames that did not include the galaxy nucleus. Two sky-subtraction methods were used: for standard stars and objects far from the nucleus we used running skies (usually a median of the 8 frames nearest in time), and for each object near the nucleus we observed a separate sky position, median-combined those images to make a sky frame, and subtracted the sky from the object frames. We performed galaxy subtraction on some of the co-added object frames, again using the ring median filter.

We observed about a dozen Elias et al. (1982) standard stars per night, and fit a two-component (zeropoint and airmass coefficient) photometric solution using their measured aperture magnitudes. We tried including a color term in the solution, but this did not improve the fit. Others' experience also indicates that the color term for this camera is negligible, so we did not use it in our final solution. Residuals from the photometric solution were $\lesssim 0.02$ mag for both nights and both filters.

We identified the clusters and candidates on the final coadded fields by visual comparison with the optical finding charts. In addition to the target objects, many fields contained brighter objects with published photometry and/or additional, fainter objects. We measured aperture magnitudes for all the identified objects, again using APPHOT. We constructed growth curves for the brightest clusters and found that a 12-arcsec diameter aperture contained $\sim 95\%$ of the M31 clusters' light. This is comparable to the aperture sizes used in most previous IR photometry; the fact that a smaller aperture is required for IR than for optical photometry is a consequence of the better seeing in the IR. The measured magnitudes are in Table 2.4.

Following the procedure used for the optical photometry, we performed both "internal" (night-to-night and frame-to-frame) and "external" (previously published) photometry comparisons. The within-night scatter is the standard deviation of the differences in magnitudes of the same object on different co-added images, and it is approximately 0.06 mag in J and 0.08 mag in K. In both J and K this scatter is ~ 0.02 mag larger than the average photometric errors, a measure of how "photometric" the conditions were. The scatter between observations of the

same object on adjacent nights is comparable to the within-night scatter.

Figure 2.4 shows the results of the external photometry comparison. Because the camera's field of view is small compared to the size of M31, and because we observed objects without previous photometry, the number of comparison objects is small. For the 24 objects with published photometry, both offsets are consistent with zero: $\overline{\Delta K} = -0.014 \pm 0.031$, $\overline{\Delta J} = +0.001 \pm 0.019$. The standard deviations of the photometry differences (~ 0.15 mag in K and ~ 0.10 mag in J) are larger than is comfortable, but the small numbers make it difficult to tell if this is due to some systematic problem in our own photometry or in the previous work.

2.3.3 Spectroscopy

We acquired new spectra of 61 cluster candidates, most with the Keck LRIS spectrograph (Oke et al. 1995) in 1995 December and 1996 September, and a few with the MMT Blue Channel spectrograph in 1993 October. With LRIS we used a 600 line/mm grating, giving 1.2 Å/pixel dispersion from 3670-6200 Å and a resolution of 4-5Å. With the Blue Channel, we used a 300 line/mm grating, giving 3.2 Å/pixel dispersion, spectral coverage from 3400-7200 Å, and 9-11 Å resolution. Typical exposure times were 4 minutes with LRIS and 15 minutes with the Blue Channel. We performed the usual reduction steps for CCD spectra (bias subtraction, flat fielding, sky subtraction) using IRAF. The wavelength calibration used arc lamp spectra taken in temporal proximity to the object spectra, and the relative flux calibration used standard star spectra taken on the same or adjacent nights; both were also done in IRAF.

We used visual inspection of the spectra and radial velocity information to determine which objects were bona fide globular clusters. Objects with strong Na D lines, narrow line widths, continuum slope more appropriate to stars, and/or low radial velocities were classified as stars, while objects with large radial velocities were classified as galaxies. Both classifications are noted in Table 2.6. We determined velocities of the clusters by cross-correlating their spectra against spectra of template clusters with well-determined velocities (225-280, 163-217, 158-213), taken on the same night, using the XCSAO cross-correlation package. The new velocities are in Table 2.6. Figure 2.5 shows examples of some of the new Keck spectra.

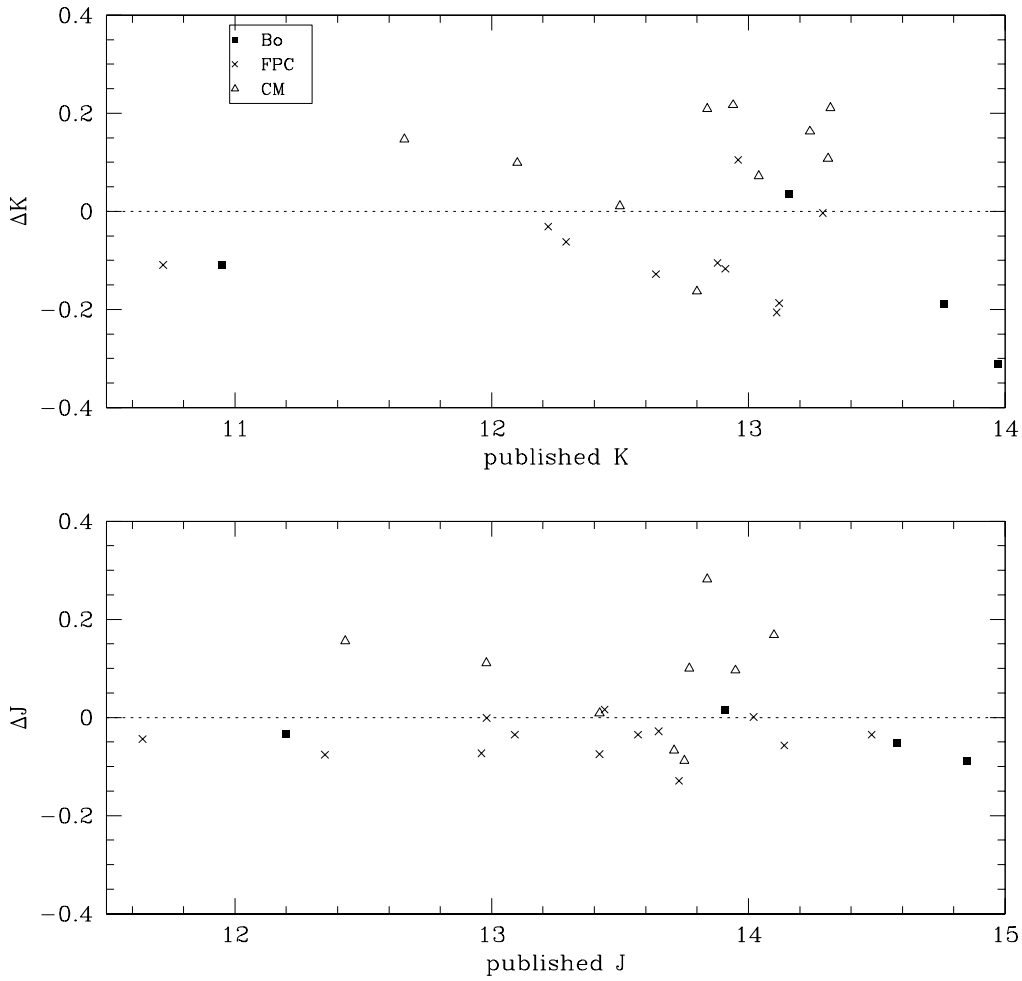

Fig. 2.4.— Comparison of near-IR photometry to previous results. Bo: Bònoli et al. (1987, 1992); FPC: Frogel et al. (1980); CM: Cohen & Matthews (1994).

Table 2.6. New spectroscopic data for M31 globular clusters

name	velocity km s^{-1}	[Fe/H] dex	comments
025-084	-230 ± 41	-1.43 ± 0.18	···
036-000	-341 ± 24	-0.99 ± 0.25	···
125-183	-514 ± 54	-1.71 ± 0.14	···
126-184	-182 ± 14	-1.20 ± 0.47	···
134-190	-401 ± 32	-1.12 ± 0.16	···
167-000	-235 ± 16	-0.49 ± 0.43	···
222-277	-282 ± 20	-1.11 ± 0.37	···
234-290	-226 ± 16	-0.84 ± 0.13	···
292-010	-331 ± 23	-1.42 ± 0.16	···
301-022	-30 ± 20	-1.22 ± 0.18	···
302-023	-371 ± 23	-1.50 ± 0.12	···
304-028	-353 ± 15	-1.32 ± 0.22	···
305-D024	-466 ± 20	-1.29 ± 0.57	···
307-030	-384 ± 14	-0.78 ± 0.41	···
310-032	-189 ± 18	-1.43 ± 0.28	···
313-036	-446 ± 6	-0.83 ± 0.13	···
314-037	-318 ± 66	···	young?
316-040	-344 ± 20	-0.64 ± 0.40	···
321-046	-527 ± 35	···	young?
322-049	-581 ± 29	···	young?
324-051	-299 ± 35	···	young?
327-053	-658 ± 29	···	young?
328-054	-243 ± 23	-1.51 ± 0.28	···
331-057	-60 ± 24	-1.44 ± 0.69	···
337-068	50 ± 12	-1.09 ± 0.32	···
347-154	-312 ± 36	···	young?
350-162	-457 ± 18	-1.47 ± 0.17	···
354-186	-283 ± 26	-1.46 ± 0.38	···
365-284	-78 ± 13	-1.35 ± 0.14	···
380-313	-121 ± 31	···	young?
383-318	-250 ± 10	-0.48 ± 0.20	···

Table 2.6—Continued

name	velocity km s^{-1}	[Fe/H] dex	comments
393-330	-331 ± 10	-1.02 ± 0.29	···
398-341	-227 ± 5	-0.34 ± 0.30	···
401-344	-273 ± 52	-1.75 ± 0.29	···
NB16	-115 ± 15	···	young?
NB67	-113 ± 17	-1.43 ± 0.13	···
NB68	-157 ± 11	-0.76 ± 0.33	···
NB74	-60 ± 12	-0.02 ± 0.43	···
NB81	15 ± 11	-0.75 ± 0.33	···
NB83	-150 ± 14	-1.26 ± 0.16	···
NB87	-47 ± 10	0.26 ± 0.41	···
NB89	-332 ± 6	-0.53 ± 0.57	···
NB91	-187 ± 10	-0.71 ± 0.33	···
non-clusters			
000-034	26745 ± 26	···	gal
000-314	-54 ± 22	···	star
000-340	32418 ± 24	···	gal
007-059	41899 ± 31	···	gal
053D-NB20	-204 ± 62	···	star
055-116	-287 ± 10	···	star
080D-NB93	-84 ± 18	···	star
113-000	74 ± 87	···	star
132-000	35 ± 28	···	star
264-000	198 ± 36	···	star
308-000	13964 ± 28	···	gal
341-081	-283 ± 16	···	star
392-329	-25 ± 20	···	star
395-332	32184 ± 24	···	gal
DAO018	-22 ± 13	···	star
NB94	-276 ± 22	···	star
NB95	-21 ± 9	···	star
NB96	-26 ± 21	···	star

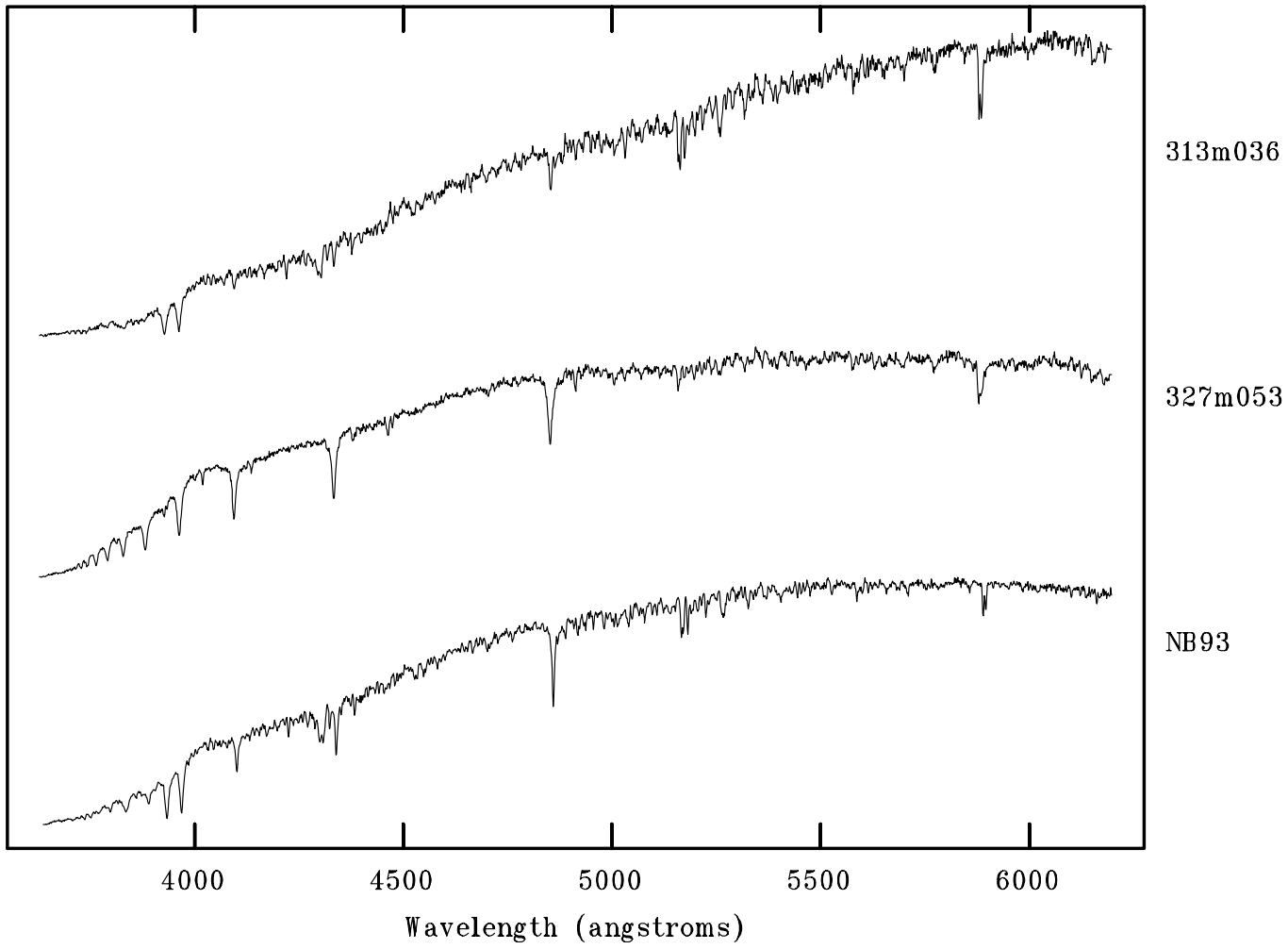

Fig. 2.5.— Examples of new spectra, showing Galactic star (NB93), A-star like 'young' globular (327-053), true globular (313-036).

Several of the clusters with new spectra had spectra with large Balmer absorption lines, but with cross-correlation velocities too large for them to be likely Galactic A stars. Examining the archived spectra used by HBK, we identified several more clusters with similar spectra, bringing the total number to 15. We tentatively classify these objects as young globular clusters; other authors, including Sargent et al. (1977) and Elson & Walterbos (1988), have similarly classified some of these objects. We flag these objects as 'young?' in Table 2.6 and do not attempt to determine their metallicities. A detailed examination of these objects will follow in a subsequent paper.

We modified the IRAF task SBANDS to compute absorption line indices according to the prescription of Brodie & Huchra (1990). We tested this modified task on the archived MMT spectra of HBK and found excellent agreement: our measurements differed from the published values (Huchra 1996) by less than 0.01 mag, on average, for all indices.[2] We measured the indices on flux-calibrated versions of our new spectra and determined the index errors using non-fluxed versions of the same spectra, again according to the prescription given in Brodie & Huchra (1990). The measured indices were combined using the metallicity calibration defined in that paper to determine metallicities; the resulting metallicity measurements are in Table 2.6. It is clearly possible to do a more detailed metallicity analysis using the new Keck spectra, since they have better signal-to-noise than most of the MMT spectra used by HBK; however, since most of the spectroscopic data still come from that paper, we used its methods to maintain consistency across the cluster sample.

2.3.4 Data summary

We have compiled the results of our new photometry and spectroscopy with the existing data from the literature into a final catalog of M31 cluster data. Optical photometry is the only subset of the data where our new data significantly overlap with published work; to keep this data set as uniform as possible, we used our photometry in preference to published data unless our photometric errors were larger than 0.10 mag. Of 435 clusters and cluster candidates, 268 have

[2]When the archived spectra were transformed from the original data format to FITS format, the details of the original wavelength solution were lost, so we did not expect to exactly duplicate the original index measurements. One large discrepancy deserves mention: we found the Fe5270 index for 034-096 to have a value of 0.0367±0.013, but the HBK value (published in Huchra et al. 1996) is ten times as large. We suspect that the HBK value is a typographical error, since our value is more consistent with the other indices. The resulting weighted metallicity is -0.64 ± 0.37, compared to HBK's 0.31 ± 2.08.

optical photometry in four or more filters, 224 have near-infrared photometry, 200 have velocities, and 188 have spectroscopic metallicities. This catalog is the basis for the analysis to follow in the next section and is, to our knowledge, the most comprehensive catalog of information available for M31 globular clusters and plausible cluster candidates. The catalog is available electronically at `http://cfa-www.harvard.edu/~huchra/m31globulars/m31gc.html`. The electronic version contains additional information not given in this work, e.g. duplicate object names.

2.4 Analysis

Our classification of some M31 clusters as possibly young from their spectra made us suspect that the cluster catalog could be contaminated by other young objects. We checked this using $B-V$ as a rough age indicator, since this color is available for the largest number of objects. We found that most of the 'young' clusters were blue, with an average $B-V$ of 0.37 ± 0.07; the average $B-V$ for all objects in the catalog was 0.87 ± 0.02. The two bluest Galactic globulars in the June 1999 version of the Harris (1996) catalog have $(B-V)_0 = 0.40$ and 0.42, but these are the most- and least-reddened clusters in the catalog (Terzan 5 has $E(B-V) = 2.37$ and NGC 7492 has $E(B-V) = 0.0$), so their colors are somewhat suspect. The next bluest clusters have $(B-V)_0 = 0.55$. It seems likely, then, that objects in M31 with $B-V < 0.55$ are not true globular clusters. There are 49 such objects in our catalog, and their other colors are blue as well: for example, they lie along an extension of the sequence in $B-V$ vs. $U-B$ formed by the redder objects. We removed these blue objects and the remaining 'young' clusters (which might be reddened and thus have $B-V > 0.55$) from our dataset before beginning the analysis. $B-V$ color is not a perfect selection criterion, of course: some objects do not have $B-V$ values, and some may have photometric errors that put them on the wrong side of the boundary. However, except for a few clusters with poor-quality spectra, all of the spectroscopically-observed clusters with $B-V < 0.55$ had already been identified as young from their spectra. This suggests that our $B-V$ criterion is reasonable.

2.4.1 Reddening

Previous photometric studies of the M31 GCS have dealt with the problem of determining the cluster reddening in several ways. Frogel et al. (1980) (hereafter

FPC) corrected the colors of 35 clusters for reddening, using the reddening-free parameter Q_K from unpublished spectroscopic work by L. Searle. Crampton et al. (1985) used the intrinsic colors of the same 35 clusters to calibrate $(B-V)_0$ as a function of their spectroscopic slope parameter S. Numerous authors (e.g. Bajaja & Gergeley 1977; Sharov 1977; Iye & Richter 1985) have used the globular clusters as reddening probes, often by assuming them to have a single intrinsic color. Most studies of the M31 GCLF (Reed et al. 1992, 1994; Secker 1992; Kavelaars & Hanes 1997; Gnedin 1997) studied only clusters outside the ellipse used by Racine (1991) to define the outer boundary of the M31 disk. These authors assumed that only foreground Galactic extinction affected these 'halo' clusters.

For the disk clusters, there is almost certainly extinction due to dust in the disk of M31, so merely correcting for Galactic extinction is not sufficient. Determining the reddening from the total HI column density and dust-to-gas ratio is also not sufficient, since the clusters lie at different (and unknown) distances along the line of sight through the M31 disk. The assumption that the halo clusters suffer only foreground reddening may also be incorrect: recent far-infrared observations of spiral galaxies (Nelson et al. 1998; Alton et al. 1998) indicate that the dust is more extended than the starlight. It is important to test this by determining the reddening of the halo clusters.

With our larger database of multicolor photometry we attempted to determine the reddening for each individual cluster, using correlations between optical and infrared colors and metallicity, and by defining various 'reddening-free' parameters. To calibrate these methods we used the June 1999 version of the Harris (1996) database of Galactic GC parameters. This database contains colors from Peterson (1993) and Reed (1996), reddening values from multiple sources (mainly Reed et al. 1988, Webbink 1985, and Zinn 1985), and metallicities from multiple sources (mainly Zinn 1985 and Armandroff & Zinn 1988). We corrected the colors for reddening using the $R_V = 3.1$ extinction curve of Cardelli, Clayton, & Mathis (1989). There are two major unavoidable assumptions in this procedure: that in the Galaxy and M31, both the extinction law and the globular cluster intrinsic colors are the same. There is conflicting evidence on whether this first assumption is correct: Massey et al. (1995) find $E(U-B)/E(B-V) = 0.4-0.5$, Iye & Richter (1985) found this ratio to be 1.01 ± 0.11, and Walterbos & Kennicutt (1988) found it to be 0.6 ± 0.2. Since there is no alternative optical-infrared extinction curve for M31, using the Galactic curve is the only option. We will show below that this is reasonable.

We performed linear regressions of intrinsic optical colors against metallicity for the 88 Galactic clusters with $E(B-V) < 0.5$. Colors used were $(B-V)_0, (B-$

$R)_0, (B-I)_0, (U-B)_0, (U-V)_0, (U-R)_0, (V-R)_0, (V-I)_0, (J-K)_0$, and $(V-K)_0$. The correlation coefficients r ranged from 0.91 for $(U-R)_0$ to 0.77 for $(V-R)_0$; $(V-R)_0$ is a poor metallicity indicator because of its small range and we do not consider it further. The color excess is determined from the observed color, the metallicity-derived intrinsic color, and the reddening ratio from Cardelli et al. (1989):

$$(X-Y)_0 = a[\mathrm{Fe/H}] + b \tag{2.1}$$

$$E(B-V) = \frac{E(B-V)}{E(X-Y)}[(X-Y) - (X-Y)_0] \tag{2.2}$$

We use $X-Y$ as generic notation to represent any color.

These color-metallicity relations allow us to check the assumption that the reddening laws in M31 and the Galaxy are the same. To do this, we used the colors of the 'old' M31 clusters with spectroscopic metallicities. For each cluster, we used the above linear regressions to determine the color excess in each color, then derived the various reddening ratios by dividing these color excesses by the color excess for $B-V$, also determined from the intrinsic color-metallicity relation. Within the (admittedly large) uncertainties, the medians of these reddening ratios over all clusters were consistent with the Galactic values; see Table 2.7. This result validates our use of the Galactic extinction curve to determine the reddening. We must still show that the color-metallicity relations are the same for the two sets of clusters and we do so in the following section.

To estimate the reddening for objects without spectroscopic data, we also determined relationships between 'reddening-free parameters' and intrinsic colors. We derived all six possible reddening-free parameters (hereafter referred to as Q-parameters) from the same Galactic cluster *UBVRI* data used to calibrate the color-metallicity relations. The Q-parameters are defined as:

$$Q_{XYZ} \equiv (X-Y) - \frac{E(X-Y)}{E(Y-Z)}(Y-Z) = (X-Y)_0 - \frac{E(X-Y)}{E(Y-Z)}(Y-Z)_0 \tag{2.3}$$

We then regressed these against the clusters' intrinsic colors, and used the results to determine the color excess. Schematically:

$$Q_{XYZ} \Rightarrow (X-Y)_0 \Rightarrow E(B-V) \tag{2.4}$$

The correlation coefficients for the Q-parameters were poorer than those for the color-metallicity relations, ranging from 0.80 for Q_{BVR} to 0.27 for Q_{VRI}. Since there is significant scatter in all of these correlations (due to age or 'second parameter' effects?) applying them will yield only a rough estimate of the individual cluster

Table 2.7. Extinction law derived from M31 globular clusters

	$E(X-Y)/E(B-V)$	
$X-Y$	MW[a]	M31
$U-B$	0.72	0.72 ± 0.15
$U-V$	1.72	1.54 ± 0.14
$U-R$	2.30	2.19 ± 0.22
$B-R$	1.58	1.61 ± 0.16
$B-I$	2.26	2.45 ± 0.23
$V-I$	1.26	1.40 ± 0.22
$V-K$	2.75	2.48 ± 0.33
$J-K$	0.52	0.53 ± 0.19

[a]From Cardelli et al. (1989).

reddening, and we do not attempt to treat the results in a statistically rigorous manner.

Our final reddening determination used seven of the nine colors in Table 2.7 (we dropped $U-B$ and $J-K$, since these colors are not very sensitive to reddening) and all six Q-parameters. For each of the two methods we averaged the results over all colors or parameters to produce one value of $E(B-V)$ per method. The standard deviations of these averages serve as an estimate of the precision of the methods. We tested the methods first on 25 heavily-reddened Galactic clusters not used for the calibration. The results were encouraging – the precision of both methods, defined as $\sigma_{E(B-V)}/\overline{E(B-V)}$, had a median value of $\sim 7\%$. The two methods agreed quite well both with each other and with the color excesses from the Harris catalog: the average offset between $E(B-V)$ from the Q-parameter method and the Harris value was 0.03 ± 0.03; for the color-metallicity method the average offset was 0.00 ± 0.02 (see Figure 2.6).

To determine the reddening for the M31 clusters we combined the results from the two methods, subtracting 0.03 from the Q-method results because of the offset noted in the previous paragraph. We examined the errors in the cluster reddenings from the two methods, and determined that the errors were the same when the error in [Fe/H] was approximately 0.4, and that the error in the metallicity-derived $E(B-V)$ increased dramatically for $\sigma_{[\mathrm{Fe/H}]} > 0.7$.

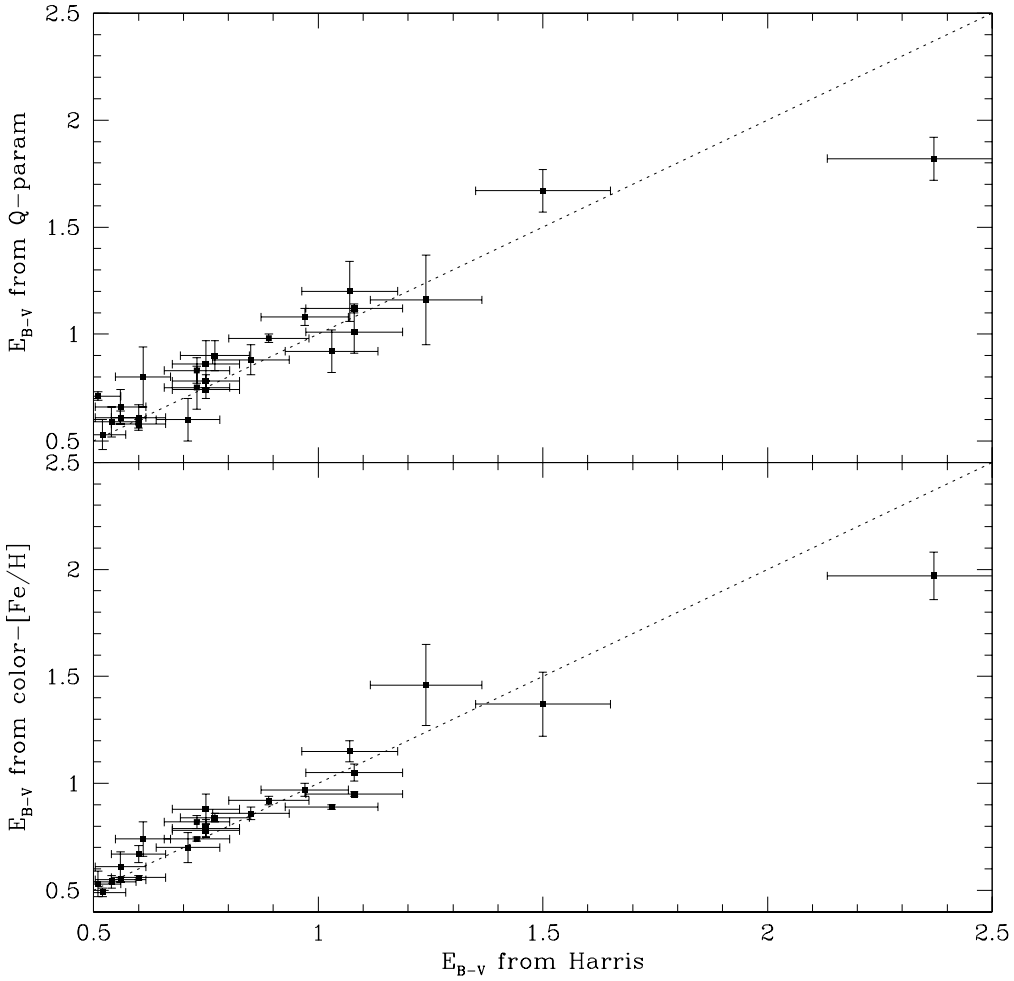

Fig. 2.6.— High-reddening Galactic clusters: $E(B-V)$ from Harris (1996) vs. $E(B-V)$ from new methods.

The $E(B-V)$ and [Fe/H] errors are related by

$$\sigma_{E(B-V)} = \left| \frac{\partial \overline{E(B-V)}}{\partial [\mathrm{Fe/H}]} \right| \sigma_{[\mathrm{Fe/H}]} = \left(\frac{1}{N} \sum \frac{E(B-V)}{E(X-Y)} a_{X-Y} \right) \sigma_{[\mathrm{Fe/H}]} \qquad (2.5)$$

(where N is the number of colors and a is the same as in equation 2.2). We weighted the metallicity-derived $E(B-V)$ by the inverse of the bracketed term in the above equation. The zeropoint of the weighting was set so that the weight of $E(B-V)([\mathrm{Fe/H}])$ would be zero at $\sigma_{[\mathrm{Fe/H}]} = 0.7$, and the weight for $E(B-V)(\mathrm{Q})$ was set to give the two methods equal weight at $\sigma_{[\mathrm{Fe/H}]} = 0.4$.

To check our results, we compared our reddenings with the $E(V-K)$ given for 34 clusters in FPC. A typical error in our values of $E(B-V)$ for these clusters was 0.04. For 24 of these clusters FPC quote $E(V-K) = 0.28$, which corresponds to $E(B-V) = 0.10$, their value for the foreground reddening. For these clusters our $E(B-V)$ ranges from 0.01 to 0.18 with a mean $E(B-V) = 0.13 \pm 0.02$. For the 10 clusters with larger reddening, we find the median $E(B-V)/E(V-K) = 2.7 \pm 0.2$, which is consistent with the Cardelli et al. value of 2.75, or the FPC value of 2.8.

We also compared our results with the predicted $E(B-V)$ from the Galactic dust maps of Schlegel et al. (1998), hereafter SFD. Since their map does not account for reddening internal to the M31 disk, we compared only reddening for objects in the halo, as defined by Racine (1991). We were able to determine a reddening for 60 of these clusters, with typical errors of 0.06 in $E(B-V)$. The mean offset (SFD$-$our value) is -0.02 ± 0.01, consistent with zero. However, the standard deviation of the offset (0.08) is large, and, for low reddening, our values scatter between 0 and 0.2 and show little correlation with the SFD results (which have values between 0.05 and 0.1). The SFD maps show a large reddening for one cluster (462–000), and for it the agreement is fairly good: the SFD maps give $E(B-V) = 0.29$ and we find $E(B-V) = 0.28 \pm 0.16$. From the comparisons with SFD and FPC, we estimate that our values of $E(B-V)$ have total errors between 0.05 and 0.10. These are large errors, but we believe this method is preferable to the alternatives of correcting only for the foreground reddening or doing no reddening correction at all.

We estimated reddenings for all the M31 clusters with sufficient data, a total of 314 objects. Some values are more reliable than others: unreliable measurements are those with with no reddening errors (those with only one color-metallicity relation or Q-parameter) and those with large reddening errors (arbitrarily chosen as $\sigma_{E(B-V)}/\overline{E(B-V)} > 0.5$ for $\overline{E(B-V)} > 0.15$, $\sigma_{E(B-V)}/\overline{E(B-V)} > 1.0$ for $\overline{E(B-V)} < 0.15$). We do not use these reddenings in the analysis that follows. The distribution of the 221 reliable reddenings (Figure 2.7) has a mean

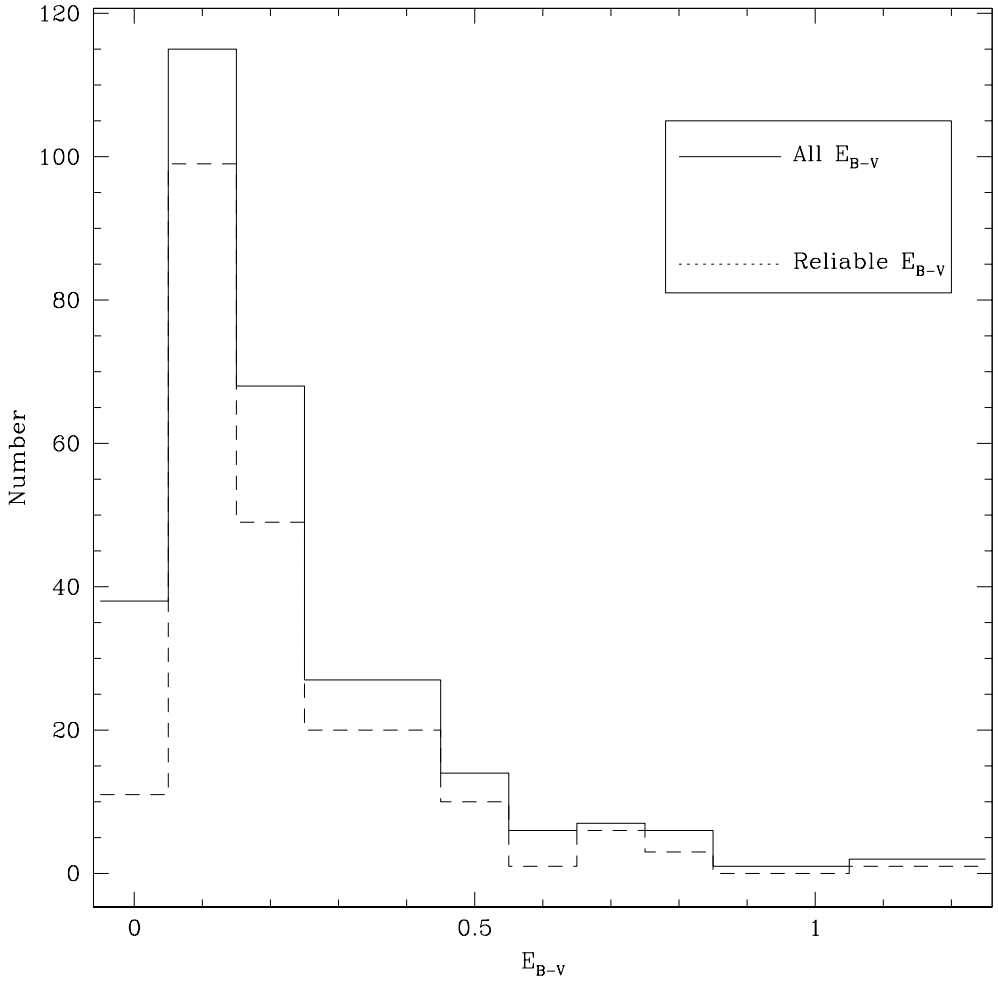

Fig. 2.7.— Distribution of $E(B-V)$ for M31 clusters

of $E(B-V) = 0.22$, a median of $E(B-V) = 0.16$, and a standard deviation of 0.19. Three-quarters of the clusters have $E(B-V) < 0.27$. The largest 'reliable' reddening is that of 037–B327, $E(B-V) = 1.38$; van den Bergh (1969) notes that this cluster is "the most highly-reddened cluster known in M31". If this reddening value is correct, 037–B327 is twice as luminous as 000–001 (=G1), one of the brightest M31 GCs. Assuming an M31 distance modulus of 24.47 (Stanek & Garnavich 1998; Holland 1998) means that 037–B327 has $M_V \approx -12$ and is more than four times as luminous as the brightest Galactic GC (ω Cen at $M_V = -10.29$; Harris 1996). This object is puzzling: as van den Bergh states, there is no obvious reason why the intrinsically brightest GC in M31 should also be the most heavily-reddened. However, the nature of 037–B327 is still uncertain: the reddening estimate is from color information alone, and a spectrum of this object would be extremely valuable.

All of the reddening values are shown in as functions of position in Figure 2.8. The map appears reasonable in that the objects with the lowest reddening are distributed roughly spherically, while those with the highest reddening are projected onto the galaxy disk. The higher-reddening clusters in the disk tend to lie on the northwest side of the major axis. This accords with statements in previous work (Iye & Richter 1985; Elson & Walterbos 1988) that this side of the disk is nearer to us along the line of sight. We note that a substantial number of clusters outside the 'halo' boundary have $E(B-V) > 0.1$. While some of these values are undoubtedly due to the large errors in our method, some clusters (such as 004–050, with $E(B-V) = 0.19 \pm 0.04$) have reddening values that are very consistent over a number of colors and Q-parameters. It seems unlikely that some systematic problem in our method or photometry could affect all of the individual colors to make them give the same erroneous reddening. Two possibilities remain: (1) the M31 dust distribution extends to greater projected distances than previously suspected, and/or (2) the Galactic foreground extinction in the direction of M31 is patchy on scales smaller than the SFD spatial resolution of $6.1'$. In either case, the assumption that the M31 halo clusters are subject to only foreground reddening is in some doubt and should be re-examined.

2.4.2 Color-metallicity relation

We showed in Section 2.4.1 that the assumption of a similar reddening law in M31 and the Galaxy was reasonable. The second major assumption made in our reddening correction procedure was that the relation between intrinsic color and metallicity is the same for M31 GCs and Galactic GCs. We tested this assumption

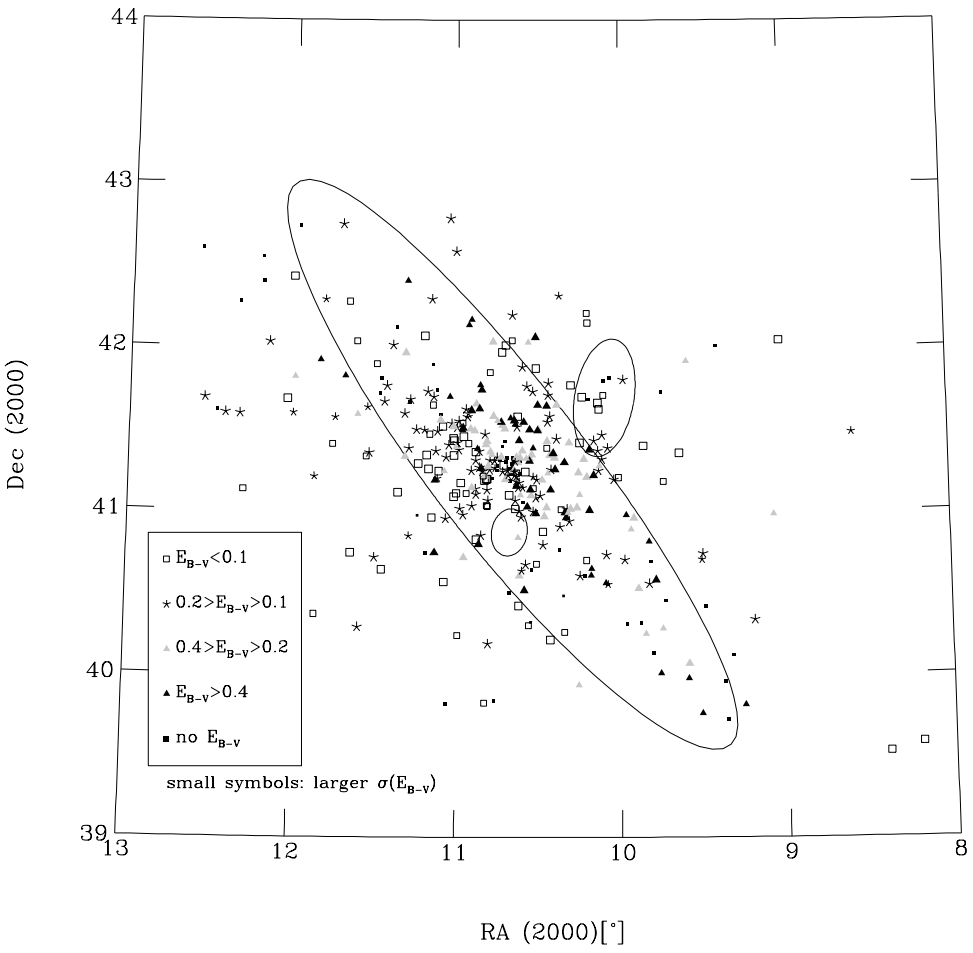

Fig. 2.8.— Map of M31 globular clusters in RA and Dec, in groups according to reddening. Large ellipse is M31 disk/halo boundary as defined by Racine (1991); smaller ellipses are D_{25} isophotes of NGC 205 (NW) and M32 (SE).

Table 2.8. Color-metallicity relations for Galactic GCs

	$(X-Y)_0 = a[\mathrm{Fe/H}] + b$		$[\mathrm{Fe/H}] = a(X-Y)_0 + b$		
$(X-Y)_0$	a	b	a	b	N
$(B-V)_0$	0.159 ± 0.011	0.92 ± 0.02	5.50 ± 0.33	-5.26 ± 0.23	88
$(B-R)_0$	0.262 ± 0.014	1.51 ± 0.02	3.69 ± 0.26	-5.62 ± 0.30	66
$(B-I)_0$	0.318 ± 0.024	2.07 ± 0.04	2.79 ± 0.26	-5.94 ± 0.42	76
$(U-B)_0$	0.289 ± 0.018	0.57 ± 0.03	2.76 ± 0.20	-1.86 ± 0.04	81
$(U-V)_0$	0.457 ± 0.026	1.50 ± 0.04	1.92 ± 0.09	-3.05 ± 0.09	81
$(U-R)_0$	0.572 ± 0.027	2.11 ± 0.04	1.62 ± 0.09	-3.52 ± 0.11	66
$(V-I)_0$	0.156 ± 0.015	1.15 ± 0.02	4.22 ± 0.39	-5.39 ± 0.35	75
$(J-K)_0$	0.177 ± 0.021	0.91 ± 0.03	5.86 ± 0.86	-5.25 ± 0.52	37
$(V-K)_0$[a]	0.593 ± 0.080	3.15 ± 0.12	1.30 ± 0.15	-4.45 ± 0.36	23
$(V-K)_0$[b]	0.611 ± 0.070	3.14 ± 0.10	1.40 ± 0.17	-4.62 ± 0.38	35

[a]low $E(B-V)$ only

[b]all data

by doing BCES (bivariate correlated errors and intrinsic scatter) bisector linear fits (as described in Akritas & Bershady 1996) of color against metallicity for the M31 and Galactic clusters and comparing the results. The bisector fit is appropriate since we are interested in both the case where metallicity is used to predict color, as in the determination of reddening, and the case where color is used to predict metallicity, as follows in Section 2.4.4. (To do the actual predictions we used the BCES(Y|X) fit, an extension of the ordinary least-squares fit which allows for measurement error in both variables and intrinsic scatter. For reference, these fits for the Galactic data are given in Table 2.8.)

For the Galactic color-metallicity fits we used the same data used to determine the color-metallicity relations in Section 2.4.1; we estimated the intrinsic color errors as:

$$\sigma_{X-Y} = ({\sigma_{\mathrm{phot}}}^2 + (\sigma_{E(B-V)} E(X-Y)/E(B-V))^2)^{1/2} \tag{2.6}$$

We set σ_{phot} to 0.02 mag, as this is a typical uncertainty in Reed (1996), one of the main sources of integrated colors, and $\sigma_{E(B-V)}$ as $0.1E(B-V)$, following Harris (1996). We set $\sigma_{[\mathrm{Fe/H}]}$ for the Galactic clusters to 0.10 dex; typical uncertainties in Zinn (1985) (one of the major sources for Harris 1996) are 0.15 dex, but many

of the [Fe/H] values are averages from several sources. For the M31 fits we used 101 M31 clusters with reliable reddening and $\sigma_{\rm [Fe/H]} < 0.5$ dex. We estimated color errors using equation 2.6, with $\sigma_{\rm phot}$ set to 0.04 mag and $\sigma_{E(B-V)}$ to our measured value.

The BCES method produces estimates of the uncertainty in the slopes and intercepts of the linear fits, so one way to compare the two sets of fits is to compare the ratio of the parameter differences to the parameter uncertainty. However, unlike the case for ordinary least-squares fitting, the distribution of this ratio in the case of the null hypothesis is unknown, so it is impossible to determine its statistical significance. A more empirical approach is to simply compare the predictions of the two fits. We determined the differences in color predicted by the two fits at the metal-rich (red) and metal-poor (blue) ends of the data range, and compared these to the rms color residuals of the fits. We found the differences between the Galactic and M31 fits to be comparable to the fit residuals for all the colors.

The $(V-K)_0$ and $(J-K)_0$ fits are shown in Figure 2.9; these deserve particular attention for several reasons. The Galactic relations as originally derived by Brodie & Huchra (1990) rely on only 23 low-reddening calibrators in their Table 5A.[3] Only four of these Galactic calibrators have [Fe/H] > -1.2. To maintain consistency with the optical color-metallicity fits, we did the optical-infrared color-metallicity fits using the metallicity and reddening values in Harris (1996), rather than those in Brodie & Huchra's table. We also added the 14 "high-reddening" clusters in their Table 5B to see whether this made a difference to the fits. As Figure 2.9 shows, adding the additional clusters made a difference for $(V-K)_0$, bringing the fit closer to that for the M31 clusters (the second $(V-K)_0$ row in Table 2.8 shows the Galactic fit with all clusters included). Calibrating the color-metallicity relation with a small number of clusters means that even a small change in the input data can change the result.

For $(V-K)_0$ there are several M31 clusters that are either too blue for their metallicities or too metal-rich for their colors, compared to the Galactic clusters and the bulk of the M31 clusters. We have examined the spectra of these clusters and their photometry, and find no obvious problems with either. These clusters are not different from the bulk of M31 clusters in any obvious way (location, reddening, Hβ strength, etc.), and we are unable to explain their anomalous colors.

There is little difference in the $(J-K)_0$ fit when all clusters, instead of just

[3]The text of Brodie & Huchra (1990) indicates that their Table 5 contains the 'raw' (i.e. uncorrected for reddening) colors. This is incorrect – *the colors in this table have already been reddening-corrected.*

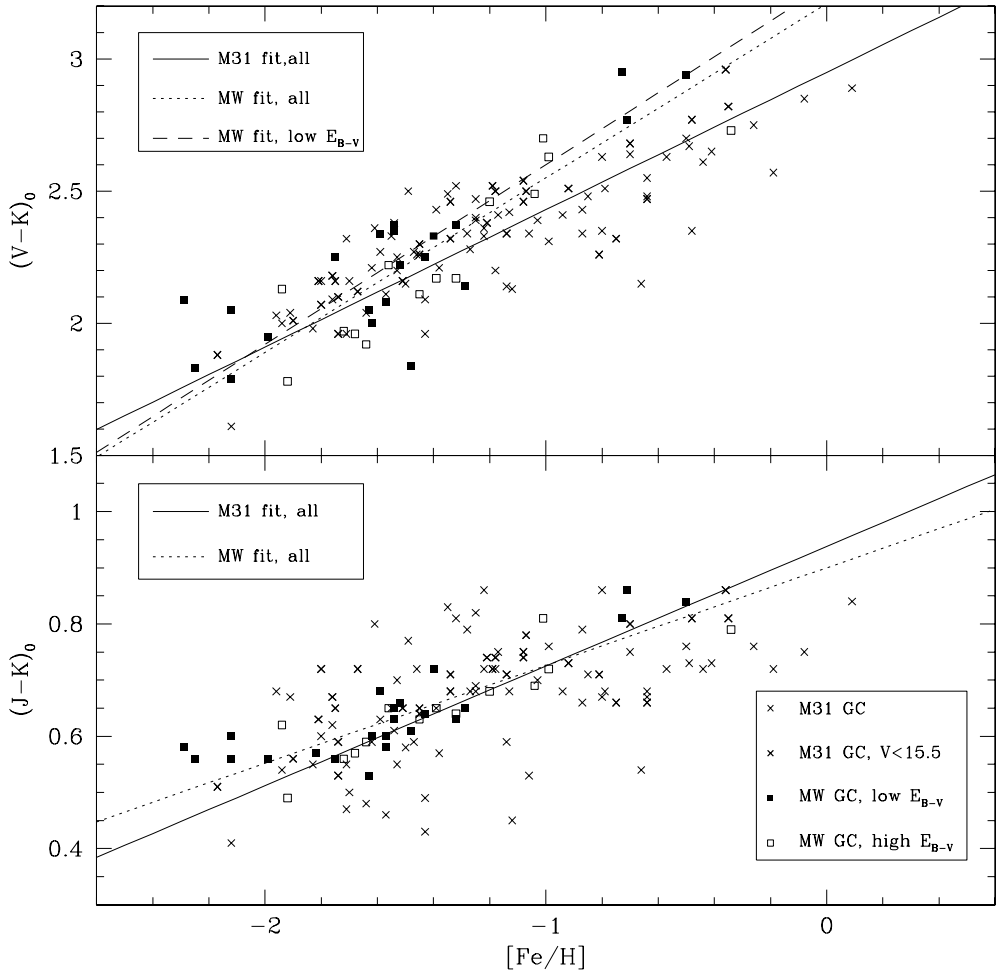

Fig. 2.9.— $(J-K)_0$ and $(V-K)_0$ color-metallicity relations for M31 and Galactic GCs.

low-reddening ones, are included. This is unsurprising since $J-K$ is much less sensitive to reddening than $V-K$. However, the $(J-K)_0$ vs. metallicity fit shows much larger rms residuals for the M31 clusters than the Galactic clusters. If we restrict the M31 data to the 31 clusters brighter than $V = 15.5$ – presumably these should have smaller photometric and spectroscopic errors because they are brighter – the residuals are much closer to the Galactic values, although the fit does not change significantly. This suggests that errors in the $J-K$ photometry may have been underestimated, and points to the need for precise $J-K$ colors if $(J-K)_0$ is to be used as a metallicity indicator. As Table 2.8 shows, $(J-K)_0$ is not as sensitive to metallicity as most of the other colors; its advantage as a metallicity indicator is its insensitivity to reddening.

Eighty-seven of the cluster candidates in our sample of 221 with 'reliable' reddening (as defined in the previous section) have no spectroscopic information, so we attempted to estimate their metallicities from their intrinsic colors. We applied the BCES(Y|X) fits of metallicity as a function of color, and averaged the resulting metallicities over all available colors. As in the reddening determination, the standard deviation of the metallicities from individual colors was used as the error estimate. We tested this procedure by using it on the clusters *with* spectroscopic information; this includes all the clusters used to do the metallicity-color fits as well as additional objects with large metallicity errors. The results are shown in Figure 2.10; the mean offset (spectroscopic−color-derived metallicity) is 0.020 ± 0.021, there is no evidence of a bias in the prediction with metallicity, and the largest offsets are for objects with large errors in color- or spectroscopically-determined metallicity or both.

Applying the method to the clusters without spectroscopic data produced equally encouraging results. 57% of the color-derived metallicities had uncertainties $\sigma_{\rm [Fe/H]} < 0.5$, compared to 76% within the same error range for spectroscopic metallicities. Six objects had very large or small values of [Fe/H] ($> +0.5$ or < -2.5); these had only a few colors and large errors in their derived [Fe/H]. These objects do not lie on the same two-color sequences as the confirmed globular clusters, so we suspect that they are either compact background galaxies, compact H II regions, or foreground stars. We do not include these outlying metallicities in the analysis that follows.

2.4.3 Color distributions

We analyzed the distribution of intrinsic colors for the 221 M31 GCs with reliable reddening. The histograms of colors are shown in Figures 2.11–2.13, and parameters

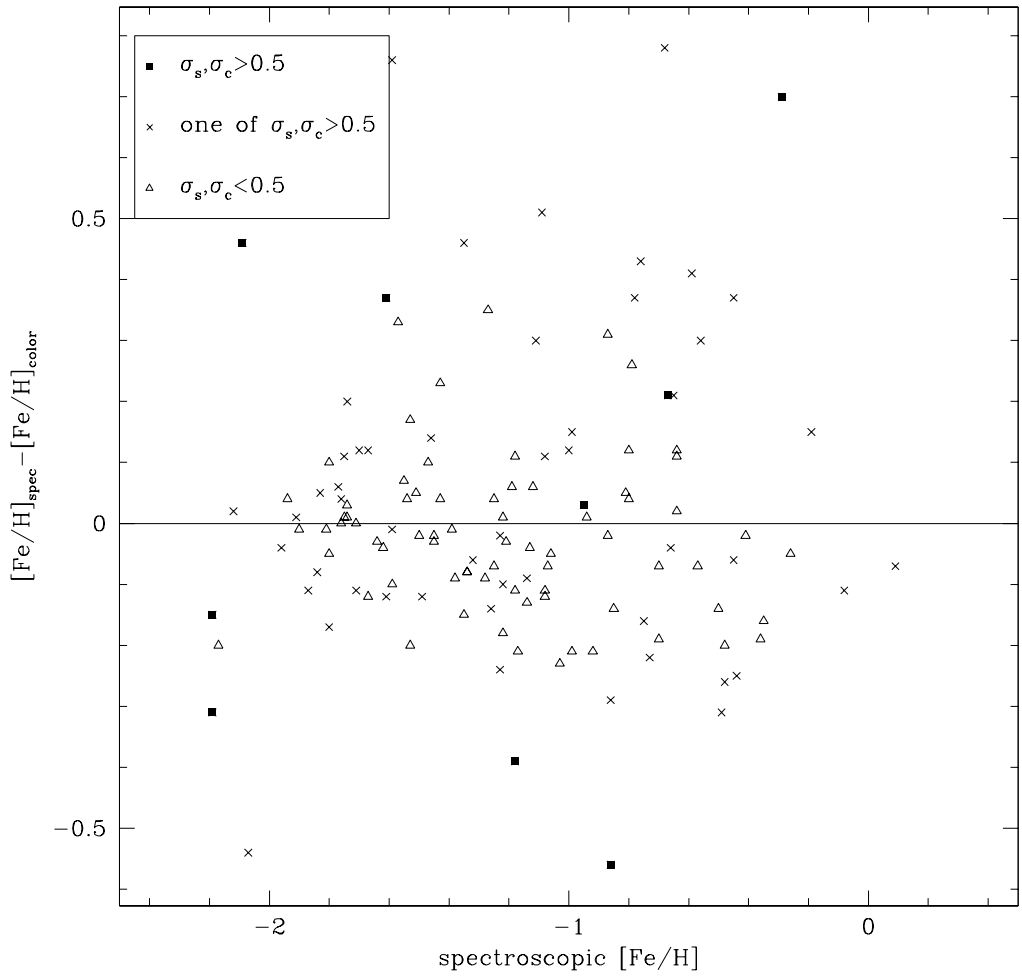

Fig. 2.10.— Comparison of spectroscopic and color-derived metallicities for M31 clusters with spectroscopic data.

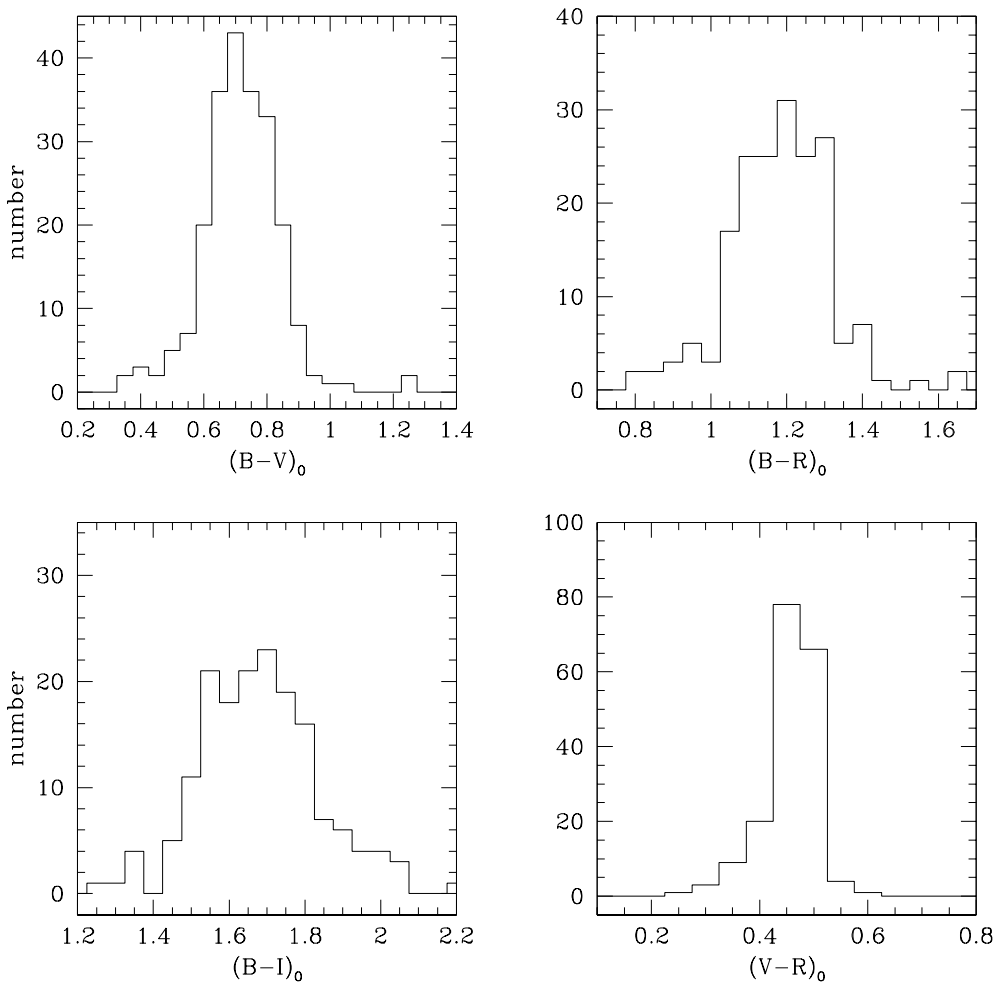

Fig. 2.11.— Intrinsic optical color distributions for M31 GCs.

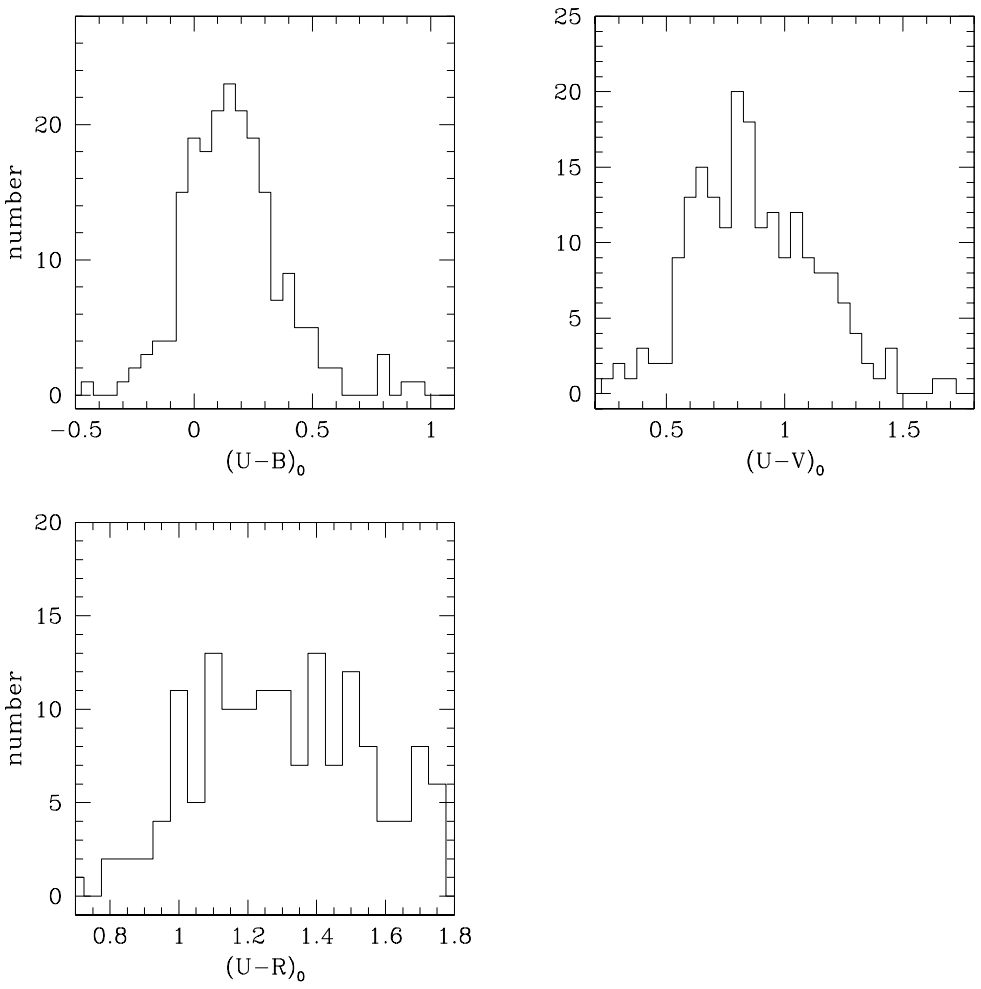

Fig. 2.12.— Intrinsic optical color distributions for M31 GCs.

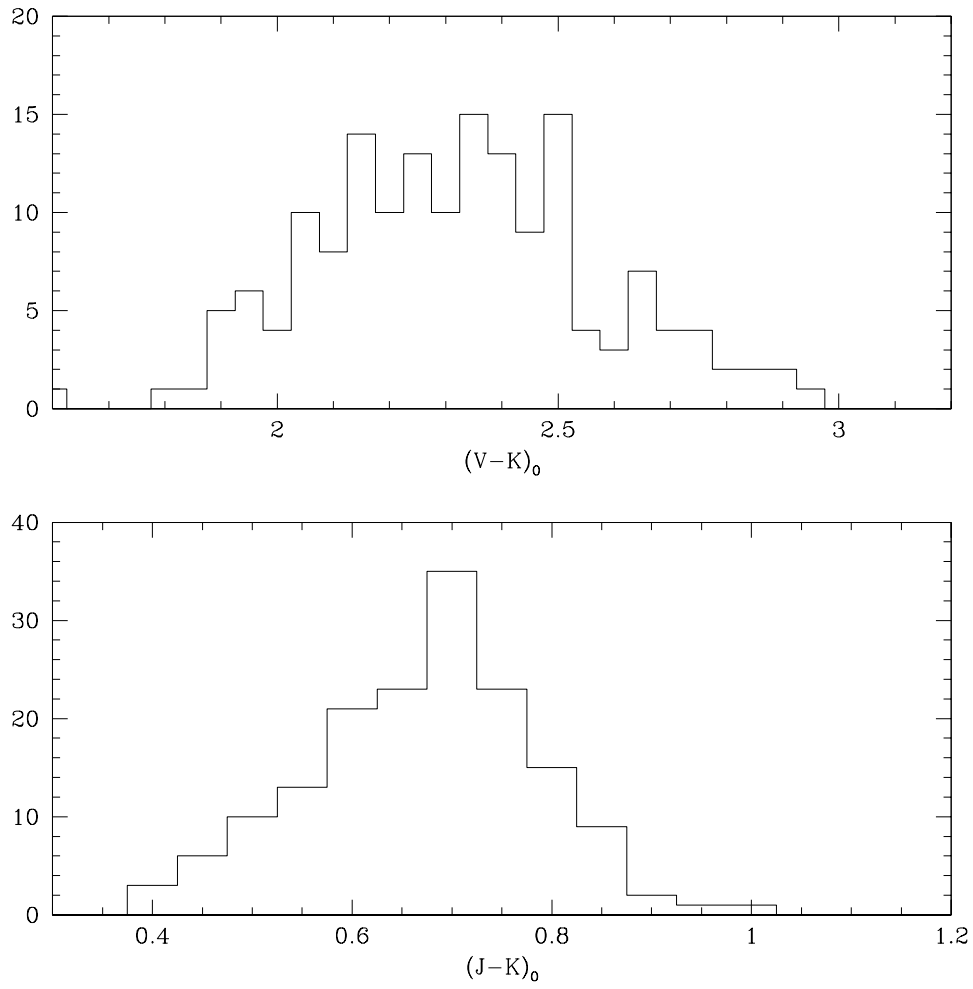

Fig. 2.13.— Intrinsic optical-infrared color distributions for M31 GCs.

Table 2.9. Distribution of intrinsic colors for M31 clusters

color	M31 mean	median	σ	MW mean	M31 predicted metal-poor	metal-rich
$(B-V)_0$	0.72 ± 0.01	0.72	0.12	0.71 ± 0.01	0.68	0.83
$(B-R)_0$	1.18 ± 0.01	1.19	0.12	1.18 ± 0.02	1.12	1.35
$(B-I)_0$	1.68 ± 0.01	1.68	0.16	1.64 ± 0.02	1.59	1.88
$(U-B)_0$	0.16 ± 0.02	0.16	0.23	0.20 ± 0.02	0.13	0.39
$(U-V)_0$	0.88 ± 0.02	0.84	0.31	0.89 ± 0.03	0.81	1.23
$(U-R)_0$	1.35 ± 0.03	1.32	0.34	1.38 ± 0.03	1.25	1.77
$(V-R)_0$	0.46 ± 0.01	0.47	0.05	0.47 ± 0.01	0.45	0.52
$(V-I)_0$	0.96 ± 0.01	0.96	0.11	0.94 ± 0.01	0.92	1.06
$(J-K)_0$	0.67 ± 0.01	0.68	0.13	0.64 ± 0.02	0.64	0.81
$(V-K)_0$	2.32 ± 0.02	2.32	0.26	2.24 ± 0.05	2.26	2.72

of the color distributions are given in Table 2.9. For comparison, the table also shows the mean intrinsic colors of the Galactic clusters (optical from Harris (1996), $(V-K)_0$ and $(J-K)_0$ from Brodie & Huchra 1990). The mean colors of the M31 clusters are consistent with corresponding Galactic mean colors. The large standard deviations in the M31 cluster colors incorporating U probably reflect the larger photometric errors in this filter. $(V-K)_0$ is notable for having a larger range (~ 1.5 mag) than most other colors. This is, of course, the basis for its use as a metallicity indicator. $(V-R)_0$ is notable for having a very small range; as Reed et al. (1992) reported, this can be exploited to discriminate against background galaxies (which have $(V-R)_0 \gtrsim 0.7$) in cluster searches.

We tested the color distributions of the M31 clusters for bimodality using the KMM algorithm (McLachlan & Basford 1988; Ashman et al. 1994). The input to this algorithm includes the individual data points, the number of Gaussian groups to be fit, and starting points for the groups' means and dispersions (the final solution is not very sensitive to the starting points unless there are many outliers). We used the results of Ashman & Bird (1993) to choose our starting points: they found two groups of M31 clusters with [Fe/H] $= -1.5$ and -0.6, with the metal-poor clusters comprising two-thirds of the total. Our input data specified two groups, with the bluer group twice as large, and the two mean colors corresponding to [Fe/H] $= -1.5, -0.6$ from our color-metallicity relations (Section 2.4.2). The predicted mean colors for the two groups appear in the last

two columns of Table 2.9. We specified the same dispersions for both groups in each color; in this case ('homoscedastic' fitting as opposed to 'heteroscedastic') the p-value returned by KMM adequately measures the statistical significance of the improvement in the fit in going from one to two groups. As a rough estimate, we specified a value of 80% of the overall dispersion in Table 2.9 as the starting point for the groups' dispersions in each color.

The hypothesis of a unimodal color distribution was rejected for only three colors: $(U-V)_0$ and $(U-R)_0$ at the 95% confidence level and $(V-K)_0$ at the 92% level. The mean colors of the two groups in all three colors correspond to metallicities of approximately -1.5 and -0.6. These three colors are the most sensitive to metallicity (Table 2.8), so it would be expected that they would show the strongest evidence for bimodality. In the other colors, the photometric errors are probably large enough to mask any color separations between the metal-rich and metal-poor populations. Visual inspection of the color histograms suggested that these same three colors might actually have trimodal distributions. We tested for this, again using KMM, and found that three-group fits were not superior to either one- or two-group fits for $(U-V)_0$ and $(U-R)_0$. Three groups were preferred to one or two for $(V-K)_0$. We are reluctant to claim a physical meaning for this, since this color is the most sensitive to both photometric errors (separate optical and infrared photometry is combined) and reddening. In the following section we show that two metallicity groups are preferred.

Figure 2.14 shows the distribution of $(V-I)_0$, which is often used as a metallicity indicator for globular cluster systems despite its fairly low metallicity sensitivity (see Table 2.8). From HST imaging in V and I, Kundu (1999) finds that 25-50% of the GCSs of a sample of ~ 50 galaxies show evidence for bimodal color distributions; Gebhardt & Kissler-Patig (1999) find similar results. The bottom two panels of the figure show the color distributions for elliptical galaxy GCSs with and without bimodality. The M87 (data from Kundu et al. 1999) and NGC 5846 GCs (data from Forbes et al. 1997b) clearly show bimodal distributions in $(V-I)_0$. The 'unimodal E' panel is the sum of 12 elliptical GCS color distributions which Forbes et al. (1996b) find *not* to be bimodal; although the histogram bins are larger in these data, the distribution is remarkably symmetric and unimodal. Comparing the color distribution for the ellipticals and spirals yields two interesting conclusions: first, M31 and the Galaxy clearly lack the extremely red (and presumably metal-rich) GCs found in massive ellipticals. Second, the blue peaks of the M87 and NGC 5846 color distributions are at approximately the same color as the M31 and Galactic peaks. This is consistent with the finding that these galaxies' metal-poor GC populations and the total M31 GC population have approximately the same mean

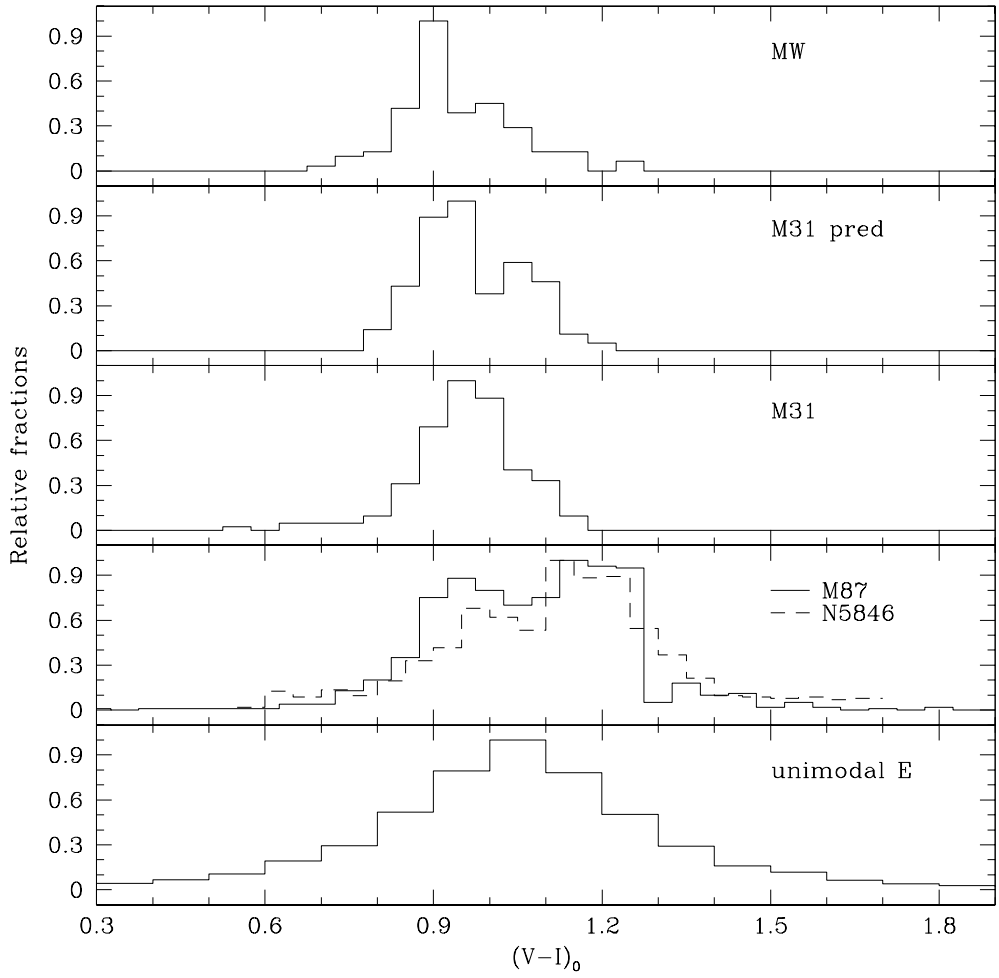

Fig. 2.14.— Distribution of $(V-I)_0$ for GCs of several galaxies. 'M31 pred' refers to $(V-I)_0$ predicted from [Fe/H] of M31 GCs.

metallicity ([Fe/H] ≈ -1.2; Forbes et al. (1997a) and the following section), and is also an interesting hint of a possible connection between ellipticals' metal-poor GCs and spirals' GCs.

The Galactic GCs (see, e.g. Côté 1999) and the M31 GCs (Ashman & Bird 1993, and the following section) are known to have bimodal metallicity distributions, and we have just shown that some M31 cluster colors are bimodal – why not $(V-I)_0$? We did Monte Carlo simulations of our observations of the $V-I$ distribution, and, as suggested above, we found that observational errors in the reddening and photometry can wash out the signature of bimodality. We predicted the M31 GCs' 'true' $(V-I)_0$ colors from their spectroscopically-determined [Fe/H] (see the second panel in Figure 2.14); we found this 'true' distribution to be bimodal at the $> 99\%$ confidence level. We then added to each color datum a Gaussian random error, drawn from a distribution with mean of 0 and standard deviation expected from the errors in our photometry and reddening determination. Of the 1000 color distributions generated in this manner, KMM detected bimodality in only about 250, implying that observational errors wash out the bimodal signal three-quarters of the time. Detection of multiple populations in GCS color distributions thus clearly requires precise photometry and/or the use of metal-sensitive colors.

We examined the correlation of M31 cluster intrinsic colors with distance from the galaxy's center, using the coordinate system of Baade & Arp (1964), as defined in HBK. In this system, X is the projected distance from the center of M31 along the major axis (positive X is to the northeast), Y is the projected distance along the minor axis (positive Y is to the northwest), and R_{gc} is the projected radial distance from the galaxy center, $R_{gc} = \sqrt{X^2 + Y^2}$. Ideally we would use the true spatial distance and not the projected distance from M31, but this information is not available for the M31 GCs. We binned the clusters in $20'$ bins in X and Y and $10'$ bins in R_{gc}, then calculated the weighted least-squares fit of the bin median colors against distance. It is well-known (Iye & Richter 1985; Elson & Walterbos 1988) that the observed colors of M31 clusters are redder for $Y > 0$, because the northwest side of the M31 disk is closer to us and more clusters are projected behind it. If our reddening correction was adequate this trend should be removed from the intrinsic colors. None of the colors showed a significant trend with X or Y, confirming that our reddening correction worked. More surprising was the fact that none of the colors showed a significant trend with R_{gc}; such a trend would be expected if there was any gradient in the metallicity of the system. However, even a large metallicity gradient (for example, 0.5 dex over $100'$) would produce a fairly small change in most colors ($\lesssim 0.15$ mag) so perhaps photometric errors and

scatter within the bins masked any true gradient.

Comparing the clusters' location in two-color diagrams to models produced by population synthesis provides useful checks on our photometry and on the models' accuracy. We obtained predicted colors for populations of ages 8 and 16 Gyr from three sets of models: Worthey (1996), Bruzual & Charlot (1996) (hereafter BC), and Kurth, Fritze-von Alvensleben, & Fricke (1999) (hereafter KFF). We used Worthey's 'vanilla' models and his interpolation program to generate colors for values of [Fe/H] from -2.0 to -0.1 in steps of 0.1 dex. We used the Salpeter IMF versions of the Bruzual & Charlot and Kurth et al. models, without interpolation, and obtained colors at metallicities of -2.33 (KFF models only), -1.63, -0.63, -0.32, 0.07 and 0.47 dex. Worthey (1994) states that, compared to Galactic GCs, his models are too red by 0.08 mag in $B-V$ and too blue by 0.03 mag in $J-K$, so we corrected the model colors by these amounts. Worthey attributes these offsets to defects in the stellar flux library; since all three sets of the models share the same stellar atmosphere models we applied the same corrections to the BC and KFF models.

In Figures 2.15–2.17 we plot two-color diagrams for M31 clusters, Galactic clusters and the models, using optical and IR colors often found in the literature. Confirmation that our photometry suffers no major systematic errors is provided by the fact that the Galactic and M31 clusters lie on essentially the same loci in all the diagrams. As expected, the M31 clusters show much more scatter than the Galactic GCs (because the photometric and reddening errors are larger), but much of this scatter is due to objects that are not confirmed clusters. It is clear from the diagrams that integrated photometry and model predictions are not precise enough to distinguish any possible age differences between the two sets of old clusters.

In Figure 2.15 the corrected models agree reasonably well with the data in $B-V$ and $U-B$, although the agreement becomes poorer in the high-metallicity region. The models also agree fairly well with each other in these colors, which is not the case in Figures 2.16 and 2.17. The model disagreement is not surprising; Charlot et al. (1996) found a difference of 0.3 mag in predicted $V-K$ between the solar-metallicity models of Worthey and those of Bruzual & Charlot. These authors attribute most of the discrepancy to differences in the underlying stellar evolution prescriptions. Shifting the Worthey models by ~ 0.2 mag to bluer $V-K$ to match the data in Figure 2.16 (since Figure 2.15 implies that the $B-V$ color is acceptable) would then require shifting the same models to bluer $J-K$ by ~ 0.1 mag to match the data in Figure 2.17. The shifts required for the BC and KFF models to fit the data in the $B-V/V-K$ and $J-K/V-K$ planes are in the same direction, but about half the magnitude, as those required for the Worthey

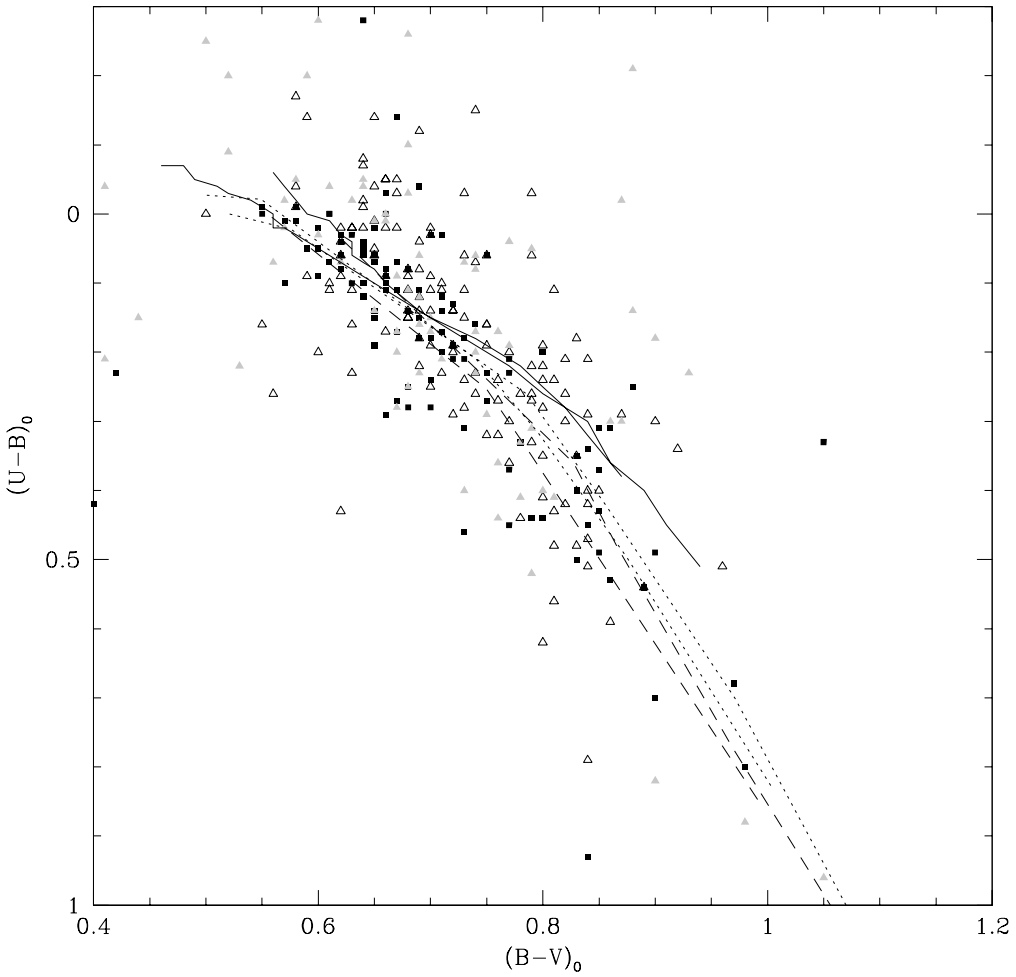

Fig. 2.15.— $(B-V)_0$ vs. $(U-B)_0$ for Galactic GCs (squares), confirmed M31 GCs (open triangles), and M31 GC candidates (shaded triangles). Lines are population synthesis models of ages 8 Gyr (bluer colors) and 16 Gyr (redder colors): Worthey (1996) (solid), Bruzual & Charlot (1996) (dashed), Kurth et al. (1999) (dotted). Models have been corrected as described in the text.

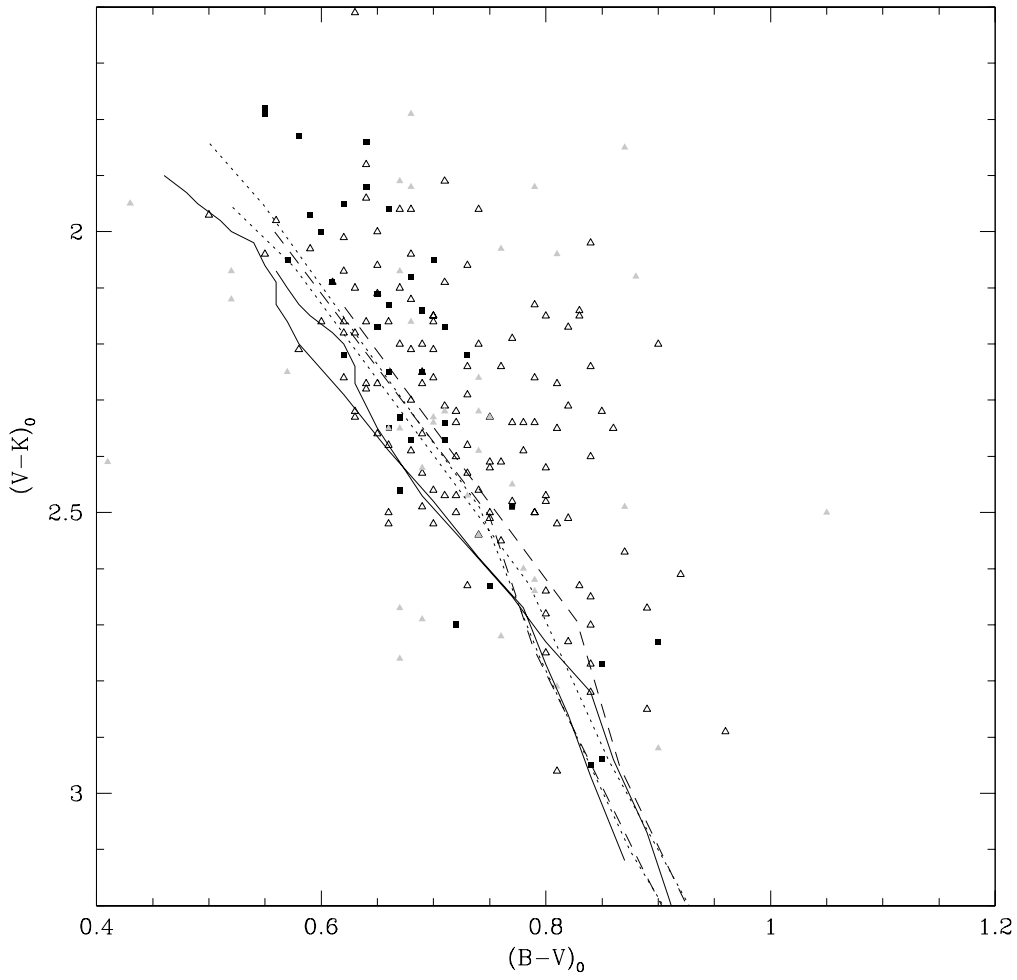

Fig. 2.16.— $(B-V)_0$ vs. $(V-K)_0$ for M31 and Galactic GCs. Symbols as in Figure 2.15.

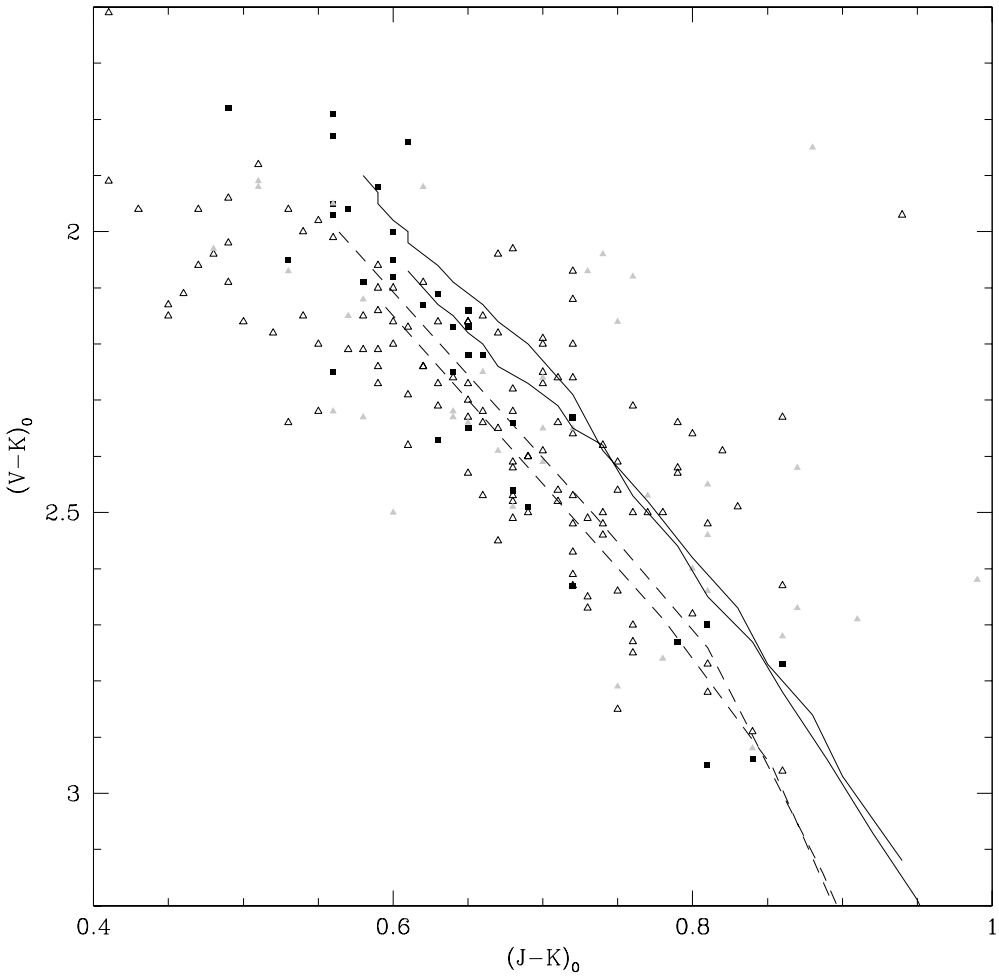

Fig. 2.17.— $(J-K)_0$ vs. $(V-K)_0$ for M31 and Galactic GCs. Symbols as in Figure 2.15; the KFF models do not predict J so are absent from this figure.

models. This arbitrary shifting of predicted colors to match the data does not uniquely determine the reasons for the disagreements between models and data. We speculate that the mismatches may be caused by problems in the treatment of the late stages of stellar evolution in the models, since most of the K-band light comes from evolved stars. The theoretical and observation photometric systems could also have systematic offsets. Clearly this is an area requiring more detailed examination by modelers, and the colors of globular clusters provide important constraints on the models.

In Figure 2.18 we plot [Fe/H] as a function of $(V-K)_0$. Some M31 GCs are too blue for their metallicities or too metal-rich for their colors, as discussed in Section 2.4.2. Covino et al. (1994) noted that some low-metallicity Galactic clusters were "exceedingly blue" in $V-K$ with respect to the models of Buzzoni (1989); they attributed this to a systematic problem with the photometry.[4] However, we find that the M31 clusters and Galactic clusters overlap in the region $(V-K)_0 \lesssim 2.1$ (Figure 2.18), and that the $(V-K)_0$ – [Fe/H] relations for the two sets of clusters are very similar at the metal-poor end (Figure 2.9). This implies that the Buzzoni (1989) models are too red, rather than the clusters being too blue, and indeed the Buzzoni models are about 0.1 mag redder than the models we examine here. We showed in the previous paragraph that substantial shifts in model $V-K$ colors were required to match the clusters in two-color diagrams. Shifting the model $V-K$ to the blue to match the $B-V$ colors would make the model $V-K$ too blue for the clusters' metallicities. This again emphasizes the difficulties of trying to match population synthesis models to cluster colors by applying uniform shifts for all metallicities.

2.4.4 Metallicity distributions

The metallicity distribution of a galaxy's GCS can provide important clues to galaxy formation. For example, Zinn (1993) finds a significant metallicity gradient in the Galactic 'old halo' clusters and no gradient in the 'younger halo'. He interprets this and other properties of the Galactic GCS as evidence that the old clusters were formed in a monolithic collapse and the younger ones were accreted from satellite galaxies. Accordingly, we want to examine the distribution of cluster metallicities in M31, and to do so for the largest number of clusters. We thus include metallicities estimated from colors in our analysis, even though this method

[4]Covino et al. incorrectly attributed the Galactic cluster photometry to Brodie & Huchra (1990). While the photometry is tabulated in the Brodie & Huchra paper, the actual data are from Frogel et al. (1980).

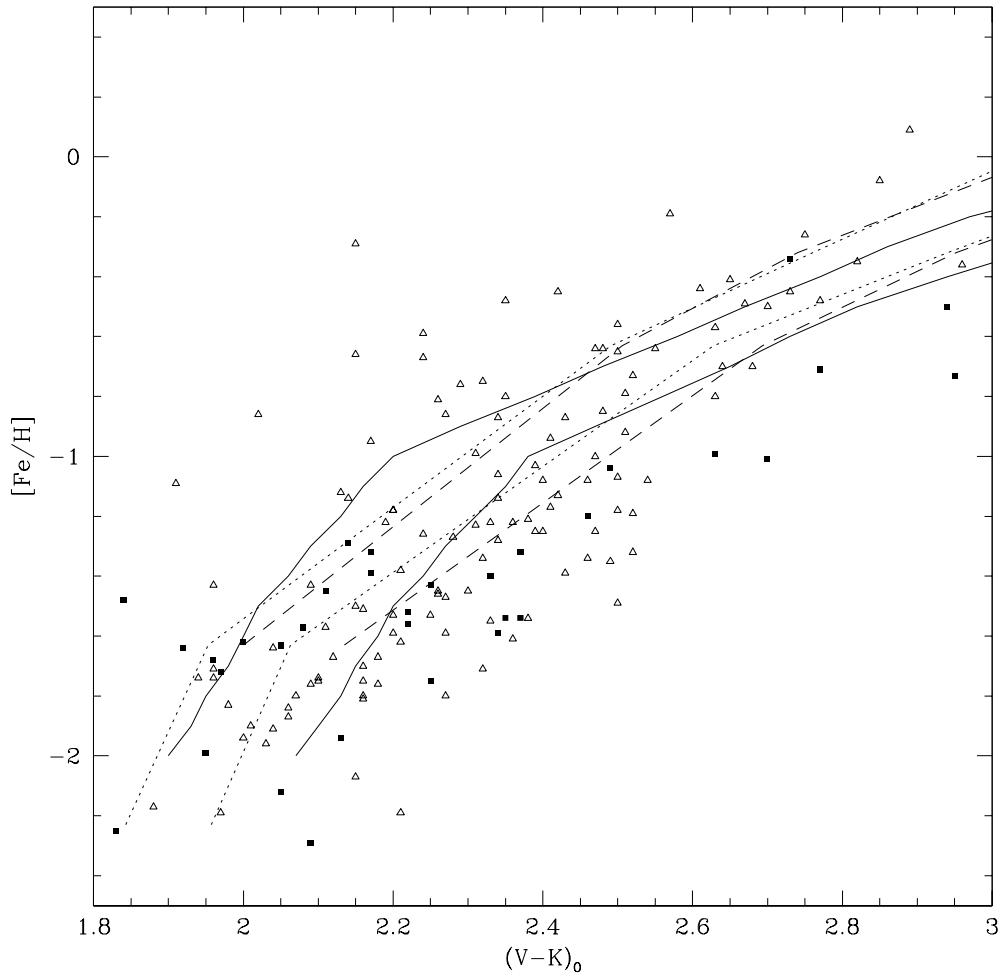

Fig. 2.18.— $(V-K)_0$ vs. [Fe/H] for M31 and Galactic GCs. Symbols same as Figure 2.15.

Table 2.10. Distribution of [Fe/H] for M31 clusters

dataset	$\overline{\text{[Fe/H]}}$	$\sigma_{\text{[Fe/H]}}$	median [Fe/H]	KMM $\overline{\text{[Fe/H]}}_1$	$\overline{\text{[Fe/H]}}_2$	n_1	n_2	$\sigma_{\text{[Fe/H]}}$	p
1	-1.22 ± 0.04	0.58	-1.25	-1.48	-0.63	169	78	0.43	0.102
1a	-1.21 ± 0.04	0.53	-1.25	-1.42	-0.64	135	43	0.40	0.098
2	-1.15 ± 0.04	0.54	-1.23	-1.43	-0.60	110	56	0.38	0.042
2a	-1.14 ± 0.05	0.52	-1.19	-1.36	-0.53	94	31	0.37	0.034

is not as precise as determining metallicity spectroscopically. We also include clusters for which we were unable to determine a reliable reddening value (usually because of inadequate photometric data) in the metallicity analysis.

To assess whether the determination of metallicities from colors has an effect on our results, we consider four data sets in our analysis of the metallicity distribution. Set 1 contains all the objects for which metallicities have been determined, regardless of method or error. Set 1a is a subset of this, containing only objects with $\sigma_{\text{[Fe/H]}} < 0.5$. Set 2 contains only objects with spectroscopic metallicities, and set 2a is the subset of these objects with $\sigma_{\text{[Fe/H]}} < 0.5$. The first step is to characterize the distribution of [Fe/H]. Table 2.10 shows that restricting the metallicities to spectroscopic alone slightly increases the mean metallicity, but not by a significant amount. This is good evidence that our color-derived metallicities are not systematically offset from the spectroscopic ones. A KS-test shows that the Galactic and M31 GC metallicity distributions are not drawn from the same distribution, unsurprising given the difference in mean metallicity; however, the shapes of the distributions are fairly similar (see Figure 2.19).

The asymmetric nature of the [Fe/H] distributions suggests the possibility of bimodality. We used the KMM algorithm to search for bimodality in the distributions, following Ashman and Bird as in Section 2.4.3. All four datasets showed bimodality, although including the color-derived metallicities made the detections only marginally significant (see the p-values in Table 2.10). The [Fe/H] histograms and the Gaussian subgroups found by KMM are shown in Figure 2.19. Most clusters were assigned to the same (metal-rich or metal-poor) group regardless of which dataset was considered; however, there were about 20 clusters that showed substantial probability of membership in both groups and these switched groups from metal-rich to metal-poor depending on whether or not the large-error metallicities were included. This is the primary cause of the

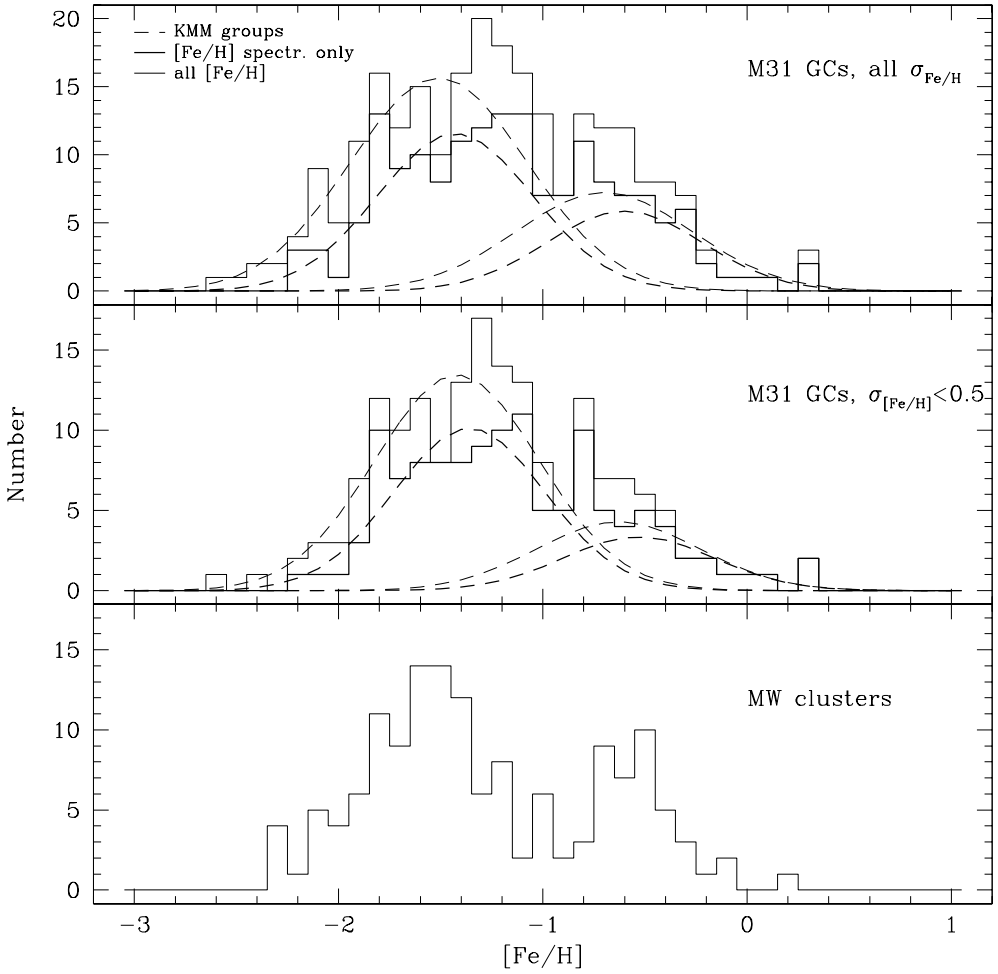

Fig. 2.19.— [Fe/H] distribution for M31 GCs, subdivided by metallicity source and uncertainty, and Galactic GCs.

differences between samples 1/1a and 2/2a in Table 2.10. We conclude that these clusters cannot be unambiguously assigned on the basis of their metallicities alone, so we classify them as 'intermediate' and assign them to neither group. As with the color distributions, visual inspection of the metallicity histograms suggested the possibility of trimodality in the distribution. The results of running KMM with three groups specified were similar to those for the color distributions: three-group fits were worse than both one- and two-group fits. The mean colors of the metal-rich and metal-poor groups are generally within 0.05 mag of the predicted colors in Table 2.9. This is not surprising since the metallicities used to predict these colors are close to the mean metallicities of the two groups KMM found. Perhaps more surprising is our failure to detect bimodality in most colors. This underscores the need for precise photometry if a single color is used to determine metallicity: such precision was obviously not achieved in our heterogeneous data set.

Do these metal-rich and metal-poor groups represent the M31 equivalent of the Galactic disk (or bulge – see Côté 1999) and halo clusters? One way to find out is to see where the two groups lie in relation to the galaxy; we show the KMM assignments as a function of position on the sky in Figure 2.20. There are more metal-poor clusters at large projected radius, and as a result the median radius of the metal-poor clusters is about 50% larger than that of the metal-rich clusters. However, we find, as did HBK, that this is partly a selection effect: faint clusters are more easily discovered away from the disk, and these distant clusters are more likely to be metal-poor. When the sample is magnitude-limited at $V = 16.5$ or $V = 17$ we find that the median radius of the metal-poor clusters is about 30% larger than that of the metal-rich clusters, which is similar to the results of HBK. A KS test shows that this difference in R_{gc} distributions is significant at the 95% level. While most of the metal-rich clusters are projected onto the M31 disk, a few lie in the halo. Two of these clusters have color-magnitude diagrams (379-312 from Holland et al. (1997) and 006-058 from Fusi Pecci et al. 1996) that give values of [Fe/H] consistent with our spectroscopic values. The CMD of 384-319 (Couture et al. 1995) is so sparse that it cannot put any useful constraints on [Fe/H]. The existence of several metal-rich globular clusters in the Galactic halo (Terzan 7, NGC 6366, Pal 12; Da Costa & Armandroff 1995) also suggests that similar results for the M31 clusters are not unreasonable.

The kinematics of the metal-rich and metal-poor groups will be the most powerful determinant of their similarity (or lack thereof) to the two Galactic groups. We did not perform a detailed kinematical analysis, since two forthcoming velocity studies of the M31 clusters (Seitzer et al. 1999; Perrett et al. 1999) have substantially improved precision from HBK's observations (the source of over

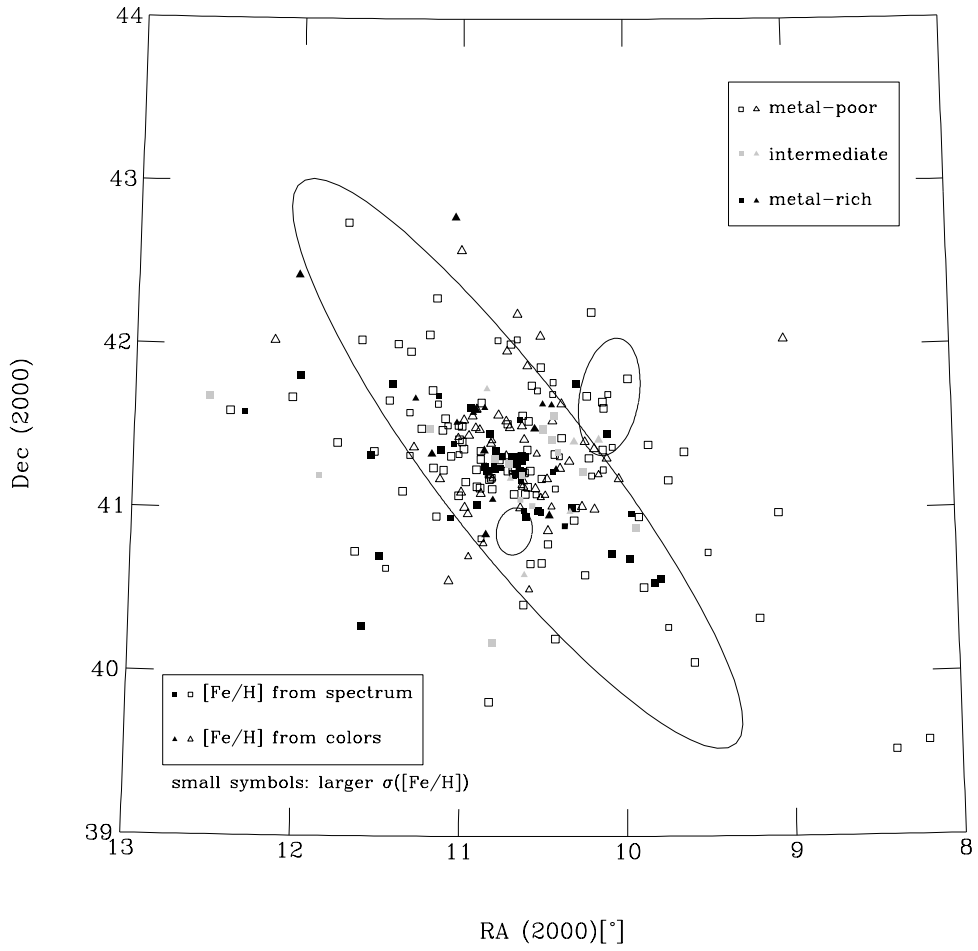

Fig. 2.20.— Projected location of metal-poor and metal-rich M31 clusters. Ellipses same as Figure 2.8.

three-quarters of our velocity data). We did repeat the HBK analysis (see their Figure 6 and Table 3), including our new velocities and using our division of the clusters, and found essentially the same results. At small projected distances, the metal-rich clusters rotate faster than the metal-poor clusters, and at large distances, there is essentially no difference between the two groups in either rotation velocity or velocity dispersion. The rotation velocity for all clusters at $X > 10'$ is 59 ± 12 km s^{-1}. The similarity in the kinematics of the metal-rich and metal-poor clusters hints that, unlike the Galactic clusters, the two groups of M31 clusters might be similar in age. Velocity errors and projection effects could confuse the situation, however, and more precise velocities and metallicities are needed.

How does the distribution of M31 GCS metallicity compare to that seen in other galaxies? Table 2.11 compares some properties of spiral galaxies' globular cluster systems. Spirals with detected GCSs that do not appear in this table (see Appendix of Ashman & Zepf (1998) and also Harris 1991) have generally been observed in only one filter, so no metallicity information is available for these systems. M31 and the Galaxy are the only spiral GCSs for which the detection of multiple populations is reasonably secure, and the populations in these two galaxies are quite similar in metallicity difference and relative proportion. The small number of GCs in the other spirals' GCSs makes analysis of the metallicity distribution difficult. For the M81 GCs, Figure 16 of Perelmuter & Racine (1995) hints at a multimodal (or perhaps uniform plus one peak) distribution of $(B-R)_0$. However, many of the objects in this plot were subsequently determined to be non-clusters (Perelmuter et al. 1995), and the number of remaining *bona fide* clusters is again too small for the distribution to be analyzed. Bridges et al. (1997) do not determine individual metallicities from their spectra of GCs in NGC 4594 (M104), but Forbes et al. (1997c) do find some evidence for a difference in mean $B-I$ color between disk and bulge/halo clusters in this galaxy.

The presence or absence of a radial trend in GCS metallicity is an important test of galaxy formation theory. We show the GC metallicity as a function of projected radius in Figure 2.21.[5] This figure shows that the most metal-rich clusters are near the M31 nucleus, and also shows the decrease in the 'upper envelope' of GC metallicity noted by HBK. We binned the clusters in distance as in Section 2.4.3, and looked for trends of metallicity with radial distance R_{gc}. The entire sample of clusters does not have a significant radial metallicity gradient, but the clusters with spectroscopic metallicities have a marginally significant gradient

[5]The absence of clusters with $100' < R < 150'$ in Figure 2.21 is a selection effect. The Battistini et al. (1987) catalog extends to $R \sim 120'$, and the Sargent et al. (1977) extends to $R \sim 155'$ only along the M31 major axis, so most of the region $120' < R < 150'$ has not been searched for GCs.

Table 2.11. Comparison of spiral galaxy globular cluster systems

galaxy	N_{GC}	M_V	S_N	[Fe/H]	σ_v	Ref.
MW total	180 ± 20	-21.3	0.5 ± 0.1	-1.34 ± 0.07	$\cdots$	(1)
MW halo	0.69	$\cdots$	$\cdots$	-1.59	100	(2)
MW disk	0.31	$\cdots$	$\cdots$	-0.55	124	(2)
M31 total	450 ± 100	-21.8	0.9 ± 0.2	-1.15 ± 0.04	142	(1,3)
M31 halo	0.66	$\cdots$	$\cdots$	-1.43	148	(3)
M31 disk	0.34	$\cdots$	$\cdots$	-0.60	146	(3)
M33	~ 25	-19.4	0.6 ± 0.2	-1.6	70	(1,4)
M81	210 ± 30	-21.1	0.7 ± 0.1	-1.48 ± 0.19	152	(5,6)
M104	1600 ± 800	-22.2	2 ± 1	-0.7 ± 0.3	260	(7,8)

Note. — Velocity dispersions σ_v are in km s^{-1}. Numbers in N_{GC} column for M31/MW disk/halo are fraction of total.

References. — (1) Ashman & Zepf 1998; (2) Côté 1999; (3) this work; (4) Schommer 1993; (5) Perelmuter & Racine 1995; (6) Perelmuter et al. 1995; (7) Bridges & Hanes 1992; (8) Bridges et al. 1997

(-0.023 ± 0.01 dex/kpc). This metallicity gradient is close to the value Zaritsky et al. (1994) find for the [O/H] gradient in M31 HII regions (-0.018 ± 0.006 dex/kpc), emphasizing that the properties of M31 and its GCS are closely linked. The metallicity gradient of the Galactic halo clusters (excluding six distant clusters; see Armandroff et al. 1992), -0.011 ± 0.004 dex/kpc, is smaller than the M31 GCS gradient, probably because the M31 sample includes the very metal-rich clusters in the nucleus. We cannot determine the metallicity gradients for M31 'disk' and 'halo' clusters separately because using metallicity itself to assign the M31 clusters to disk/halo groups would strongly bias the result. Better kinematical data will allow an independent group assignment, and hence better understanding of the groups' properties.

The relation of cluster mass to metallicity is important in globular cluster formation theory. If self-enrichment is important in GCs, massive clusters should be more metal-rich; the opposite is true if cooling from metals determines the

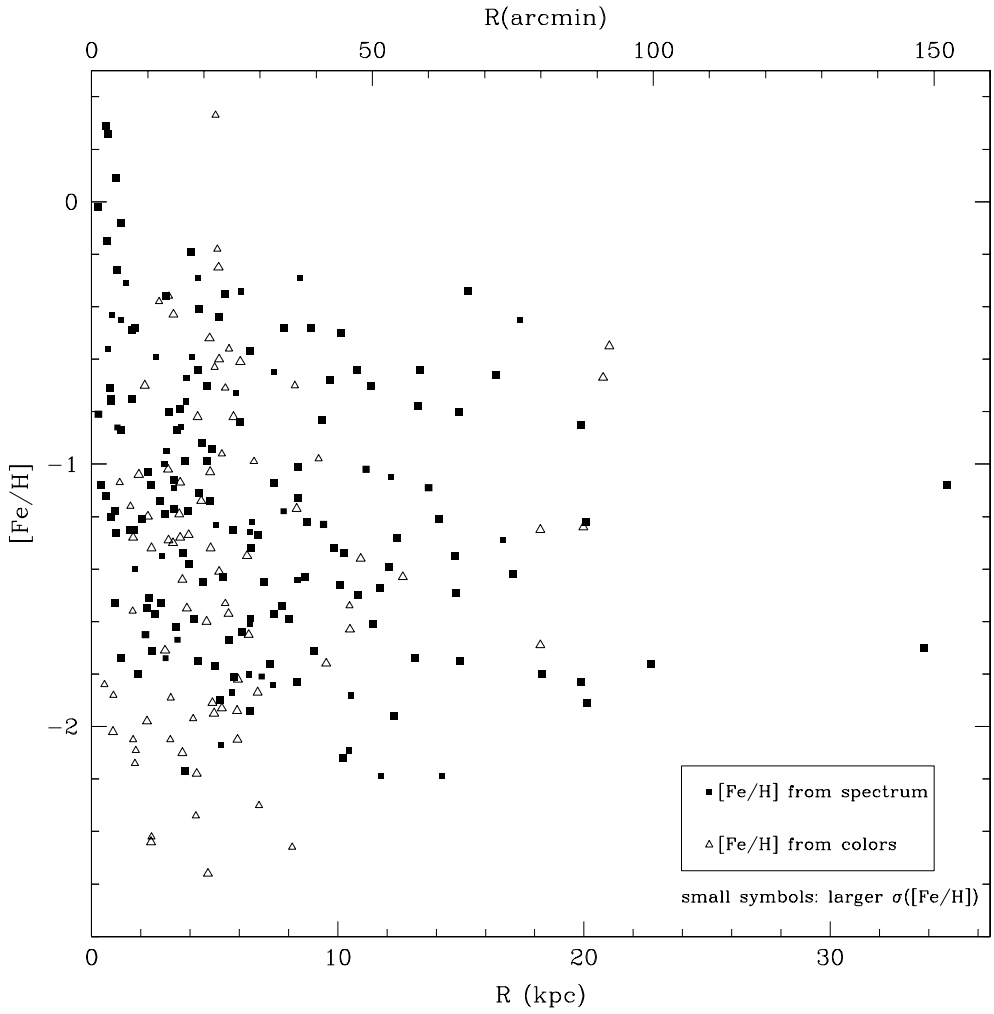

Fig. 2.21.— [Fe/H] vs. R_{gc} for M31 clusters.

temperature (and thus the Jeans mass) in the cluster-forming clouds. Globular cluster destruction rates are higher for low-mass clusters closer to the galaxy center (Ashman & Zepf 1998). If significant destruction has occurred in the M31 GCS, one might expect there to be few faint, high-metallicity clusters, since the highest-metallicity clusters are near the nucleus and hence would have a greater chance of destruction. In Figure 2.22 we plot metallicity versus (dereddened) apparent magnitude; as in a similar plot by HBK, no trend is obvious. Least-squares fits both binned and unbinned in V_0 show no evidence for non-zero slopes, so we conclude that there is no evidence for a relationship between luminosity (and presumably mass) and metallicity in the M31 clusters.

2.5 Conclusions

We have presented the results from a catalog of photometric and spectroscopic information for M31 globular clusters. We determine the reddening for 314 objects, with 221 of these values considered reliable. From the color excesses of clusters with spectroscopic metallicities, we find that the M31 and Galactic extinction laws are consistent. The M31 and Galactic GC color-metallicity relations are also consistent, and we use these relations to estimate metallicities for M31 clusters without spectroscopic data.

The average intrinsic colors of M31 clusters are consistent with those of Galactic clusters: the slightly higher mean metallicity of the M31 clusters does not make a measurable difference in their colors. There are no significant trends in M31 cluster color with projected radius or distance along the disk axes. The optical colors of M31 and Galactic GCs in two-color diagrams agree fairly well with the predictions of population synthesis models after the models have been corrected for known defects. However, there are significant ($0.05 - 0.2$ mag) additional corrections required for the predicted optical-infrared and infrared colors to match the data. This indicates the presence of systematic errors in the models, and the fact that corrections are required so that the simplest model predictions – broadband colors – agree with observations of the simplest stellar populations available – globular clusters – is disturbing. It is important to understand and remedy the problems in the models before attempting to use them to study systems comprised of multiple populations.

The distributions of the most metal-sensitive colors, and of metallicity, show evidence for bimodality. The two metallicity groups have means of [Fe/H]≈ -1.4 and -0.6. The metal-poor clusters have a larger average projected distance

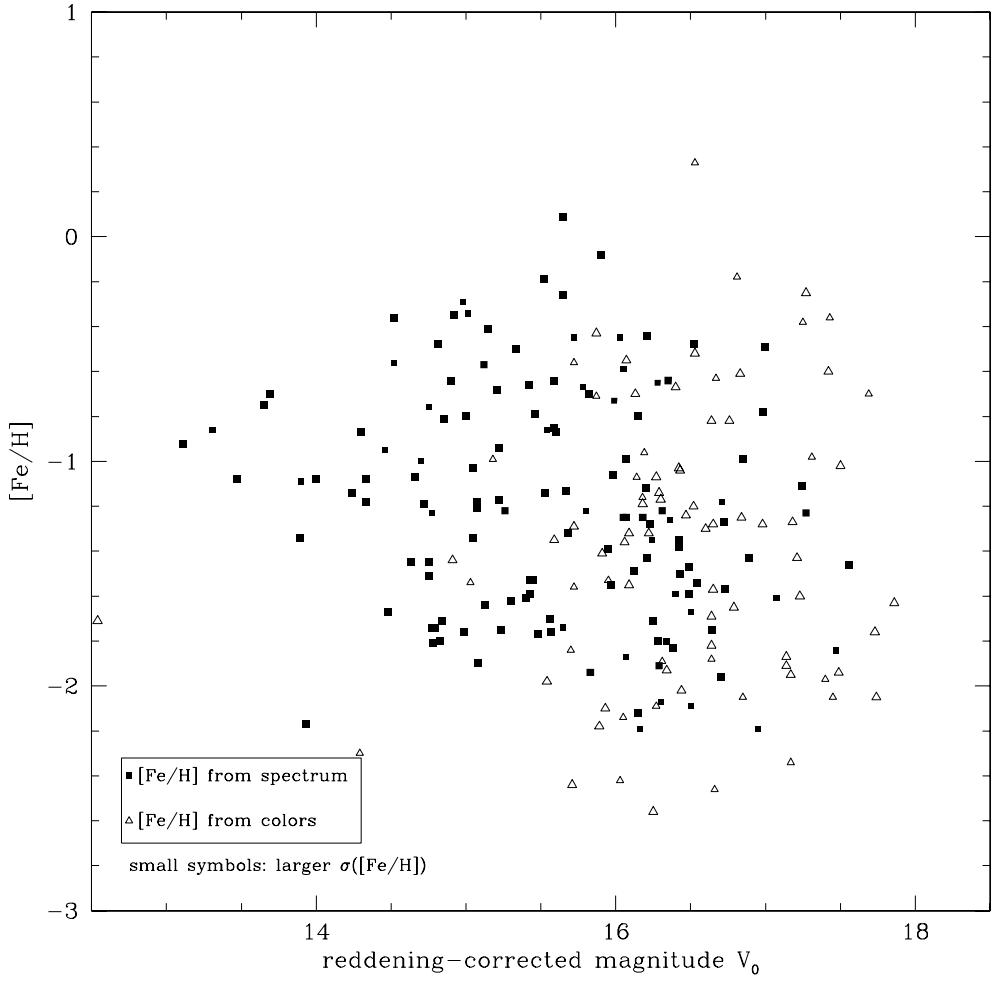

Fig. 2.22.— [Fe/H] vs. V_0, dereddened total magnitude, for M31 GCs. The brightest object is 037–B327; see discussion in Section 2.4.1.

from the galaxy, and show slower rotation near the nucleus than the metal-rich clusters. These properties suggest that the two metallicity groups are analogs of the Galactic 'halo' and 'bulge/disk' clusters. The presence of these two distinct populations in the globular clusters as well as the stars emphasizes that GCS formation is intimately related to galaxy formation. The cluster system shows a small overall metallicity gradient, which implies that the enrichment timescale for the proto-galactic gas was shorter than the collapse timescale. The lack of a corresponding color gradient is probably due to a combination of the weak metallicity gradient and errors in intrinsic colors, and emphasizes the difficulties in using color as a metallicity indicator in galaxies where the extinction is also radially varying.

There is no correlation between luminosity and metallicity, which implies that neither self-enrichment or cooling from metals is important in GC formation. The presence of faint, high-metallicity clusters in the galaxy disk constrains the destruction rate of such objects. The M31 globular cluster system is very similar to the Galactic system in many respects: mean metallicity, presence of two metallicity groups, broadband color distributions. The possible presence of young globular clusters in M31 is an important difference between the properties of the two GCSs. The properties of the two galaxies themselves also show similarities and differences, and the relations between the galaxies and their globular cluster systems remain important clues in the study of galaxy formation. The detailed study of these two most accessible systems of globular clusters provides an important stepping stone on the path to understanding galaxy and cluster system formation in more distant, younger, systems.

Chapter 3

Testing Population Synthesis Models with Globular Cluster Colors

3.1 Introduction

Predicting the integrated spectral energy distributions of stellar populations is important in the solution of many problems in astronomy, from determining the ages of globular clusters to modeling counts of faint galaxies at high redshift. Beginning with the early work of Tinsley (1968), successive generations of modelers have combined the best available data on stellar structure and evolution to predict the appearance of the combined light of generations of stars. Although the subject of population synthesis has a long history, it is an active area of research: synthesis techniques and many of the input data (isochrones, opacities, spectral libraries) continue to be improved.

There is good evidence that globular clusters (GCs) are internally homogeneous in age and metallicity (Heald et al. 1999; Stetson 1993). GCs are the best observational analogs of modelers' 'simple stellar populations', i.e. populations of stars formed over a short time out of gas with homogeneous chemical composition. Broadband colors are among the simplest predictions of population synthesis models, so comparing the models' predicted colors to cluster colors is the natural zeroth-order test of compatibility between the models and reality (Huchra 1996). In this paper we compare the broad-band $UBVRIJHK$ colors predicted by three modern population synthesis models with the colors of Galactic

and M31 GCs. Our observational database is the first one to include extensive coverage of the JHK bandpasses, and the first with spectroscopic metallicities for all clusters. We use the cluster metallicities to bin the clusters for comparison to the appropriate models. In this way we determine the cluster-to-model offset separately for each color and avoid the ambiguity in comparing model and cluster colors in two-color diagrams.

3.2 Input data and comparison procedure

For M31 clusters, the observational data are from the catalog contained in Chapter 2. For the Galactic clusters we obtained optical colors, metallicity, and reddening from the June 1999 version of the Harris (1996) catalog, and IR colors from Frogel et al. (1980), as reported in Brodie & Huchra (1990) (but with the reddening correction applied by Brodie & Huchra (1990) removed and the reddening values in Harris (1996) used instead). We dereddened the clusters' colors using the values of $E(B-V)$ given in the catalogs and the Cardelli et al. (1989) extinction curve for $R_V = 3.1$. For M31, we excluded clusters where the error in the spectroscopic metallicity was $\sigma_{\rm [Fe/H]} > 0.5$, and clusters suspected of being young on the basis of strong Balmer absorption or blue $B-V$ colors (see Chapter 2). For both galaxies, we excluded clusters with $E(B-V) > 0.5$; there are 103 M31 and 85 Galactic clusters in the final sample. Photometric data is not available in all bandpasses for all clusters: only about two-thirds have measured R and I, and less than half have H.

We compare the cluster colors to those for simple stellar populations of ages 8, 12, and 16 Gyr from three sets of models: those of Worthey[1], Bruzual and Charlot (hereafter BC) (both the Worthey and BC models are reported in Leitherer et al. 1996), and Kurth et al. (1999). Although model colors are tabulated in smaller age increments (typically 1 Gyr), initially it is more reasonable to use the models as a rough guide to relative ages rather than attempting to derive precise cluster ages from them. The Worthey models are computed at [Fe/H] values of -2.0,-1.5,-1.0,-0.5, and -0.25 dex, and the BC and KFF models are computed at [Fe/H] values of -2.33 (KFF models only), -1.63, -0.63, and -0.32 dex. We compared clusters to both the Salpeter initial mass function (IMF; Worthey's 'vanilla' models) and Scalo (1986) (Miller & Scalo 1979, in the Worthey models) IMF version of the models. Worthey (1994) finds that some of his model colors have

[1]The version we used updates the Worthey (1994) models by including a more realistic treatment of the horizontal branch for [Fe/H] < -1.0.

defects (e.g. $B-V$ is too red by 0.04–0.06 mag due to problems in the theoretical stellar atmospheres and the color-temperature calibration), but the sizes of these defects are not well-determined so we do not correct for them. Figure 3.1 shows data and models in two frequently-used two-color diagrams.

Since the models are computed at discrete values of [Fe/H], we use the spectroscopic metallicities of the clusters to compare only clusters with comparable metallicities (± 0.25 dex) to each model. The Galactic cluster metallicities given in Harris (1996) are on the Zinn & West (1984) (ZW) metallicity scale, and the M31 cluster metallicities are also tied to this scale through the calibration of Brodie & Huchra (1990). Recent work (Carretta & Gratton 1997; Rutledge, Hesser, & Stetson 1997) suggests that the ZW scale may be non-linear at both high and low metallicities. We retain the ZW scale in this paper because we found that using the Carretta & Gratton (1997) scale to assign clusters to model comparison bins made little difference in our results. We caution, however, that the effect of changing the metallicity scale is unknown for the [Fe/H] $= -0.25$ model bin. The transformation from the ZW to the Carretta & Gratton metallicity scale is only defined for $[\mathrm{Fe/H}]_{\mathrm{ZW}} < -0.5$, the lower limit of this metallicity bin.

We calculated the mean offsets between model and cluster colors (referenced to V) for each metallicity bin; Figures 3.2 and 3.3 show some representative comparisons. We plot $\Delta(X-V)$ for all bandpasses X to make clear the differences in spectral energy distributions between models and data; we remind the reader that the offsets for bandpasses redward of V thus have the opposite sign from the usual colors. One general characteristic of the models visible in the Figures is that younger-aged models predict bluer colors. The exception is the KFF Scalo model for [Fe/H] $= -1.63$, which predicts only very small color differences ($\lesssim 0.01^m$) between ages of 12 and 16 Gyr. The effect of the IMF on the colors appears to depend on both metallicity and age. For the Worthey [Fe/H] $= -1.50$ models, Miller-Scalo IMF colors are redder than Salpeter model colors at all ages, but for the [Fe/H] $= -0.50$ models, the Miller-Scalo IMF colors are bluer for 8 and 12 Gyr and almost identical for 16 Gyr. BC predict almost no color difference between the Salpeter and Scalo IMF models of the same age and metallicity.

A striking feature in Figures 3.2 and 3.3 is the range of discrepancies between models and data. For example, the largest difference between the Worthey model with parameters (Salpeter IMF, [Fe/H] $= -1.50$, age 16 Gyr) and the mean colors of clusters with $-1.75 \leq$ [Fe/H] ≤ -1.25 is 0.04^m in $U-V$. The same models with [Fe/H] $= -0.50$ are well offset from the data at all colors except $U-V$; the largest offset is 0.23^m in $V-K$. To determine the best-fitting models, we quantify the

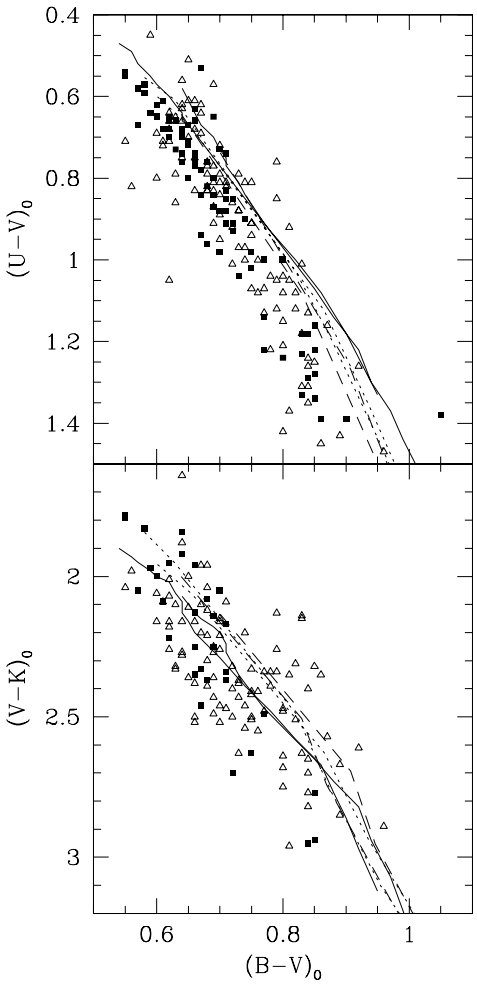

Fig. 3.1.— $(B-V)_0$ vs. $(U-V)_0$ and $(V-K)_0$ for M31 globular clusters (triangles) and Galactic GCs (squares). Lines are population synthesis models of ages 8 Gyr (bluer colors) and 16 Gyr (redder colors): Worthey (solid), BC (dashed), KFF (dotted).

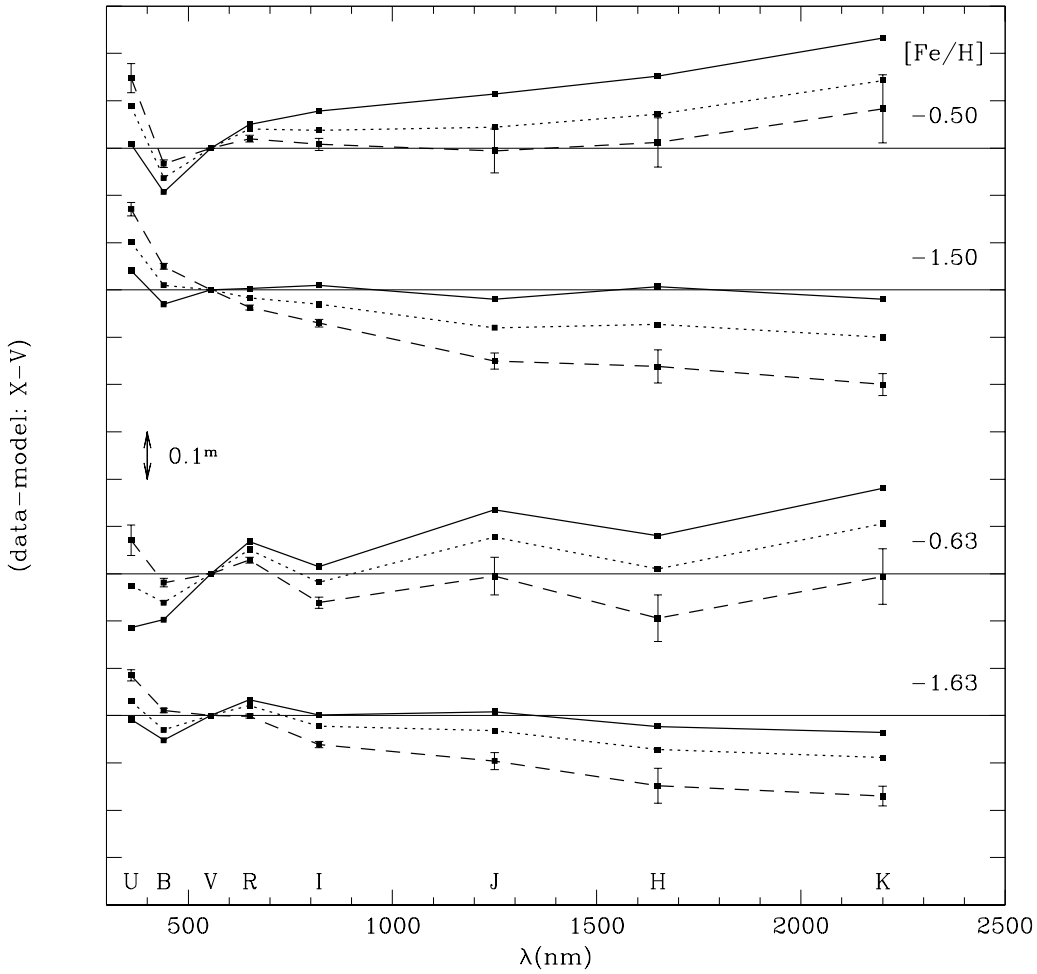

Fig. 3.2.— Color offsets $\Delta(X-V)$ (data−models) for Salpeter IMF. ($\Delta V = 0$ is plotted to emphasize that the models are normalized to the data at V.) Solid lines: 16 Gyr models, dotted lines: 12 Gyr models, dashed lines: 8 Gyr models. The -1.5 and -0.5 bins in [Fe/H] are Worthey models; the -1.63 and -0.63 [Fe/H] bins are BC models. Error bars (plotted only on the 8 Gyr models for clarity) are the standard errors of the mean cluster colors and do not include observational uncertainties.

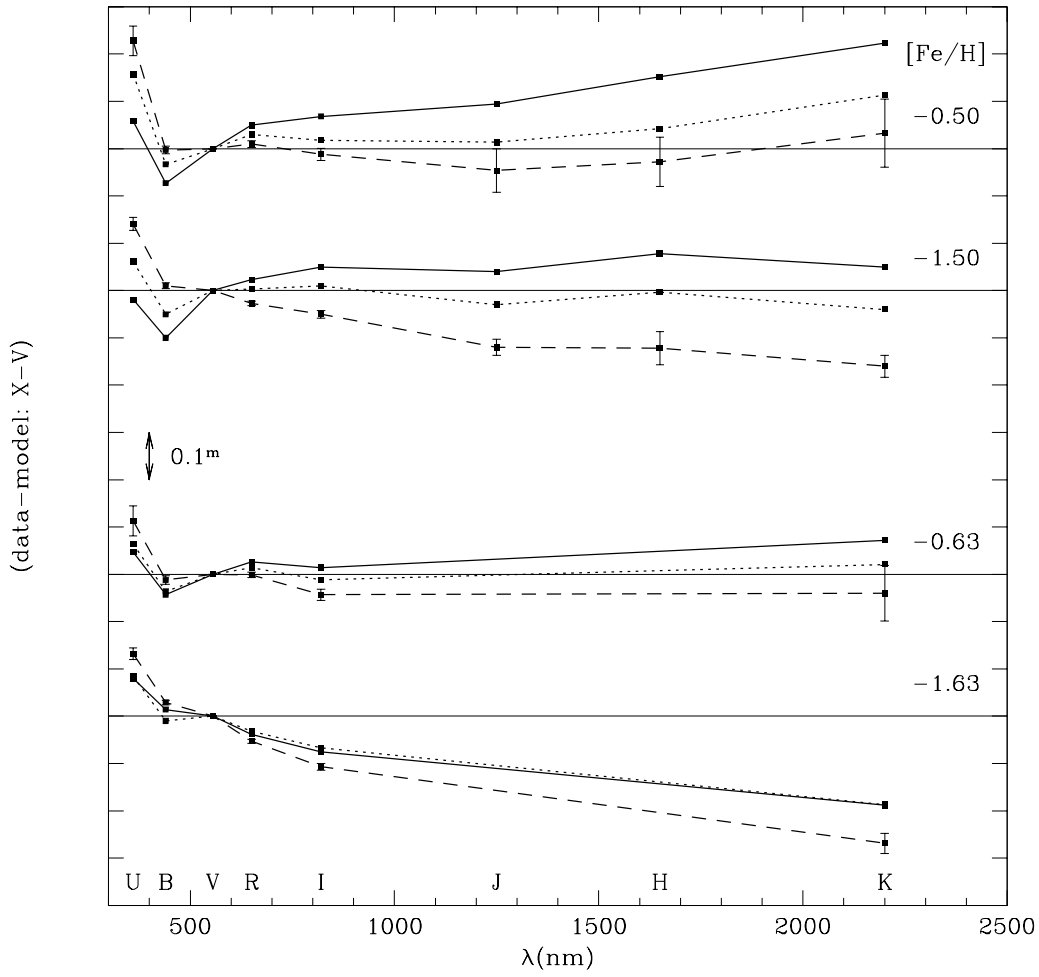

Fig. 3.3.— Color offsets $\Delta(X-V)$ or $\Delta(V-X)$ (data−models) for Scalo or Miller-Scalo IMF. Symbols same as Figure 3.2. The -1.5 and -0.5 bins in [Fe/H] are Worthey models; the -1.63 and -0.63 [Fe/H] bins are KFF models (which have no $\Delta(J-V), \Delta(H-V)$ since they do not predict these colors).

overall goodness-of-fit for each model/cluster metallicity bin pair as:

$$F = \frac{\sum_k |\Delta(X-V)_k|/\sigma_k^2}{\sum_k 1/\sigma_k^2} \tag{3.1}$$

The color differences $\Delta(X-V)_k$ are weighted by $1/\sigma_k^2$, where σ_k are the standard errors in the mean colors of objects in the bin. Table 3.1 gives the Δ and F values for the best fitting models in each metallicity bin.

3.3 Discussion

Table 3.1 shows that the best-fitting models fit the data quite well, with typical color offsets of $0.02 - 0.03^m$. The two bandpasses with the most significant offsets are U and B: the models are too blue in $U-V$ and too red in $B-V$. Neither offset shows a clear trend with metallicity. The offsets are likely not due to systematics in the photometric system or in the extinction curve. While problems with the photometric systems might be expected in the R and I bands (due to conversion between the Johnson and Cousins RI systems), both data and models use the well-defined Johnson UBV system. Problems in the reddening curve also seem unlikely for the same reasons. We suspect that the offsets are more likely due to systematic errors in the models. The $B-V$ offset in particular is likely due to the flux libraries used. Both Worthey (1994) and Lejeune (1997) found their model $B-V$ colors to be $0.04 - 0.06^m$ too red compared to empirical solar-metallicity spectra, even after correcting to the empirical color-temperature scale. This suggests a possible problem with the stellar atmosphere models of Kurucz (1995), upon which both libraries are based.

Table 3.1. Color offsets for best-fitting models

[Fe/H]	model	F	$N_{\rm gc}$	$\Delta(U-V)$	$\Delta(B-V)$	$\Delta(V-R)$	$\Delta(V-I)$	$\Delta(V-J)$	$\Delta(V-H)$	$\Delta(V-K)$
-0.25	W8sc	0.023	15	23.4 ± 2.4	-0.4 ± 0.9	-3.0 ± 1.1	-0.3 ± 1.0	3.2 ± 2.6	-1.4 ± 6.0	-6.0 ± 4.9
-0.32	K8sc	0.022	17	11.5 ± 2.2	-2.5 ± 0.8	-2.1 ± 1.0	0.2 ± 0.9	$\cdots$	$\cdots$	-3.9 ± 4.6
-0.50	W8sc	0.013	30	22.8 ± 3.1	-0.3 ± 0.8	-1.0 ± 0.7	1.2 ± 1.3	4.6 ± 4.6	2.8 ± 5.2	-3.3 ± 7.2
-0.63	K8sp	0.012	35	12.2 ± 3.2	-1.0 ± 0.9	-0.6 ± 0.6	2.4 ± 1.2	$\cdots$	$\cdots$	2.1 ± 5.9
-1.00	W12sc	0.014	48	13.7 ± 2.2	-2.3 ± 1.0	0.0 ± 0.5	-1.1 ± 1.2	3.2 ± 1.8	6.9 ± 2.5	4.3 ± 2.1
-1.50	W16sp	0.016	75	4.1 ± 1.4	-3.0 ± 0.6	-0.3 ± 0.5	-1.0 ± 0.8	2.0 ± 1.7	-0.7 ± 3.5	2.0 ± 2.3
-1.63	K16sp	0.019	77	5.1 ± 1.2	-0.7 ± 0.5	1.7 ± 0.4	2.8 ± 0.7	$\cdots$	$\cdots$	10.8 ± 2.1
-2.00	W16sp	0.027	37	8.2 ± 1.2	-2.6 ± 0.6	-0.3 ± 0.8	-1.6 ± 1.2	-6.7 ± 2.6	-5.2 ± 3.7	-5.8 ± 3.5
-2.23	K16sp	0.027	12	4.1 ± 2.3	1.8 ± 1.3	2.3 ± 2.1	3.4 ± 2.0	$\cdots$	$\cdots$	-7.1 ± 6.2

Note. — Units are hundredths of a magnitude. The capital letter in the model column indicates the best-fitting model (Worthey, BC or KFF), the number is the model age in Gyr, and 'sp' or 'sc' indicate Salpeter or Scalo IMF, respectively.

The cause of the offset in $U-V$ is not as clear. This offset is actually worse than it appears: since we compute the $U-V$ colors for the BC and KFF models as $(U-B)+(B-V)$, the red $B-V$ colors *compensate* for some of the $U-B$ defect, which is actually larger than the defect in $U-V$. Worthey (1994) – whose models give $U-V$ directly – finds that his model $U-V$ is too blue compared to solar neighborhood stars and elliptical galaxies. Worthey cites problems with the U fluxes from the stellar libraries as a possible cause: modeling the many blended atomic and molecular lines blueward of B is difficult, and many of the necessary opacities are not well determined. This cannot be the only cause of model problems in U, since the BC and KFF models, which use the same stellar library, predict different $U-V$ colors. The treatment of the horizontal branch in the models is another possible source of problems in the $U-V$ colors because the horizontal branch emits most of the blue light. However, systematic problems with the model HB color (which depends on metallicity), would presumably produce a $U-V$ offset dependent on metallicity, which we do not observe. Observational error is another possible contributor to the $U-V$ offset, as many of the $U-B$ colors of the M31 clusters are poorly determined (see Tables 2.3 and 2.4). Understanding the rest-frame U flux of stellar populations becomes increasingly important when studying high-redshift galaxies and global star formation history, and further investigation of the models in this bandpass is clearly warranted.

A secondary result in Table 3.1 is that age determines which model best fits the data. Higher-metallicity cluster colors are best fit by 8 Gyr models, regardless of IMF. Lower-metallicity cluster colors ($[\mathrm{Fe/H}]_{\mathrm{bin}} \leq -1.00$) are best fit by 12 or 16 Gyr models. The best-fit age depends on the IMF for several of the models, but not in any systematic fashion. This result is consistent with the determinations of relative ages for Galactic clusters by Rosenberg et al. (1999). These authors determined relative ages of 35 Galactic globular clusters from a homogeneous set of V, $V-I$ color-magnitude diagrams. They compared theoretical isochrones with the observational color-magnitude diagrams to determine ages using two independent methods. They found that the clusters with $[\mathrm{Fe/H}]_{\mathrm{CG}} > -0.9$ were $\sim 17\%$ younger than clusters with $[\mathrm{Fe/H}]_{\mathrm{CG}} < -1.2$, with the intermediate-metallicity clusters showing a $\sim 25\%$ age dispersion. These results are model-dependent, as are ours, but the similarity of the results implies that there is either a real difference between metal-rich and metal-poor clusters or a systematic problem in the models in one of the metallicity regimes.

What possible systematic errors in our input data or comparison procedure could produce the result that the metal-rich clusters are younger? We redid the comparison procedure considering the clusters of each galaxy separately, and

still found younger ages for the most metal-rich clusters. Although M31 has a greater proportion of the metal-rich clusters, younger ages are found for both M31 and Galactic metal-rich clusters. Cohen & Matthews (1994) suggest that the spectroscopic metallicities of the most metal-rich M31 clusters measured by Huchra et al. (1991) are systematically too high. If this is true, the clusters would appear too blue compared to old, higher-metallicity models and the best-fit model would be younger. We compared the metal-rich M31 clusters to the Worthey [Fe/H] $= -1.0$ models, and the best-fitting model had age 16 Gyr. However, the goodness-of-fit was better for the young, metal-rich models than for the older, more metal-poor model, so we conclude that younger ages are still favored for these clusters. Overestimating the reddening of the metal-rich clusters would make the derived intrinsic colors too blue and yield younger ages. This seems unlikely, given that the color-metallicity relations for Galactic and M31 clusters match well throughout their metallicity range (see Chapter 2), and the methods of reddening determination for M31 and Galactic clusters are different.

If the detection of younger ages for metal-rich globular clusters is correct, it has implications for galaxy formation. A range of GC ages implies that GC formation took place over an extended period of time. Conditions for GC formation were not particular to the early universe, an assertion supported by observations of 'proto-globular' clusters in present-day merging galaxies (e.g., Zepf et al. 1999). More precise knowledge of the distribution of cluster ages in each galaxy would be extremely useful in understanding cluster system formation. If the age distribution is continuous, the relation between age and metallicity might hold clues as to what factors controlled the cluster formation rate. If the age distribution is bimodal — with most clusters old and coeval and the remainder younger and coeval — then some event must have triggered the second episode of GC formation. Perhaps the younger clusters were stripped from or accreted along with satellite galaxies of M31 and the Galaxy.

3.4 Conclusions

Comparison of three sets of population synthesis models with integrated colors of M31 and Galactic globular clusters shows that the models reproduce the redder average cluster colors to within the observational uncertainties. The poorer agreement in $U-V$ and $B-V$ is likely due to systematic errors in the models. Younger-age models are required to best match the colors of the metal-rich clusters, consistent with the findings of Rosenberg et al. (1999) that the most metal-rich

Galactic globular clusters are younger than the bulk of the GC population. A range of cluster ages implies that conditions for GC formation were not restricted to the early universe. The cluster age distribution has important implications for galaxy and GCS formation, and attempts to determine it more precisely are needed.

Chapter 4

The M31 Globular Cluster Luminosity Function

4.1 Introduction

The distribution of integrated GC magnitudes, known as the globular cluster luminosity function (GCLF), has long been known to be unimodal and approximately symmetric in the Milky Way. The assumption that these properties are universal has allowed the determination of GCLF parameters for over a hundred other galaxies, and the peak absolute magnitude is found to be roughly constant from galaxy to galaxy (Harris 1988). Since the variation in mass-to-light ratios among GCs is fairly small (see, e.g., Dubath & Grillmair 1997) the constant peak magnitude implies the existence of a characteristic mass scale. Theorists have attempted to explain why there should be a characteristic mass scale for globular clusters: is it a property of formation (e.g. Peebles & Dicke 1968), a result of subsequent dynamical processes (e.g. Okazaki & Tosa 1995), or a combination? The constant peak magnitude also presents a challenge to observers, who have attempted to quantify the variation in peak magnitude by environment (Blakeslee & Tonry 1996), galaxy type and luminosity (Whitmore 1997), and color (Kundu et al. 1999). Many observers have also attempted to use the GCLF peak as a standard candle for distance measurement. This method has had a mixed reception, with some authors (e.g. Whitmore 1997) claiming good results and others (e.g. Ferrarese et al. 2000) less complimentary.

*Based partially on observations made with the NASA/ESA Hubble Space Telescope, obtained from the data archive at Space Telescope Science Institute. STScI is operated by the Association of Universities for Research in Astronomy, Inc. under NASA contract NAS 5-26555.

GCLF measurements are made in a number of different bandpasses. The most widely used are V and B, (and their Hubble Space Telescope (HST) equivalents, F555W and F450W); the I-band equivalent F814W is also commonly used for HST data. B and V band mass-to-light ratios are sensitive to metallicity, so GCSs with the same underlying mass distribution but different average metallicities will have different GCLFs. Ashman, Conti, & Zepf (1995) used the relation between metallicity and mass-to-light ratio as predicted by Worthey's (1994) simple stellar population models to estimate the effects of metallicity variations on the GCLF peak. Metal-rich clusters should be fainter (their M/L is larger), and the effect on the GCLF can be substantial. For example, Ashman et al. (1995) predict that a change in mean GCS metallicity from $\overline{\mathrm{[Fe/H]}} = -1.35$ dex (the Milky Way value) to -0.60 dex (the value for the elliptical NGC 3923; Zepf et al. 1995) shifts the GCLF peak by $\Delta B^0 = 0.35$ and $\Delta V^0 = 0.22$. The same metallicity change shifts the J band GCLF peak by $\Delta J^0 = -0.09$, because the metallicity effect on M/L changes direction for bandpasses redward of I. Observing at longer wavelengths also reduces the effects of extinction, both Galactic and within the GCS parent galaxy.

Destruction of globular clusters through dynamical effects could produce a globular cluster mass function (GCMF) that varies with distance from the center of the host galaxy. The three effects usually considered by modelers are disk shocking, evaporation, and dynamical friction; the first two destroy low-mass, low-concentration clusters, while the last is most effective for massive clusters. All three effects are strongest at small galactocentric distance R_{gc}. Even at small R_{gc}, the dynamical friction timescale for typical-mass GCs is much longer than a Hubble time, and dynamical friction is probably not important in GCMF evolution (Okazaki & Tosa 1995). Low-mass clusters near the Galactic center are thus most prone to destruction. Assuming a mass-to-light ratio independent of R_{gc} – if the GCS has a radial metallicity gradient this is not strictly true since M/L depends on [Fe/H] – the radial difference in the GCMF can be translated into a radial difference in the GCLF. Many authors (Baumgardt 1997; Ostriker & Gnedin 1997; Vesperini 1998) have predicted the size of the GCLF variation, with widely differing results.

In Chapter 2 we compiled the best available photometry for 435 M31 globular clusters and plausible candidates. This catalog contains V magnitudes for almost all objects and B magnitudes for about 90%, but completeness in the longer-wavelength bands is much lower. About 55% of the objects have I magnitudes, and the same fraction, although not the same objects, have JK; Figure 4.1 shows the completeness of the existing IR photometry. In this Chapter

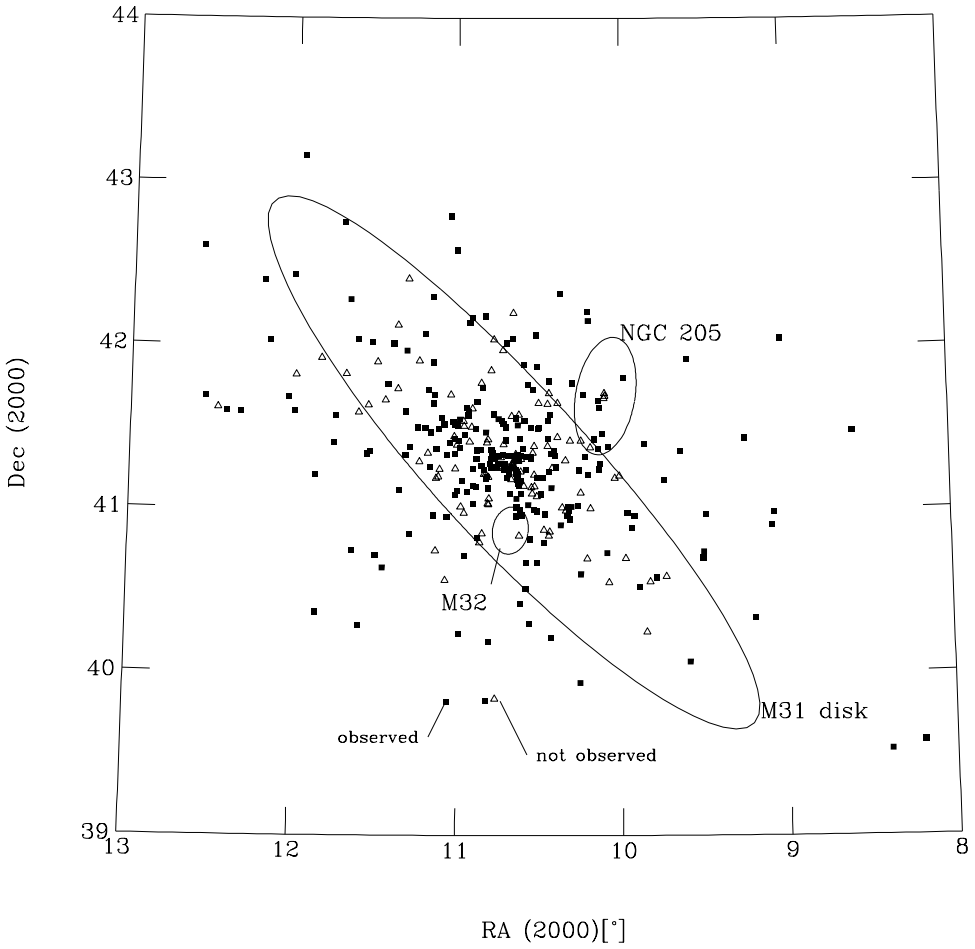

Fig. 4.1.— Photometric completeness for IR photometry (at least one of J, H, or K) of M31 GCs. Symbols indicate whether an object has been observed.

we estimate the parameters of the halo clusters' GCLF in six different bandpasses, including the first GCLF measurements in the near-IR. We investigate the variation in the V-band GCLF parameters for several different subsamples of M31 GCs, and consider the implications of the measured variations for GCS and galaxy formation and evolution.

4.2 New observations and data reduction

We obtained new near-IR photometry for M31 GCs and candidates using two telescope/instrument combinations: Gemini (McLean et al. 1994) on the Lick Observatory 3-m telescope, and Stelircam (Tollestrup & Willner 1998) on the F. L. Whipple Observatory 1.2-m. The Lick observations (in J, H and K') were made on 1999 October 15-17 and the Whipple observations (in J and K) on 1999 December 26. Total integration times ranged from 90 seconds (re-observations of bright clusters in J with Gemini) to 1900 seconds (observations of the faintest halo clusters with Stelircam), using 4 to 9 dithered frames per object.

We used almost the same data reduction procedure for both cameras, which consisted of bias-subtraction (Gemini only), dark-frame subtraction, non-linearity correction (Stelircam only), flat-fielding (using a 'superflat' made from 50-100 blank-sky frames), sky-subtraction, registration, and co-addition. Two methods of sky-subtraction were used: for objects on the galaxy disk we made separate sky observations and subtracted their median, and for objects without galaxy background we subtracted a 'running sky' made from the median of 4-8 temporally contiguous frames. We measured large-aperture magnitudes for Elias et al. (1982) and Persson et al. (1998) standard stars, typically 10-15 stars per filter per night, and fit a two-component (zeropoint and airmass coefficient) photometric solution using standard star magnitudes. Residuals of the photometric solution were typically about $0.01 - 0.02$ mag. The difference between K and K' magnitudes of standard stars is smaller than these residuals (M. Pahre, 2000, private communication), so we assume that our K' measurements adequately represent the K-band.

Our previous aperture photometry of globular clusters used 12-arcsec diameter apertures, and we found that, for the Gemini and Stelircam data, this aperture again contained about 95% of the total cluster light. The new measurements appear in Table 4.1. Some of these data are for objects whose previous IR photometry disagreed strongly with their spectroscopic metallicities (mostly blue clusters in Chapter 2); our new measurements yielded colors more consistent with

the spectroscopic data. The original goal of these observations was to complete the IR photometry for the M31 halo sample of Reed et al. (1994). Poor observing conditions prevented us from completing the halo sample but we did obtain new photometry for 38 objects in total. The total number of M31 clusters and cluster candidates with JK photometry is now ~ 250, including the 30 objects measured for the first time in this paper.

Table 4.1. New infrared photometry for M31 GCs

name	J	H	K
005-052	14.14(1)	13.78(2)	13.54(3)
150D	15.72(1)	15.17(1)	15.16(3)
167D	16.33(2)	15.69(2)	15.57(6)
196-246	15.37(1)	14.73(2)	14.60(3)
208-259	15.39(4)	14.71(4)	14.54(6)
232-286	14.05(1)	13.52(1)	13.34(2)
236-298	15.67(2)	14.99(2)	15.05(5)
242D	16.47(3)	16.32(5)	16.09(8)
316-040	15.36(4)	···	···
320-000	15.44(2)	···	14.15(3)
328-054	15.82(9)	···	···
329-000	15.94(3)	···	14.84(6)
330-056	15.84(7)	···	···
331-057	15.92(9)	···	14.89(12)
333-000	16.36(10)	···	···
336-067	16.14(2)	15.78(3)	15.65(7)
344D	15.39(7)	···	···
384-319	13.87(1)	13.14(1)	12.91(1)
399-342	15.69(2)	15.14(2)	15.07(4)
423-000	16.10(2)	15.48(2)	15.66(3)
450-000	16.65(5)	···	15.69(11)
457-097	15.38(2)	14.79(2)	14.79(3)
461-131	15.43(1)	14.78(1)	14.68(3)
469-220	15.92(2)	15.42(3)	14.92(4)
472-D064	13.46(1)	12.84(1)	12.63(2)
BA11	15.98(2)	15.65(3)	15.19(4)
DAO054	15.94(2)	···	14.90(4)
DAO055	17.02(7)	···	···
DAO094	15.88(3)	···	14.84(5)
DAO104	16.86(5)	···	15.82(11)
Objects with previous photometry			
024-082	14.77(1)	14.13(1)	13.99(1)

Table 4.1—Continued

name	J	H	K
027-087	13.85(1)	13.20(2)	13.13(2)
042-104	13.21(1)	12.44(1)	12.28(1)
068-130	13.67(1)	12.86(1)	12.67(1)
082-144	12.43(1)	11.73(1)	11.44(1)
217-269	14.47(2)	13.82(2)	13.66(3)
298-021	14.97(1)	14.44(1)	14.39(3)
317-041	15.05(1)	14.62(2)	14.54(3)

Note. — Objects with H-band measurements were observed at Lick; others were observed at FLWO. Bracketed numbers are measurement uncertainties in hundredths of a magnitude.

4.3 Preliminaries to the GCLF

4.3.1 Sample definitions

The standard approach to correcting for incompleteness and contamination in the GCLF (see, e.g., Forbes et al. 1996a) is not feasible for M31. Our catalog is a compilation of several previous cluster searches, each with different sky coverage and selection functions. Foreground contamination is a more severe problem for M31 than for more distant galaxies: because M31 is nearby, it covers a large angular area and its GCs have apparent magnitudes comparable to those of Galactic stars. A list of 'failed' M31 GC candidates in Chapter 2 shows that about 15% are foreground stars. Other possible contaminants are background galaxies and objects such as open clusters and H II regions in the galaxy itself. Spectroscopy or high-resolution imaging are the only ways to unambiguously discriminate M31 GCs from contaminating objects, but these techniques have been used mostly on the brighter clusters (see Section 4.4.2). Battistini et al. (1987), the major source of clusters and candidates for our catalog, estimated that 80-90% of their probable (class A and B) cluster candidates with $V < 18$ are true M31 GCs.

Defining a complete, uncontaminated sample of M31 clusters to a magnitude limit well past the GCLF turnover is not possible with currently available data. There is no quantitative estimate of either the completeness or contamination rate, and any attempt to estimate these from the confirmed clusters is hampered by the strong dependence of both completeness and contamination on apparent magnitude and position in the galaxy. To reduce these effects as much as possible while still retaining a reasonable sample size, we define our 'full sample' to be all clusters in the Chapter 2 catalog with $V < 18$, $B - V > 0.45$, and $R > 5'$, where R_{gc} is the projected distance from the center of M31. The magnitude criterion restricts the sample to the range where incompleteness and contamination should be minimal. The color criterion is needed to remove objects in M31 which are bluer than any Galactic globular cluster and may possibly be younger clusters. We use here a slightly less stringent color criterion than in Chapter 2 in order to retain as many of the halo clusters as possible; many of them are slightly (~ 0.02 mag) bluer than the previous limit of $B - V = 0.55$. Restricting the sample to $R > 5'$ also aims to reduce the incompleteness and contamination, as the bright galaxy background near the M31 bulge makes cluster identification and confirmation more difficult. Several groups (Wirth, Smarr, & Bruno 1985; Aurière, Coupinot, & Hecquet 1992; Battistini et al. 1993) have attempted to define a complete sample of GCs near the M31 nucleus. However, the published catalogs are likely to be both contaminated and incomplete: in Chapter 2, we showed that many of the objects listed by Battistini et al. (1993) are not globular clusters, and Mostek et al. (1999) recently identified 33 previously unknown GC candidates in the M31 bulge.

Our full sample has a total of 294 clusters and cluster candidates. The overlap with Battistini et al.'s (1993) 'adopted best sample' is about 85%; the differences are largely due to our exclusion of GCs with $R_{gc} < 5'$ and Battistini et al.'s use of a red color limit. To investigate the effects of metallicity on the GCLF, we define metal-poor (MP) and metal-rich (MR) subsamples by splitting the full sample at [Fe/H] $= -1.0$. Metallicities for most objects without spectroscopic data were estimated from colors as in Chapter 2; we accounted for clusters without metallicities by modifying the completeness functions. The metal-rich subsample has 75 objects and the metal-poor has 191. For comparison with the halo sample (see below), we define a disk sample consisting of all objects in the full sample which are not members of the halo. There are a total of 226 'disk' objects (the number of disk plus halo objects is greater than the number of objects in the full sample because 18 halo objects have $V > 18$).

Measuring the GCLF of halo GCs in M31 avoids the problem of having to determine individual extinctions for each cluster, since these clusters should be

subject to only foreground extinction. Racine (1991) began a concerted effort to define a sample of GCs in the M31 halo that was complete to a faint magnitude limit ($V \approx 19$) and free of contamination. He defined the halo boundary as a $260' \times 56'$ ellipse with position angle 38°, centered on the M31 nucleus (see Figure 4.1). The effort to produce a complete, uncontaminated halo sample was continued by Reed et al. (1992), Racine & Harris (1992) and Reed et al. (1994), and culminated in the published GCLFs of Secker (1992), Secker & Harris (1993, hereafter SH93), and Reed et al. (1994). Because of this work, incompleteness and contamination are much less severe for the halo clusters than for the overall population of GCs in M31. To construct our halo sample, we start with the sample of Reed et al. (1994). We remove the following three objects (see Chapter 2 for our naming convention) as probable non-clusters:

- 168D–D020: "probably not a cluster" (Battistini et al. 1987)
- 109D–000: suspected to be foreground star by both Battistini et al. (1987) and Reed et al. (1994)
- 007–059: shown spectroscopically to be a foreground star (Chapter 2)

Some of the GCs around M31 are near its companion, the dwarf elliptical NGC 205; the clusters' formation and evolution may have been influenced by NGC 205's presence as well as that of M31. There is some evidence that the GCLF peak absolute magnitude in dE galaxies is fainter than that in large galaxies (Durrell et al. 1996; Harris 2000), so we attempt to remove these 'contaminating' objects from the M31 halo sample. We follow Reed et al. (1992) in considering 011–063, 324–051, 331–057, and 330–056 to be 'NGC 205 clusters' and dropping them from the M31 halo. We also remove three additional clusters from the M31 halo list:

- 328–054: very close to NGC 205 in both position ($1.2'$) and radial velocity (18 km s^{-1})
- 326–000, 333–000: both $< 2'$ (400 pc) from NGC 205. No radial velocity information is available for these objects, and their projection onto NGC 205 also makes accurate photometry difficult.

We add 227–000 to our list, although Reed et al. (1992) reject this object from their halo sample because of its previous photometry. The rejection appears to have been a mistake, since their observations of this object put it within their color

and curve-of-growth acceptance criteria. Our final halo list has 86 objects. The list used by Secker (1992) has 82 objects, as he excludes some 'low-probability' objects (469–220, DAO054, DAO055, DAO094, 456–000) while we retain these for the sake of completeness. The faintest object in our halo sample has $V = 18.98$, and we believe the sample to be essentially complete. Our catalog is probably missing a few distant, Palomar-type clusters in the M31 outer halo, but no M31 GC survey yet performed would have revealed such objects. (Finding Palomar-type GCs in M31 would require surveys to $V \approx 22$, in excellent seeing, to a radius of 5 degrees from M31.) In any case, the luminosity function should be little affected by the presence or absence of a few clusters far from the LF peak.

4.3.2 Extinction correction

One of the major problems with using the Milky Way and M31 globular cluster systems to calibrate the GCLF is the uncertain effect of extinction. Many of the Galactic GCs are in the Galactic plane and are highly extinguished; however, at least for those clusters the extinction can be determined from the color-magnitude diagram (CMD) and spectroscopy of individual stars. In M31, globular clusters' CMDs are not precise enough for determination of extinction, and only about a dozen clusters have published CMDs. Instead, measurements of extinction for individual clusters (Vetešnik 1962b; Crampton et al. 1985; Sharov & Lyutyi 1989, and Chapter 2) have relied on correlations of spectroscopic metallicity and/or reddening-free parameters with intrinsic color. This procedure necessarily requires a calibration from the Galactic clusters and the assumption of similar extinction laws, but Chapter 2 showed that both of the these steps were reasonable.

The first step in determining the extinction of the M31 GCs is to decide on a value for the foreground extinction. The H I maps of Burstein (1984) and the DIRBE/IRAS maps of Schlegel et al. (1998) agree that the Galactic reddening in the direction of M31 is $E(B-V) = 0.08$, corresponding to $A_V = 0.25$. In Chapter 2, we found that the average reddening of the M31 halo GCs is consistent with this value, although the individual reddening values had a large scatter. Since about half the halo clusters do not have reliable reddening values, and about 20% have no reddening determination at all, we choose to use a single value, the foreground reddening, for all the halo clusters. A few halo objects had well-determined reddening values that were higher than this, but adopting a single value for all objects simplifies comparison of our results with those of other authors.

Adopting a single extinction value for the M31 disk clusters is, of course, not reasonable. Fortunately, most of the disk objects in our GCLF sample (161/226)

have reliable reddening values determined in Chapter 2. A few of the reliable values are actually below the foreground value, and we replaced them with the foreground value. Some of the objects without reliable reddening had a high value of $\sigma_{E(B-V)}$. We examined the values of $E(B-V)$ from individual colors for these objects, and found that removing one or two discrepant values usually yielded an acceptable error in the resulting reddening value. This left 42 objects without reddening values. For these objects we estimated the reddening by computing the average reddening of objects projected within $10'$, weighted by the inverse of the projected distance. This procedure is somewhat arbitrary, and may yield erroneous results if the 'nearby' clusters are at significantly different distances along the line of sight. A test of the technique on GCs with measured reddening values produced reassuring results: the average offset between measured and estimated reddening values was 0.00 ± 0.01 mag, although the scatter in the offset was large (0.19 mag). We computed extinction values from $E(B-V)$ using the curve for $R_V = 3.1$ given in Cardelli et al. (1989).

4.3.3 Completeness correction

While we do not have a quantitative estimate of the magnitude of completeness and contamination in our catalog as a whole, there are two effects for which we can correct. One effect is incompleteness caused by our magnitude limit. This is somewhat complicated because we use an observational (i.e. uncorrected for extinction) magnitude limit but we need to determine the completeness function in extinction-corrected magnitudes, where we measure the GCLF. For example, we believe our sample of all M31 clusters is complete to $V_{\rm lim} = 18$, but this does not mean it is complete to $V_0 = 17.75 = 18 - A_V(\rm min)$. Heavily-extinguished clusters would have $V > 18$ but $V_0 < 17.75$. We compute the required completeness correction in V_0 bins as follows. First, we divide each bin into five smaller sub-bins. For each sub-bin, we use the observed distribution of extinction values to determine the fraction of the bin which could have been observed, i.e. for which $V_0 + A_V < V_{\rm lim}$. This fraction is the completeness fraction, which we average over the sub-bins to determine the completeness for each bin. We use the same procedure to correct for the effects of the magnitude limit in V on data in other bandpasses (written generically as X_0). In this case both the color and extinction distributions are taken into account, and the objects which could have been observed have $X_0 + (V - X_0) = X_0 + (V - X)_0 + A_V < V_{\rm lim}$. We compute individual completeness functions for all of the different M31 GC samples discussed in this paper.

We performed Monte Carlo simulations to check that this correction procedure did not introduce a bias in the GCLF results. We generated V_0 GCLFs from Gaussian and t_5 (Secker 1992) distributions with $V_0 = 17.0$, $\sigma_g = 1.1$, $\sigma_t = 0.9$, $N_{gc} = 300$, parameters appropriate to the M31 GCLF. We applied to each object an extinction chosen randomly from the observed distribution, removed the objects with $V > V_{\rm lim}$, generated the completeness function using the remaining objects, and measured the GCLF parameters of the sample. We corrected the GCLF parameters for the magnitude limit of each of the 200 trials using the method described in the following section. Over all trials, the averages of the peak location measure were 16.97 ± 0.01 for Gaussian and 17.04 ± 0.01 for the t_5 distribution; the average measures of dispersion were $\sigma_g = 1.10 \pm 0.01$, $\sigma_t = 0.92 \pm 0.01$. The uncertainties in the 200 individual measurements of peak location and dispersion (~ 0.18 and 0.13 mag, respectively) are large compared to the average difference between input (simulated) and output (measured) GCLF parameters, so we conclude that our completeness correction does not introduce a significant bias.

Another kind of incompleteness we correct for is missing photometry. We have V magnitudes for all of our objects, but observations in other filters are not always available. Estimating the photometric completeness in bands other than V is a simple procedure:

1. Set up a series of bins in magnitude X_0.
2. Sort objects with known X_0 magnitude into the appropriate bin.
3. Estimate the X_0 magnitudes of the other objects as $V - (V - X_0)$, where $(V - X_0)$ is drawn at random from the probability distribution of the objects with X_0, and sort them into the appropriate bins.
4. Add the bin totals from the previous two steps.
5. For each bin, the photometric completeness is (number of objects with measured X_0)/(total number of objects in bin).

The final completeness function is the average of 500 trials of steps 3–5, in order to average out the noise produced by drawing colors at random from the observed color distribution. The completeness function from missing photometry is multiplied by the completeness function for the magnitude limit to produce the final estimate of completeness in each bandpass.

We also checked the effects of errors in photometry and reddening on the GCLF results. Photometric uncertainties for the CCD and photoelectric photometry in

our catalog are generally $\lesssim 0.05$ mag; uncertainties for photographic photometry (which is relatively uncommon in our catalog) are larger, perhaps 0.15 mag. These uncertainties are smaller than the errors in individual extinctions: in Chapter 2 we estimated uncertainties in $E(B-V)$ to be $0.05-0.10$ mag, corresponding to A_V uncertainties of $0.16-0.31$ mag. Using the same Monte Carlo simulations described above, we added Gaussian errors (from distributions with zero mean and standard deviations from 0.15–0.50 mag) to every individual extinction in each of the 200 GCLFs. If an 'extinction-with-error' value fell below the foreground value of 0.25, the extinction was changed to the foreground value as in our observational procedure. We also added errors to the measured magnitudes, again drawn from Gaussian distributions with zero mean and dispersion increasing as $10^{0.2m}$ (the behavior expected from photon statistics).

Even large ($\sigma_{A_V} = 0.50$ mag) extinction errors did not change the average peak and dispersion measured for the GCLF ensemble by more than about 0.03 mag. Little change in the peak is expected, since the extinction errors have zero mean and even an error of 0.5 mag does not shift many observed magnitudes beyond the magnitude limit. The small effect of σ_{A_V} on the measured GCLF dispersion ($\sigma_g \approx 1.1$ mag) is explained by noting that the two dispersions combine in quadrature and, for large values of σ_{A_V}, the magnitude limit truncates the observed distribution width. Large magnitude errors ($\sigma_m \gtrsim 0.3$ at $V = 17$, much larger than our estimated uncertainties) biased the average GCLF peaks to brighter values but did not significantly affect the dispersions. These effects are not unexpected: large magnitude errors push more objects beyond the magnitude limit (resulting in a brighter peak) and the magnitude again limit truncates the observed distribution width. We conclude that extinction errors and magnitude uncertainties do not significantly affect our measurement of the GCLF parameters.

4.4 The GCLF

To compute the globular cluster luminosity functions, we used version 2.01 of the maximum-likelihood code described by SH93. This program estimates the maximum-likelihood values of the parameters $\hat{\Theta} = (\hat{m}^0, \hat{\sigma})$ by finding the maximum in the likelihood function

$$L(\Theta) = \log l(\Theta) = \sum_{i=1}^{N} \log[\phi(m_i)]. \tag{4.1}$$

The simultaneous distribution function $\phi(m)$ is evaluated for each of the N magnitude observations m_i:

$$\phi(m) = I(m)\gamma(m) \tag{4.2}$$

$I(m)$ is the completeness function and $\gamma(m)$ is the intrinsic GCLF — a Gaussian or t_5 distribution with center m^0 and dispersion σ. This is a simplified version of SH93's $\phi(m)$; we set the number of background objects to zero as we do not have a quantitative estimate of the contamination rate. We also do not use the option to convolve the GCLF with the photometric error distribution: our photometry and extinction errors are not well-defined functions of magnitude, and trials using rough estimates of the error distributions showed that this did not significantly change the results. Uncertainties in the parameters are determined by computing $l(\Theta)$ over a grid in parameter space centered on the most probable parameter values. The resulting grid of likelihood values is normalized to have a total probability of unity and collapsed along the parameter axes; the 1σ ranges for the parameter estimates are the ranges containing 0.68 of the total probability along each axis.

SH93 show that the results of their maximum likelihood procedure are biased by the existence of a magnitude cutoff. The brighter the limiting magnitude, the more the parameter estimates are biased toward brighter m^0 and lower σ. To correct for this effect, we use the results of their simulations, shown in their Figure 3.[1] The equation used is:

$$\hat{m}^0 = m^0 + \delta(m_l - m^0) \tag{4.3}$$

where $\hat{m}^0$ is the estimated value of the turnover produced by the ML method, m^0 is the true, unbiased value, m_l is the limiting magnitude, and δ is the function plotted in the top panel of Figure 3 in SH93. We fit a fourth-order polynomial to δ, and use it to solve for m^0 given $\hat{m}^0$ and m_l. We fit a different polynomial $\tilde{\delta}$ to $\hat{\sigma} = \sigma + \tilde{\delta}(m_l - m^0)$ and compute σ directly after computing m^0.

4.4.1 Results

We discuss the halo sample first, because most of the recent determinations of the M31 GCLF have been for this sample. Since the halo sample is close to complete, we can also estimate the GCLFs in other bandpasses without correcting for a V magnitude limit. Table 4.2 and Figure 4.2 show the GCLFs for the halo clusters in six bandpasses. The Gaussian and t_5 distributions give indistinguishable results

[1] We note what appears to be a misprint in SH93: in both Figure 3 and the text, $(m^0 - m_l)$ appears where $(m_l - m^0)$ is clearly implied.

Table 4.2. M31 Halo GCLF

bandpass	m_g^0	σ_g	m_t^0	σ_t	Δ_t	N
U_0	17.68 ± 0.21	1.05 ± 0.15	17.65 ± 0.13	0.87 ± 0.14	0.01	74
B_0	17.61 ± 0.21	1.12 ± 0.17	17.57 ± 0.14	0.95 ± 0.16	0.07	80
V_0	16.81 ± 0.13	1.06 ± 0.10	16.84 ± 0.11	0.93 ± 0.13	$\cdots$	86
R_0	16.42 ± 0.19	1.10 ± 0.14	16.40 ± 0.14	0.95 ± 0.14	0.05	68
J_0	15.26 ± 0.20	1.08 ± 0.14	15.26 ± 0.14	0.98 ± 0.16	0.09	73
K_0	14.39 ± 0.20	0.97 ± 0.15	14.45 ± 0.18	0.89 ± 0.15	0.04	67

Note. — $\Delta = \overline{(V-X)_0} - (V_0^0 - X_0^0)$ is the difference between the mean object color and the peak color. The superscript in V_0^0 refers to the GCLF peak, while the subscript refers to the extinction correction (Harris 1988).

for the location of the GCLF peak. The best-fit Gaussians have smaller values of the dispersion: the characteristic $\sigma_g \approx 1.05$ corresponds to $\sigma_t = 0.82$. This is not a serious concern; Secker (1997) notes that the theoretical correspondence between σ_g and σ_t ($\sigma_g = 1.29\sigma_t$) is seldom observed for the small number of objects used here. The t_5 form of the GCLF has smaller parameter uncertainties than the Gaussian form. This implies that the t_5 function is a better fit to the GCLFs than the Gaussian, and indeed a comparison of the maximum likelihood values shows this to be true in almost all cases. The superiority of the t_5 function over the Gaussian was first pointed out by Secker (1992), and confirmed by SH93. In the remainder of this paper, we consider only the t_5 estimates of the GCLF parameters. The sixth column of Table 4.2 shows the differences between the mean colors of the objects and the mean peak colors, measured relative to V. The differences are well within the uncertainties of the peak locations, as would be expected if the halo GCs have no correlation of color with magnitude. This means that, given sufficiently accurate estimates of the clusters' mean intrinsic colors (which requires an accurate determination of the reddening), the GCLF peak in one filter can be used to estimate peak locations in other filters.

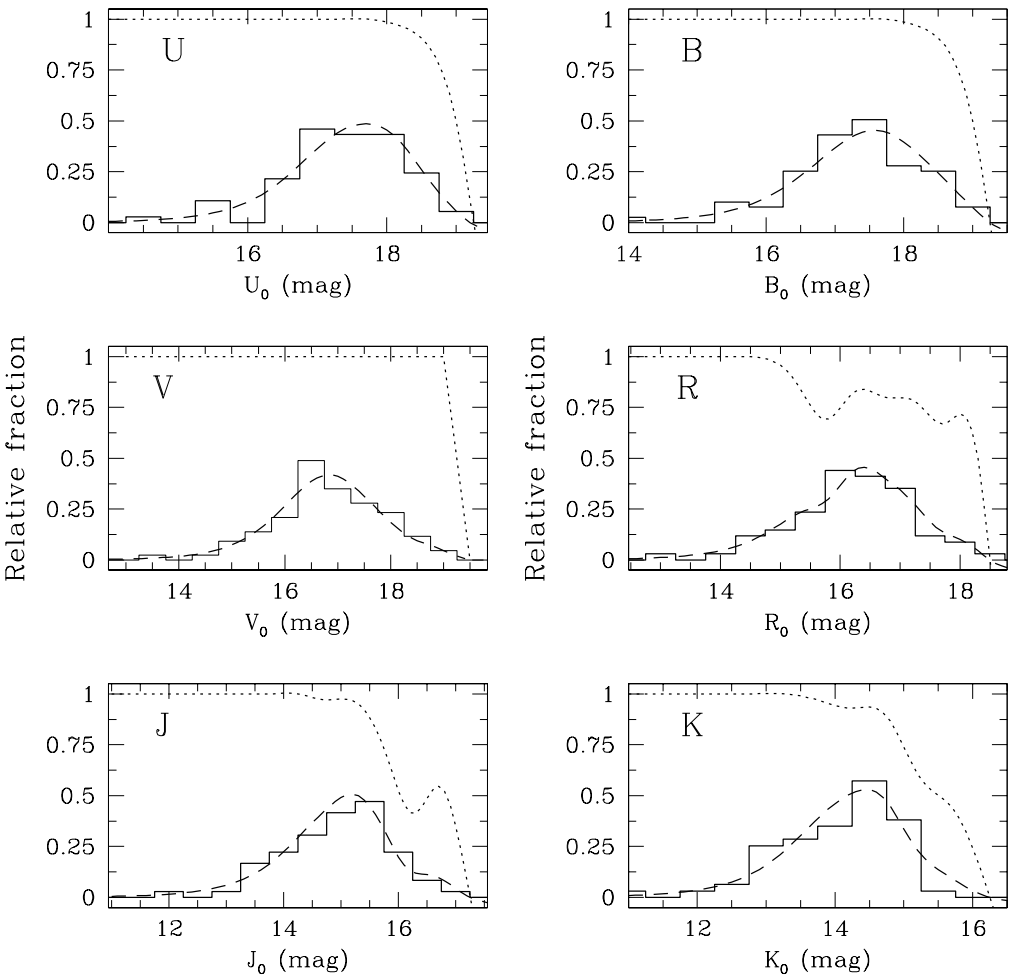

Fig. 4.2.— GCLFs and completeness functions for M31 halo clusters. The dip in the R-band completeness function is real; five clusters with $16.25 < V < 16.75$ (estimated $15.5 < R_0 < 16.0$) do not have measured R magnitudes.

Next we compare our results to previously published M31 GCLFs, given in Table 4.3. We correct the values for the GCLF peak for our preferred extinction value, $A_V = 0.25$. Where the peak values were given as extinction-corrected absolute magnitudes M_V^0, we used the corresponding apparent distance moduli μ_V to convert the values to V_0^0. The relation used was

$$V_0^0 = M_V^0 + \mu_V - A_V{}' + \Delta A_V \tag{4.4}$$

where $A_V{}'$ is the previous author's assumed extinction and $\Delta A_V = A_V{}' - 0.25$. [Sharov & Lyutyi (1989) estimated extinction internal to M31 for each cluster, using $R_V = 2.65$. We could not correct these extinctions to our values because the individual magnitudes and extinctions were not given, but we did apply a correction for the foreground extinction.] Our results for the halo GCLF peak and dispersion, $V^0 = 16.84 \pm 0.11$, $\sigma_t = 0.93 \pm 0.13$, are consistent at the 1σ level with the results for the $R > 10$ kpc sample of Crampton et al. (1985), the halo sample of Secker (1992), and the 'outer' sample of Gnedin (1997). We find a brighter peak than Racine & Shara (1979); their photographic photometry may be suspect. Because the number of halo clusters is small, the composition of the sample can measurably change the derived GCLF parameters. If we drop the five 'low-probability' clusters mentioned in Section 4.3.1 from our sample, we recover the slightly brighter peak value reported by Secker (1992). We are aware of only one measurement of a non-V-band GCLF peak in M31: Sandage & Tammann (1995) average the B magnitudes of Secker's halo sample to obtain $<B>= 17.75 \pm 0.11$, which corresponds to $B_0^0 = 17.42 \pm 0.11$. This is again consistent with our result at the 1σ level.

Table 4.3. M31 V-band GCLF parameters

sample	V^0	σ (Gaussian)	N[a]	Ext. correction[b]	Ref.
halo	16.54 ± 0.12	1.13	86	fg	(1)
all	16.95	1.2	188	fg	(2)
all	16.5	1.2	408	[c]	(3)
$R < 10$ kpc	16.2	1.5	265	[c]	(3)
$R > 10$ kpc	17.0	1.8	143	[c]	(3)
all	16.13 ± 0.08	1.16 ± 0.08	294	M31+fg	(4)
halo	16.75 ± 0.11	1.10 ± 0.11	82	fg	(5)
halo	16.75 ± 0.15	1.10 ± 0.11	82	fg	(6)
halo	16.75 ± 0.15	$\cdots$	81	fg	(7)
halo	17.20 ± 0.08	0.76 ± 0.05	161	fg	(8)
inner halo	17.05 ± 0.10	0.57 ± 0.10	64	fg	(8)
outer halo	17.04 ± 0.17	0.94 ± 0.13	97	fg	(8)
all	16.27 ± 0.06	0.86 ± 0.04	164	[c]	(9)
inner	15.92 ± 0.08	0.70 ± 0.05	82	[c]	(9)
outer	16.71 ± 0.09	0.96 ± 0.08	82	[c]	(9)

[a] N is the number of objects used in the GCLF measurement, not an estimate of the total number of GCs N_{gc}.

[b] 'fg' indicates correction for foreground extinction of $A_V = 0.25$ mag

[c] Paper text implies that these values are corrected for extinction, but method not clearly described.

References. — (1) Racine & Shara (1979); (2) van den Bergh (1985); (3) Crampton et al. (1985); (4) Sharov & Lyutyi (1989); (5) Secker (1992); (6) Racine & Harris (1992); (7) Reed et al. (1994); (8) Kavelaars & Hanes (1997); (9) Gnedin (1997)

We now turn to the other samples of M31 GCs. Here we consider only the V-band GCLF, as the photometric completeness in other bands is generally much poorer. We correct the GCLF peaks and dispersions for the magnitude cutoff at $V = 18$. The full and disk samples have similar GCLF peaks (16.70 ± 0.11, 16.67 ± 0.16) and dispersions ($\sigma_t = 1.11 \pm 0.09$, 1.18 ± 0.12); this is unsurprising as the full sample is 77% disk clusters.[2] We find a fainter GCLF peak for the GCS as a whole than do Crampton et al. (1985), Sharov & Lyutyi (1989), and Gnedin (1997) (considering here the 'all clusters' samples of Crampton et al. and Gnedin). There are several likely reasons for this: the older samples are less complete and have poorer photometry, and their corrections for incompleteness are either non-existent or do not account for the extinction effect discussed in Section 4.3.3.

Neither the full or disk samples has a GCLF peak significantly different from that of the halo, but the disk sample has a 2σ higher dispersion than the halo. This is in contrast to previous results: both Crampton et al. (1985) and Gnedin (1997) found the GCLF peak to be brighter and the GCLF dispersion lower for the inner ('disk') clusters. We suspected that the peak difference found by other groups was because they failed to correct for incompleteness due to extinction. To test this, we tried setting the completeness function to a step function with the step at $V_0 = 17.75$. The result was a much brighter disk peak, resulting in a difference of 0.6 mag between the halo and disk GCLF peaks. The completeness correction thus has a large effect on the resulting GCLF, and the extinction cannot be ignored in a spiral galaxy like M31. We address the question of lower halo dispersion in Section 4.4.3.

Models of GCS evolution predict that low-mass clusters near the center of a galaxy are most susceptible to dynamical destruction. We suspected that our disk/halo division might be too crude to detect any radial GCLF differences. We followed the method of Gnedin (1997) in sorting the M31 clusters by projected distance from the center of M31 and dividing them into equal-sized groups. As Figure 4.3 shows, there is a definite trend for the GCLF peak to be fainter with increasing projected distance, although the GCLF dispersion does not show any obvious trend. The difference between the inner- and outer-most groups ranges from 0.44 to 0.56 (± 0.18) mag in V_0, depending on the number of groups, with $\Delta m^0/\sigma(m^0) = 2.5 - 2.8$. The trend in the peak is largely due to the objects with $R \lesssim 3$ kpc. The disk is dominated by GCs with larger R_{gc}, which is why we see

[2]The GCLF parameter uncertainties are smaller for the halo than for the disk sample, even though the disk has about 2.5 times as many objects. This is caused by extinction-induced incompleteness: when completeness is not corrected for, the uncertainties drop by $\sim 50\%$. In the halo sample, the uncertainties are close to the limit imposed by the small numbers: $\sigma_g/\sqrt{N} \approx 0.11$.

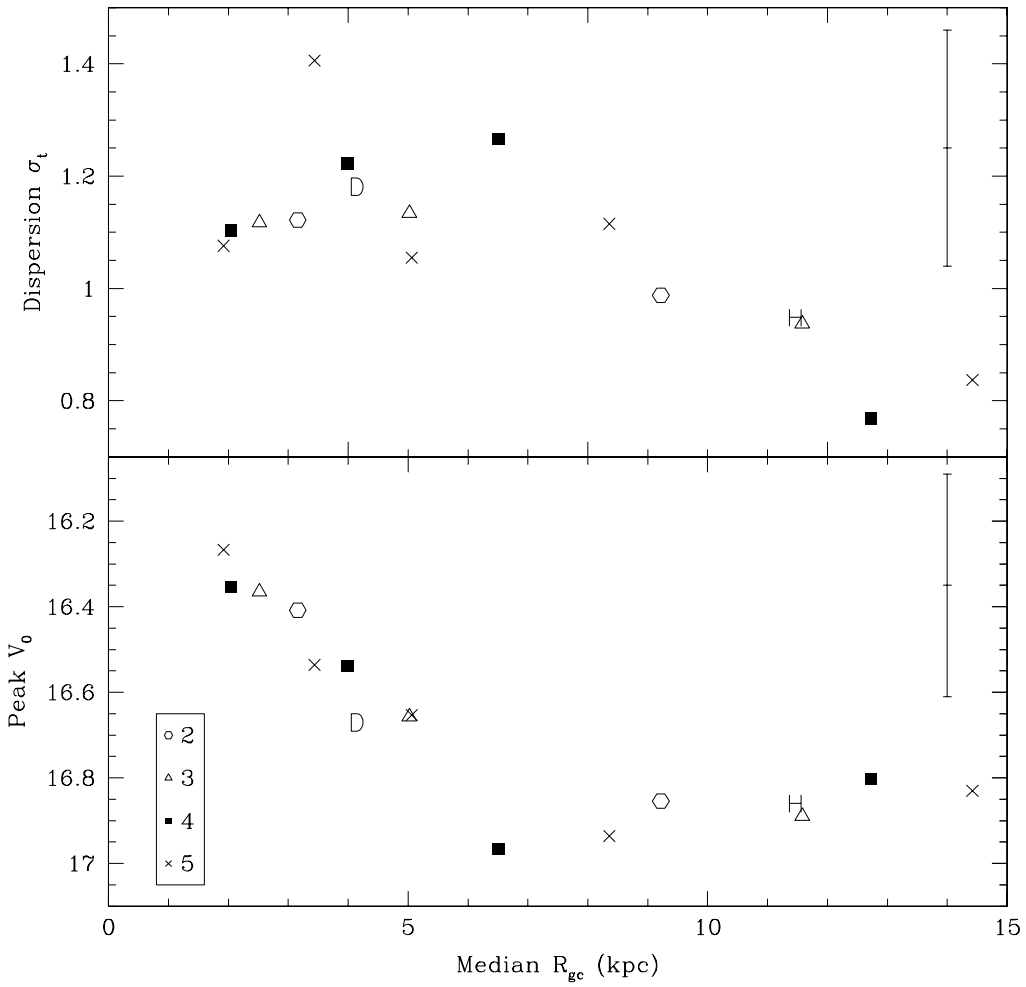

Fig. 4.3.— GCLF peaks and dispersions for groups of M31 clusters, sorted by projected distance from the center of M31. The different symbols represent the division of the GCS into different numbers of groups; 'D' and 'H' show the location of the disk and halo samples.

Table 4.4. GCLF for different samples of M31 GCs

Sample	m_t^0	σ_t	[Fe/H]	R_{gc} (kpc)	N
MP inner	16.32 ± 0.21	1.00 ± 0.17	-1.51	2.6	60
MP outer	17.02 ± 0.22	1.08 ± 0.13	-1.59	8.2	131
MR inner	16.15 ± 0.58	1.51 ± 0.32	-0.59	2.6	25
MR outer	16.46 ± 0.23	0.93 ± 0.18	-0.65	5.8	50
MP	16.84 ± 0.16	1.09 ± 0.11	-1.57	5.5	191
MR	16.43 ± 0.27	1.11 ± 0.19	-0.61	5.2	75
inner	16.37 ± 0.21	1.12 ± 0.17	-1.27	2.5	98
outer	16.80 ± 0.14	1.05 ± 0.10	-1.41	7.4	196

Note. — [Fe/H] and R_{gc} are median values.

little difference between the disk and halo samples. This again underscores the importance of having a complete, uncontaminated sample of the GCs near the M31 nucleus.

Both Huchra et al. (1991) and this thesis (Chapter 2) found that the metal-rich clusters were more centrally concentrated. Could a difference between MR and MP GCLFs produce a radial GCLF difference? To disentangle the effects of age and metallicity, we divided our full sample by both metallicity and projected galactocentric distance. Since the radial GCLF variation is mostly due to the innermost clusters, we put the inner/outer dividing line at the galactocentric distance containing one-third of the clusters, $R \approx 3.8$ kpc$= 19'$. The resulting GCLFs and completeness functions are shown in Figure 4.4; the GCLF parameters are in Table 4.4. The significant difference between GCLF parameters of MR and MP clusters in the outer two-thirds of M31 strongly implies that both metallicity (or some parameter related to it) and galactocentric distance affect the GCLF peak. To check that the effect we measured was not due to the details of sample division, we carried out 200 trials in which we divided the full sample in both metallicity and R_{gc}, with randomly chosen division points. While the differences between subsamples depended on the exact division point (as expected), the relative ordering of the GCLF peaks was always the same as that shown in Table 4.4.

The size of each parameter's contribution to the GCLF peak can be estimated

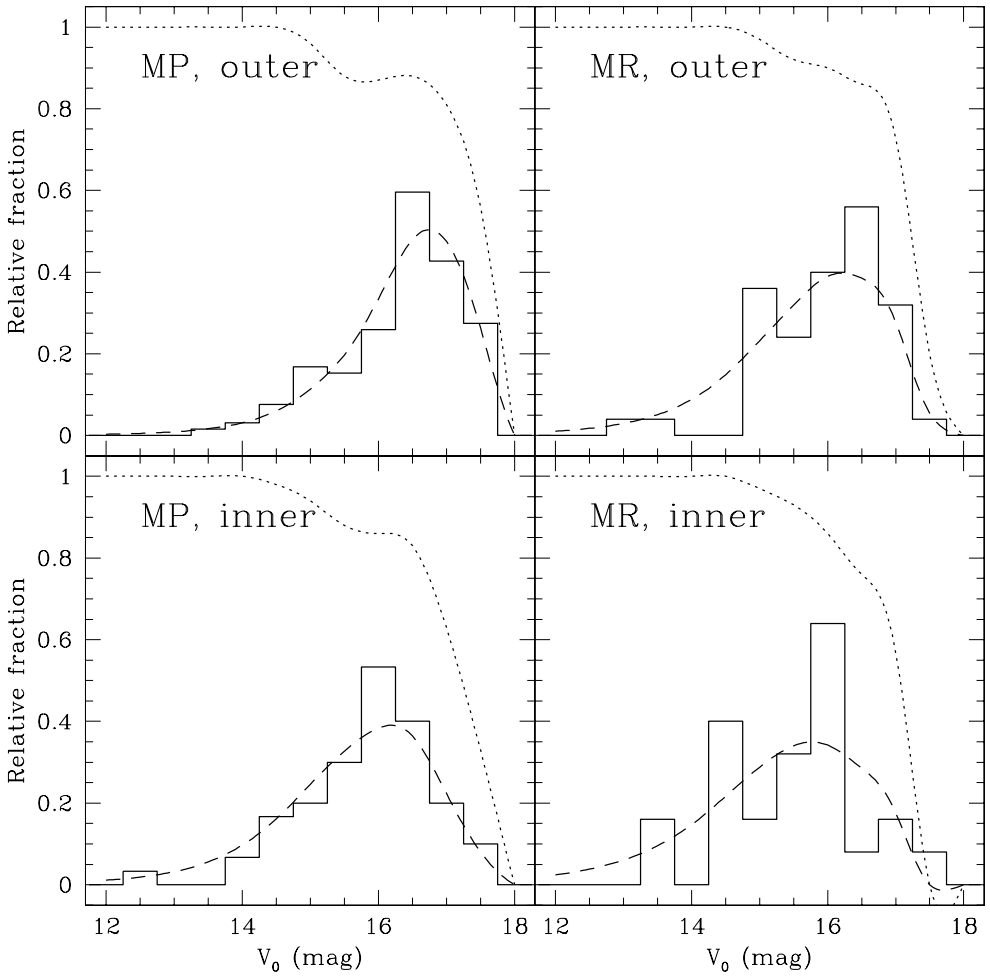

Fig. 4.4.— GCLFs and completeness functions for four groups of M31 GCs: (a) MP, outer (b) MR, outer (c) MP, inner (d) MR, inner. The dip in the completeness function for the MP clusters is due to the presence of a few bright objects without metallicities (likely to be metal-poor because MP clusters make up two-thirds of the population).

by writing the values as:

$$\begin{pmatrix} \mathrm{MP}_i & \mathrm{MR}_i \\ \mathrm{MP}_o & \mathrm{MR}_o \end{pmatrix} = \begin{pmatrix} 16.32 & 16.15 \\ 17.02 & 16.46 \end{pmatrix} = \begin{pmatrix} 16.42 & 16.06 \\ 16.92 & 16.56 \end{pmatrix} + \begin{pmatrix} -0.10 & 0.10 \\ 0.10 & -0.10 \end{pmatrix} \tag{4.5}$$

so 0.50 mag of GCLF variation is due to galactocentric distance, 0.36 mag to metallicity, and 0.10 to the interaction of the two. This is very similar to the average results from the 200 'random division point' trials. The existence of the interaction term is not surprising, since we know that metallicity and galactocentric distance are correlated (e.g., see Figure 2.21).

Another way to quantify the GCLF variation is a multiple regression of V_0^0 on [Fe/H] and projected galactocentric distance R_{gc}. We performed such a fit for the data in the first four rows of Table 4.4. Although using four points to define a plane is not statistically rigorous, it is a reasonable way to estimate the size of the effects [Fe/H] and R_{gc} have on the GCLF. (Defining the relation more rigorously will be difficult, since measuring GCLF parameters with reasonable precision requires sample sizes $N \gtrsim 50$ and the full M31 GC sample of 294 objects can only be divided into a few independent subsamples.) The regression equation is:

$$V_0^0 = 15.67 - 0.24[\mathrm{Fe/H}] + 0.12R_{gc} \tag{4.6}$$

with [Fe/H] in dex and R_{gc} in kpc. This equation predicts V_0^0 to within ≤ 0.15 mag for the last four samples in Table 4.4 (see Figure 4.5), where the clusters are separated on either metallicity or R_{gc} but not both. A multiple regression of V_0 on [Fe/H] and R_{gc} for the individual cluster data (with no incompleteness correction) gives similar regression parameters, but the correlation is much poorer because of the luminosity dispersion. This is why we did not did not detect any correlation of luminosity with metallicity in Chapter 2, and why we believe that binning the clusters into samples, although arbitrary, is necessary.

The surprising result here is that the MR clusters are *brighter* than the MP clusters. For clusters of the same age, and average metallicities [Fe/H] ~ -1.6 and -0.6, Ashman et al. (1995) predict that the MR clusters should be fainter in V by 0.29 mag. If the metal-rich clusters were 80% as old as the metal-poor clusters, as suggested by Rosenberg et al. (1999), the population synthesis models used in Chapter 3 predict that the metal-rich clusters should be fainter in V by ≤ 0.13 mag. A larger difference in age between the two metallicity groups could be responsible for the measured GCLF differences; we return to this point in the following section. The only systematic error we can conjecture which would cause overly bright magnitudes for the MR clusters is an overestimation of their extinction. However, this would also make the derived intrinsic colors of the MR

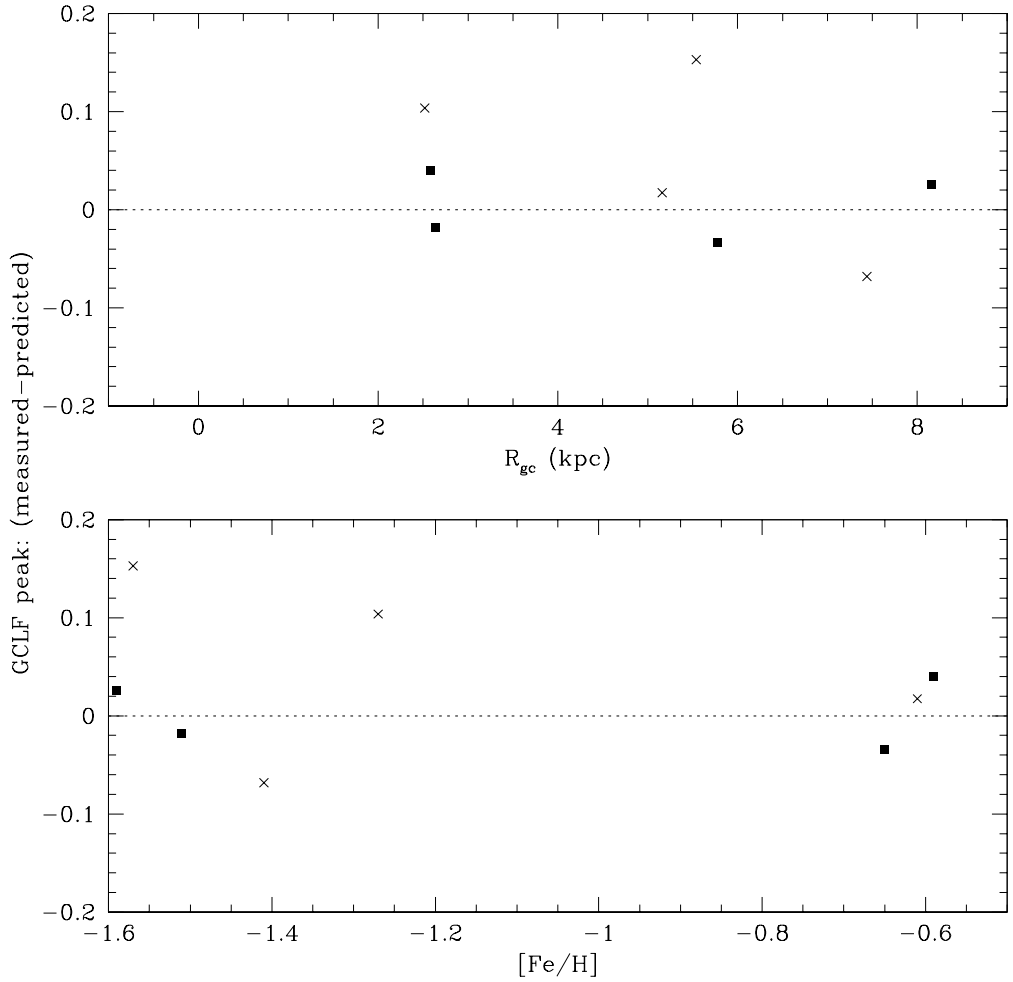

Fig. 4.5.— Difference between predicted (from Equation 4.6) and measured GCLF peaks for the data in Table 4.4. Crosses are data from the first four lines of the table, used in fitting the regression equation. Squares are data from the last four lines, which were not used in the regression because they are not independent samples of the M31 GC population.

clusters too blue, which seems unlikely given that the color-metallicity relations for Galactic and M31 clusters match well throughout their metallicity range (see Chapter 2).

Reports of large GCLF variations with either R_{gc} or metallicity are not common in the literature. Armandroff (1989) assigned Milky Way GCs to the disk or halo based on [Fe/H] (with a dividing line at -0.80 dex) and found no difference in the luminosity functions of the two groups. Kavelaars & Hanes (1997) found no difference in GCLF peak magnitudes of the inner and outer halo clusters in the Milky Way and M31; Gnedin (1997) found a 0.47 mag difference between GCLF peaks of the same samples and claimed that the histogram-fitting method used by Kavelaars & Hanes was responsible for their failure to detect the difference. Gnedin (1997) also found a difference of 0.79 ± 0.12 mag in GCLF peak magnitudes between inner and outer GCs in M31. This difference is larger than the one we measure, but certainly compatible with it at the 1σ level. Selection effects in our M31 GC catalog are a possible cause of the differences between our results and those of previous authors; we consider this in the following section.

Most published GCLFs are actually for elliptical galaxies – M31 and the Milky Way are the only two spirals whose GCLFs are well-measured (but these two galaxies are often used, e.g. by Sandage & Tammann (1995), to define the GCLF peak absolute magnitude for use in distance measurement). In ellipticals where GCLFs have been determined separately for the red (MR) and blue (MP) GCs (e.g. Kundu et al. 1999; Puzia et al. 1999; Grillmair et al. 1999) the metal-poor clusters are typically found to be brighter (0.1–0.5 mag) in V, and fainter or similar in I, as predicted by Ashman et al. (1995). Lee & Kim (2000) analyzed the same HST data as Puzia et al. (1999), but found that GCLF peaks of the red and blue clusters were indistinguishable in both V and I. Gnedin (1997) found a 0.24 ± 0.11 mag difference between the GCLF peaks of inner and outer clusters in M87, while Kundu et al. (1999) found no evidence for radial variation in the M87 GCLF and suggested that Gnedin did not correctly account for incompleteness. Puzia et al. (1999) found that only the red clusters in NGC 4472 show a difference between inner and outer GCLF peaks (0.27 ± 0.14 in V). Our results on the radial GCLF variation are not inconsistent with those of other authors, but the variation with metallicity or color has not been reported before. It is important to know whether the GCLF variation we measure is a unique feature of the M31 GCS, a common feature of spiral galaxies' GCSs not shared by the Milky Way, or an artifact of the data and methods we used. A definitive answer to this question will require better data on the M31 clusters and their individual extinctions and information on the GCLF in other spirals.

4.4.2 Selection effects and the GCLF

Because M31 GC catalogs, including ours, suffer from both incompleteness and contamination, it is reasonable to ask how the catalog properties might affect the GCLF. Specifically, could variations in the degree of contamination and incompleteness with galactocentric distance be responsible for the radial GCLF variations we measured?

A small fraction of the objects in our cluster catalog are probably not M31 GCs. Of the 294 objects in our full sample, 178 (about 60%) have been confirmed as clusters by spectroscopy or high-resolution imaging. Most of the halo sample (73/86) is confirmed, and Figure 4.6a shows that the fraction of confirmed clusters is highest in the outer regions. The confirmed objects also tend to be brighter, as Figure 4.6b shows: this is not surprising since the largest spectroscopic survey (that of Huchra et al. 1991) was performed descending a magnitude-ordered list. We are not aware of any 'false positives' — objects whose confirmation as a GC was later shown to be incorrect — among M31 GC candidates, so any non-clusters must therefore be among the 116 unconfirmed objects. Since these objects are, on average, fainter than the confirmed clusters, dropping contaminating objects from the sample should make the resulting GCLFs brighter. A larger effect would be expected for the inner region, since it has more unconfirmed objects.

We tested this hypothesis using a Monte Carlo experiment. For the full sample and each of the subsamples listed in Table 4.4, we performed 200 trials in which we chose 34% of the unconfirmed clusters at random, dropped them from the sample, and computed the GCLF with the remaining objects. The 34% figure comes from the Battistini et al. (1987) classification of these objects and Racine's (1991) estimate of the actual cluster fractions in each class. Table 4.5 shows the average of the GCLF parameters over all 200 trials[3]. Compared to the full samples (Table 4.4), the GCLFs found for the 'decontaminated' samples had brighter average peaks and almost identical dispersions; this was expected because most of the unconfirmed clusters are faint. The change caused by decontamination was was larger for the inner and metal-rich clusters; again, this was expected because these clusters are less likely to be confirmed. Table 4.6 shows that decontaminating the cluster catalog actually increases the GCLF peak and dispersion differences between different samples. We conclude that contamination of the GCLF sample by non-clusters cannot be responsible for the GCLF differences we measure.

[3]Uncertainties in the parameter values from the 200 individual trials are comparable to those given in Table 4.4. Statistical uncertainties in the averages are much smaller, typically 0.05 mag.

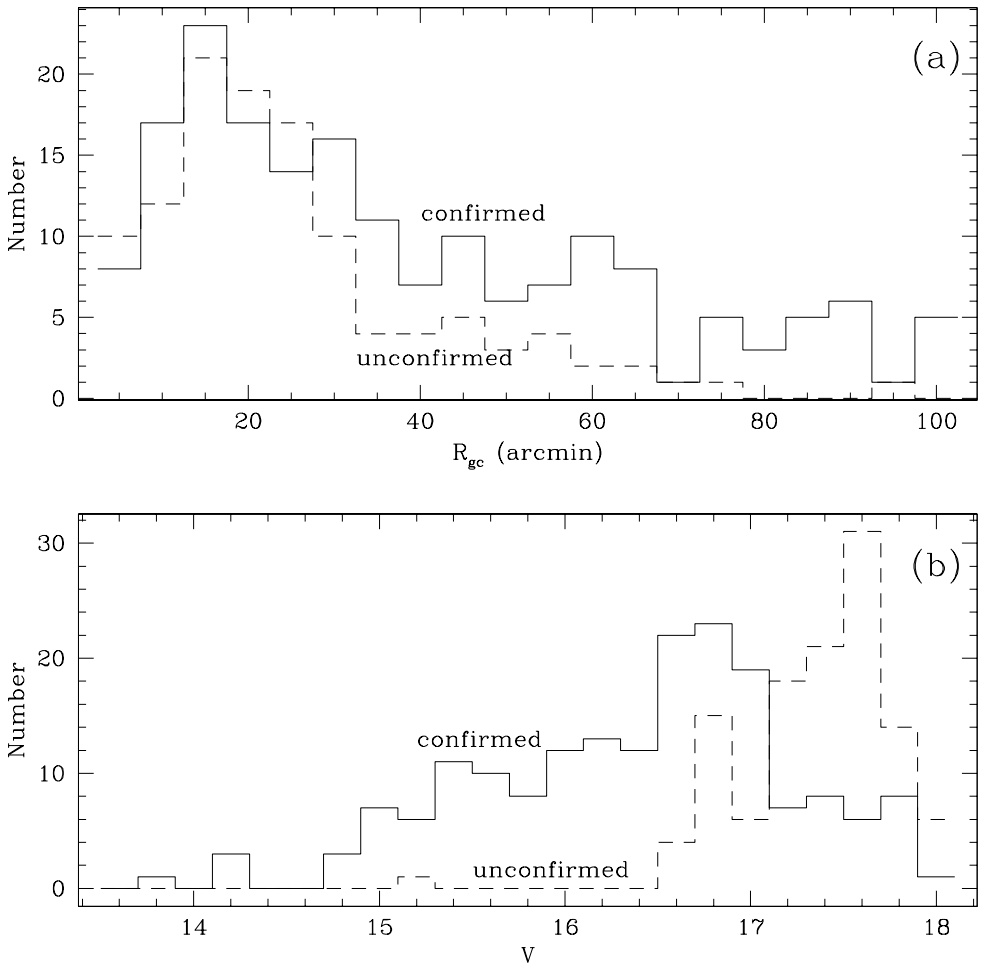

Fig. 4.6.— Distribution of R_{gc} and V for confirmed and unconfirmed M31 GCs. The fraction of confirmed clusters rises slowly with R_{gc} and drops rapidly with V.

Table 4.5. Average GCLF parameters for de-contaminated samples of M31 GCs

Sample	m_t^0	σ_t
MP inner	16.17	0.92
MP outer	17.00	1.12
MR inner	15.91	1.33
MR outer	16.35	0.93
MP	16.80	1.13
MR	16.28	1.12
inner	16.18	1.08
outer	16.74	1.07

Table 4.6. GCLF differences for full and de-contaminated samples of M31 GCs

	Full samples		Decontaminated	
Samples	Δm_t^0	$\Delta\sigma_t$	Δm_t^0	$\Delta\sigma_t$
outer−inner	0.43	−0.07	0.56	−0.01
MP−MR	0.39	−0.02	0.52	0.01
MP outer−MP inner	0.70	0.08	0.83	0.20
MR outer−MR inner	0.31	−0.58	0.44	−0.40
MP outer−MR outer	0.56	0.15	0.65	0.19
MP inner−MR inner	0.17	−0.51	0.26	−0.41

A first attempt at estimating the catalog incompleteness can be made using the work of Mochejska et al. (1998). They searched for globular clusters in four fields on the eastern side of the M31 disk (R_{gc} ∼20–40′) with a total area of 440.7 square arcmin. Mochejska et al. discovered 67 new GC candidates in this region, but considered all except five to be low-probability candidates. Two of the five good candidates had $V < 18$ and three had $V > 18.5$. The area of the the M31 disk (the large ellipse in Figure 4.1) is 1.14×10^4 square arcmin, so can we scale the Mochejska et al. (1998) result by area to estimate that our catalog could be missing as many as 50 clusters with $V < 18$. We do not have any information on the magnitude distribution of the possible missing clusters, other than the fact that virtually all of Mochejska et al.'s new cluster candidates have $V \gtrsim 17.5$. If our catalog were truly missing 50 objects, it would be about 83% complete. Because this value is a large extrapolation from very few data points, it can only be considered a rough estimate of our catalog's completeness, and it yields no information on completeness variation with magnitude or galactocentric distance.

An incompleteness estimate based on the work of Mochejska et al. (1998) is suitable for the outskirts of M31, but not for the crowded inner region. To estimate the number of missing GCs and contaminating objects in this regions, we used data in the HST Archive to search for new and previously known M31 GCs; the details of this effort will be described in the following chapter. Briefly, we examined all 79 WFPC2 fields with $R_{gc} \leq 30'$ imaged with broadband optical filters (F300W to F814W) and with exposure times ≥ 100 s. We chose $R_{gc} = 30'$ as the outer limit because the fractional area of M31 covered by HST fields is only 5% at this distance and the chances of finding globular clusters in more distant fields are small. Working independently, two of us (PB and JH) visually searched each image for globular clusters. The searches were conducted 'blind', i.e., with no reference to the positions of known M31 GCs. To estimate our cluster detection efficiency, we inserted 'artificial' globular clusters, made by randomly rotating and re-scaling HST images of known M31 globulars, into some of the images. Our overall success rate for detection of the artificial clusters over the magnitude range $14 < V < 22$ was 80%; for objects with $V < 18$, our primary concern for this work, our success rate was 96%. We conclude that we should have detected essentially all true M31 GCs with $V < 18$ in the HST images.

Our final list of cluster candidates contains 62 objects. 40 of these are previously-discovered objects appearing in our Chapter 2 catalog of plausible cluster and candidates, 9 are previously-discovered objects not in our catalog because they had been classified as 'low-probability' candidates, and 13 objects are newly-discovered cluster candidates. We estimated V magnitudes for the new

candidates from the HST images, using the transformations given in Holtzman et al. (1995). Figure 4.7 shows the distribution of the HST cluster candidates in V and R_{gc}. Only about half of the non-cataloged objects are unquestionably globular clusters, so we mark 'good' and 'marginal' candidates with different symbols. Most of the newly-discovered candidates are either faint objects at large galactocentric distances, or bright objects very close to the galaxy center. The discovery of bright new cluster candidates having $R_{gc} \leq 5'$ shows that incompleteness is substantial in the region, and validates our decision to exclude it from GCLF computations.

The important question here is whether there is a difference in catalog completeness between inner and outer clusters with $V < 18$. In the inner region there were 20 good GC candidates with $V < 18$; 17 of these objects were in our catalog, so its completeness is 85%. In the outer region there were 8 good GC candidates with $V < 18$; only one of these objects was not in our catalog, so the completeness is 88%. Although the numbers are small because the covering fraction of the HST images on the sky is only 10–20%, there is no evidence that the inner sample of clusters is substantially less complete than the outer one. The new cluster candidates in both regions have similar magnitudes, $V \sim 17.7$, indicating that the magnitude limit of the existing catalogs does not change drastically with R_{gc}.

To the best of our ability to model them, the selection effects of incompleteness and contamination in the M31 cluster sample are not responsible for the GCLF variations which we measure. The M31 GC catalog can certainly be improved, and our conclusions would be strengthened if the same GCLF differences were measured in less-contaminated samples with better-understood and spatially uniform completeness. However, analysis of the GCLF does not require a perfect catalog — something which does not exist even for the Milky Way GCs. As a final comment on catalog incompleteness, we speculate on the possibility that there exists a heavily-obscured population of GCs in M31. If such objects exist and are fainter than the known population *and* preferentially located near the center of M31 or metal-rich, then the brighter peaks found for the metal-rich and inner clusters might be an artifact of incompleteness. There is presently no evidence for a population of heavily-extinguished GCs in M31, so we believe our GCLF results to be valid, and consider their implications in the following section.

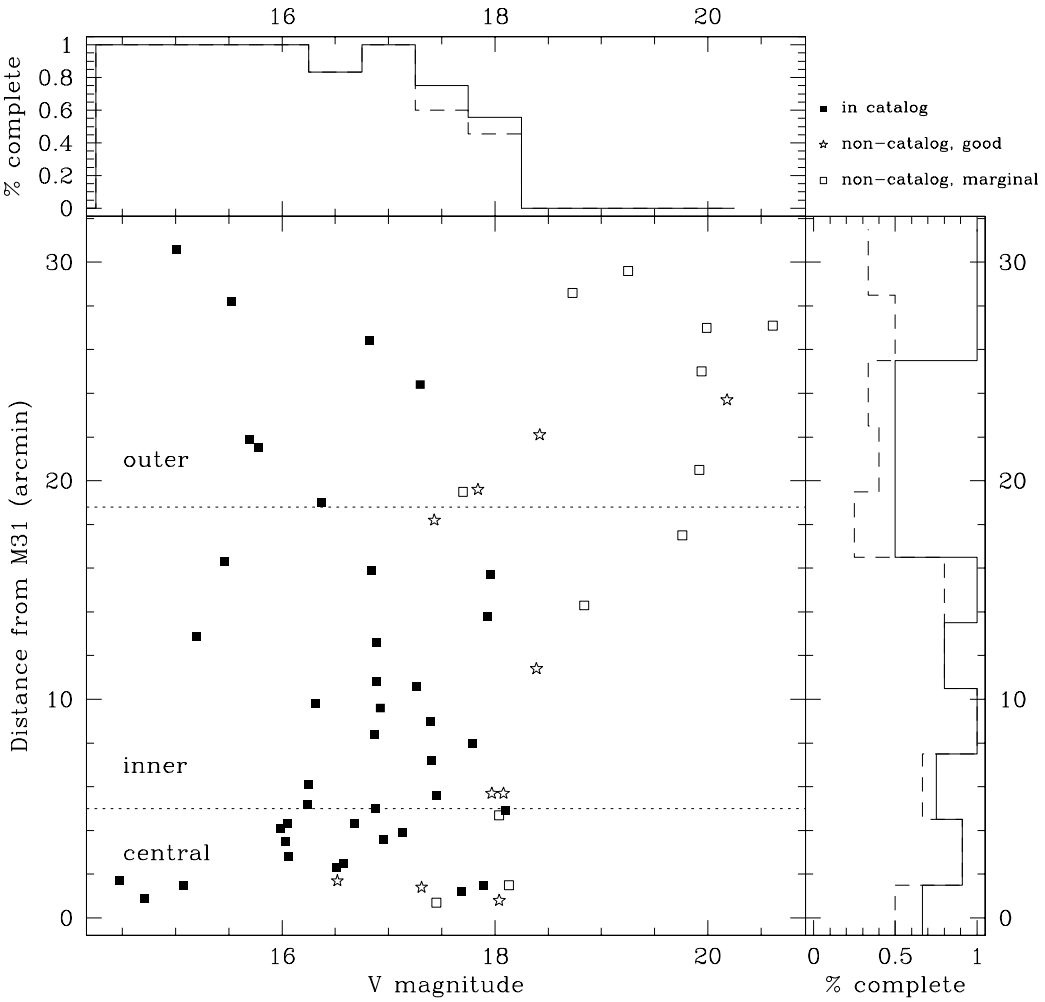

Fig. 4.7.— Distribution in R_{gc} and V for cluster candidates in HST fields. The catalog completeness as a function of R_{gc} and V is (number of cataloged clusters) divided by (total number of clusters); solid lines are the completeness computed using good GC candidates only and dashed lines include marginal candidates.

4.4.3 Implications for GCS destruction and formation models

Variation of the GCLF with R_{gc} is a key prediction of GCS evolution models. The shorter destruction timescales for clusters near the center of a galaxy potential may lead to a mass difference, and hence a GCLF difference, between 'inner' and 'outer' GCs in a galaxy. Several authors have predicted differences between the inner and outer GCLFs for Milky Way clusters. The dividing line between inner and outer varies from 5–10 kpc, and the size of the predicted difference in the GCLF peaks ranges from essentially zero (Vesperini 1998) to 1.4 magnitudes (Baumgardt 1997). Vesperini (1998) finds that there is a particular initial GCMF for which the balance between cluster disruption and mass evolution of the surviving clusters keeps the shape and initial parameters of the mass function unchanged. The only prediction made specifically for the M31 GCS is that of Ostriker & Gnedin (1997). For an inner/outer split at $R = 27' = 5.5$ kpc,[4] they predict a peak location difference of 0.49 ± 0.18. Our results on the GCLF peak are in in excellent agreement with this prediction. For two populations of the same age and metallicity, a magnitude difference of 0.5 corresponds to a mass ratio of $10^{0.2} = 1.58$. For populations with the same age and metallicities differing by 1 dex, a magnitude difference of 0.35 in V implies a mass ratio of 1.87; the larger mass ratio is due to the increase of mass-to-light ratio with metallicity.

Ostriker & Gnedin (1997) predict that destruction of low-mass inner clusters results in a (Gaussian) GCLF dispersion for the inner clusters 0.17 ± 0.12 mag lower than that of the outer clusters. Vesperini (1998) also predicts a lower inner GCLF dispersion for most initial conditions. We do not measure a lower GCLF dispersion for the inner clusters: if anything, the dispersion seems to decrease, not increase, with projected distance. While photometric and extinction errors are probably larger for the inner clusters, we showed in Section 4.3.3 that only very large errors strongly bias the GCLF parameters. The completeness limit is brighter for the inner clusters; again, this should not affect the GCLF parameters since we correct for the resulting bias. We are unable to devise any other systematic effects which might lead to erroneous measurements of the GCLF dispersion. A larger age spread in the inner clusters might mask a decrease in GCLF dispersion. If such an age spread existed in M31, it would be in contrast to the Galactic GCS, where the age spread is larger for the outer clusters (Chaboyer, Demarque, & Sarajedini 1996b). It is also possible that the inner clusters had a log-normal initial GCMF

[4]It is unclear whether this value is a projected or true 3-D distance from the center of M31; we assume it to be a projected distance.

with parameters that resulted in evolution in mean mass but not in dispersion (see Vesperini 1998). Since the theoretically predicted dispersion differences are small compared to the peak location differences, we do not consider our failure to detect such differences a serious problem for either our method or the theoretical models.

Key assumptions made when calculating the effects of dynamical destruction on the GCLF are that the initial age and mass distributions of the GCs are not functions of R_{gc}, and that metallicity effects are not important. These assumptions may not be correct. In Chapter 3, we found evidence that the metal-rich clusters in M31 and the Milky Way were younger than the metal-poor clusters; Rosenberg et al. (1999) found similar results from the color-magnitude diagrams for a sample of Milky Way clusters. If age differences do exist, they should affect the GCLF. To estimate the size of the age difference, we examined the predictions of V-band luminosity in the models of Bruzual & Charlot (1996), Kurth et al. (1999), and Worthey (1996). We computed the age differences implied by $\Delta V = 0.35$ mag, with (fainter, brighter) populations at [Fe/H] $= (-1.63, -0.63)$ (Bruzual & Charlot 1996; Kurth et al. 1999) or $(-1.50, -0.50)$ (Worthey 1996). Worthey's models cover only the age range from 8–16 Gyr at these low metallicities, and the only age pair with the required ΔV is $\mathrm{age_{MR}} = 8$ Gyr, $\mathrm{age_{MP}} = 16$ Gyr. For the other two sets of models, which cover the age range 1–16 Gyr, several age pairs reproduce the GCLF peak difference. In each case the MR clusters are about half as old as the MP clusters. Explaining the GCLF difference of outer and inner clusters as an age difference is also possible. For populations of the same metallicity (the median [Fe/H] values of the inner and outer clusters are not very different at -1.27 and -1.41), a 0.5 mag difference in V corresponds to the brighter clusters being 55% as old as the fainter clusters.

If the two sets of clusters have the same stellar initial mass function (IMF), the effect of IMF on the derived age differences is fairly small. For a Scalo (1986) or Miller & Scalo (1979) IMF instead of Salpeter (1955), $\Delta V = 0.35$ at different metallicities makes the MR clusters about 55% as old as the MP clusters, and $\Delta V = 0.5$ at the same metallicity makes the bright clusters 60% as old as the fainter ones. However, if the two sets of clusters had *different* IMFs, this could produce a large difference in the average V magnitudes. All three models predict that Scalo-IMF populations should be brighter than Salpeter-IMF populations of the same age and mass, by $0.6 - 1.0$ mag in V for ages > 8 Gyr. A difference in IMF with metallicity would still require explanation, however; at least for Galactic GCs, De Marchi & Paresce (1999) find no evidence of IMF variation.

Independent constraints on cluster ages and IMFs are needed in order for GCLF variations to be used in the study of GCMF evolution. If different

populations start with the same GCMF, differing dynamical evolution could lead to mass differences and explain the observed GCLF differences. However, combinations of age, metallicity and IMF differences could also reproduce the observations. With only one observable it is not possible to constrain all of the cluster parameters. Measuring the GCLF variations in the K-band, which is less sensitive to age and more sensitive to metallicity (the mass-to-light ratio in K is expected to decrease with metallicity, rather than increase as it does in V; Worthey 1994) would be helpful in disentangling the two effects. Unfortunately, our catalog lacks near-IR photometry for many clusters in the disk, so it is not possible to accurately measure the near-IR GCLF for the inner clusters.

Examining the measured GCLF parameters leads to several important conclusions. The fact that metal-rich clusters are, on average, brighter than metal-poor clusters implies that there must be some mass, age, or IMF difference between the two groups. A given population of clusters will be brighter than another if its average age is younger, its average mass more massive, or its average IMF more steep. Many combinations of these properties could also produce the same effect. We consider here the extreme possibilities for age and mass differences that could reproduce this effect (we neglect possible IMF differences, since these seem the least likely). Either (1) the MR clusters are younger by $\sim 50\%$, or (2) the MR clusters are more massive by a factor of ~ 1.9. The fact that inner MP clusters are brighter than outer MP clusters means that there is also a GCLF variation with R_{gc}. Again, the two extreme possibilities are: (3) the inner clusters are younger by $\sim 45\%$, or (4) the inner clusters are more massive by a factor of ~ 1.6. Each of these possibilities has important implications for the understanding of GCS and galaxy formation and evolution; we examine each in turn, drawing on the review given by Kissler-Patig (2000).

1) If the MR clusters are younger than the MP clusters, an age-metallicity relation exists in the M31 GCS. Such a relation has long been suspected for the Galactic clusters, although it has not been demonstrated conclusively (see Sarajedini et al. 1997). Lee & Kim (2000) and Kundu et al. (1999) compared their GCLF measurements in NGC 4472 and M87, respectively, to population synthesis models. Both found that, in addition to the metallicity effect, younger ages for the metal-rich clusters were required to account for the observed GCLF peak differences. A relation between age and metallicity is consistent with several scenarios for the formation of globular cluster systems. These include the merger scenario of Ashman & Zepf (1992), the in situ/two-phase scenario of Forbes et al. (1997a), and the pre-galactic scenario of Kissler-Patig (1997b) (see also Peebles & Dicke 1968). Fitting young MR GCs in M31 into the merger scenario would require

some modifications. The scenario attempts to account for the presence of multiple populations of GCs in *elliptical* galaxies by postulating that the MR clusters form when star formation is induced in the spiral/spiral merger which produces the elliptical. M31 would thus have to be a merger product itself. While there is little evidence that M31 has had a recent major merger, perhaps the 'minor merger' of a satellite galaxy with M31 could have excited star formation in the M31 disk (Hernquist & Mihos 1995), generating a population of younger GCs.

Forbes et al. (1997a) suggested that the two populations of GCs in ellipticals formed in two distinct phases separated by several Gyr, with the disk GCs in spirals representing a third collapse phase. The pre-galactic scenario also has two phases, but the difference is that the MP clusters are unrelated to the final galaxy. Either scenario is is compatible with our results, although neither specifically predicts the large age difference we estimate or the relative number of MR and MP clusters. It is interesting that all three scenarios were devised to explain the multiple GC populations of ellipticals, but there is, so far, little evidence for any age-metallicity relation in the GCs of such galaxies. Cohen et al. (1998) found that their samples of MR and MP GCs in M87 are coeval and old (although they suggested that there may be a problem with their model calibration). Puzia et al. (1999) and Kissler-Patig et al. (1998) found similar results for NGC 4472 and NGC 1399, respectively.

2) Is the mass of M31 GCs somehow related to their metallicity? Massive clusters could have their metallicity increased by self-enrichment, and self-enriched GCs must be massive enough to survive disruption by supernova explosions. Morgan & Lake (1989) give a minimum mass for surviving GCs of $10^{4.6}$ $M_{\odot}$, low enough to include almost all Galactic and M31 GCs. They state that "it is difficult to 'predict' any trend of metallicity with mass without extra information on the IMF", but it seems logical that more massive clusters would generate a larger first generation of stars and hence have more enrichment. If self-enrichment occurred in Galactic GCs, it had to be rapid enough to produce the chemical homogeneity observed in most clusters (e.g. Suntzeff 1993). Parmentier et al. (1999) claim that, contrary to previous conclusions, the formation time for the second generation of stars is longer than the mixing timescale; if true, this means that self-enrichment and a mass-metallicity relation are realistic possibilities. Instead of larger masses causing higher metallicity, could higher-metallicity gas induce the formation of more massive GCs? If metallicity is important in GC formation, the opposite seems more likely to be true. In models relying on a cooling condition (e.g. Murray & Lin 1992), MR clusters are predicted to be less massive (for the same IMF) because cooling is more efficient in high-metallicity clouds. An age-metallicity relation with

a small mass-metallicity contribution from self-enrichment is our preferred scenario for explaining the GCLF differences between MR and MP GCs in M31.

3) The possible explanations for younger inner clusters are similar to those for younger metal-rich clusters. The inner clusters could 'naturally' have formed much later than the outer clusters (during the end of the galaxy collapse phase?), or perhaps some external event caused the formation of inner GCs much later than the bulk of the population. Another possibility is that the inner clusters were accreted along with dwarf galaxies cannibalized by M31, although there is no obvious reason why dwarf galaxy GCs should be younger than those in larger galaxies. All of these scenarios are rather *ad hoc* and none are obviously related to theoretical ideas for globular cluster system formation. We do not consider any to be well-supported.

4) Globular cluster mass and galactocentric distance might be causally connected in either direction. Low-mass clusters are thought to be more easily destroyed near the galaxy center, leading to a larger average mass. This is is one of the major predictions of models of GC destruction. Although model predictions vary widely, at least some models (e.g. Ostriker & Gnedin 1997) predict values for the GCLF difference close to what we observe. We do not measure the model-predicted difference in GCLF dispersion, but this may not be a serious problem. Could conditions near the galaxy center affect the average GC mass at formation? In the Murray & Lin (1992) GC formation scenario, GC mass is expected to *increase* with galactocentric distance, and we are aware of no models which explicitly predict a decrease in mean GC mass with distance. GC destruction by dynamical effects in the inner part of M31 is our preferred scenario for explaining the GCLF differences between inner and outer GCs in M31.

4.5 Conclusions

We have calculated the first $URJK$ GCLFs for M31 halo globular clusters, and find that the GCLF peak colors are consistent with the average cluster colors. Our parameters for the V- and B-band halo GCLFs are consistent with those of other groups. We find no significant differences between the disk and halo GCLF peaks, although the disk GCLF has a lower dispersion. A difference in GCLF peak at the 2σ level occurs when we consider the inner and outer-most groups, as determined by projected galactocentric distance. This difference is consistent with that predicted by Ostriker & Gnedin (1997) for M31; however, we do not detect the predicted difference in GCLF dispersion. We separate the M31 clusters by metallicity and find that the metal-rich clusters have a brighter GCLF peak than the metal-poor

clusters, even when the difference in R_{gc} is taken into account. Modeling of the catalog selection effects suggests that they are not responsible for the measured GCLF differences. However, an M31 GC catalog with well-understood and spatially uniform completeness and contamination is required in order to definitively confirm our results. Such a catalog might be produced by a near-IR, high spatial resolution survey of M31. We consider the implications of the GCLF differences for models of globular cluster and GCS formation, and conclude that younger ages for metal-rich clusters plus dynamical destruction of inner clusters are the most likely causes of the observed GCLF variations. Our results also provide evidence against several models for GC formation: the model of Murray & Lin (1992) predicts that GC mass increases with R_{gc}, and the model of Fall & Rees (1985) predicts that GC mass decreases with metallicity. Both effects are the opposite of what we observe.

Chapter 5

Structural parameters of M31 globular clusters

5.1 Introduction

Globular clusters (GCs) are among the oldest surviving stellar objects in the universe. They provide collections of Population II stars with homogeneous abundances and histories, and unique stellar dynamical conditions. The Milky Way's globular cluster system (GCS) is, of course, the prototypical one, and its study has contributed much to our knowledge of stellar evolution and galactic structure. It is important to make sure that conclusions drawn from this study are not biased either because the Milky Way's GCS is somehow unusual or because our location in the Galaxy prevents us from fully characterizing its properties.

Globular clusters in Local Group galaxies are particularly valuable for comparison with Milky Way globular clusters. They are distant enough that their integrated properties can be easily derived, but near enough that their individual stars can also be resolved. Local Group globulars therefore provide an important bridge between the study of Milky Way globulars and those in more distant galaxies. M31 has the Local Group's largest globular cluster population, so it is a natural starting place for studies of extragalactic globular clusters. The M31 GCS is known to be similar to the Milky Way's in numerous ways (e.g., metallicity and spatial distributions; see Chapter 2), but has some important differences as well

*Based on observations made with the NASA/ESA Hubble Space Telescope, obtained from the data archive at Space Telescope Science Institute. STScI is operated by the Association of Universities for Research in Astronomy, Inc. under NASA contract NAS 5-26555.

(chemical composition and possibly age and luminosity distribution: Brodie & Huchra 1991, and Chapter 4). While many properties of the M31 globular clusters can be elicited with ground-based imaging and spectroscopy, the high spatial resolution of space-based studies allow the derivation of a much clearer picture their spatial structure and stellar populations.

The high angular resolution of the Hubble Space Telescope's WFPC2 camera ($0.1''$= 0.38 pc at the distance modulus of M31 given by Stanek & Garnavich (1998) and Holland (1998), $(m - M)_0 = 24.47$) is ideal for the identification of globular clusters in M31. The differences between globular clusters and objects which contaminate cluster candidate lists (foreground stars, background galaxies, and H II regions) are much more obvious than with ground-based imaging. HST imaging is also important for the accurate measurement of structural parameters in M31 clusters, since their sizes are comparable to that of ground-based seeing disks. [Schweizer (1979, 1981) showed that seeing can lead to substantial errors in the derived structural parameters of galaxies with similar sizes.] The goal of most targeted HST observations of M31 globular clusters has been the production of color-magnitude diagrams for the clusters and the surrounding stellar population. HST programs which specifically targeted M31 globular clusters include GOs 5112, 5420, 5464, 5907, 6477, 6671, 7826, 8296, and 8664. Our study uses the publicly-available archival data from these programs and many others.

M31 has been a popular target for HST: as of 1 December 2000, the Hubble Data Archive contained almost 1100 WFPC2 images within $150'$ of the center of the galaxy. As of the same date, about two dozen M31 globular clusters had been specifically targeted for observation with HST, and the images of these clusters comprise about 20% of all the M31 images. We began a project to search for globular clusters in archival HST images for the purpose of quantifying the incompleteness of existing cluster catalogs; preliminary results were described in Chapter 4. The present paper has two goals: to report the results of our efforts to find globular and other star clusters in archival HST/WFPC2 images and their implications for catalog completeness and contamination, and to present measurements of the structural parameters of the clusters and their implications. We do not attempt to construct CMDs for the clusters, since much of this work is already being carried out by other groups.

The history of globular cluster catalogs in M31 begins with Hubble (1932), and continues through Seyfert & Nassau (1945) to Vetešnik (1962a), Sargent et al. (1977), and Crampton et al. (1985). The most comprehensive recent catalog is that of Battistini et al. (1987); more recent works by Battistini et al. (1993) and Mochejska et al. (1998) cover only portions of M31. All of these catalogs contain

objects which are not M31 globular clusters: for example, Table 2 of Chapter 2 lists 199 cluster candidates later shown to be non-clusters. The existing catalogs are also likely to be missing clusters due to magnitude, spatial coverage, and/or resolution limits. Battistini et al. (1993) defined several samples of M31 globular clusters, including a 'confirmed' sample (199 objects), an 'adopted best' sample (298 objects), and an 'extended' sample (356 objects). In Chapter 2 we compiled a list of clusters and plausible candidates containing 435 objects.

Quantifying the extent of incompleteness and contamination in M31 globular cluster catalogs is extremely important for the interpretation of globular cluster system properties. For example, the spatial distribution of clusters is flatter, and the GCLF brighter, near the nucleus (Battistini et al. 1993, and Chapter 4) — is this because the clusters there are truly fewer and brighter, or because existing surveys have not detected the entire cluster population? Even the census of Milky Way clusters is likely to be incomplete: Minniti (1995) estimates that 10–30 Milky Way globulars may be hidden behind the Galactic bulge (two such clusters were found by Hurt et al. 2000), and therefore missing from current catalogs, which list about 150 objects (Harris 1996). It is not unreasonable to suspect that the M31 cluster catalogs could be incomplete by at least a similar fraction.

Ground-based high-resolution imaging and spectroscopy have been used to distinguish M31 globular clusters from interlopers such as foreground stars, background galaxies, and other objects belonging to M31 (e.g., H II regions and open clusters). The bright ($V \lesssim 17$) portion of M31 globular cluster catalogs has been fairly thoroughly examined using one or both of these methods. Racine (1991) and Racine & Harris (1992) used short-exposure CCD images taken in excellent seeing to determine if cluster candidates in the M31 halo were resolved into stars; they found that majority of the halo cluster candidates were background galaxies, not clusters. Radial velocities from optical spectroscopy have also been used by several groups (e.g., Huchra et al. 1982; Federici et al. 1990; Huchra et al. 1991; Federici et al. 1993, and Chapter 2) to eliminate background galaxies and foreground stars from cluster candidate lists. Neither method is infallible, however: compact clusters may be mistaken for background galaxies if not resolved into stars, or for stars if they have a small radial velocity.[1] HST imaging, with its superior spatial resolution, is a useful tool for removing some of the ambiguities inherent in the ground-based studies.

[1]Recall that M31 has a heliocentric radial velocity $v_r = -300$ km s^{-1}. The velocity range of M31 globular clusters is +70 to −700 km s^{-1}, and the Galactic models of Ratnatunga, Casertano, & Bahcall (1989) predict that the radial velocities of Milky Way stars with similar colors and magnitudes to M31 globulars are in the range −400 to +100 km s^{-1}.

HST imaging is vital for the measurement of internal structural parameters of M31 GCs. The clusters' structure yields important information about their dynamical state and also about the environmental effects of M31's tidal field. The core radii and ellipticities of Galactic globulars are known to vary with position (van den Bergh 1994; White & Shawl 1987), and the mean structural parameters of clusters also vary between, for example, the Milky Way and the LMC (van den Bergh 1993). These findings have led to many suggestions and theories about the histories of GCSs and their parent galaxies (e.g., van den Bergh 2000), but these conclusions would be much stronger if structural parameters were accurately measured for clusters in more galaxies. The history of M31 GC structural measurements (a thorough summary is given by Holland, Fahlman, & Richer 1997) shows that ground-based measurements of cluster sizes (e.g., Battistini et al. 1982; Crampton et al. 1985; Bendinelli et al. 1990) can be severely affected by seeing and other instrumental effects. Measurements of cluster ellipticities (e.g. Lupton 1989; Davoust & Prugniel 1990; D'Onofrio et al. 1994; Staneva et al. 1996) are also affected by seeing, guiding, and the shape of the point spread function, and there have been suggestions that some measurements are unreliable (see D'Onofrio et al. 1994). The first HST measurements (Bendinelli et al. 1993; Fusi Pecci et al. 1994) showed that the ground-based measurements of core and half-light radii were systematically overestimated. Post-repair HST measurements of M31 GC parameters (Rich et al. 1996; Grillmair et al. 1996; Holland et al. 1997) have so far included only seven objects in total. The much larger sample of the present work will be useful for understanding correlations of structural parameters with other properties such as galactocentric distance, and for determining mean structural properties for comparison with other galaxies.

5.2 Searching the HST archive

5.2.1 Method

We searched the HST Archive for all WPFC2 observations with the following properties:

- center of field within $< 150'$ of the center of M31
- broadband filter with central wavelength 300 nm or longer
- total exposure time longer than 100 s.

Many images met these requirements, but since most positions had observations in more than one filter (usually with more than one observation per filter), the images comprised only 157 separate fields. Some of these fields were known to contain M31 globular clusters; we retained these fields in our search as a check on our ability to identify clusters. We searched the images in only one filter per field. If more than one filter was available, we chose filters in the following order: F555W, F814W, F606W, F450W, F439W, F336W, F300W. (This ordering reflects the distribution of the filters combined with our desire to examine as many fields as possible in the same filter.) Information on the fields searched, including dataset name, location, filter, and exposure time is given in Table 5.1. The images searched are mostly in F555W and F814W, although there is at least one image in each of the filters listed above. The exposure times ranged from 100 to 8400 s. Figure 5.1 shows the location of all fields on the sky.

We retrieved the images from either the Space Telescope Science Institute or the Canadian Astronomy Data Centre. In both cases the images were pipeline-processed from the raw data at the time of retrieval with the best available calibration images. From STScI we retrieved single images; when multiple images existed for a single field (e.g., in the case of 'cosmic ray-split' images), we combined the images using the IRAF task CRREJ. From CADC we retrieved 'WFPC2 associations', the coadded images produced from multiple CR-split images. In this case the images were combined in the CADC pipeline using the GCOMBINE task. There were no obvious differences in the images producing using the two methods — we used both since we became aware of availability of association images from the CADC part way into the project.

Table 5.1. HST fields used in the search

RA(2000)	Dec (2000)	filter	exposure	dataset name
00 32 36.21	+39 27 43.4	F606W	1400	U4K2OI01R
00 32 36.62	+39 27 42.0	F606W	1500	U4K2OI02R
00 32 49.01	+39 35 00.4	F555W	1600	U2E20709T
00 34 13.68	+39 23 26.5	F814W	2800	U2TA0501T
00 34 13.26	+39 23 48.4	F555W	600	U4490401R
00 34 13.46	+39 24 40.5	F702W	600	U27L0501T
00 36 59.20	+39 52 21.3	F555W	800	U4710201M
00 37 43.08	+39 58 00.6	F336W	200	U4F50907R
00 37 49.14	+40 06 29.2	F555W	600	U2782X01T
00 37 58.50	+39 58 32.8	F606W	2100	U67FFP01R
00 38 32.54	+41 28 45.4	F555W	830	U39I0104T
00 38 55.51	+40 20 41.1	F606W	800	U2804I01T
00 39 32.23	+40 30 48.1	F555W	5300	U4CA0701R
00 39 47.35	+40 31 58.0	F555W	1200	U5BJ0101R
00 39 53.99	+41 47 19.2	F555W	2600	U3KL1004R
00 40 01.58	+40 34 14.8	F555W	1200	U5BJ0201R
00 40 10.11	+40 46 08.9	F814W	200	U4WOAH05R
00 40 14.10	+40 37 11.4	F555W	160	U2YE0703T
00 40 14.86	+40 49 02.8	F814W	200	U4WOC605R
00 40 15.76	+40 36 48.1	F300W	1200	U2M80C01T
00 40 22.15	+41 41 38.4	F336W	400	U2GH020CT
00 40 23.16	+41 40 55.6	F555W	2600	U3KL0704M
00 40 23.66	+41 41 55.2	F555W	2600	U3KL0804R
00 40 23.77	+41 41 40.8	F555W	100	U2EE0506T
00 40 25.50	+41 42 25.7	F555W	2600	U3KL0904R
00 40 26.84	+41 27 27.3	F555W	2000	U2830103T
00 40 29.18	+41 36 31.9	F814W	5400	U3KL0501M
00 40 29.40	+40 43 58.3	F814W	400	U2AB0103T
00 40 30.61	+40 44 50.5	F336W	400	U4F51107R
00 40 31.26	+40 42 59.6	F336W	400	U4F51007R
00 40 33.17	+40 45 39.0	F606W	350	U2G20701T
00 40 33.81	+41 39 40.2	F555W	2600	U3KL0604M

Table 5.1—Continued

RA(2000)	Dec (2000)	filter	exposure	dataset name
00 40 34.22	+41 22 06.5	F555W	5300	U4CA0201R
00 40 39.54	+40 33 25.5	F555W	520	U34L6903R
00 40 39.75	+40 53 24.0	F555W	300	U2G20E03T
00 40 46.06	+39 35 01.0	F814W	130	U4WOAU05R
00 40 50.80	+40 41 16.7	F555W	400	U2Q00101T
00 40 56.68	+40 35 29.0	F555W	5300	U4CA0101R
00 40 59.08	+40 46 42.1	F606W	1050	U581OL01R
00 40 59.54	+41 03 38.4	F439W	800	U2TR0804T
00 41 16.28	+40 56 12.6	F555W	5300	U4CA0301R
00 41 17.85	+41 09 00.7	F814W	3700	U2OT0O01T
00 41 22.08	+40 37 06.7	F555W	1200	U5BJ0301R
00 41 38.85	+39 35 39.8	F814W	130	U4WOBK05R
00 41 42.21	+40 12 22.4	F814W	2000	U2830201T
00 41 43.30	+41 34 20.4	F555W	2000	U2830303T
00 41 53.85	+40 50 30.2	F814W	1200	U2806A02T
00 41 55.58	+40 47 15.0	F555W	5300	U4CA0601R
00 42 05.02	+41 12 14.9	F300W	2300	U2OU7501T
00 42 05.27	+40 57 33.9	F555W	520	U34L7003R
00 42 06.07	+41 07 55.5	F814W	6200	U3B83Y01T
00 42 14.14	+41 10 22.6	F606W	160	U2OURQ01T
00 42 14.36	+41 06 24.7	F606W	1800	U581R201R
00 42 14.40	+41 10 11.7	F555W	8400	U3D90207T
00 42 18.01	+40 45 03.7	F555W	900	U3DG0107T
00 42 27.21	+41 08 28.0	F300W	1600	U2OUUT01T
00 42 28.88	+41 03 05.2	F606W	800	U4K2RG01R
00 42 31.00	+41 10 12.2	F814W	400	U4WO9N05R
00 42 32.47	+41 13 39.5	F555W	5200	U2Y30204T
00 42 32.70	+40 33 55.5	F555W	1200	U3YK0101R
00 42 35.13	+41 10 35.1	F555W	5200	U2Y30305T
00 42 38.97	+41 15 29.2	F555W	1680	U2KJ0109T
00 42 39.28	+40 51 42.2	F814W	600	U2E20401T
00 42 39.49	+40 51 46.9	F555W	104	U2LG0101T

Table 5.1—Continued

RA(2000)	Dec (2000)	filter	exposure	dataset name
00 42 39.88	+41 10 48.9	F814W	400	U42Z2302R
00 42 40.85	+41 15 51.2	F555W	2500	U5LT0104R
00 42 40.96	+40 51 07.3	F555W	110	U2EE0405T
00 42 41.68	+40 51 04.3	F555W	2000	U2880704T
00 42 41.74	+41 15 57.9	F814W	600	U2E20201T
00 42 42.21	+40 52 22.4	F555W	1200	U2E20307T
00 42 44.64	+41 16 39.2	F555W	1680	U2E2010BT
00 42 46.91	+41 16 15.9	F555W	2200	U2LG0201T
00 42 47.63	+41 16 11.0	F336W	460	U2LH0103T
00 42 50.04	+41 36 17.8	F814W	700	U4WOC805R
00 42 50.15	+40 59 56.0	F814W	8000	U2OQ3201T
00 42 50.34	+41 17 54.4	F814W	7000	U2OQF801T
00 42 51.45	+41 06 52.9	F814W	400	U4WOA305R
00 42 52.07	+41 24 53.4	F814W	6700	U2OQF301T
00 42 52.26	+41 08 06.8	F814W	4500	U26KCZ01T
00 42 52.37	+41 10 31.7	F814W	400	U42Z3402R
00 42 52.73	+40 56 30.4	F814W	2000	U4XI0101R
00 42 53.03	+41 14 23.4	F814W	400	U42Z1102R
00 42 54.11	+41 08 08.9	F814W	800	U4WOA205R
00 42 54.87	+41 10 35.0	F814W	700	U4WOBC05R
00 42 58.84	+40 50 34.3	F814W	4400	U3VJ0103R
00 43 00.93	+41 13 17.7	F300W	2600	U31K0109T
00 43 01.94	+41 19 19.9	F555W	5200	U38K0103T
00 43 04.61	+40 54 33.0	F555W	2000	U2880801T
00 43 05.28	+40 50 37.8	F300W	5400	U27H0F01T
00 43 05.38	+40 56 40.4	F606W	350	U4G40104R
00 43 06.12	+41 12 59.7	F555W	2000	U5850103R
00 43 06.14	+41 13 00.0	F555W	2000	U5850107R
00 43 06.19	+40 56 52.0	F606W	350	U4G40103R
00 43 06.40	+40 56 31.2	F814W	350	U4G40101R
00 43 07.21	+40 56 42.8	F814W	260	U4G40102R
00 43 07.85	+40 53 32.8	F814W	1100	U4C80403R

Table 5.1—Continued

RA(2000)	Dec (2000)	filter	exposure	dataset name
00 43 08.59	+41 14 51.7	F300W	8400	U27H0E01T
00 43 09.06	+40 51 18.6	F814W	1000	U4WOBJ05R
00 43 12.49	+41 02 02.7	F606W	350	U4G40204R
00 43 12.82	+41 02 17.0	F606W	350	U4G40203R
00 43 13.76	+41 01 59.0	F814W	350	U4G40201R
00 43 14.09	+41 02 13.3	F814W	260	U4G40202R
00 43 18.05	+39 49 13.1	F814W	2000	U2830401T
00 43 20.30	+41 05 36.2	F814W	400	U42Z1202R
00 43 20.80	+41 06 14.5	F814W	300	U42Z4602R
00 43 22.39	+41 13 53.8	F814W	1500	U2OT0S01T
00 43 25.28	+41 04 02.2	F814W	4400	U3VJ0203R
00 43 36.72	+41 26 15.4	F555W	350	U2KW0601T
00 43 43.26	+41 00 32.4	F814W	400	U4WOA105R
00 43 46.58	+41 11 14.7	F814W	300	U42Z5702R
00 43 47.85	+41 11 00.6	F814W	300	U42Z5802R
00 43 54.55	+41 24 10.8	F300W	600	U2M80G01T
00 43 57.06	+41 25 33.4	F300W	600	U2M80H01T
00 44 14.38	+41 20 45.2	F336W	400	U4F51207R
00 44 23.45	+41 20 40.8	F336W	320	U4F51307R
00 44 23.74	+41 45 16.3	F555W	800	U4710101M
00 44 34.81	+41 38 38.4	F336W	800	U5750101R
00 44 35.25	+41 31 21.6	F814W	500	U4WOBH08R
00 44 36.29	+41 35 05.6	F814W	500	U4WOBS05R
00 44 42.45	+41 44 24.2	F555W	5300	U4CA0401M
00 44 42.52	+41 44 24.1	F555W	5300	U4CA0501R
00 44 42.59	+41 14 30.3	F814W	500	U4WOA005R
00 44 44.23	+41 27 33.9	F555W	140	U2Y20106T
00 44 46.19	+41 51 33.4	F555W	1200	U5BJ0401R
00 44 49.34	+41 28 59.0	F555W	140	U2Y20206T
00 44 50.61	+41 19 11.1	F555W	3800	U2GV0401T
00 44 51.22	+41 30 03.7	F555W	160	U2YE0603T
00 44 57.63	+41 30 51.7	F555W	140	U2Y20306T

Table 5.1—Continued

RA(2000)	Dec (2000)	filter	exposure	dataset name
00 45 00.36	+41 31 55.1	F300W	600	U2M80A01T
00 45 03.79	+41 31 09.6	F300W	600	U2M80E01T
00 45 05.66	+41 38 00.4	F336W	320	U4F51407R
00 45 07.76	+41 36 46.8	F336W	280	U4F51507R
00 45 09.25	+41 34 30.7	F555W	140	U2Y20406T
00 45 11.95	+41 36 57.0	F555W	140	U2Y20506T
00 45 28.46	+41 05 53.9	F555W	4320	U2UG010AT
00 45 36.98	+41 42 17.3	F606W	2300	U5HNM301R
00 45 38.15	+41 36 02.4	F300W	650	U4WOBG0ER
00 45 39.00	+41 36 36.3	F814W	580	U4WOBG09R
00 45 39.25	+41 36 32.4	F606W	1140	U4WOBG01R
00 46 01.64	+40 41 58.3	F555W	4320	U2UG020AT
00 46 20.46	+40 16 34.1	F555W	5300	U4CA0801R
00 46 24.33	+42 07 01.7	F814W	350	U4WOC905R
00 46 24.56	+42 01 38.7	F555W	5300	U4CA0901R
00 46 29.85	+42 04 50.4	F336W	320	U4F51707R
00 48 15.15	+40 26 31.0	F606W	1000	U36Z7801R
00 48 21.29	+40 29 02.4	F606W	1000	U36Z8401R
00 48 42.83	+40 24 47.2	F606W	1000	U36Z7701R
00 48 44.22	+40 33 06.0	F606W	1000	U36Z8201R
00 49 08.22	+40 30 33.9	F606W	1000	U36Z8301R
00 49 13.48	+40 21 51.1	F606W	1000	U36Z8001R
00 49 18.35	+40 30 12.0	F606W	1000	U36Z8501R
00 49 28.48	+40 21 54.4	F606W	1000	U36Z8101R
00 49 31.26	+40 27 57.9	F606W	1000	U36Z8601R
00 50 06.13	+41 33 56.0	F606W	2100	U67FGY01R

Note. — 'Exposure' is the combined exposure time, in seconds, of all images in the specified filter and position.

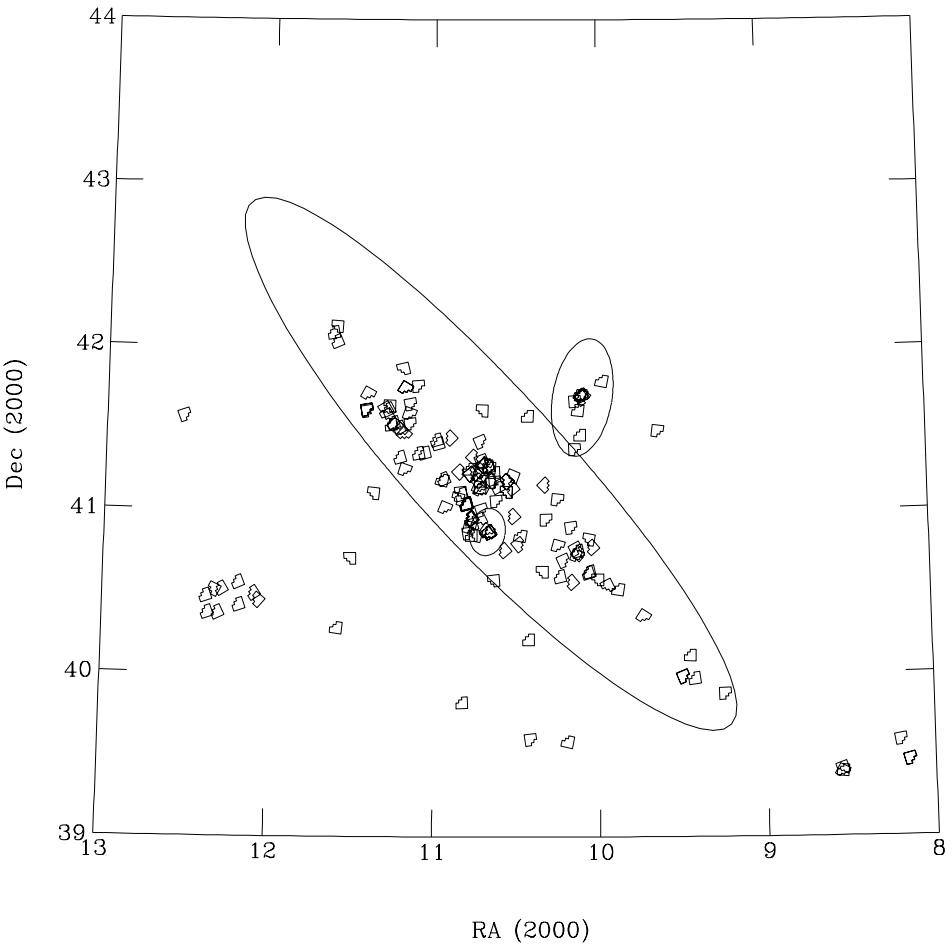

Fig. 5.1.— Location and orientation of M31 HST fields. Large ellipse is M31 disk/halo boundary as defined by Racine (1991); smaller ellipses are D_{25} isophotes of NGC 205 (NW) and M32 (SE). The symbols are drawn about 1.5× actual size to make them easier to see. The group of fields at $\alpha \sim 12°$, $\delta \sim 40.5°$ is part of a snapshot survey of field galaxies (GO-6354).

Once the images were processed, we began the search for star clusters. The first step was carried out 'blind', that is, without any knowledge of the positions of cataloged clusters. Working independently, each of us visually examined each image. PB used SExtractor (Bertin & Arnouts 1996) to automatically identify objects with large areas and/or extended profiles, then visually checked the SExtractor candidates (many of these were actually bright stars) and searched for additional candidates. JH used only visual examination. An important feature of the globular cluster images which allowed us to distinguish them from stars was the absence of diffraction spikes.

We combined the two lists of cluster candidates to make a final list; for objects where we disagreed on the classification (about 10% of the total), we re-examined the images together to make a final decision. Although we were interested primarily in globular clusters, we recorded positions of objects likely to be open clusters as well. Following previous authors (e.g., Battistini et al. 1987; Mochejska et al. 1998), we classified our globulars in classes A through D, where A is 'very likely to be a globular cluster' and D is 'likely not a globular cluster'. We refer to objects in classes A and B as good candidates, and objects in classes C and D as marginal cluster candidates. After generating our final list of cluster candidates, we checked our image positions against existing catalogs of M31 globular clusters. This allowed us to gauge our detection efficiency and locate objects we would otherwise have missed. The globular cluster list used was a 'master list' of globular clusters and candidates, produced by combining the lists of Sargent et al. (1977), Crampton et al. (1985), Battistini et al. (1987), Battistini et al. (1993), and Mochejska et al. (1998); it includes all the objects listed in the Chapter 2 catalog, plus additional low-probability candidates and non-clusters.

5.2.2 Results

Globular clusters

We consider the low and high-probability globular clusters separately. 'High probability' are clusters A or B class clusters from Battistini et al. (1987), Battistini et al. (1993), or Mochejska et al. (1998); all other objects are 'low probability'. Racine (1991) showed that the Battistini et al. (1987) classification correlates well with the probability that a candidate will be subsequently shown to be a cluster. 75 high-probability clusters from our master list were located in the HST fields; we detected 71. Three of the four non-detections were objects which did not appear to be globular clusters (138–000, 166–000, and 133–191); for the fourth object,

DAO040, we did not detect any object at the coordinates given by Crampton et al. (1985). Of the 64 low-probability (class C or D) cluster candidates in our HST fields, we found 7 good candidates (000–D038, 000–M91, 020D–089, 097D–000, 132-000, 264–NB19, and NB39), 4 marginal candidates (000–M045, 257–000, NB41 and NB86), and 39 objects which did not appear to be clusters. We did not detect the other 14 objects in our visual search. On re-examining the positions of these objects, we found that none were good or even marginal cluster candidates. Several were clearly stars, and the others were blends of stars or blank fields. We show a selection of images of previously-cataloged clusters in Figure 5.2.

Uncataloged globular clusters

Our visual search of the HST fields produced 32 objects not included in any cluster catalog. 10 of these were good candidates, although only about half are as obviously clusters as most of the brighter objects. The good candidates' images are shown in Figure 5.3. The nature of the remaining 22 objects is unclear. They are clearly not stars; all are at least marginally resolved (FWHM $> 0.2''$). However, most are quite faint, and they are not obviously resolved into stars as is the case for most of the globular clusters. They may be blended stars in M31, compact background galaxies, or compact star clusters. We show images of these low-quality objects in Figure 5.4. Table 5.2 gives the location and quality of all the new cluster candidates.

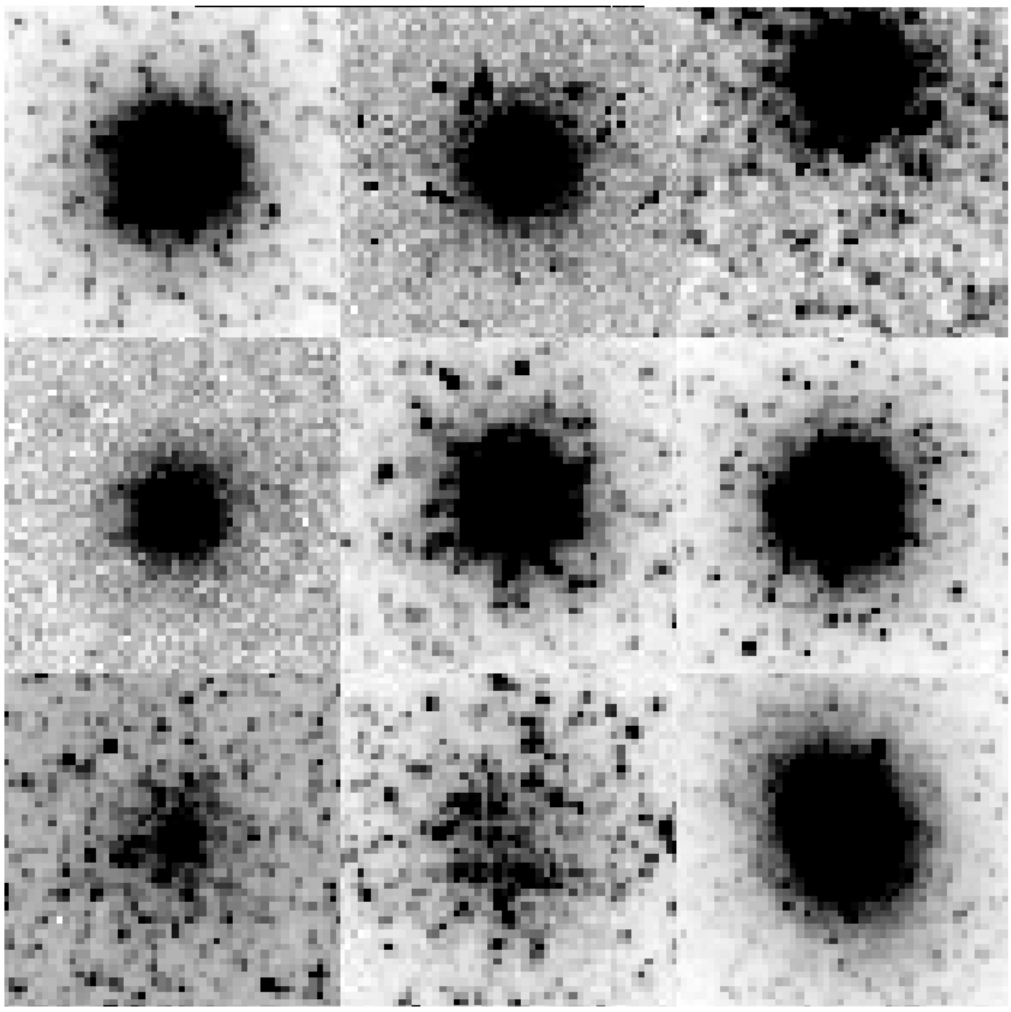

Fig. 5.2.— HST images of M31 globular clusters. In row order, from top left: 006–058, 064–125, 077–138, 146–000, 156–211, 311–033, 331–057, 468–000, 000–001. All images are in filter F555W or F606W except those of 064–125 and 146–000 (in F300W). All images are 5″ square; 077–138 is not centered in its image because it fell near the edge of a WFPC2 chip.

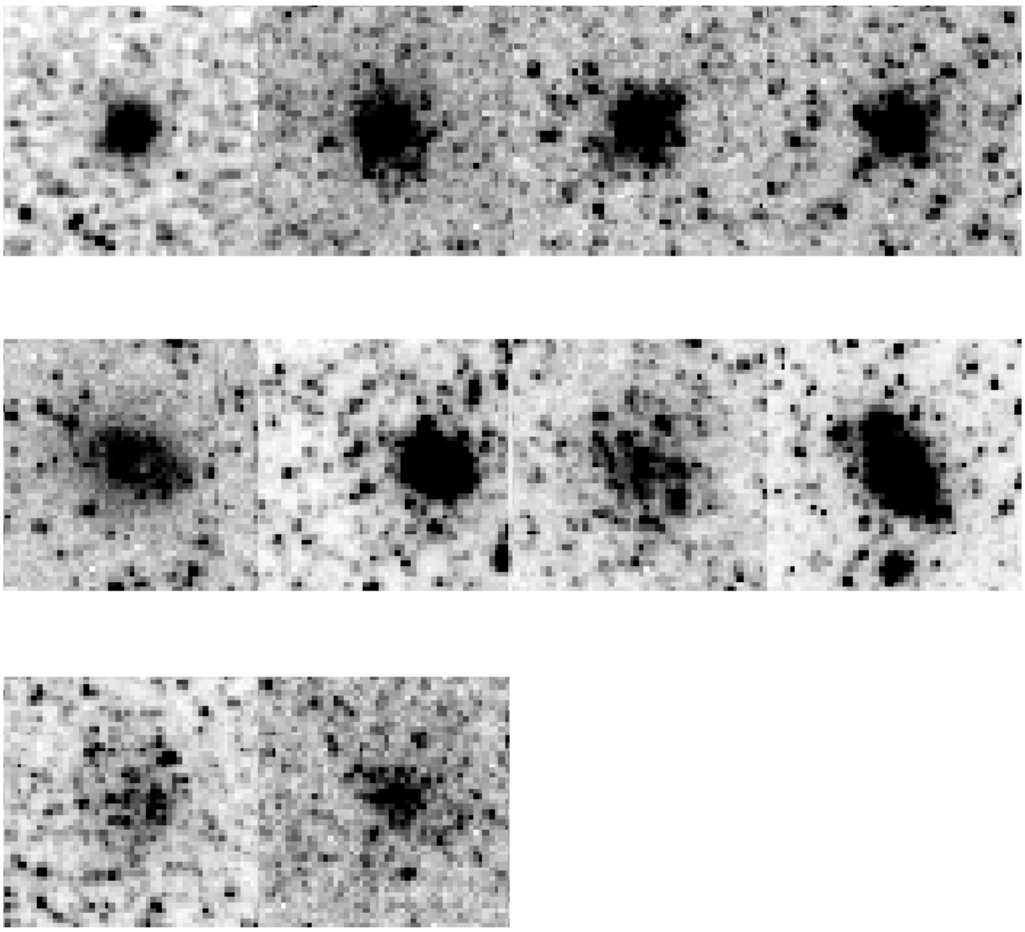

Fig. 5.3.— New globular cluster candidates found in HST images. All images are 5″ square.

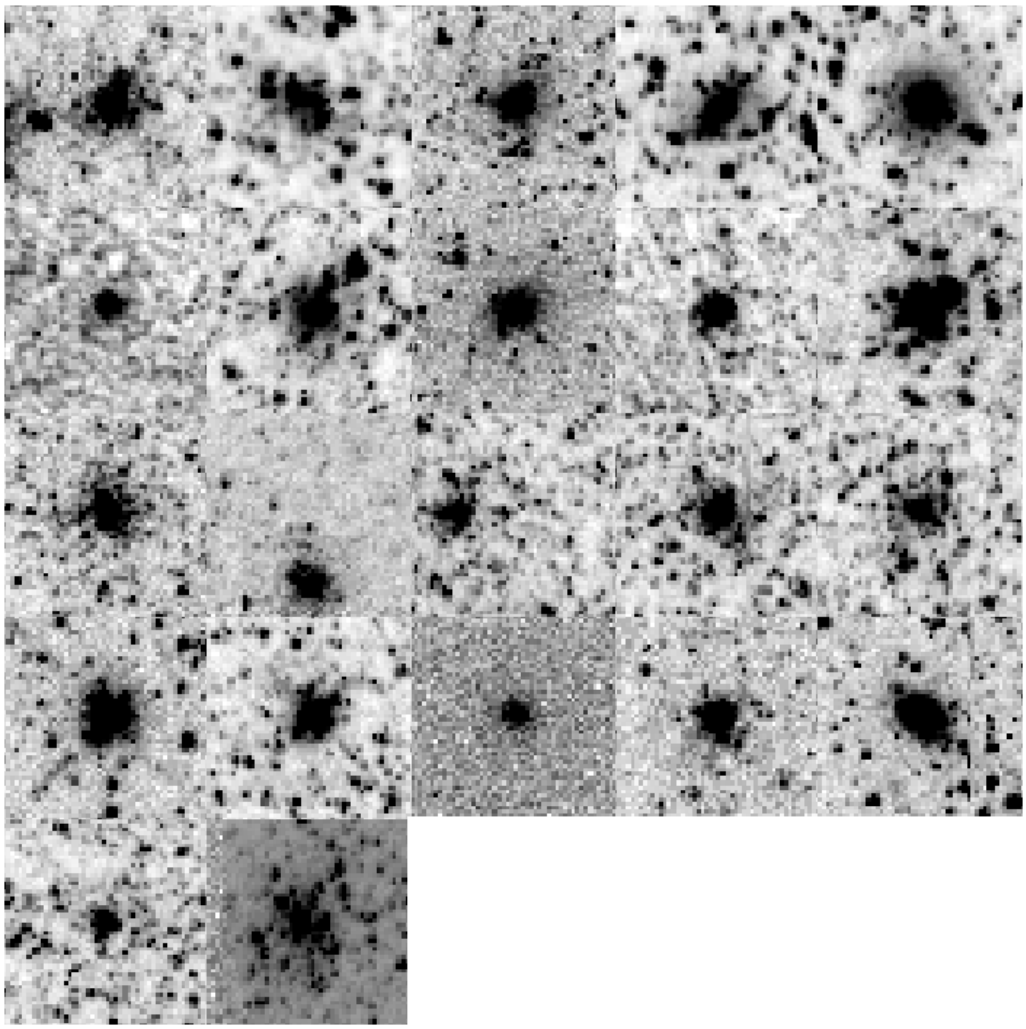

Fig. 5.4.— Marginal objects found in HST images: these objects are non-stellar but not obviously star clusters. All images are 5″ square.

Table 5.2. New globular cluster candidates found in M31 HST fields

name	RA(2000)	Dec (2000)	quality	comments
M31GC J003411+392359	00 34 11.48	39 23 59.1	C/D	···
M31GC J004010+403625	00 40 10.33	40 36 24.7	C/D	···
M31GC J004023+414045	00 40 22.68	41 40 44.5	C	···
M31GC J004027+414225	00 40 27.25	41 42 24.8	B	···
M31GC J004030+404530	00 40 30.46	40 45 29.6	B	···
M31GC J004031+404454	00 40 30.63	40 44 54.3	C	···
M31GC J004031+412627	00 40 30.68	41 26 27.1	C	···
M31GC J004034+413905	00 40 34.42	41 39 04.8	C/D	···
M31GC J004037+403321	00 40 37.15	40 33 21.4	C	···
M31GC J004045+405308	00 40 44.92	40 53 07.6	C	···
M31GC J004051+404039	00 40 50.68	40 40 38.6	B/C	···
M31GC J004103+403458	00 41 02.88	40 34 57.9	B	Hodge 119?
M31GC J004146+413326	00 41 45.57	41 33 26.2	C	···
M31GC J004200+404746	00 42 00.39	40 47 45.8	C	···
M31GC J004228+403330	00 42 27.56	40 33 29.8	C/D	···
M31GC J004246+411737	00 42 46.01	41 17 36.5	C	···
M31GC J004251+405841	00 42 50.80	40 58 40.7	C	···
M31GC J004251+411035	00 42 50.78	41 10 34.7	A	···
M31GC J004257+404916	00 42 57.05	40 49 16.4	C	Hodge 195?
M31GC J004258+405645	00 42 58.02	40 56 45.4	A	···
M31GC J004301+405418	00 43 01.35	40 54 17.5	B	···
M31GC J004304+405129	00 43 04.27	40 51 29.2	C	···
M31GC J004304+412028	00 43 03.75	41 20 28.2	A	···
M31GC J004312+405303	00 43 11.86	40 53 02.8	B	···
M31GC J004312+410249	00 43 11.99	41 02 49.1	C	···
M31GC J004424+414502	00 44 23.71	41 45 02.3	C	X-ray src: SHP278?
M31GC J004425+414529	00 44 25.21	41 45 29.1	C/D	···
M31GC J004439+414426	00 44 39.07	41 44 26.3	C	···
M31GC J004537+413644	00 45 37.25	41 36 44.3	B	···
M31GC J004537+414332	00 45 36.75	41 43 32.2	C	···
M31GC J004622+420631	00 46 21.80	42 06 30.8	C	···
M31GC J004624+420059	00 46 23.50	42 00 58.5	C	···
M31OC J003836+412739	00 38 35.73	41 27 39.3	B	···
M31OC J003941+403154	00 39 40.52	40 31 53.6	C	···
M31OC J003943+403116	00 39 43.21	40 31 15.6	C	···
M31OC J004000+403326	00 39 59.99	40 33 25.9	C	···
M31OC J004008+403507	00 40 07.55	40 35 06.6	B	···
M31OC J004027+404524	00 40 27.26	40 45 23.7	C	···
M31OC J004031+404537	00 40 30.51	40 45 37.4	C	···

Table 5.2—Continued

name	RA(2000)	Dec (2000)	quality	comments
M31OC J004053+403519	00 40 52.94	40 35 19.2	D	···
M31OC J004054+404625	00 40 54.14	40 46 24.7	C	···
M31OC J004057+403425	00 40 56.62	40 34 24.7	C	···
M31OC J004119+403608	00 41 18.69	40 36 08.2	B/C	···
M31OC J004123+403756	00 41 23.30	40 37 56.1	C	···
M31OC J004421+414516	00 44 21.44	41 45 15.9	C	···
M31OC J004442+415122	00 44 41.84	41 51 22.4	C	···
M31OC J004442+415237	00 44 42.25	41 52 36.7	C	···
M31OC J004449+414430	00 44 48.83	41 44 30.3	C/D	···
M31OC J004450+415211	00 44 50.27	41 52 11.1	C	···
M31OC J004510+413646	00 45 10.45	41 36 46.3	C	Hodge 311?
M31OC J004512+413712	00 45 11.81	41 37 11.6	C	H II region, Hodge 313?
M31OC J004539+414220	00 45 38.88	41 42 20.4	C	Radio src MY0042+414?

Open clusters

The dividing line between open and globular clusters is somewhat blurred, even in the Milky Way. In their compilation of data on Milky Way globular clusters, Djorgovski & Meylan (1993) note that several proposed galactic globulars might actually be open clusters. In our search, we noted several concentrated objects which could be M31 open clusters. Their nature is uncertain: they could also be low-concentration globulars, or just chance superpositions of stars. Their images are shown in Figure 5.5. We checked the cluster coordinates against those given in Hodge's (1979) list of M31 open clusters. The coordinates in that catalog have rather low precision (20″ in both right ascension and declination), so we searched for coordinate matches within an error circle of radius 30″. We found 5 matches and attempted to confirm these by comparing the finding charts in Hodge (1982) to our images. The results were inconclusive: either the clusters were not clearly identified on the charts, or the objects were located too close to the edge of the HST image to make a positive identification. We note the possible matches in Table 5.2.

To see if any of newly-proposed globular and open cluster candidates had been previously cataloged as background galaxies, we checked their positions against those of galaxies listed in NED.[2] None of the new clusters matched the position of

[2]The NASA/IPAC Extragalactic Database (NED) is operated by the Jet Propulsion Laboratory, California Institute of Technology, under contract with the National Aeronautics and Space

any galaxy listed in NED, although one is listed as a possible H II region (Strauss et al. 1992) and two others may contain radio and X–ray sources (Zhang et al. 1993; Supper et al. 1997); the matches are also noted in Table 5.2. The matches are uncertain, however, since positional uncertainties for the other surveys are large. Figure 5.6 shows the positions on the sky of all the M31 clusters, both previously-known and newly-discovered. The open cluster near NGC 205 is well outside the disk and is probably not a real cluster.

5.2.3 Integrated photometry

After the M31 clusters had been identified on the 'search' images, we retrieved images of their fields in other available filters to extract all the possible photometric information from the HST Archive. All but 18 objects had been imaged by WFPC2 in more than one filter. We combined images for cosmic-ray rejection in the same manner used for the search images. Additional processing steps included removing cosmic rays interactively using the IRAF task IMEDIT (this was especially important for non-cosmic-ray-split images) and correcting for warm pixels using the IRAF task COSMICRAYS. While the STSDAS task WARMPIX is the preferred method of dealing with warm pixels, it is slow and requires correction of individual images before they are combined for cosmic ray rejection. Since we had hundreds of individual images to deal with, we chose the more expedient method of treating the warm pixels as if they were as cosmic ray hits on ground-based images. Nearby bright stars and CCD flaws were masked out of the images to prevent contamination of the photometry. A few images were not useful for photometry at all: the globular clusters were either very faint (mostly in the F300W and F336W filters), too close to an image edge, or saturated.

Photometry of extragalactic globular clusters is unfortunately not as simple as photometry of isolated stars or galaxies. There are two key steps in integrated photometry of M31 clusters: measuring the background light, and identifying an appropriate aperture size. The background light consists of two components: unresolved light from the sky and M31, and light from resolved stars in M31 (the latter are a lesser problem in ground-based photometry of M31 GCs since many fewer M31 stars are resolved). Standard background estimators are usually designed to determine the sky background level by rejecting the stars in the background annulus. Since we expect there to be stars overlapping our clusters as well, we estimated the background value for each image as the mean (rather than the more commonly used median or mode) of the pixel values around the image

Administration

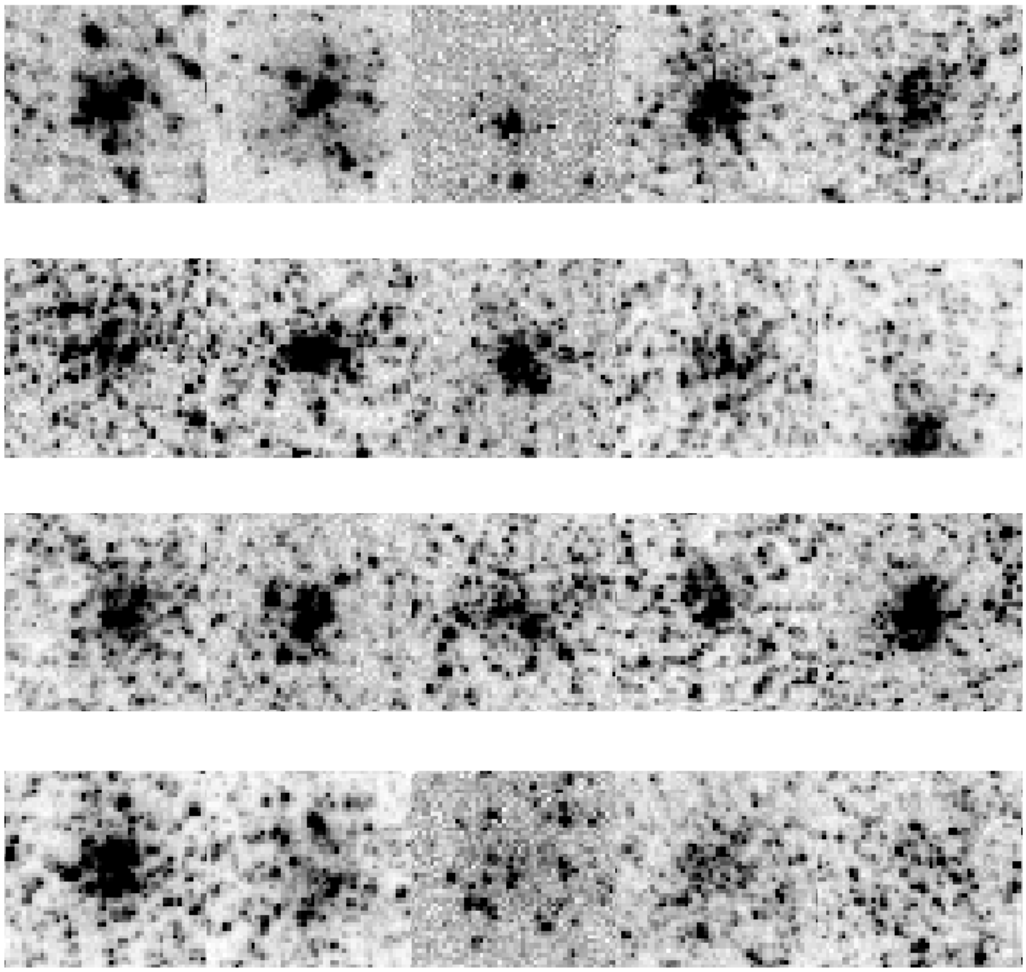

Fig. 5.5.— Possible M31 open clusters found in HST images. All images are 5″ square.

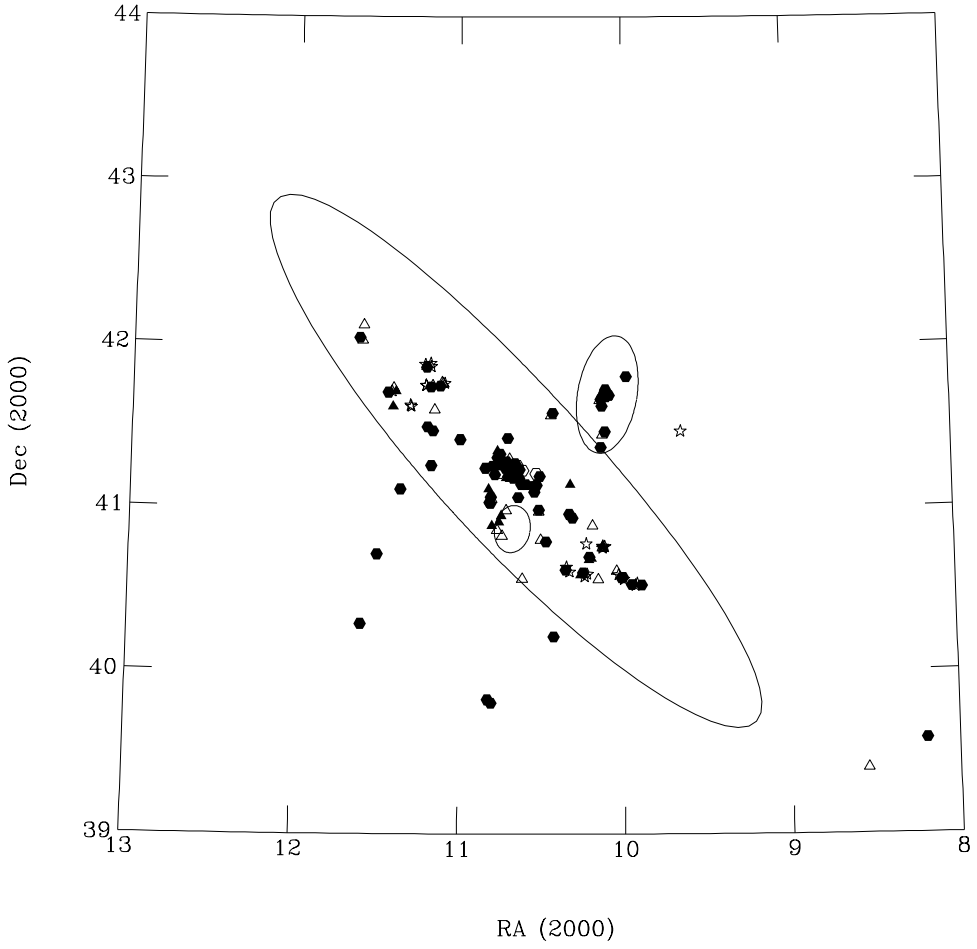

Fig. 5.6.— Position on the sky of all GCs, GC candidates and open clusters. Ellipses are the same as in Figure 1. Filled symbols are good-quality GC candidates; open symbols are marginal candidates. Hexagons are previously-cataloged objects; triangles are newly-discovered objects; stars are open clusters.

edge, and subtracted it from the image before doing photometry.

Determining the 'correct' aperture size to be used for integrated photometry is non-trivial since the clusters are not all the same size. We estimated the total flux for each object by measuring aperture magnitudes in concentric apertures spaced 0.15″ apart, plotting magnitude growth curves, and noting where the flux stopped increasing. Using these measurements of the total flux of each cluster, we determined the half-light radius[3] by interpolating the aperture magnitudes. We calibrated the instrumental magnitudes from the WFPC2 system to the standard system by iteratively solving the equations given in Holtzman et al. (1995), using the charge-transfer-efficiency corrections given by Dolphin (2000). The zero points given by Dolphin (2000) were increased by 0.10 magnitudes to correct them to 'infinite aperture', since we are attempting to measure the total light of the M31 clusters. The iterative solution of the calibration equations requires instrumental magnitudes in at least two filters; for objects with only one instrumental magnitude, we fixed the 'standard color' as either the measured ground-based color from Chapter 2, or if that was unavailable, the average M31 GC color. The results for integrated magnitudes and half-light radii are given in Table 5.3. In Figure 5.7, we compare the new HST photometry to the ground-based measurements compiled in Chapter 2. The agreement is gratifying: the median offset in V is 0.01 ± 0.04 magnitudes, and in I is 0.06 ± 0.04 mag. Most of the large offsets are for objects near the edge of a WFPC2 chip, or whose previous photometry was estimated from photographic plates.

[3]The half-light radius r_h is that which contains half of the integrated cluster light. It should not be confused with the radius at which the surface brightness drops to half of its central value, called variously the core radius r_c, the half-intensity radius, or the half-width at half maximum (HWHM).

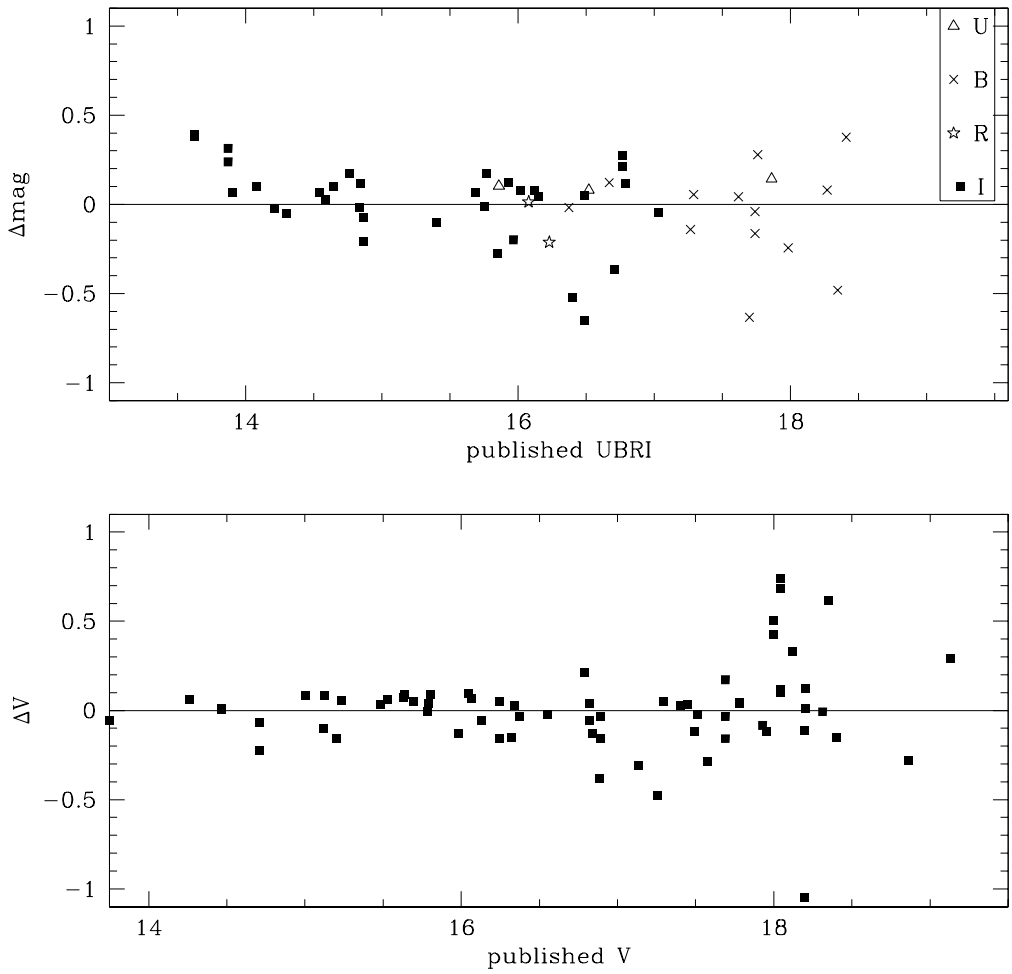

Fig. 5.7.— Comparison of integrated HST photometry to ground-based photometry: vertical axis is (published photometry)–(HST photometry).

Table 5.3. Photometry of new clusters and candidates in M31 HST fields

name	U^{a}	B	V	R	I	$\langle r_{1/2} \rangle$ ($''$)
Cataloged clusters						
000–001	···	···	13.807	···	12.684	0.40
000–D38	···	···	19.247	···	18.276	0.37
000–M045	···	19.391	18.723	···	17.446	1.49
000–M91	···	···	19.143	···	···	0.89
006–058	···	···	15.463	···	14.354	0.38
009–061	···	···	···	···	15.809	0.71
011–063	···	···	16.578	···	15.624	0.31
012–064	···	···	15.042	···	13.979	0.42
018–071	···	···	17.533	···	16.385	1.14
020D–089	···	···	···	···	16.039	0.80
027–087	···	···	15.559	···	14.409	0.41
030–091	···	···	17.377	···	15.593	0.59
045–108	···	···	15.784	···	14.477	0.42
058–119	···	···	14.925	···	13.837	0.36
064–125	17.461*	···	···	···	···	0.69
068–130	···	17.575	16.407	···	14.849	0.68
070–133	···	···	17.262	···	16.165	0.20
071–000	22.716*	···	···	···	···	0.07
076–138	17.720	17.483	16.927	···	15.626	0.53
077–139	···	18.829	17.734	···	16.125	0.42
092–152	18.766*	···	···	···	···	0.41
097D–000	···	···	···	17.878	17.121	1.08
101–164	18.523*	···	···	···	···	0.42
109–170	···	17.407	16.197	···	14.936	0.61
110–172	···	···	15.355	···	···	0.66
114–175	···	···	17.439	···	15.940	0.47
115–177	···	···	15.997	···	14.560	0.25
118–NB6	···	···	16.431	···	15.207	0.52
123–182	···	···	17.416	16.754	16.126	0.58
124–NB10	16.094	···	14.777	···	13.631	0.53
127–185	15.756	···	14.467	···	13.239	0.75

Table 5.3—Continued

name	U^a	B	V	R	I	$\langle r_{1/2} \rangle$ ($''$)
128–187	···	···	···	16.441	15.764	0.41
132–000	···	···	17.739	17.244	16.440	0.34
134–190	···	···	···	16.064	15.502	0.52
143–198	···	···	15.954	···	14.731	0.25
145–000	19.901*	···	···	···	···	0.47
146–000	18.458*	···	···	···	···	0.59
148–200	···	···	16.110	···	···	0.51
153–000	18.220*	···	···	···	···	0.38
155–210	···	···	18.011	···	16.672	0.40
156–211	···	···	16.969	···	15.873	0.64
160–214	···	···	18.076	···	17.075	0.52
167–000	···	···	···	···	16.109	0.33
205–256	16.938*	···	···	···	···	0.32
231–285	···	18.227	17.248	···	···	0.48
232–286	16.440	16.391	15.646	···	14.543	0.66
233–287	···	···	15.718	···	14.585	0.41
234–290	···	17.780	16.783	···	···	0.51
240–302	···	···	15.181	···	14.230	0.80
257–000	···	11.907	20.960	···	16.312	0.65
264–000	18.652*	···	17.577	···	16.811	0.67
268–000	···	···	18.314	···	16.880	0.39
279–D068	···	···	18.549	···	16.964	0.68
311–033	···	···	15.445	···	14.215	0.38
315–038	···	16.548	16.473	···	···	0.56
317–041	···	···	16.573	···	15.713	0.73
318–042	···	17.234	17.047	···	···	0.63
319–044	···	18.333	17.608	···	···	0.41
324–051	···	···	18.446	···	17.633	0.30
328–054	···	···	17.861	···	16.918	0.85
330–056	···	···	17.724	···	16.555	0.56
331–057	···	···	18.191	···	17.076	0.56
333–000	···	···	18.840	···	17.711	0.90

Table 5.3—Continued

name	U^a	B	V	R	I	$\langle r_{1/2} \rangle$ ($''$)
338–076	···	···	14.195	···	13.174	0.56
342–094	···	18.033	17.733	···	···	0.92
343–105	···	···	16.310	···	15.274	0.36
358–219	···	···	15.219	···	14.122	0.55
368–293	···	18.189	17.924	···	···	0.54
374–306	19.128*	···	18.319	···	···	0.68
379–312	···	···	16.183	···	14.936	0.65
384–319	···	···	15.752	···	14.564	0.36
386–322	···	···	15.547	···	14.393	0.36
468–000	···	···	17.788	···	16.626	1.95
NB21	···	···	17.865	···	16.771	0.41
NB39	18.551	···	17.941	···	17.876	0.38
NB41	···	···	18.097	···	17.183	0.43
NB81	···	···	17.025	···	···	0.35
NB83	···	···	17.585	···	16.599	0.25
NB86	···	···	18.522	···	17.446	0.17
NB89	···	···	17.965	···	16.888	0.34
New clusters						
M31GC J003411+392359	···	···	···	22.302	···	4.44
M31GC J004010+403625	···	18.906	18.505	···	···	0.24
M31GC J004023+414045	···	···	18.289	···	16.990	1.08
M31GC J004027+414225	···	···	19.691	···	19.138	0.76
M31GC J004030+404530	···	···	16.064	···	···	0.37
M31GC J004031+404454	···	15.090	22.708	···	20.337	0.29
M31GC J004031+412627	···	···	20.930	···	19.477	0.57
M31GC J004034+413905	···	···	18.666	···	···	7.52
M31GC J004037+403321	···	···	19.773	···	18.773	0.49
M31GC J004051+404039	···	···	19.862	···	18.616	0.73
M31GC J004103+403458	···	···	18.487	···	17.920	0.38
M31GC J004146+413326	···	···	20.716	···	18.826	0.39
M31GC J004200+404746	···	···	20.327	···	19.636	0.45
M31GC J004228+403330	···	···	21.195	···	19.477	0.51

Table 5.3—Continued

name	U^{a}	B	V	R	I	$\langle r_{1/2} \rangle$ ($''$)
M31GC J004246+411737	19.507*	···	18.111	···	17.706	0.43
M31GC J004251+405841	···	···	20.296	···	19.309	0.20
M31GC J004251+411035	···	19.177	18.178	···	16.886	0.21
M31GC J004257+404916	···	···	20.271	···	18.648	1.18
M31GC J004258+405645	···	···	18.066	···	···	0.31
M31GC J004301+405418	···	···	18.613	···	17.290	0.45
M31GC J004304+405129	···	···	19.666	···	18.392	1.12
M31GC J004304+412028	···	···	18.828	···	16.857	0.38
M31GC J004312+405303	···	···	20.670	···	19.150	0.73
M31GC J004312+410249	···	···	18.810	···	18.816	0.52
M31GC J004424+414502	···	···	21.143	···	19.232	0.31
M31GC J004425+414529	···	···	20.597	···	20.580	0.99
M31GC J004439+414426	···	···	19.840	···	18.746	0.67
M31GC J004537+413644	···	20.350	19.648	···	18.724	0.92
M31GC J004537+414332	22.529*	···	19.759	···	···	0.47
M31GC J004622+420631	···	20.085	18.614	···	17.135	2.86
M31GC J004624+420059	···	···	20.445	···	19.188	0.70
M31OC J004539+414220	20.812*	···	20.163	···	···	0.61
M31OC J004027+404524	···	···	18.148	···	18.046	0.55
M31OC J004512+413712	···	18.352	17.466	···	···	0.65
M31OC J003941+403154	···	20.398	20.002	···	···	0.68
M31OC J004123+403756	···	21.752	19.965	···	···	0.78
M31OC J004442+415122	···	19.788	19.533	···	···	1.08
M31OC J004442+415237	···	19.997	19.812	···	···	0.50
M31OC J004450+415211	···	20.599	20.439	···	···	0.40
M31OC J004449+414430	···	···	20.229	···	19.455	0.75
M31OC J004054+404625	···	23.432	22.082	···	21.504	0.18
M31OC J003943+403116	···	20.854	21.014	···	···	0.45
M31OC J004000+403326	···	19.232	19.006	···	···	1.09
M31OC J004031+404537	···	···	17.806	···	···	4.75
M31OC J004057+403425	···	···	18.756	···	18.675	0.86
M31OC J004053+403519	···	···	18.579	···	18.634	0.99

Table 5.3—Continued

name	U[a]	B	V	R	I	$\langle r_{1/2} \rangle$ ($''$)
M31OC J003836+412739	···	···	20.406	···	···	1.43
M31OC J004008+403507	···	20.773	20.298	···	···	0.84
M31OC J004119+403608	···	···	19.501	···	···	1.88

[a]Asterisks indicate F300W, instead of standard U-band magnitudes.

5.2.4 Completeness of globular cluster catalogs in M31

To estimate the completeness of globular cluster catalogs in M31, we first need to understand our own detection efficiency. We estimated this by inserting artificial globular clusters into the inner images, for which the distance from the center of M31 R_{gc} was $< 30'$. The artificial clusters were actually images of the brightest real globular clusters we detected. We retrieved the HST archival images of these clusters in as many filters as possible, so that we could insert images of template clusters observed in the correct filter for each image. To insert the template clusters, we scaled the image template fluxes 0–4 magnitudes fainter, adjusted for the exposure time of the inserted image, rotated the templates to a random position angle, and applied a random axial ratio from 0.85 to 1.0. This may not have been an entirely correct method of generating artificial clusters, since cluster size, surface brightness, and integrated magnitude are known to be correlated for Milky Way clusters. However, we decided it was better not to introduce additional assumptions about the correlation of these parameters into our detection test. Once a template cluster was inserted into a copy of each HST frame, we extracted a $15'' \times 15''$ region around the inserted template, and examined only that portion of the image. This cut-out procedure was similar to the procedure used for the re-examination of 'problem' images. In fact the visual examination of the two groups of images was done at the same time, with no reference to which were the inserted clusters and which were the real objects. For each cut-out image, we attempted to determine whether or not it was a *bona fide* globular cluster.

The results of our search for the inserted globular cluster templates are in Figure 5.8, where detection of each inserted template is indicated as a function of template V magnitude and R_{gc}. The figure shows, as expected, that our detection efficiency was generally worse for fainter objects and objects near the center of M31. Faint clusters are more difficult to find against the bright background of the

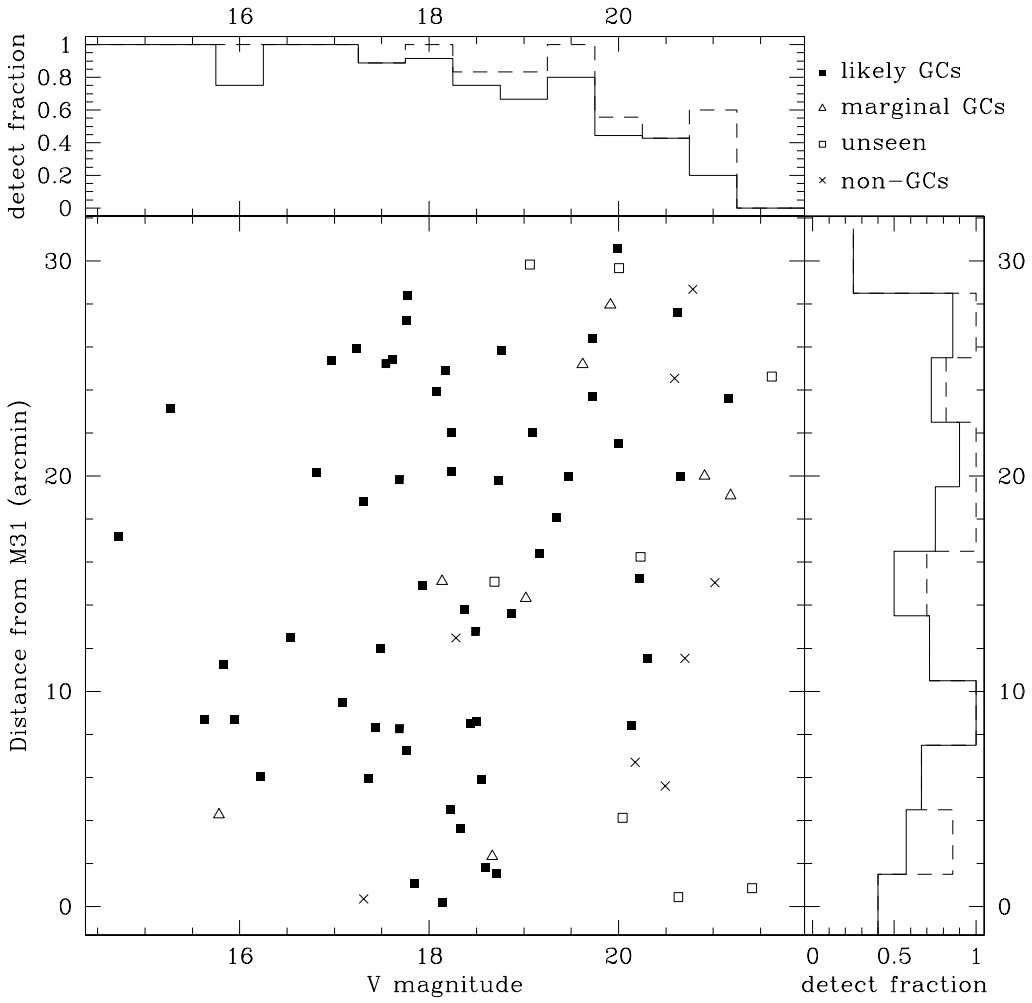

Fig. 5.8.— Measurement of globular cluster detection efficiency. Large plot: V magnitude vs. R_{gc} for artificial clusters. Symbol type indicates whether an object was detected and at what level of confidence. The histograms are the fraction of inserted objects detected; solid lines include only A or B class GCs, and dashed lines include marginal objects.

M31 disk and nucleus. We also failed to detect a few bright objects, mostly in short exposures or in the near-UV filters F300W and F336W. Overall, we correctly identified 80% of the inserted clusters, and 92% of the objects which appeared in long F555W and F814W exposures.

The distribution of the real globular clusters and candidates detected in the HST images is shown in Figure 5.9. The number of newly-detected objects increases at fainter magnitudes; there is no clear trend in the number of new objects with R_{gc}. We use the data in Figures 5.8 and 5.9 to estimate the completeness of existing catalogs. While it would be desirable to estimate the completeness as a joint function of magnitude and position, the small number of objects we have to work with makes deriving $C(V, R_{gc})$ difficult. Instead we summed over one variable to produce separate functions $C(V)$ and $C(R_{gc})$, which are plotted in Figure 5.10. The completeness is computed by dividing the number of cataloged objects in a given bin by the true number of objects. The 'true' object total is the sum of the number of cataloged objects and (the number of new objects)/(our detection efficiency). The number of new objects includes the marginal objects, only a fraction ($f \lesssim 0.5$) of which are likely to be true globular clusters. We therefore give a range of solutions for the completeness functions in Figure 5.10, corresponding to $f = 0, 0.5$ and 1.0. The figure shows, as expected, that existing catalogs are reasonably complete to $V = 18$, after which the completeness drops drastically. To compute the completeness as a function of R_{gc}, we assumed that detection efficiency at $R_{gc} > 30'$ was the same as that in the $R_{gc} = 30'$ bin. The completeness as a functions of R_{gc} does not follow any particular pattern; the most important point is the low completeness in the innermost bin. $C(R_{gc})$ can only be measured out to about $R_{gc} \leq 70'$, and averaging over this region yields values for the overall completeness of 50–85%. The small number of objects per radial bin and the uncertainty about the nature of the marginal objects make this estimate rather imprecise.

It is interesting to try to estimate the total number of globular clusters in M31 using the results of the completeness study. For $V < 18$ and $R_{gc} > 5'$, the existing sample is close to complete. We can therefore use the GCLF for this sample to estimate the number of clusters fainter than the magnitude limit; the GCLF computed in Chapter 4 gives the total number of clusters as $N_{gc} = 406$. There are 294 clusters with $V < 18$, implying that 112 objects should have $V > 18$. Our catalog contains 68 such clusters with $R_{gc} > 5'$, so its completeness is about 55%, in agreement with the above estimate. In the region $R \leq 5'$, there are 37 cataloged clusters or candidates and the average catalog completeness is about 70%. This implies that the true number of clusters is about 53, so the total number

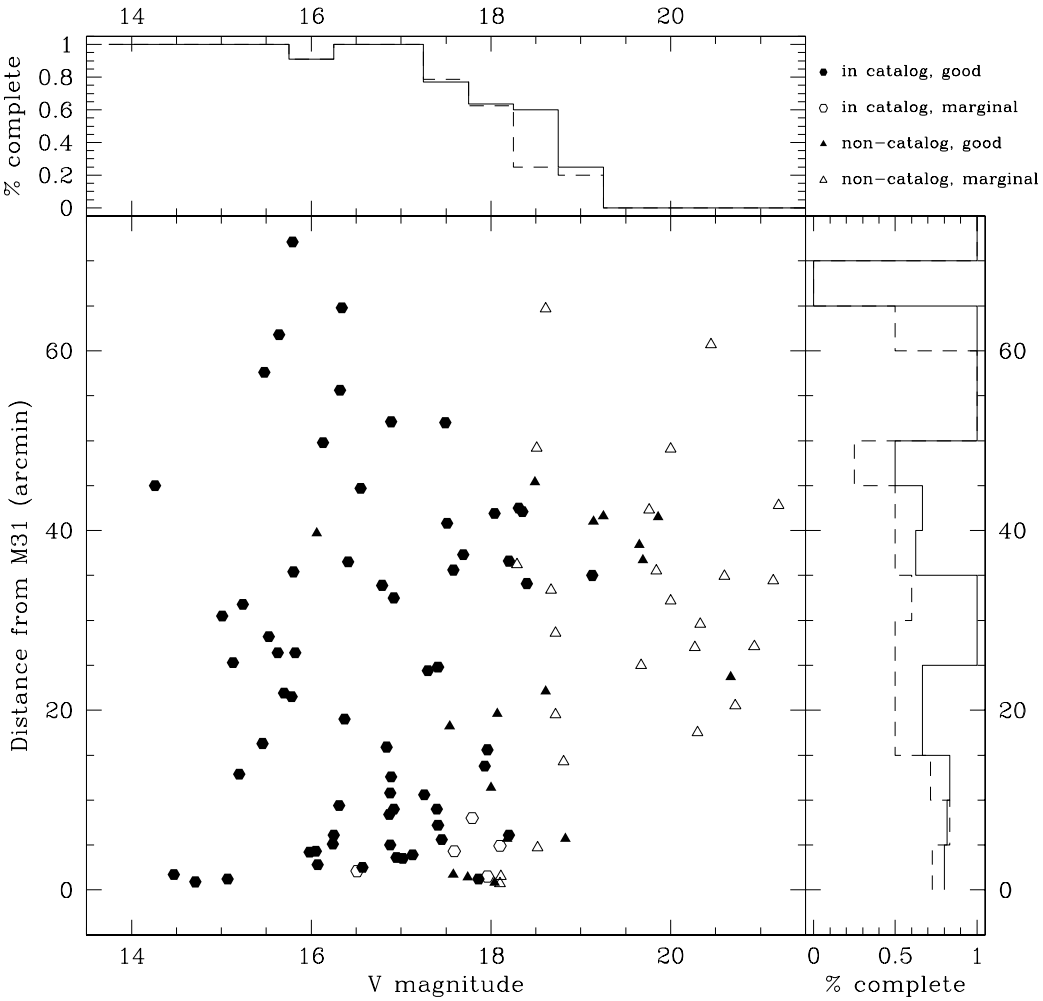

Fig. 5.9.— Location of previously-cataloged and newly-discovered M31 globular clusters in V vs. R_{gc} space. Symbols indicate object quality and presence in existing catalogs. Histograms estimate the existing catalogs' completeness by showing (number of previously known objects per bin)/(number of known + number of new objects per bin). Solid line histograms include only A or B class GCs, and dashed line histograms include marginal objects.

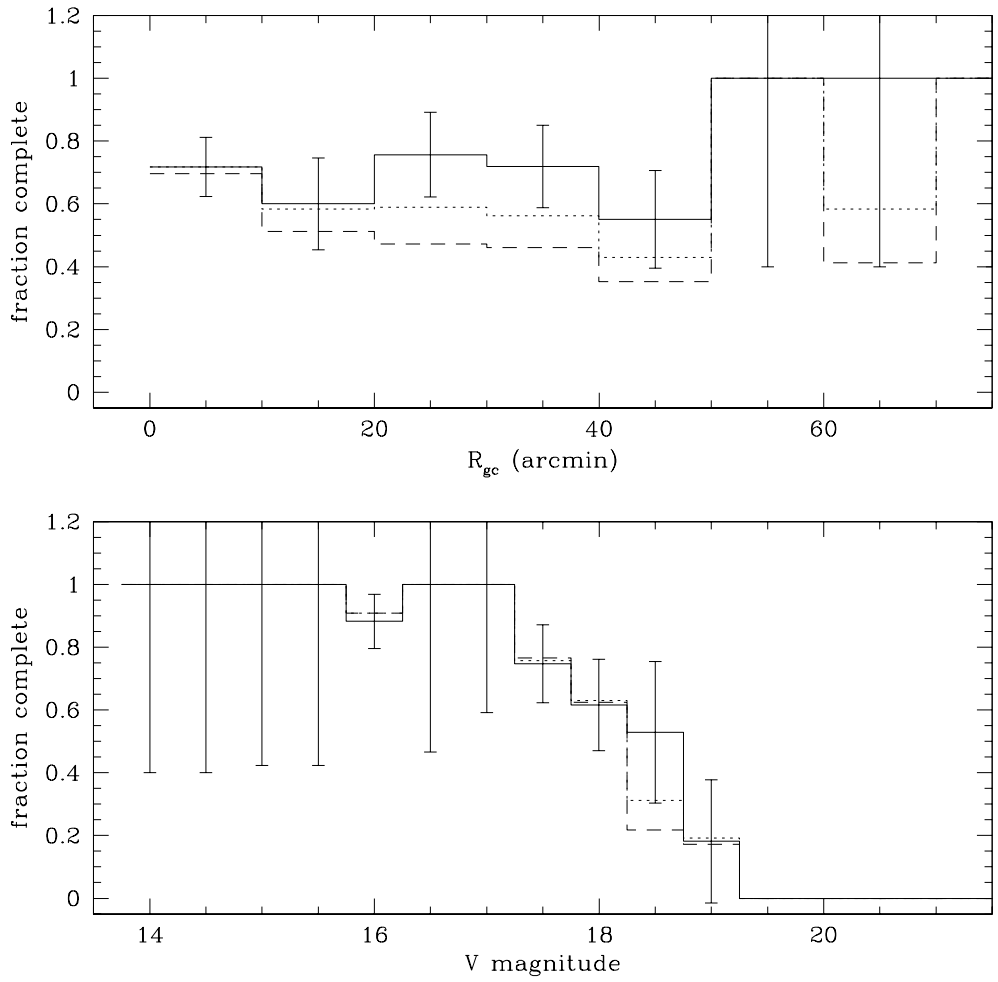

Fig. 5.10.— Completeness functions for existing surveys of globular clusters in M31. Top panel, $C(R_{gc})$, is summed over entire magnitude range, and bottom panel, $C(V)$, is summed over entire radial range. Different line type reflect different assumptions about how many marginal objects are true M31 clusters. Solid lines: none, dotted lines: half, and dashed lines: all.

of GCs in M31 is approximately $406 + 53 = 459$. It is unclear how to best define the uncertainties of this estimate, but it appears to be compatible with value given elsewhere (e.g., by Battistini et al. 1993).

5.3 Properties of M31 GCs from HST imaging

In the remainder of this chapter, we consider only the good (category A and B) cluster candidates; the marginal candidates were usually fainter and smaller, making measurements of their structural properties difficult even on HST images. It is important to point out that the objects studied here do not constitute a complete or magnitude-limited sample of globular clusters in M31, and only the clusters which were not specific HST targets can be considered to be a random sample. Some of our new cluster candidates may not be M31 globulars at all, of course: the nature of bright candidates in long-exposure images is quite clear, but many of our candidates require further examination. We also note that several of the clusters in our sample may actually belong to M31's companion galaxy NGC 205; these clusters were the targets of D. Geisler's HST program GO-6699. We retain these objects in our sample except when computing correlations between cluster properties and location in the galaxy.

5.3.1 Color gradients

Aperture photometry in multiple apertures and filters can be used to search for radial color gradients in GCs. Since there is no evidence for internal extinction in GCs, radial color variations are thought to indicate variations in the cluster stellar population. Djorgovski et al. (1991a,b) studied 12 Milky Way globulars and found that core-collapsed clusters are bluer in the center, either because of an excess of blue straggler stars or a deficit of red giants. Non-collapsed clusters did not show any color gradient. Djorgovski et al. measured color gradients in the core-collapsed clusters over linear scales of 0.04–4 pc and found the gradient sizes to be 0.1–0.3 mag per decade in radius. We thought that color gradients in M31 GCs might be a useful indicator of core-collapse, especially since the clusters' small angular sizes could make it difficult to detect core-collapsed clusters from the surface brightness profiles alone. We measured color profiles using our aperture photometry results; the color in each annulus was computed as

$$C_i = C_0 - 2.5 \log \left(\frac{f_1(r_i) - f_1(r_{i-1})}{f_2(r_i) - f_2(r_{i-2})} \right) \tag{5.1}$$

referenced to the color in the central aperture C_0. The color profiles showed a wide variety of appearances: bright, rich clusters tended to have smooth color profiles, while the looser clusters had much more variable profiles. The profile appearance also depends on the filters and exposure times, of course: shorter exposure times and bluer filters yield much more uncertain fluxes and hence color profiles. We show a sample of color profiles in Figure 5.11. We checked the profiles for significant color gradients using a Monte Carlo technique: we resampled each profile 10^4 times by bootstrapping, and computed the weighted least-squares fit to a straight line. If the absolute value of the computed slope for the real dataset was in the 95^{th} percentile of the distribution of |slope| for the bootstrapped datasets, we considered it to be significant.

We found a total of 18 significant color gradients, with two objects having gradients in more than one color. Strangely, the two gradients for 109–170 are in opposite directions: the center of the cluster is redder in F450−F606W and bluer in F555W−F814W. The F450W/F606W and F555W/F814W image pairs were obtained at different times, so the different color gradients might be due to a bright variable star in the cluster or to cosmic ray contamination in one image pair. Overall, two thirds of the slopes are positive (the center is bluer, as found for Milky Way core-collapse objects) and one third are negative, as might be expected for clusters which are really background galaxies, or those in which mass segregation has increased the number of red giants in the cluster center without a corresponding increase in the number of blue stragglers. The least-squares fit parameters are given in Table 5.4 and plotted against the color profiles in Figure 5.12. The gradients are comparable in size to those obtained by Djorgovski et al. (1991a) for Milky Way globulars. In previous work on M31 GC color gradients, Holland et al. (1997) found gradients of −0.028 and −0.090 magnitudes/arcsec for 240–302 and 379–312, respectively. We find no significant gradient for 240–302 (shown in Figure 5.11), and a smaller gradient for 379–312. Since we use the same observational data as Holland et al. (1997), the discrepancy may be related to the fitting or background subtraction methods. Grillmair et al. (1996) found no significant color gradients for 006–058, 045–108, 343–105, and 358–319; we agree with their results for the first three clusters and find a small gradient for 358–319.

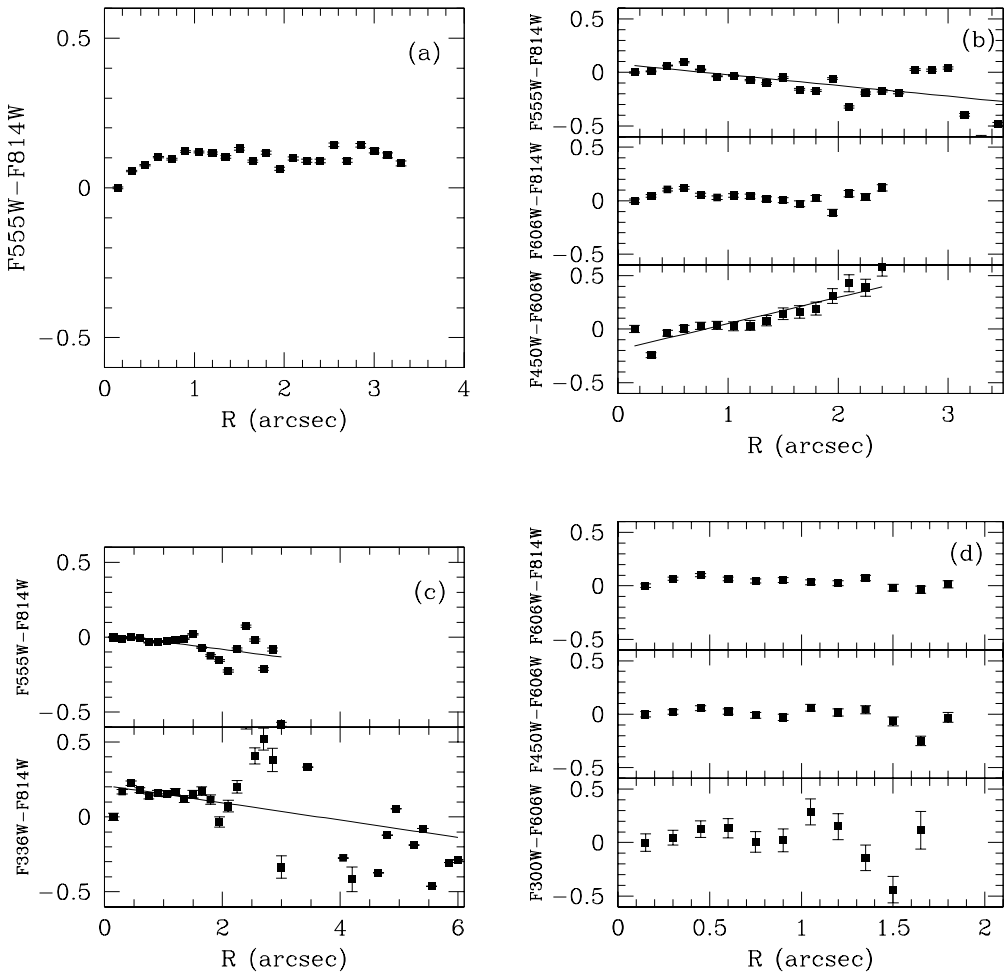

Fig. 5.11.— Sample color profiles of M31 globular clusters: (a) 240–302 (b) 109–170 (c) 342–094 (d) 076–138.

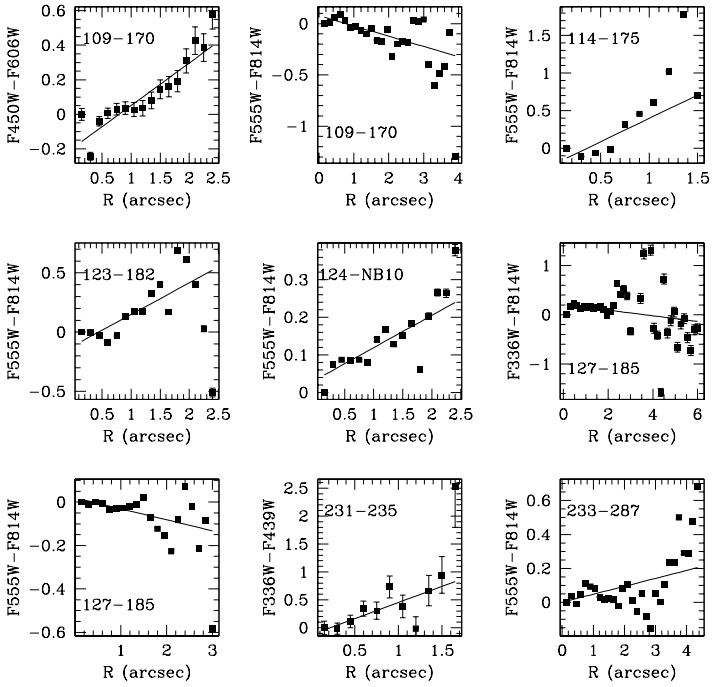

Fig. 5.12.— Color profiles of M31 globular clusters with gradients.

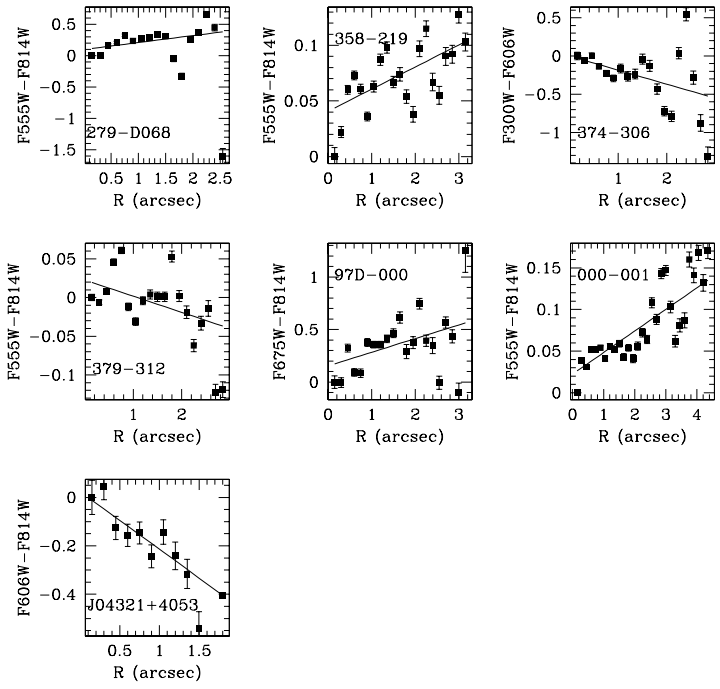

Fig. 5.12.— Continued.

Table 5.4. Least-squares fits for M31 GCs with color gradients

name	filters	slope (mag/arcsec)	intercept
109–170	F450W, F606W	0.246 ± 0.018	-0.194 ± 0.017
109–170	F555W, F814W	-0.100 ± 0.001	0.078 ± 0.002
114–175	F555W, F814W	0.620 ± 0.003	-0.222 ± 0.004
123–182	F555W, F814W	0.266 ± 0.004	-0.117 ± 0.004
124–NB10	F555W, F814W	0.086 ± 0.002	0.033 ± 0.002
127–185	F336W, F814W	-0.058 ± 0.005	0.210 ± 0.008
127–185	F555W, F814W	-0.051 ± 0.001	0.020 ± 0.002
231–235	F336W, F439W	0.577 ± 0.132	-0.125 ± 0.089
233–287	F555W, F814W	0.047 ± 0.001	0.001 ± 0.001
279–D068	F555W, F814W	0.111 ± 0.011	0.096 ± 0.012
358–219	F555W, F814W	0.020 ± 0.002	0.041 ± 0.002
374–306	F300W, F606W	-0.183 ± 0.017	-0.003 ± 0.021
379–312	F555W, F814W	-0.021 ± 0.002	0.023 ± 0.002
97D–000	F675W, F814W	0.130 ± 0.014	0.155 ± 0.021
000–001	F555W, F814W	0.026 ± 0.001	0.022 ± 0.001
GC J004312+405303	F606W, F814W	-0.238 ± 0.016	0.024 ± 0.028

5.3.2 Surface photometry

To measure clusters' shapes, we used the IRAF task ELLIPSE to fit elliptical isophotes to the clusters, using the background-subtracted images generated for integrated photometry. Isophotes were fit over a range of semi-major axes spaced logarithmically from $0.2''$ to $5.0''$ or the largest measurable size. We averaged the ELLIPSE output over the isophotal semi-major axes to determine the overall ellipticity ($\epsilon = 1 - b/a$, where a and b are the isophote semi-major and semi-minor axis lengths), position angle, and central position for each of the cluster images. We further averaged over the different filters to compute the ellipticities and position angles given in Table 5.5. The ELLIPSE algorithm could not be made to work at all on some sparse clusters. This was not unexpected, since the algorithm was designed for galaxies and expects the surface brightness distribution to be smooth and monotonically decreasing with distance from the center. We were able to estimate shape parameters for about a third of these objects by resampling the images to a resolution of $0.2''$/pixel and running ELLIPSE on the 'blurred' images.

This procedure did not work for the remainder of the images, and objects with no shape measurements are noted in Table 5.5 with a default zero ellipticity and position angle.

Figure 5.13 shows some sample ellipticity and position angle profiles, plotted as a function of the effective radius ($R_e = \sqrt{ab} = a\sqrt{1-\epsilon}$) to allow for simple comparison of objects with different ellipticities. In most cases, the ellipticities and position angles measured on images in different filters track well together, as we would expect. The measured position angles are occasionally wildly varying, often when the ellipticities are close to zero. This is likely an artifact of the ELLIPSE algorithm, which diverges as the ellipticity approaches zero (Jedrzejewski 1987). For these objects, we report ellipticities and position angles of zero in Table 5.5. F300W and F336W profiles often varied from those in other filters, probably because of the low signal-to-noise in these images. If stars of different colors have different spatial distributions (see discussion of color gradients above), some differences in ellipticity and position angle profiles might also be expected.

Table 5.5. Ellipticities and position angles for GCs in M31 HST fields

name	ellipticity[a]	PA[b]	filters
000–001	0.20 ± 0.01	121 ± 1	F555W, F814W
000–D38	0.34 ± 0.04	108 ± 1	F555W, F814W
000–M091	0	0	···
006–058	0.08 ± 0.02	74 ± 2	F555W, F814W
009–061	0.12	31	F814W
011–063	0.09 ± 0.02	76 ± 6	F555W, F814W
012–064	0.08 ± 0.01	46 ± 9	F555W, F814W
018–071	0.15 ± 0.04	4 ± 2	F555W, F814W
020D–089	0.14	21	F814W
027–087	0.07 ± 0.02	97 ± 29	F555W, F814W
030–091	0.10 ± 0.01	118 ± 17	F555W, F814W
045–108	0.08 ± 0.01	40 ± 1	F555W, F814W
058–119	0.10 ± 0.00	138 ± 1	F555W, F814W
064–125	0.06	53	F300W
068–130	0.22 ± 0.02	42 ± 1	F439W, F555W, F814W
076–138	0.09 ± 0.01	69 ± 1	F300W, F450W, F606W, F814W
077–139	0.14 ± 0.02	132 ± 10	F450W, F606W, F814W
092–152	0.08	109	F300W
101–164	0.07	80	F300W
109–170	0.10 ± 0.03	72 ± 9	F450W, F555W, F606W, F675W, F814W
110–172	0.05	49	F606W
114–175	0.06 ± 0.01	132 ± 4	F555W, F814W
115–177	0.08 ± 0.02	63 ± 7	F555W, F814W
123–182	0.14 ± 0.04	62 ± 6	F555W, F675W, F814W
124–NB10	0.07 ± 0.01	164 ± 3	F336W, F555W, F814W
127–185	0.08 ± 0.01	64 ± 4	F336W, F555W, F814W
128–187	0.08 ± 0.02	176 ± 1	F675W, F814W
132–000	0.09 ± 0.02	40 ± 59	F336W, F555W, F675W, F814W
134–190	0.16 ± 0.00	113 ± 1	F675W, F814W
143–198	0.05 ± 0.01	158 ± 7	F555W, F814W
145–000	0.14	92	F300W
146–000	0.06	151	F300W

Table 5.5—Continued

name	ellipticity[a]	PA[b]	filters
148–200	0.07	27	F555W
153–000	0.05	70	F300W
155–210	0.12 ± 0.01	80 ± 15	F606W, F814W
156–211	0.05 ± 0.02	67 ± 4	F606W, F814W
160–214	0.18 ± 0.00	2 ± 1	F606W, F814W
167–000	0.04	97	F814W
205–256	0.08 ± 0.04	152 ± 22	F300W
231–285	0.17 ± 0.02	136 ± 33	F439W, F555W
232–286	0.18 ± 0.01	42 ± 1	F300W, F450W, F606W, F814W
233–287	0.11 ± 0.02	74 ± 8	F555W, F814W
234–290	0.07 ± 0.01	71 ± 16	F336W, F439W, F555W
240–302	0.16 ± 0.01	98 ± 1	F555W, F814W
264–000	0.26 ± 0.04	142 ± 17	F336W, F555W, F814W
268–000	0.12 ± 0.04	103 ± 50	F555W, F814W
279–D68	0.20 ± 0.09	79 ± 77	F555W, F814W
311–033	0.09 ± 0.01	54 ± 7	F555W, F814W
315–038	0.13 ± 0.02	159 ± 11	F439W, F555W
317–041	0.11 ± 0.02	66 ± 23	F555W, F814W
318–042	0.19 ± 0.03	70 ± 5	F336W, F439W, F555W
319–044	0	0	···
324–051	0	0	···
328–054	0.27 ± 0.05	159 ± 5	F555W, F814W
330–056	0.14 ± 0.01	102 ± 8	F555W, F814W
331–057	0.24 ± 0.06	70 ± 3	F555W, F814W
333–000	0.23 ± 0.02	26 ± 17	F555W, F814W
338–076	0.06 ± 0.01	102 ± 34	F555W, F814W
342–094	0	0	···
343–105	0.09 ± 0.01	70 ± 22	F555W, F814W
358–219	0.12 ± 0.02	63 ± 5	F555W, F814W
368–293	0	0	···
374–306	0.21 ± 0.02	106 ± 1	F300W, F606W
379–312	0.09 ± 0.02	55 ± 3	F555W, F814W

Table 5.5—Continued

name	ellipticity[a]	PA[b]	filters
384–319	0.20 ± 0.01	121 ± 1	F555W, F814W
386–322	0.08 ± 0.01	140 ± 3	F555W, F814W
468–000	0	0	···
97D–000	0	0	···
NB39	0.13 ± 0.04	28 ± 17	F336W, F555W, F814W
M31GC J004304+412028	0.09 ± 0.04	75 ± 3	F555W, F814W
M31GC J004251+411035	0.10 ± 0.01	116 ± 20	F450W, F606W, F814W
M31GC J004258+405645	0.18	175	F606W
M31GC J004301+405418	0.15 ± 0.04	30 ± 14	F606W, F814W
M31GC J004312+405303	0.38 ± 0.01	44 ± 4	F606W, F814W
M31GC J004103+403458	0.38 ± 0.14	87 ± 8	F555W, F814W
M31GC J004537+413644	0	0	···
M31GC J004030+404530	0.19	123	F606W
M31GC J004027+414225	0.32 ± 0.06	128 ± 4	F555W, F814W
M31GC J004051+404039	0	0	···

[a]Ellipticity is defined as $\epsilon = 1 - (b/a)$, where a and b are the lengths of the semi-major and semi-minor axes, respectively

[b]Position angle is measured in degrees east from north

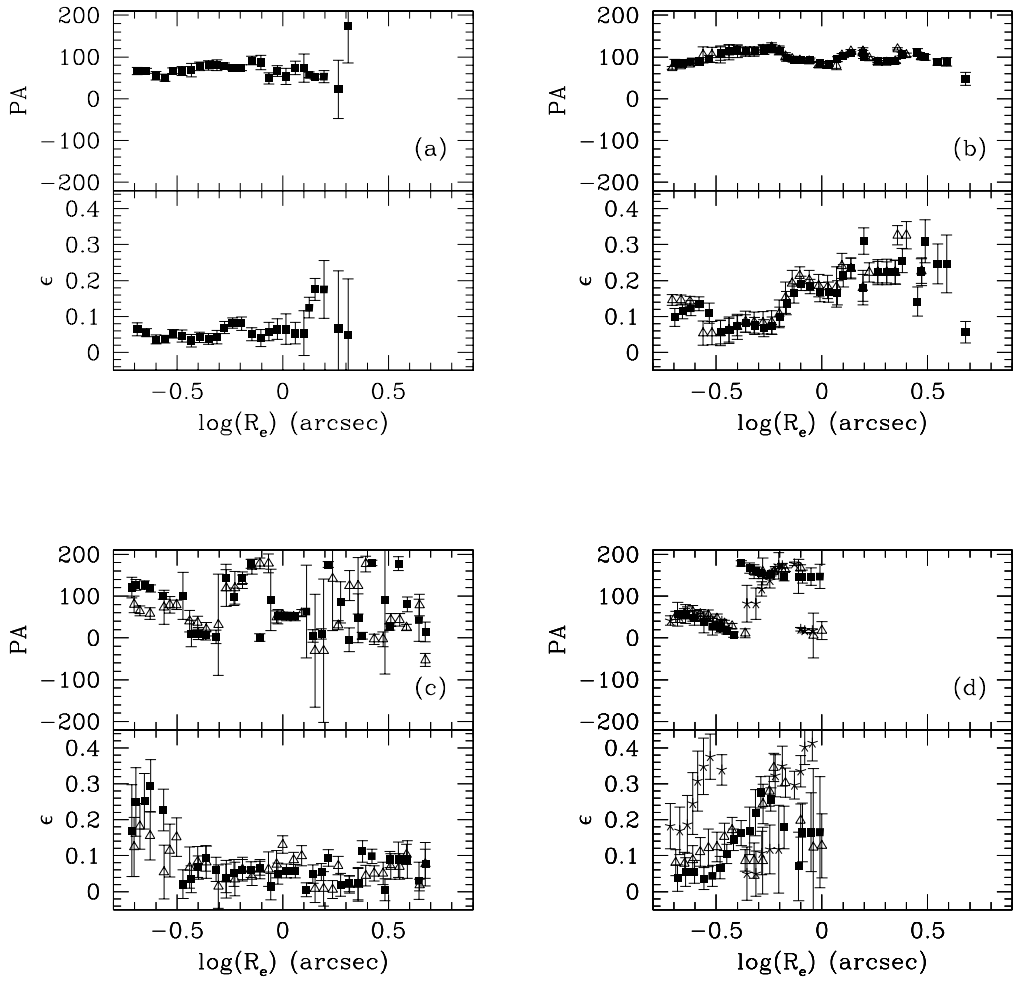

Fig. 5.13.— Sample ellipticity and position angle profiles for M31 GCs: (a) 153–000 (F300W) (b) 240–302 (F555W, F814W) (c) 338–076 (F555W, F814W) (d) NB39 (F300W, F555W, F814W)

In Figure 5.14, we compare our measurements of ellipticity and position angle with those of Staneva, Spassova, & Golev (1996), the most comprehensive published dataset. Our ellipticities generally agree quite well: the median difference between our measurements and those of Staneva et al. (1996) is 0.024 ± 0.009. However, our measured position angles are not in particularly good agreement with those measured by Staneva et al. (1996). The agreement is better for more elliptical objects, for which the position angle can be more precisely determined. We do not understand the reasons for the position angle discrepancy, although we note that it may not be due to our measurements alone: a comparison of position angles measured by Staneva et al. (1996) and Lupton (1989) shows that the measurements in these two works are also in poor agreement. As most of the ellipticities are small, precise measurement of position angles is not critical to our surface brightness modeling and the discrepancies are not a serious concern.

With the basic shape parameters of the clusters measured by ELLIPSE, we went on to fit single-mass, elliptical King models to the cluster images. These models do not have an analytic representation; the density and surface brightness profiles determined by the three model parameters — the central potential W_0, the scale radius[4] r_0 and the central intensity I_0 — are computed by solving the equations given in Michie (1963) and/or King (1966). Instead of the central potential, globular cluster surface brightness profiles are usually parameterized in terms of the tidal radius r_t (the radius at which the cluster projected density drops to zero) or the concentration c, where $c = \log(r_t/r_0)$. We used the program KM2DFIT written by S. Holland (described in Holland, Côté, & Hesser 1999) to do the model fits. Although this program can also fit for the shape parameters, increasing the number of parameters greatly increases the execution time. Experimenting with the images of a few clusters, we found that ELLIPSE and KM2DFIT returned similar values for the shape parameters, so we believe it is reasonable to use the ELLIPSE values for all objects. For most objects, we fit the models to the cluster images over sub-images $12.8''$ in size. KM2DFIT requires the sub-images to have dimensions which are powers of two, and the aperture photometry showed that images of this size contained all the flux from the clusters. Some objects near the edges of the WFPC2 chips had to be fit in smaller sub-images, and a few were so close to the chip edge that they could not be fit at all.

The models were convolved with the appropriate WFPC2 PSF before being compared to the data; this greatly increased execution time but should result in

[4]Binney & Merrifield (1998) point out that r_0 is usually called the core radius and denoted r_c, but r_0 as defined by King (1966) is approximately the same as r_c (the half-intensity radius) only for concentrated clusters.

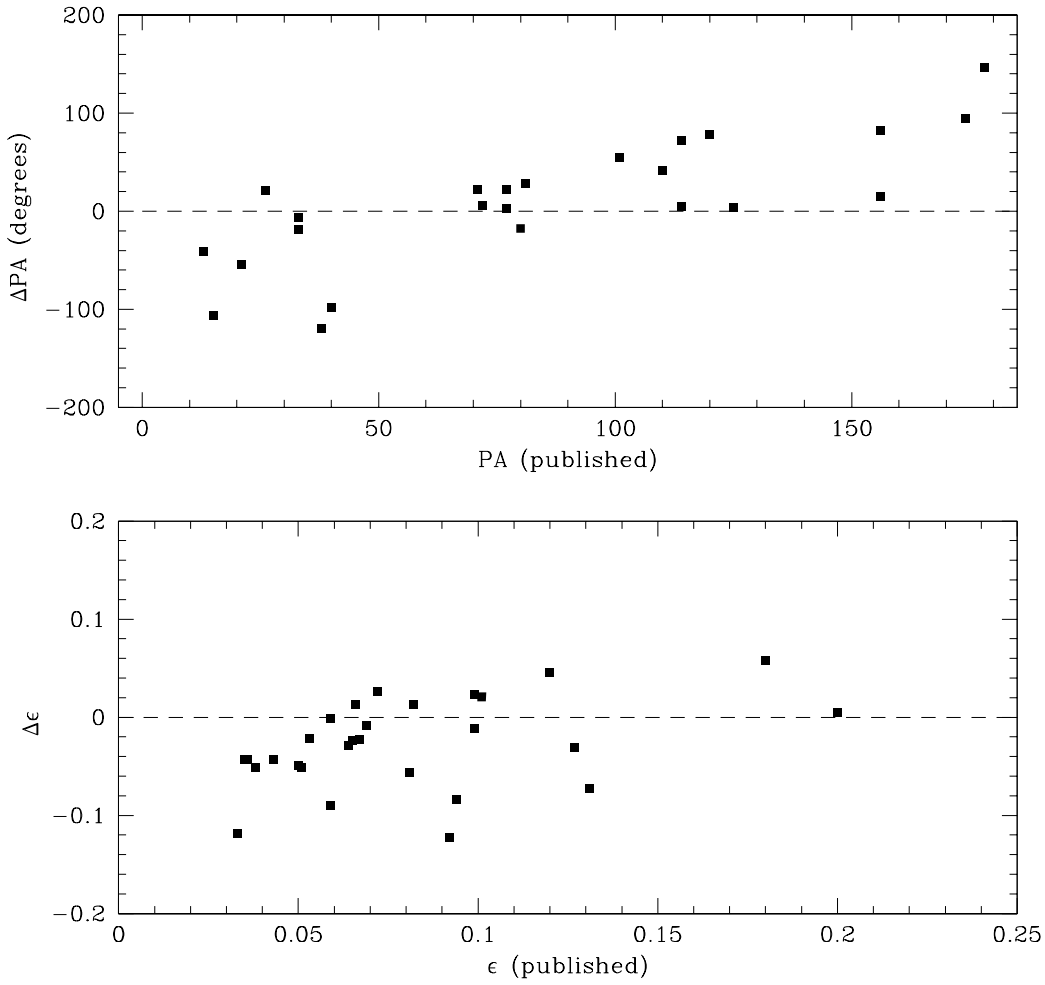

Fig. 5.14.— Comparison of our measurements of ellipticity and position angle with those of Staneva et al. (1996). The horizontal axis is the published measurement; vertical axis is (published − our) measurements.

more accurate parameters for the smaller objects. We tried fitting models without PSF convolution as well, and found that the resulting scale radii were systematically larger (by $0.076 \pm 0.013''$) and the concentrations smaller (by 0.09 ± 0.02) than for the convolved models. This shows that the size of the PSF cannot be ignored, even with HST resolution. Another property of the images which might be important to the model-fitting is the pixel size, that is, whether the object was imaged on the PC or one of the WFC chips. We checked this by taking PC images of 10 clusters with a range of structural parameters, rebinning them to the lower WFC resolution, and performing the model-fitting procedure on the rebinned images. The differences between the PC and WFC models were small: median offsets were $0.01 \pm 0.04''$ in r_0, and 0.04 ± 0.04 in c. As another check on our model-fitting, we compared the half-light radii of the best-fitting models to the half-light radii measured with integrated photometry. The agreement was acceptable, with a median offset of $0.05 \pm 0.04''$ over a factor of 5 in r_h.

Another test of our model-fitting procedure is the measurement of the same object imaged in more than one filter. Such measurements generally gave quite similar results; the median absolute differences in recovered parameters for pairs of filters were 0.13 ± 0.04 in c and $0.04 \pm 0.02''$ in r_0. The medians provide reasonable estimates of the uncertainties in c and r_0; the tidal radii are more uncertain since they depends on both of these parameters. Error propagation for median values of c and r_0 yields an estimate of $\Delta r_t \approx 2''$. The situation was similar for objects imaged in more than two filters, although fits in the F300W and F336W were often discrepant from others, presumably because of the poorer signal-to-noise in these filters. Table 5.6 gives average King model parameters r_0, c and r_t for each cluster, and the central surface brightness in the V-band (or another filter if V was unavailable). The central surface brightness is determined by transforming the model central intensity in counts per pixel to magnitudes per square arcsecond and using the same calibration as in Section 5.2.3. As for ellipse fitting, some sparse clusters could not be fit well by KM2DFIT which assumes a continuous light distribution. Their parameters are not used in the following analysis.

Table 5.6. King model fitting results for GCs in M31 HST fields

name	$r_0(''$)[a]	$r_t(''$)	c	$\mu_V(0)$[b]
000–D38	0.77	3.11	0.61	19.62
000–001	0.21	10.50	1.70	13.55
000–M91	1.09	4.42	0.61	20.46
006–058	0.16	5.76	1.56	14.90
009–061	0.15	5.86	1.60	15.13 (I)
011–063	c0.06	7.28	2.06	15.30
012–064	0.21	12.33	1.77	14.81
018–071	0.37	17.42	1.68	18.63
020D-089	0.16	6.36	1.60	16.08 (I)
027–087	0.30	8.72	1.46	16.53
030–091	0.21	5.50	1.42	17.22
045–108	0.30	8.14	1.43	15.84
058–119	0.20	7.29	1.56	14.46
064–125	c0.12	6.03	1.69	17.26 (F300W)
068–130	0.12	9.04	1.87	19.18
076–138	0.12	6.92	1.77	16.02
092–152	c0.14	4.28	1.49	17.97 (F300W)
097D-000	0.75	6.83	0.97	18.81 (I)
101–164	0.19	4.39	1.37	17.87 (F300W)
109–170	0.19	7.44	1.59	15.93
110–172	0.38	4.09	1.03	15.73
114–175	0.21	3.99	1.27	16.74
115–177	0.14	5.92	1.61	14.94
123–182	c0.09	6.34	1.83	16.83
124–NB10	0.22	3.89	1.25	14.46
127–185	0.37	5.74	1.19	14.94
128–187	0.13	3.49	1.36	15.15 (I)
132–000	0.16	1.59	1.00	15.53 (I)
143–198	0.11	4.53	1.61	14.73
145–000	c0.14	3.36	1.39	19.33 (F300W)
146–000	0.12	6.12	1.69	18.09 (F300W)
155–210	0.09	3.49	1.59	17.49

Table 5.6—Continued

name	$r_0(''$)[a]	$r_t(''$)	c	$\mu_V(0)$[b]
156–211	0.19	14.37	1.84	16.35
160–214	0.18	5.44	1.48	17.70
205–256	0.53	9.12	1.17	17.04 (F300W)
231–285	c0.15	3.96	1.38	16.78
232–290	0.19	7.56	1.60	15.59
233–287	0.30	7.99	1.43	15.78
234–290	0.09	5.33	1.77	16.25
240–302	0.18	9.35	1.73	15.32
264–000	0.35	2.54	0.85	17.83
268–000	c0.14	1.56	1.06	17.52
279–D68	0.36	4.39	1.07	18.68
311–033	0.19	8.46	1.64	15.03
315–038	0.57	6.56	1.03	17.21
317–041	0.24	6.31	1.42	16.40
319–044	0.62	4.73	0.88	18.44
324–051	0.66	3.19	0.69	18.96
328–054	0.27	10.70	1.58	18.44
330–056	0.44	3.62	0.91	18.07
331–057	0.31	29.53	1.98	18.44
333–000	0.49	5.83	1.08	19.75
338–076	0.55	10.74	1.29	15.24
343–105	c0.11	11.91	2.03	15.48
358–219	0.55	7.40	1.13	16.08
368–293	1.04	3.86	0.57	19.33
374–306	0.20	7.90	1.60	18.19
379–312	0.15	8.16	1.73	16.17
384–319	0.21	8.27	1.59	15.40
386–322	0.15	8.54	1.75	14.95
468–000	1.61	11.55	0.86	20.51
NB39	0.22	1.26	0.75	17.86
M31GC J004304+412028	0.18	1.65	0.95	17.72
M31GC J004251+411035	c0.07	5.45	1.88	16.51

Table 5.6—Continued

name	$r_0(\prime\prime)$[a]	$r_t(\prime\prime)$	c	$\mu_V(0)$[b]
M31GC J004258+405645	0.11	0.80	0.86	17.23
M31GC J004301+405418	0.13	0.50	0.59	17.94
M31GC J004312+405303	0.68	3.06	0.66	21.36
M31GC J004537+413644	0.90	4.39	0.69	20.94
M31GC J004030+404530	0.10	10.66	2.03	15.31
M31GC J004027+414225	0.95	3.70	0.59	20.68
M31GC J004051+404039	0.38	4.26	1.05	20.35

[a]'c' indicates core-collapse candidates.

[b]Bandpass names indicate central surface brightness measured in other than V.

It would be useful to know if there were any systematic effect of exposure time on the model-fitting results. It is easy to imagine that longer exposure times t relative to a cluster's integrated magnitude might allow better detection of faint stars at the edges of clusters, and hence yield larger r_t and c values. We attempted to check this by plotting r_0 and r_t as a function of the number of photons from the clusters, where $N_p \propto t \times 10^{-0.4V}$ (the filter zeropoint is ignored here since it only adds a multiplicative correction to N_p). We found that clusters with higher N_p did have higher measured values of r_t and c, although there was very little difference in measured values of r_0. However, this result cannot be used to show that the model parameters are biased by exposure time. N_p is strongly related to cluster integrated magnitude: brighter clusters emit more flux *and* have longer exposure times, because they tend to be in targeted, rather than parallel observations. Because Milky Way clusters' c and r_0 are known to correlate with cluster integrated magnitude, (we will show below that the same is true for M31 clusters) we cannot say anything about possible biases in M31 cluster parameters with exposure time from these data. For the handful of M31 clusters observed in multiple fields with different exposure times, there does not appear to be a systematic difference in the measured cluster parameters, so we proceed on the assumption that the heterogeneous nature of the HST images does not induce serious biases in our measurements.

In Figure 5.15, we compare our measurements of structural parameters with previous HST and ground-based measurements. Except for Holland et al.

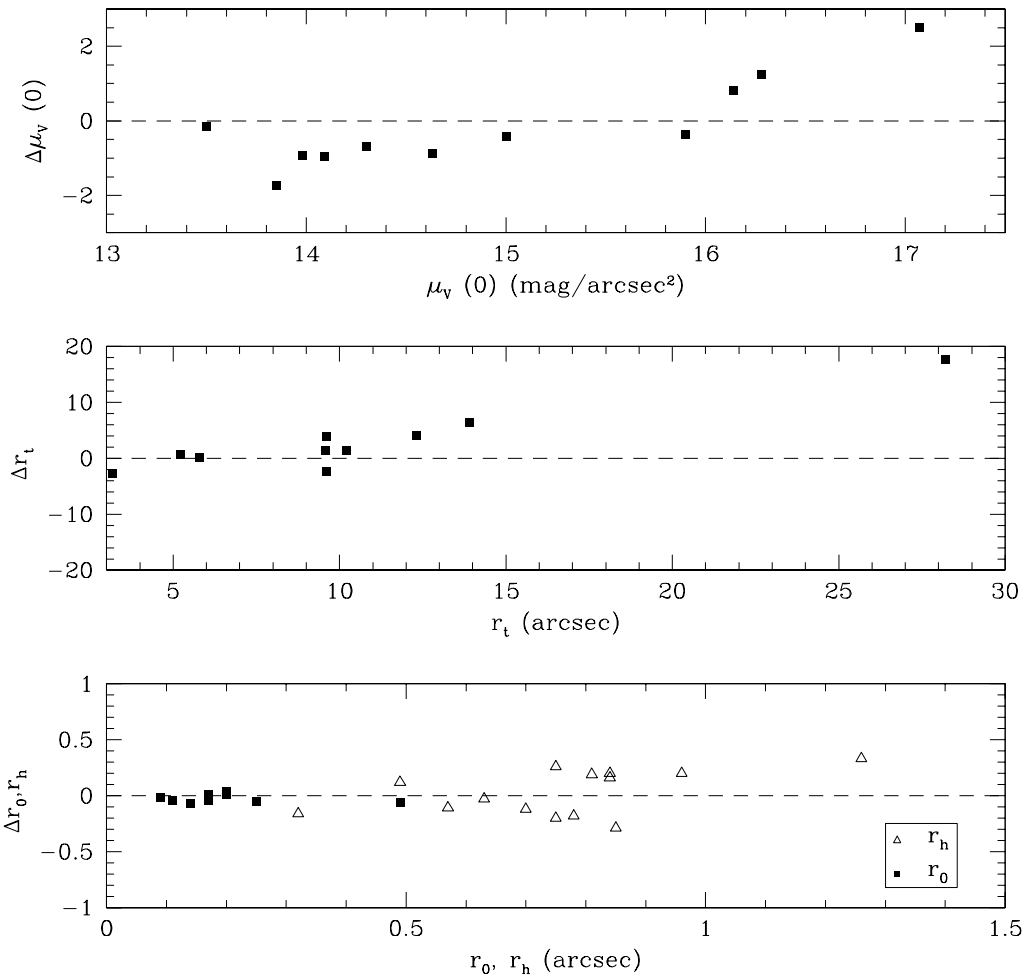

Fig. 5.15.— Comparison of our measurements of structural parameters with those of previous authors. The horizontal axis is the published measurement; vertical axis is (published − our) measurements.

(1997), all of the other authors used quite different methods to measure structural parameters, so the comparison should indicate possible systematic errors. The agreement in structural parameters is good for the scale and half-light radii and rather poor for both the central surface brightnesses and tidal radii. The poor agreement for the central surface brightness is perhaps not surprising: the majority of the previous measurement are from Fusi Pecci et al. (1994), who used deconvolved (pre-COSTAR) Faint Object Camera images, or Davoust & Prugniel (1990), who used ground-based images with PSF deconvolution. Both of these works likely suffered from cluster flux being smeared out by the PSF. The poor agreement of tidal radii is somewhat more surprising. Some of the effect may again be attributed to Fusi Pecci et al.'s use of the FOC; its small field of view may have caused them to underestimate the tidal radii. The ground-based measurements of r_t by Cohen & Freeman (1991) are also highly uncertain for individual clusters. The worst agreement in r_t is for 000–001 (aka G1 or Mayall II), previously studied by Rich et al. (1996). We agree fairly well with their measurements of both r_0 ($0.17''$ vs. $0.21''$) and r_h ($0.70''$ vs. $0.82''$), but in r_t we disagree by more than a factor of two. Their measurement is based on a detection of the tidal cutoff in the surface brightness profile, while ours is based on the c measured from the overall shape of the profile. The value of c derived from their values of r_0 and r_t is 2.22 — uncomfortably high for a non-core-collapsed cluster. Our smaller value of r_t is not due to the size of the sub-image used to fit the surface brightness profile: we tried fitting models to larger sub-images and found essentially the same parameters. Either our model-fitting procedure misses flux at large radius, and therefore underestimates r_t, or the Rich et al. (1996) star counts near the edge of the chip are overestimates.

A final step in checking the modeling results is the examination of surface brightness profiles for the clusters and models. We plotted the surface brightness profiles output by ELLIPSE together with the model profiles and found that the agreement was generally quite good. Figure 5.16 shows a sample of these profiles. The figure also demonstrates the different physical sizes of the clusters; the points stop at the radius where ELLIPSE can no longer fit the isophotes because the S/N is too poor. An important question to be addressed by examining the profiles is whether there is evidence for systematic departures of the data from the model profiles. Departures at large radii can indicate the presence of extra-tidal stars, while departures at small radii can indicate the presence of the core-collapse phenomenon. Both effects have been claimed in M31 GCs, by Holland et al. (1997), Grillmair et al. (1996), and Fusi Pecci et al. (1994). Examining the profiles, we find evidence that the following clusters have extra-tidal stars: 006–058, 058–119, 110–172, 240–302, 358–219, and 379–312. We are in agreement with the results of

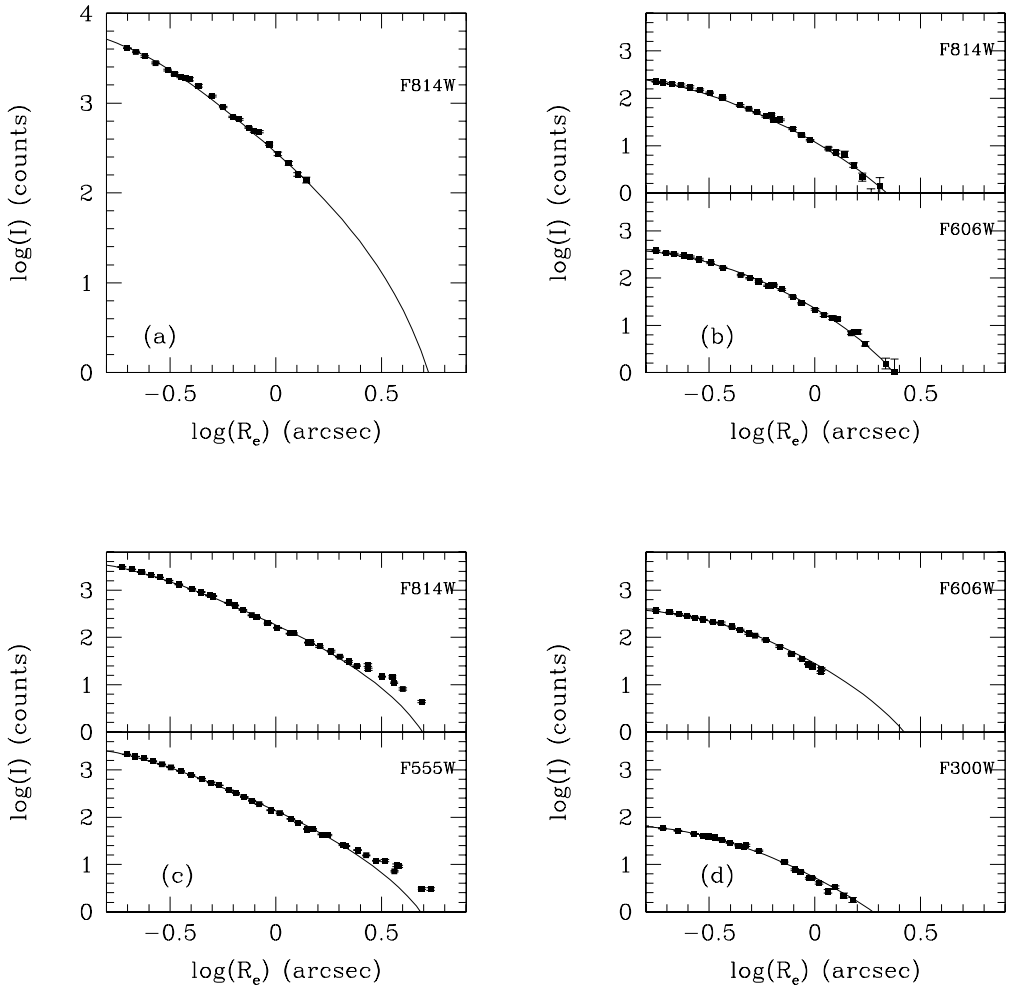

Fig. 5.16.— Sample surface brightness profiles for M31 GCs: (a) 020D–089 (b) 160–214 (c) 006–058 (d) 374–306. 006–058 may have extra-tidal stars.

Holland et al. (1997) and Grillmair et al. (1996) for all objects except 343–105, which Grillmair et al. find to have extra-tidal stars and we do not. A potential problem with detections of excess flux at large radius is the uncertain effects of background subtraction. We tried to account for this in our model-fitting by allowing the background level to vary even though it should have been set to zero by our subtraction procedure.

Detecting core-collapsed clusters is difficult: even in the Milky Way, detections of core-collapse in GC surface brightness profiles came many years after the phenomenon was first predicted (see, e.g., Djorgovski & King 1984). Core-collapsed globular clusters are distinguished from 'King-model' clusters by the fact that their surface brightness profiles are better fit by a power law. To check for core collapse in M31 GCs, we fit power-laws to the ELLIPSE surface brightness profiles and compared the RMS deviation between the power-law model profiles and the data to that between King model profiles and data. In some cases we dropped discrepant surface brightness data points at large radii before fitting the power law and doing the comparison. As we expected, most of the clusters were better fit by King models than by power laws. For a few objects, generally ones for which King model-fitting produced large values of c, the power-law fits were as good as or better than the King model fits. These may be core-collapsed clusters; we show their profiles in Figure 5.17 and mark them in Table 5.6. We note that for 343–105, which Bendinelli et al. (1993) claimed to be a core-collapsed cluster, the King model is formally a slightly better fit than the power law. As Figure 5.17 shows, there is really very little difference between the two models, and we do not believe it is possible to use existing data to differentiate between the profile of a high-concentration King model with a small scale radius (for 343–105 we measured $r_0 = 0.42$ pc) and a power-law one with existing data. The overlap between clusters with color gradients and suspected core-collapse is only two objects: 123–182 and 231–285; however, three of the nine core-collapse suspects had measurements in only one filter. At least in the present dataset, a color gradient is not a particularly good indicator of a core-collapse-like surface brightness profile.

It is expected that core-collapsed clusters should be, on average, nearer to the center of the parent galaxy (since the stronger tidal field accelerates the clusters' dynamical evolution). This is seen in the Milky Way, where the median value of R_{gc} is 2.1 kpc for core-collapsed clusters and 7 kpc for non-core-collapsed clusters. Most of the M31 core-collapse candidates are within 2 kpc of the center of M31; the exceptions are 343–105 ($R_{gc} = 14.8$ kpc), 231–285 ($R_{gc} = 5.6$ kpc), and 011–063 (7.7 kpc from M31, but 0.5 kpc from NGC 205). There is no significant trend of c with R_{gc} for the *non*-core collapsed clusters in either M31 or the Milky Way.

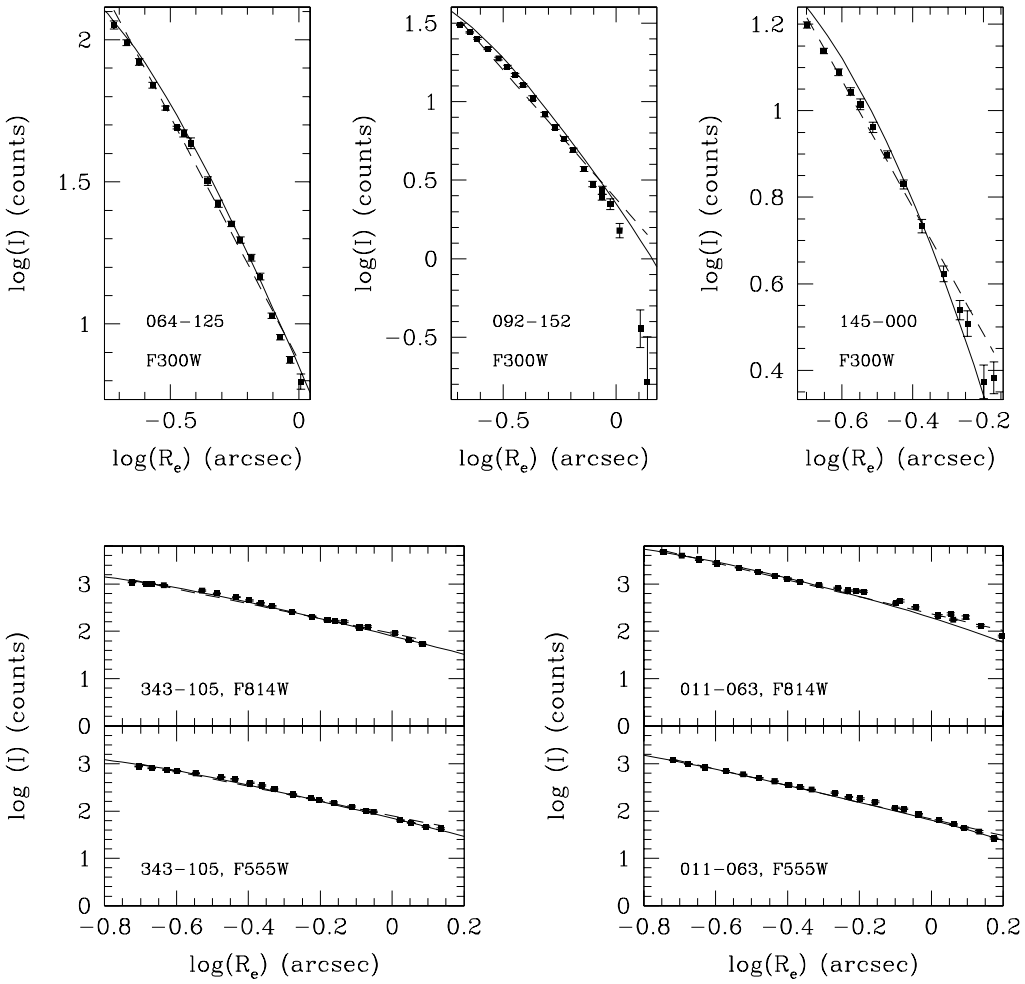

Fig. 5.17.— Surface brightness profiles for possible core-collapsed M31 GCs. Solid lines are King models; dashed lines are power-law surface brightness profiles.

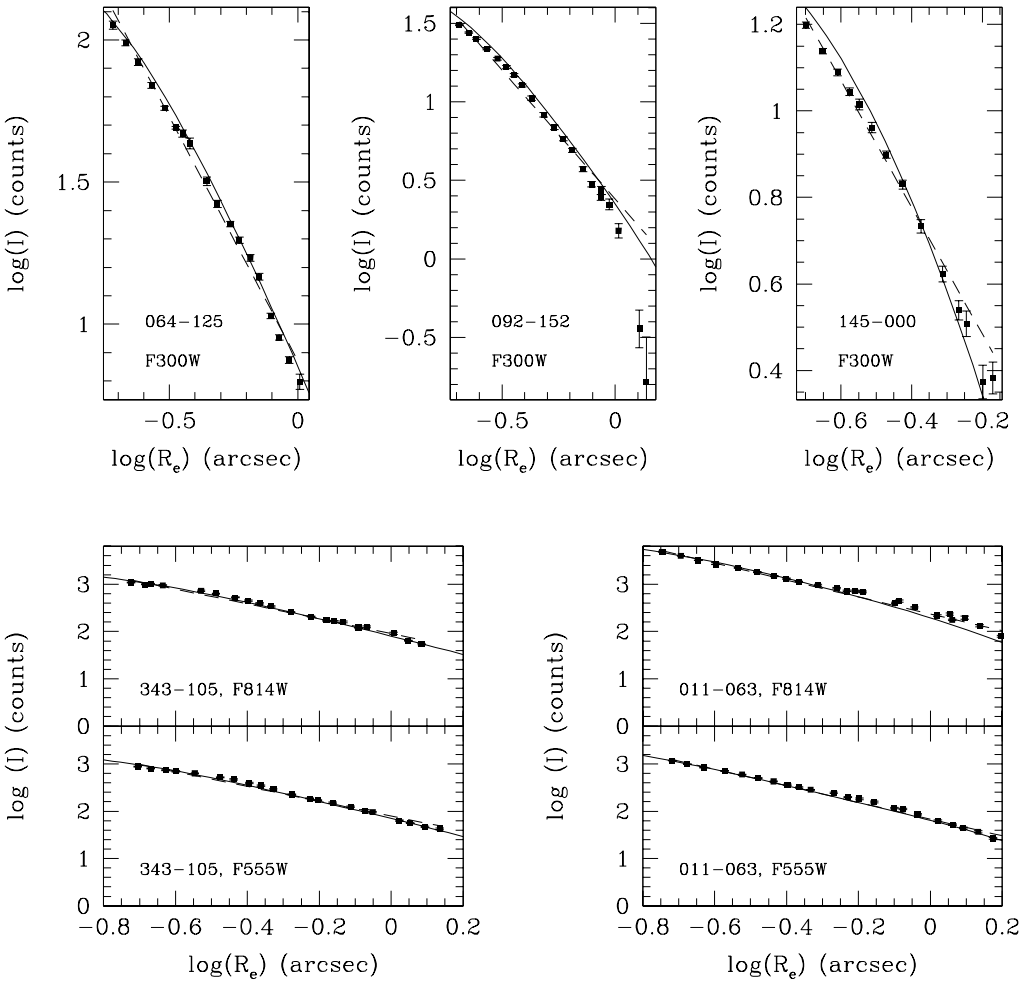

Fig. 5.17.— Continued.

5.3.3 Structural parameters: correlations and Milky Way comparison

The structural parameters of globular clusters indicate both their current dynamical conditions and their histories. It is therefore of interest to compare the measurements of M31 globular clusters to those of clusters in other galaxies, primarily the Milky Way, and to search for correlations among their properties. We used the June 1999 version of the Harris (1996) catalog as our source of Milky Way cluster properties[5], supplemented by the White & Shawl (1987) data for cluster ellipticities.

We first consider the appearance of the clusters on the sky as measured by ellipticity and position angle. We measure a median ellipticity for the M31 clusters of 0.11 ± 0.01. This is in reasonably good agreement with the measurements of Staneva et al. (1996) and Lupton (1989), who measured values of 0.09 ± 0.04 and 0.08 ± 0.02 for larger and smaller samples of clusters, respectively. It is slightly larger than the mean ellipticity measured for Milky Way clusters (White & Shawl 1987), and smaller than those measured for the LMC and SMC clusters (Kontizas et al. 1989, 1990). The median position angle on the sky is 76 ± 6 degrees east of north. As shown in Figures 5.18 and 5.19, the position angles show no tendency to align with either the major or minor axes of M31, or with the local direction toward the center of the galaxy. This indicates that tidal forces are not responsible for the M31 GCs' ellipticities; White & Shawl (1987) came to the same conclusion for the Milky Way clusters.

If tides are not the cause of cluster flattening, what is? The next obvious candidate is rotation. A general picture, summarized by Davoust & Prugniel (1990), is that GCs form with some angular momentum and are initially flattened by rotation. As escaping stars carry away angular momentum and mass, clusters rotate more slowly and become rounder. The LMC and SMC clusters are more elliptical both because they are younger and because the weaker tidal fields of the Clouds produce slower cluster dynamical evolution. The rotation scenario predicts several observable correlations: (1) more compact clusters, which evolve more quickly, should be rounder. White & Shawl (1987) found this to be the case for Milky Way clusters. We plot ellipticity against several other parameters for both sets of clusters in Figure 5.20. We find no relation between c and ϵ for Milky Way clusters, but we do see that low-concentration clusters in M31 are generally more elliptical, as predicted. (2) Clusters with larger velocity dispersions should rotate

[5]Note that the central surface brightness measurements reported there are not corrected for extinction, although the absolute magnitudes are.

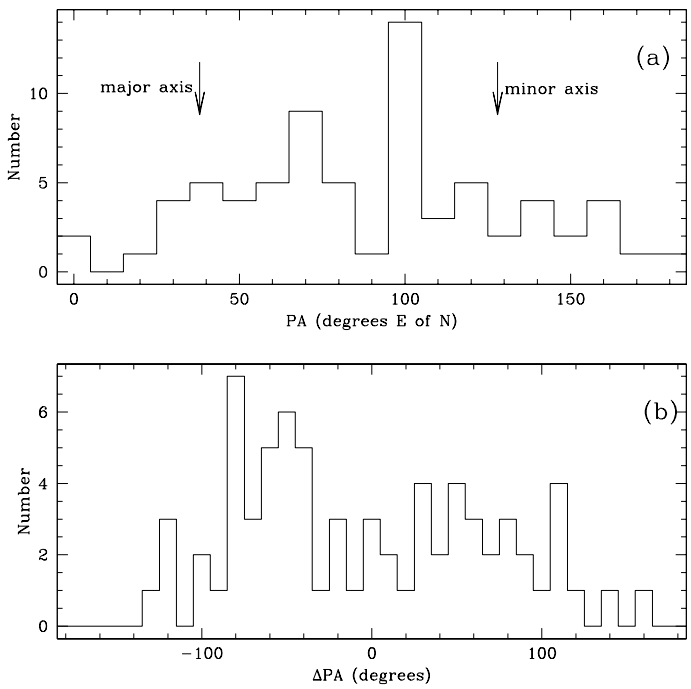

Fig. 5.18.— Position angles of M31 globular clusters: (a) on the sky and (b) with respect to the local galactocentric direction.

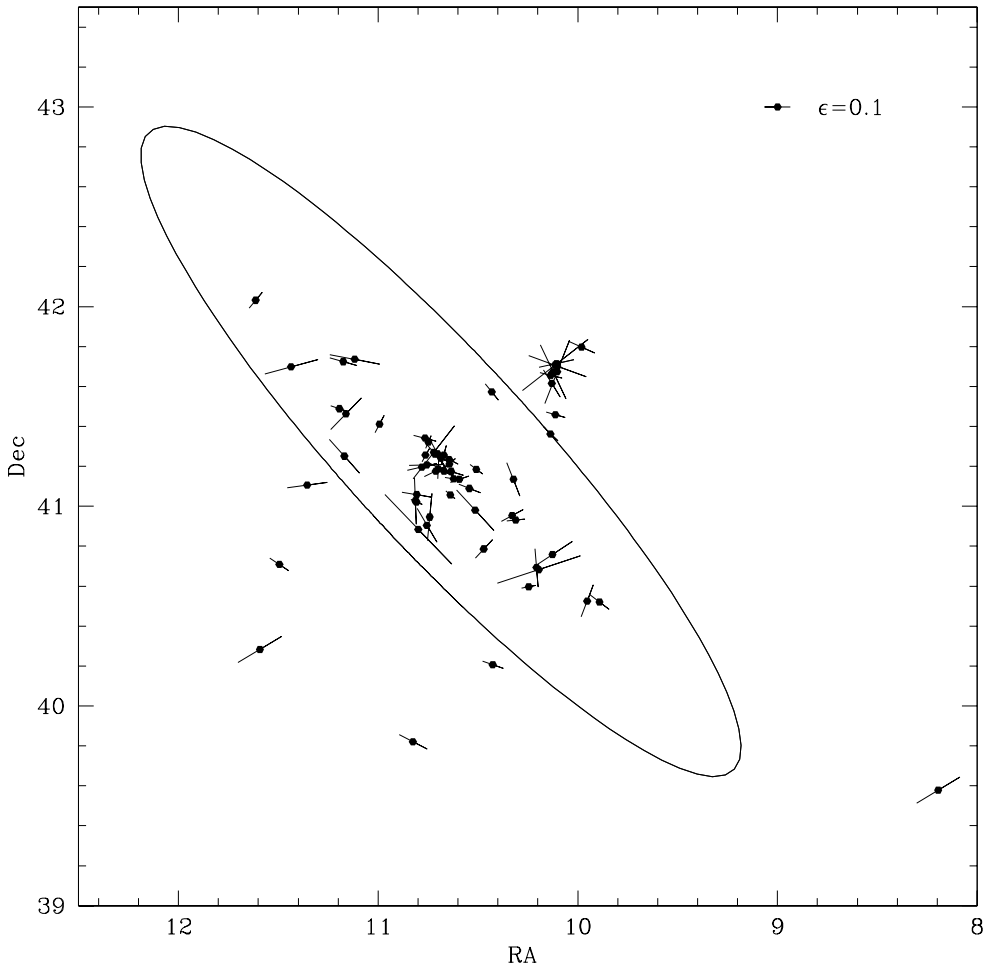

Fig. 5.19.— Ellipticities and position angles on the sky of M31 globular clusters. Size of bar indicates magnitude of ellipticity ϵ.

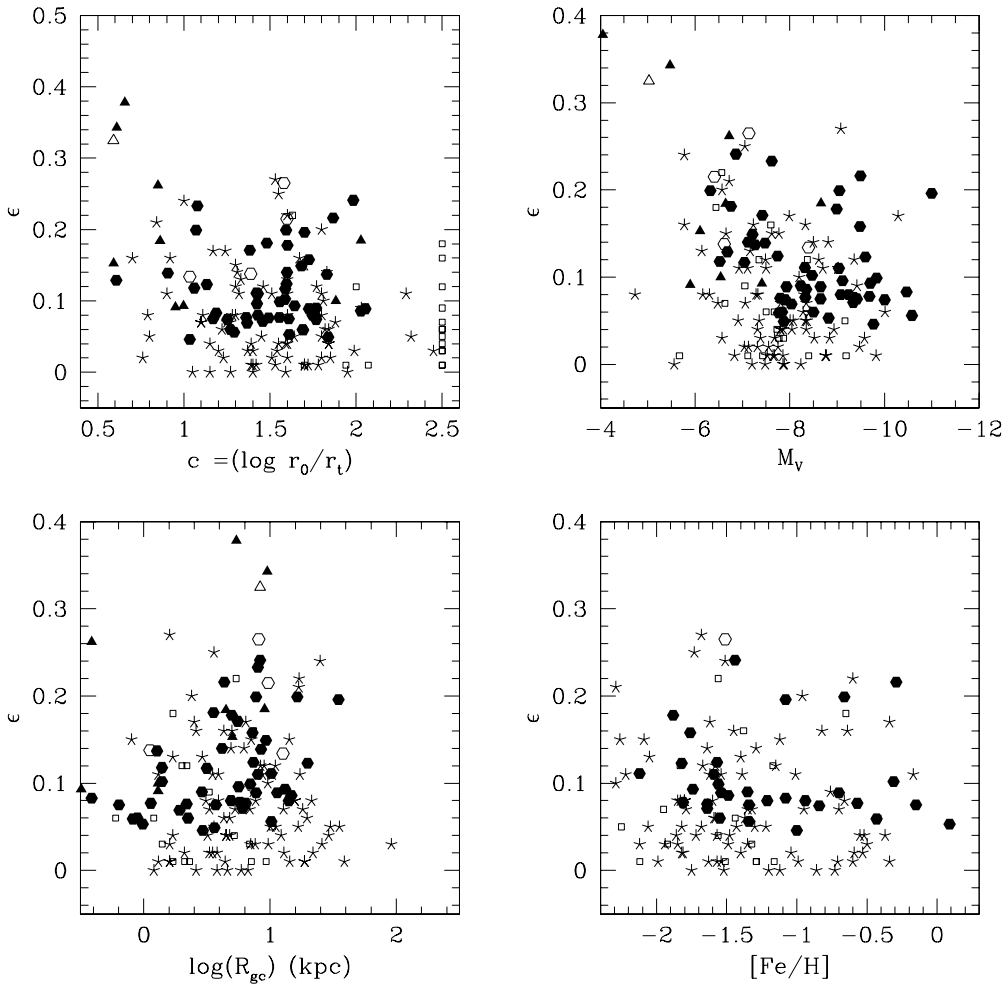

Fig. 5.20.— Ellipticity versus other properties of M31 globular clusters. Hexagons are previously-known globulars and triangles are new objects. Filled symbols are likely M31 globular clusters; outlined symbols are blue clusters which may not be old GCs. Stars are non-core-collapsed Milky Way GCs; small squares are core-collapsed Milky Way GCs.

more slowly, and hence be rounder, due to conservation of angular momentum in the sum of internal velocity dispersion and rotation (Staneva et al. 1996). The authors claim to see a relation between ϵ and σ_v in M31 clusters in their data, but when we add later velocity dispersion measurements by Djorgovski et al. (1997) to Staneva et al.'s ellipticity data (see Figure 5.21), we see no obvious correlation.

Conflicting claims have been made about correlations of globular cluster ellipticities with other properties. Lupton (1989) claimed that ellipticity is anti-correlated with metallicity for both Milky Way clusters and his sample of 18 M31 clusters; Staneva et al. (1996) and White & Shawl (1987) found no such correlation. Our data in Figure 5.20 show little correlation, but if we bin the data in [Fe/H] and compute the median ellipticity of the clusters in each bin, we find that the most metal-poor objects are slightly more elliptical. This is not a strong conclusion since only about half our sample of clusters have measured metallicities. Davoust & Prugniel (1990) claimed a relation between luminosity and ellipticity for both M31 and Milky Way clusters, with the brightest clusters being the roundest; Staneva et al. (1996) found the same for M31.[6] Lupton (1989) did not find a luminosity-ellipticity relationship in his sample. van den Bergh & Morbey (1984) find the opposite relation for LMC clusters, and suggest that high-mass LMC clusters have difficulty shedding angular momentum. Possibly this reflects differences in formation processes between clusters in the LMC and the Milky Way/M31. Our data again show no clear correlation, but with binned data we do find a tendency for the least-luminous clusters to be more elliptical.

White & Shawl (1987) found that the most elliptical Milky Way clusters were found near the galactic plane but did not claim a correlation of ϵ with R_{gc}; Staneva et al. (1996) and Lupton (1989) also found no such correlation in their M31 cluster samples. We find a slight trend in the opposite direction: the innermost clusters are slightly less elliptical. Djorgovski & Meylan (1994) found no correlations of ellipticity with any other properties, and suggest that this may be because of the difficulties in measuring ellipticity: the effect and its measurement errors are of comparable size. Our results suggest that there may be more subtle effects in the M31 globular cluster system which DM94 did not find in the MW system. Norris (1987) found a correlation between CN enhancement and cluster ellipticity in a sample of 12 Milky Way clusters, which he attributed to a connection between cluster and stellar rotation in these systems. Some M31 clusters are known to be CN-enhanced relative to Milky Way clusters (Burstein et al. 1984; Brodie &

[6]The brightest clusters in each galaxy, ω Cen and G1, are both quite flattened, with $\epsilon \sim 0.2$. There have been suggestions that neither object is a true globular cluster (Hilker & Richtler 2000; Meylan et al. 2000), so their failure to follow this trend may not be meaningful.

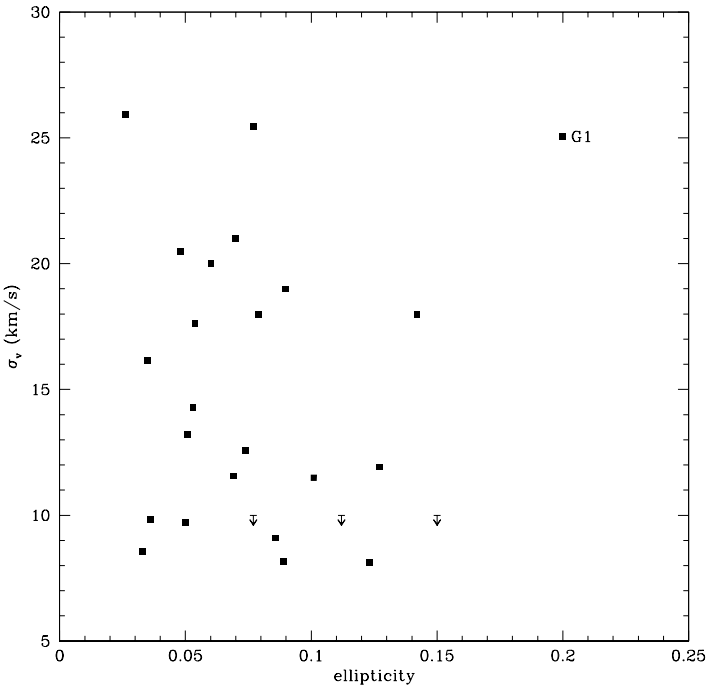

Fig. 5.21.— Ellipticities and velocity dispersions of M31 globular clusters. Velocity dispersions are from Djorgovski et al. (1997) or Peterson (1989); ellipticities are from Staneva et al. (1996), Lupton (1989), and this work. See footnote 6 for discussion of G1.

Huchra 1991), and Davoust & Prugniel (1990) speculate that perhaps the slightly higher median ellipticity for M31 clusters indicates a connection between cluster rotation and CN enhancement. It would be extremely interesting to compare CN index measurements and ϵ in M31 clusters, but higher-resolution spectroscopic data than are presently available are required to do a reliable analysis.

Djorgovski & Meylan (1994) (hereafter DM94) present an instructive discussion of the connections among integrated properties of Milky Way GCs, and we follow their approach in trying to understand the properties of M31 GCs. DM94 consider 13 properties of Milky Way GCs: absolute magnitude M_V, concentration c, scale radius r_0, half-light radius r_h, central surface brightness $\mu_V(0)$, mean surface brightness inside the half-light radius $\langle\mu_V\rangle_h$, central luminosity ρ_0, relaxation time at the scale radius t_{rc}, relaxation time at the half-light radius t_{rh}, metallicity [Fe/H], central velocity dispersion σ_0, distance from the Galactic center R and distance from the Galactic plane Z_{gp}. Only nine of these parameters are independent: $\langle\mu_V\rangle_h$, ρ_0, t_{rc}, and t_{rh} are derived from combinations of the others. We consider only the independent parameters, excluding Z_{gp} (we can measure only the projected distance to the center of M31, R_{gc}; although it is a combination of R and Z_{gp}, we use it as a substitute for R) and σ_0 (only the global velocity dispersion σ_v has been measured, for a few of our M31 clusters). We consider both the correlations between M31 GC properties and the contrast with the equivalent properties of Milky Way clusters. We consider several different samples of M31 clusters: the largest ($N = 72$) includes all the objects for which we measured structural parameters, but will be the most contaminated by non-clusters and low-precision measurements. The sample we use in the fundamental plane analysis contains only red objects likely to be old M31 GCs ($N = 62$). The smallest sample ($N = 42$) includes only objects previously cataloged as old M31 globular clusters with reliable surface brightness measurements in non-UV filters. We corrected integrated magnitudes and central surface brightness values for M31 clusters for both foreground and internal (M31) extinction, using the reddening values derived in Chapter 2. M_V for M31 GCs was computed assuming $(m - M)_{0,\mathrm{M31}} = 24.47$; no corrections are made for the positions of the clusters along the line of sight, which are unknown. Table 5.7 gives the correlation coefficients between the parameters for each of the samples. The significant correlations are essentially the same for all the samples, but the more marginal trends vary somewhat.

Table 5.7. Correlation coefficients for M31 GC properties

	M_V	c	$\log(r_0)$	$\log(r_h)$	$\mu_V(0)$	[Fe/H]	$\log(R_{gc})$	ϵ
All data ($N = 72$)								
M_v	1.000	−0.493	0.243	−0.192	0.814	−0.034	−0.179	0.571
c	−0.446	1.000	−0.715	0.185	−0.605	0.152	0.031	−0.357
$\log(r_0)$	0.132	−0.665	1.000	0.545	0.574	−0.316	0.279	0.405
$\log(r_h)$	−0.210	0.085	0.592	1.000	0.100	−0.352	0.437	0.144
$\mu_V(0)$	0.812	−0.535	0.462	0.073	1.000	−0.083	0.032	0.721
[Fe/H]	−0.034	0.182	−0.289	−0.280	−0.139	1.000	−0.261	−0.134
$\log(R_{gc})$	−0.041	0.008	0.343	0.553	0.161	−0.353	1.000	0.352
ϵ	0.488	−0.182	0.216	0.158	0.630	−0.308	0.244	1.000
All but NGC 205 clusters ($N = 66$)								
M_v	1.000	−0.516	0.192	−0.278	0.833	0.063	−0.191	0.535
c	−0.407	1.000	−0.711	0.146	−0.639	0.228	0.033	−0.422
$\log(r_0)$	0.003	−0.658	1.000	0.584	0.543	−0.375	0.284	0.375
$\log(r_h)$	−0.313	0.066	0.601	1.000	0.038	−0.398	0.447	0.041
$\mu_V(0)$	0.825	−0.539	0.354	−0.011	1.000	0.008	0.019	0.693
[Fe/H]	0.029	0.240	−0.383	−0.346	−0.126	1.000	−0.263	−0.087
$\log(R_{gc})$	−0.083	0.035	0.317	0.546	0.096	−0.407	1.000	0.318
ϵ	0.402	−0.179	0.122	0.076	0.556	−0.310	0.236	1.000
Non-blue clusters ($N = 62$)								
M_v	1.000	−0.483	0.172	−0.258	0.806	0.028	−0.212	0.515
c	−0.390	1.000	−0.652	0.294	−0.565	0.079	0.085	−0.332
$\log(r_0)$	0.007	−0.610	1.000	0.523	0.504	−0.266	0.258	0.349
$\log(r_h)$	−0.337	0.217	0.539	1.000	0.037	−0.331	0.427	0.095
$\mu_V(0)$	0.806	−0.476	0.332	−0.059	1.000	0.039	−0.025	0.663
[Fe/H]	0.047	0.117	−0.265	−0.269	−0.064	1.000	−0.242	−0.085
$\log(R_{gc})$	−0.109	0.098	0.280	0.543	0.036	−0.348	1.000	0.321
ϵ	0.423	−0.151	0.154	0.117	0.558	−0.275	0.234	1.000
Best quality cluster sample ($N = 42$)								
M_v	1.000	−0.258	−0.002	−0.231	0.834	0.167	−0.222	0.398
c	−0.069	1.000	−0.735	0.028	−0.422	0.157	−0.010	−0.271
$\log(r_0)$	−0.260	−0.640	1.000	0.648	0.352	−0.395	0.372	0.252
$\log(r_h)$	−0.360	0.141	0.574	1.000	0.104	−0.508	0.542	0.058
$\mu_V(0)$	0.838	−0.175	−0.033	−0.124	1.000	0.102	−0.034	0.585
[Fe/H]	0.164	0.166	−0.415	−0.433	−0.039	1.000	−0.306	−0.109
$\log(R_{gc})$	−0.116	0.047	0.341	0.633	−0.010	−0.430	1.000	0.372
ϵ	0.303	−0.015	0.033	0.102	0.459	−0.312	0.322	1.000

Note. — The upper right half of the tables gives Spearman rank correlation coefficients; the lower left half gives Pearson correlation coefficients.

We first consider the cluster structural parameters, shown in Figure 5.22. While the Milky Way and M31 clusters follow essentially the same trends, the M31 clusters cover a much smaller range of sizes than the Milky Way clusters. The largest scale radius for a Milky Way cluster is 20.2 pc (Pal 14); the largest scale radius we measured for a confirmed M31 GC is 6.1 pc (468–000). The lack of very large clusters in the M31 sample is not particularly surprising: most of the Milky Way clusters with large r_0 are the 'Palomar'-type clusters, and a thorough search for such faint, distant clusters around M31 has yet to be done. Our HST fields cover such a small area of the sky, relative to the size of M31, that it would be surprising if we *had* found any Palomar-type clusters.[7] As a result, we find that the M31 clusters are somewhat smaller than the Milky Way clusters: the median r_0 of the M31 clusters is 0.77 pc, while the median for the Milky Way clusters is 1.05 pc.

Except for the lack of confirmed core-collapsed clusters in M31, discussed in the previous subsection, the range of concentration parameters is similar for the M31 and Milky Way clusters. The median values of c are 1.40 ± 0.04 for the non-core-collapsed Milky Way clusters and 1.43 ± 0.05 for the M31 clusters. Six of our objects fall into a region of parameter space where no Milky Way clusters are found: $c \lesssim 1.1$, $r_0 < 1$ pc (these objects are also the outliers in the r_0, r_h plot). The identities of all are questionable: 132–000 had been previously been classified as a star from its spectrum (Chapter 2), 268–000 is an unconfirmed C-class cluster from Battistini et al. (1987) with few known properties, M91 is an unconfirmed candidate first discovered by Mochejska et al. (1998), and the other three objects are new cluster candidates. All are faint and small; several have rather poor fits to the King models. Three are projected very close to the center of M31. Their estimated relaxation times at the half-mass radius range from 2×10^7 to 2.5×10^8 yr. The relaxation times are quite short compared to the Hubble time, and if the objects projected near the center of M31 are truly near the nucleus, they should have been destroyed long ago. We are uncertain about the nature of these objects, and suggest that higher resolution images and/or spectra may be needed to fully understand them.

We find good correlations among the M31 clusters' structural parameters, as DM94 did for the Milky Way clusters. The scale radius is strongly anti-correlated with c and strongly correlated with r_h. Allowing for our lack of large-r_0 M31 clusters, the two galaxies' clusters follow very similar trends in these parameters. The correlation between r_0 and r_h is not unexpected, since both measure the physical size of the clusters. The dispersion in r_h at a given r_0 is a consequence of the range in c. DM94 found a good correlation of r_0 and $\mu_V(0)$ for Milky Way

[7] The lowest surface brightness objects we expect to detect in our median exposure have $\mu_V \approx 20$.

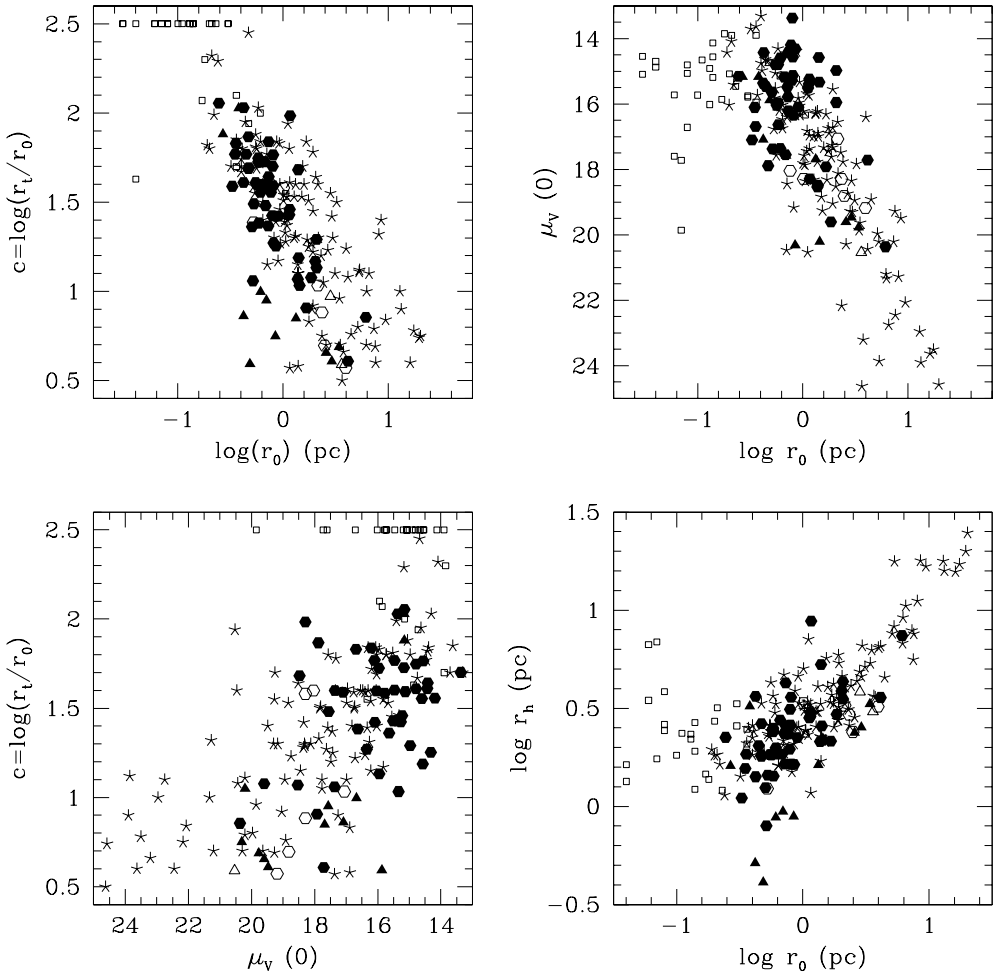

Fig. 5.22.— King model structural parameters for M31 and MW GCs. Symbols as in Figure 5.20. Milky Way clusters with collapsed cores have c set arbitrarily to 2.5.

clusters. We find a somewhat weaker one for M31 clusters, probably because our data cover a more restricted range in both parameters, but the Milky Way and M31 clusters again follow similar relations. The correlation between $\mu_V(0)$ and c is poorer for the M31 clusters than Milky Way, again probably due to lack of low surface brightness M31 clusters. DM94 (and also Bellazzini 1998) interpret the correlations between r_0, $\mu_V(0)$, and c as expected if GCs represent a family of objects with constant core mass evolving toward core collapse. McLaughlin (2000) disputes this interpretation, pointing out that cluster cores cannot be viewed as dynamically distinct entities since they do not obey the virial theorem. To confirm that the M31 clusters are well-characterized by King models, we performed a principal component analysis with the five structural parameters $M_V, \mu_V(0), r_0, r_h$, and c. We find, as did DM94, that the dimensionality of this dataset is $D = 3$, confirming that a three-parameter model is adequate to describe the data.

Examining the monovariate correlations between GC parameters can be instructive; it shows that GCs do not cover all available regions of parameter space. But the use of monovariate correlations can also be confusing, since there are so many individual parameters to consider and correlation is, of course, not causation. The three parameters usually used to describe globular cluster structure are concentration c, scale radius r_0, and central surface brightness $\mu(0)$. McLaughlin (2000) points out that a fourth parameter is needed: King models describe the mass and not the luminosity distribution, so the central mass-to-light ratio Υ_0 is needed to convert from one to the other. Any linearly independent combination of these parameters will also be a complete basis for describing GC structure, and we now follow the example of McLaughlin (2000) in considering the M31 clusters as being characterized by the following four parameters: c, Υ_0, luminosity $L = 10^{0.4(M_V(\odot)-M_V)}$ ($M_V(\odot) = 4.79$), and binding energy

$$E_b = -\frac{1}{2}\int_0^{r_t} 4\pi r^2 \rho\phi dr = \frac{1}{2}\int_0^{r_t} 4\pi r^2 \rho \left[\frac{GM}{r_t} + \sigma_0^2 W(r)\right] dr \qquad (5.2)$$

(where $W(r)$ is the dimensionless cluster potential $W(r) = [\phi(r_t) - \phi(r)]/\sigma_0^2$). McLaughlin shows that for regular 39 Milky Way clusters with σ_0 measurements, $\Upsilon_{V,0}$ has a constant value of 1.45 ± 0.1. If this same value is assumed for all Milky Way globulars, the binding energy can be computed using only photometric parameters. The resulting E_b is extremely well-correlated with L for Milky Way clusters. Υ_0 = constant and the $E_b - L$ correlation define a globular cluster fundamental plane in the four-dimensional parameter space, with a weaker $c - L$ correlation defining the distribution of globular clusters on the plane.

Guided by this work, we now try to determine the M31 GCs' place on this plane. This is complicated by the fact that only a few of our clusters have had Υ

measured, and these measurements are of the *global* mass-to-light ratio rather than the central value Υ_0. However, the 20 M31 GCs with reliable measurements of Υ have values consistent with those of Milky Way clusters (Dubath & Grillmair 1997; Djorgovski et al. 1997). To compute E_b for M31 clusters we therefore use McLaughlin's equation 5c:

$$E_b = 1.663 \times 10^{41} \mathrm{ergs} \left(\frac{r_0}{\mathrm{pc}}\right)^5 \left(\frac{\Upsilon_0 \rho_0}{\mathrm{M}_\odot \mathrm{pc}^{-3}}\right)^2 \mathcal{E}(c) \tag{5.3}$$

where $\Upsilon_0 = \mathrm{const.} = 1.45$ and ρ_0 is the central luminosity density, computed using

$$\rho_0 = \frac{10^{0.4(26.632 - \mu_V(0))}}{\mathcal{I}(c) r_0}, \tag{5.4}$$

$\mathcal{E}(c)$ and $\mathcal{I}(c)$ are the dimensionless binding energy and luminosity density computed using McLaughlin's equations B2 and B3.

Figure 5.23 shows the relations between E_b, L and c for both M31 and Milky Way clusters. This figure can be directly compared to Figure 6 of McLaughlin; the Milky Way data are the same in both. It is clear that that, with the exception of a few outliers, the M31 clusters follow the same $E_b - L$ and $c - L$ relations as the Milky Way clusters. The best-fit straight line to the 'non-blue' M31 clusters (solid points) is $\log E_b = (1.81 \pm 0.16) \log L + (40.86 \pm 0.79)$ (1σ uncertainties), which compares very well to the line for the Milky Way clusters, $\log E_b = (2.05 \pm 0.08) \log L + (39.89 \pm 0.38)$. The Spearman rank correlation coefficient of E_b against $\log L$ for the M31 clusters is 0.78, and the RMS scatter about the least-squares fit is 0.70 dex. This is not quite as good as the correlation for the Milky Way clusters, but we would hardly expect it to be, given the larger observational errors in parameters for M31 clusters. The scatter does decrease if the most obvious outliers are removed from the M31 fit. The $c - L$ correlation is not as strong as the $E_b - L$ correlation, but is seen to be essentially similar for the M31 and Milky Way clusters. McLaughlin fits the 'rough dependence' $c = -0.57 + 0.4 \log L$ to the Milky Way clusters — the solid line in Figure 5.23 — but it is not clear exactly how this fit is derived. We find best-fit straight lines of $c = -0.42 + 0.37 \log L$ for (non-core-collapsed) M31 clusters, and $c = -0.28 + 0.33 \log L$ for M31; the two sets of GCs are again quite similar.

The outliers in Figure 5.23 also deserve attention given that the correlation is otherwise quite good. The object at $M_V = -9.7, \log E_b = 48.5$ is 068–130, a cluster which is also the most conspicuous outlier in a plot of M_V against $\mu_V(0)$. This object has a large measured extinction, which is quite uncertain because of its uncertain [Fe/H]. If the reddening were reduced to the foreground value of 0.24, the

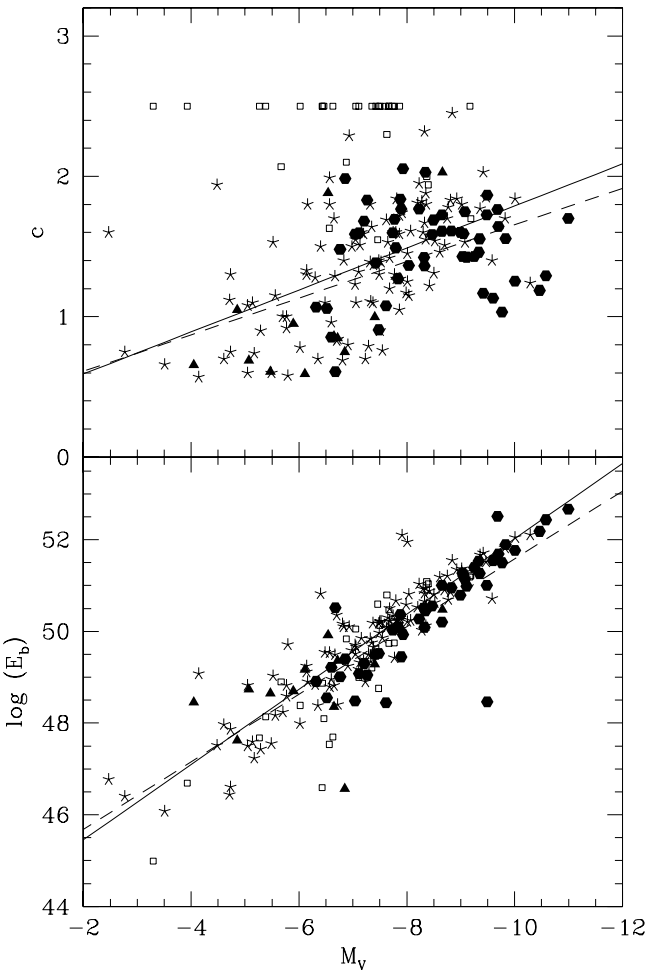

Fig. 5.23.— Fundamental plane correlations for M31 and MW GCs; solid lines are least-squares fits for Milky Way clusters, dashed lines are fits for M31 clusters. Symbols as in Figure 5.20.

cluster would move to $M_V = -8.35, \log E_b = 47.6$, closer to (but still offset from) the $E_b - L$ relation. There is also the possibility that 068–130 is a background galaxy (although for this to be the case, its radial velocity as measured by Huchra et al. (1991), -257 ± 33 km s^{-1}, would have to be seriously in error). The object at $M_V = -6.85, \log E_b = 46.6$ is M91, which is also one of the outliers in the r_0, c plot in Figure 5.22. It has not been spectroscopically confirmed as a cluster, and is only barely resolved, so it might also be a background galaxy.

It is important to point out that the $E_b - L$ correlation is non-trivial, even though it is effectively one of $\rho_0^5 {r_0}^5$ against $\rho_0 {r_0}^3$. McLaughlin shows that while $\rho_0 r_0$ and r_0 are both correlated with L, the scatter in these two relations is much larger and is anti-correlated: the specific combination $(\rho_0 r_0)^5$ is much more tightly correlated with L. McLaughlin shows that the weak dependence of r_h on L (anticipated by van den Bergh 1995), especially once corrected for R_{gc}, leads to the $E_b - L$ correlation. In Figure 5.24 we show r_h against R_{gc} and L for Milky Way and M31 clusters and find that the M31 clusters again follow the Milky Way clusters' trend. The dependence of cluster size on luminosity is removed once the dependence on galactocentric distance is removed in the variable $r_h^* = r_h/(R_{gc}/8\,\mathrm{kpc})^{0.4}$. M31 clusters have a somewhat smaller r_h^* than Milky Way clusters at the same L. This is likely due to missing large, low surface brightness clusters in the M31 sample.

McLaughlin finds that $M/L, L$ and c are relatively insensitive to Milky Way clusters' galactic position and metallicity. We have presented a detailed discussion of the relations of [Fe/H], R_{gc} and M31 GC luminosity elsewhere (Chapter 4), and will not consider them here. There are also the additional complications that only about half of our sample of clusters has measured metallicities, and that our sample lacks faint clusters. We show in Figure 5.25 an analog of McLaughlin's Figures 9 and 10; there is clearly little effect of R_{gc} or [Fe/H] on the parameters or correlation. McLaughlin finds that the $E_b - L$ relation is regulated by R_{gc} (the lowest-energy clusters lie at the largest values of R_{gc}); the normalized binding energy, $\log E_b^* \equiv \log E_b + 0.4 \log(R_{gc}/8\mathrm{kpc})$, removes this dependence. We find essentially no effect of R_{gc} on the $E_b - L$ relation for M31 clusters. This may be because the the projected R_{gc} does not sample the true full range of R_{gc} for M31 clusters, and/or because our sample lacks the large, loosely-bound Palomar-type clusters in M31. The lack of effect of [Fe/H] on the $E_b - L$ correlation is not necessarily a problem for our finding in Chapters 3 and 4 that cluster age may be different for different metallicity groups in M31. McLaughlin points out that dynamical evolution might actually have clusters evolve *along* the correlation line, so clusters of different ages would still lie on it.

We note that the $E_b - L$ correlation is not dependent on the assumption that

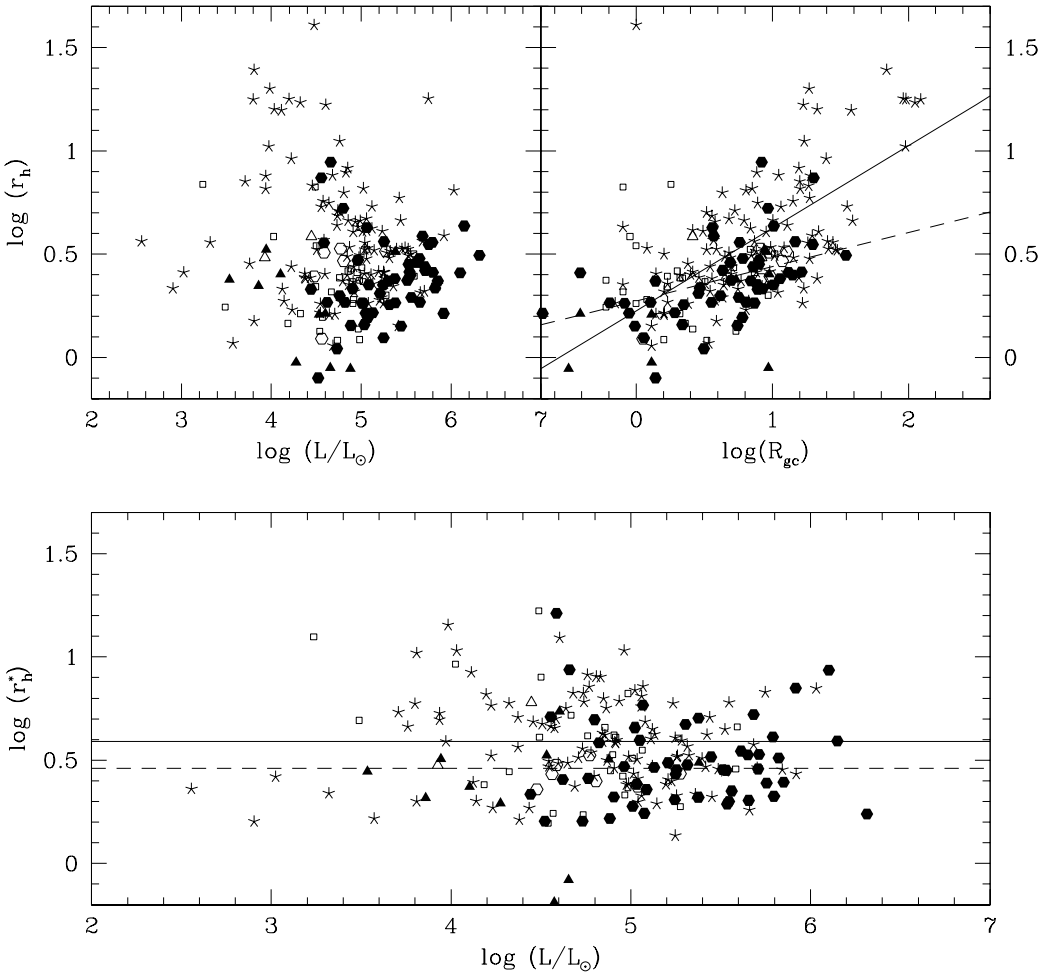

Fig. 5.24.— Half-light radius r_h versus luminosity and galactocentric distance for M31 and Milky Way GCs. R_{gc} is the true three-dimensional distance for Milky Way clusters, and the projected distance for M31 clusters. r_h^* is the normalized quantity $r_h/(R_{gc}/8\,\mathrm{kpc})^{0.4}$; the solid line in the bottom panel shows the median value for Milky Way clusters, $\log r_h^* = 0.59$; the dashed line is the median value for M31 clusters, $\log r_h^* = 0.46$. Symbols as in Figure 5.20.

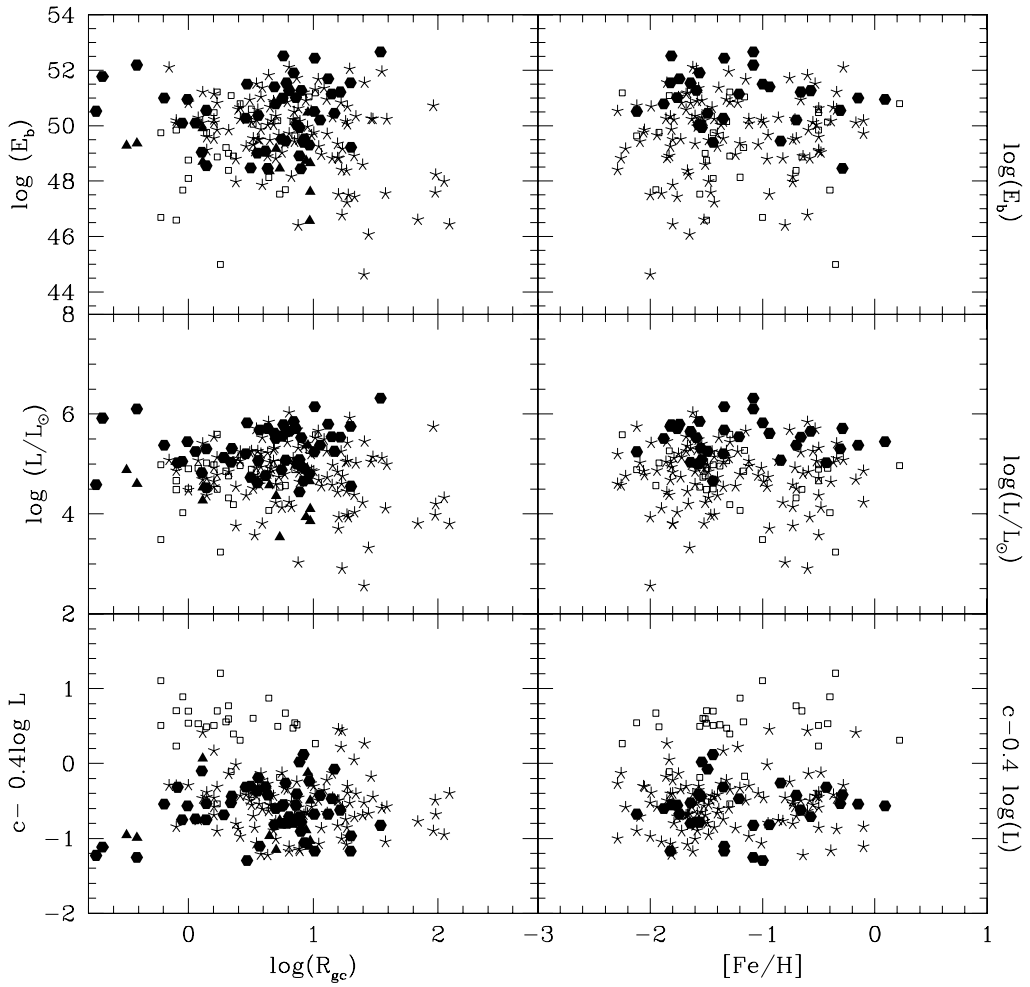

Fig. 5.25.— Fundamental plane parameters versus metallicity and R_{gc} for M31 and MW GCs. Symbols and R_{gc} as in previous figure.

the Milky Way and M31 clusters have the same constant M/L. If the M31 clusters had a different (constant) (M/L), only the intercept of the correlation would be affected; the slope and scatter would not change. We show face-on and edge-on views of the globular cluster fundamental plane in Figure 5.26. It is clear that M31 and Milky Way clusters have a limited and very similar range of properties, controlled by strong correlations. If the reasons for the correlations can be traced back to the dynamics of cluster formation, a compelling theory of cluster formation and evolution might finally be at hand.

Motivated by the recent work of Kundu et al. (1999) and Larsen et al. (2001), we looked for structural differences between metal-rich and metal-poor subgroups of M31 GCs. These might be expected since differences in radial distribution and kinematics between the two groups are well-established (Huchra et al. 1991), and we have previously suggested that there are also age and luminosity differences. We tried to assign as many clusters as possible to one group or the other. This was simple for the objects with spectroscopic metallicities; for objects without such information, we used the color-derived metallicities from Chapter 2, or an estimate based on the HST $V-I$ color (the same criterion as Larsen et al. 2001). Following Larsen et al. (2001) we compute median r_h values for metal-rich and metal-poor groups, and find similar results: the metal-rich clusters are systematically smaller. The median sizes for the two groups are similar to what the previous works found for other galaxies: 2.17 pc for the metal-rich clusters and 2.76 pc for the metal-poor ones. Figure 5.27 shows size distribution for the two groups. However, some of this effect could be due to R_{gc}: metal-rich clusters are more likely to be found near the center of M31, and we have already shown that there is a gradient of r_h with R_{gc}. Restricting our view to clusters with $R_{gc} > 2$ kpc, we find that there is still a size difference between the two metallicity groups. There is a similar difference if r_0 is compared instead of r_h, but no measurable difference for $\mu_V(0)$ or c. We caution that a KS test does not show the size differences to be statistically significant, and the small number of metal-rich clusters makes our conclusions uncertain, but the correspondence with the results for the Milky Way and other galaxies is certainly suggestive. The size difference could indicate the different pericenter distances of the clusters' orbits, as might be expected from their different kinematics.

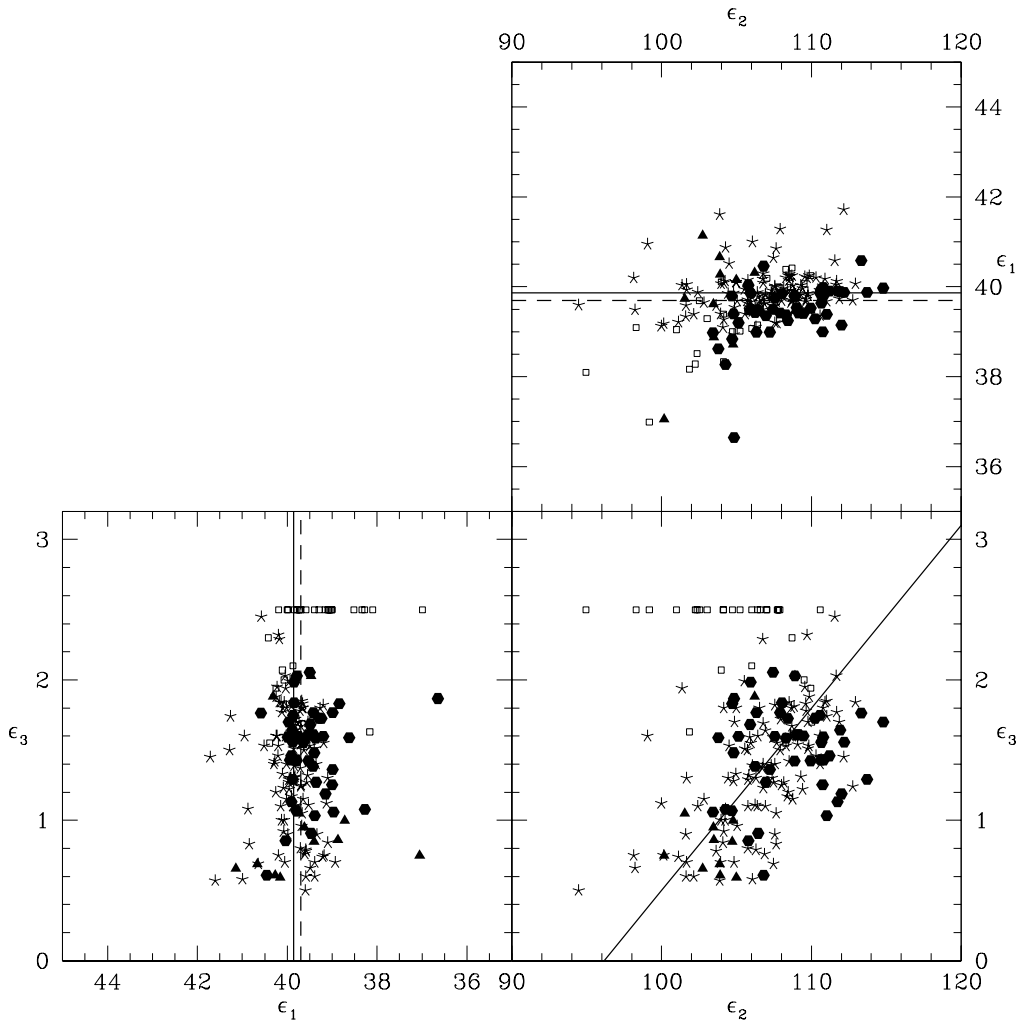

Fig. 5.26.— Face on (lower right) and edge-on (lower left, upper right) views of the globular cluster fundamental plane. The three dimensions used are the same as those in McLaughlin (2000): $\epsilon_1 \equiv \log E_b^* - 2.05 \log L$, $\epsilon_2 \equiv 2.05 \log E_b^* + \log L$, $\epsilon_3 \equiv c$. The lines in the edge-on views are the median values of ϵ_1: 39.86 for the Milky Way clusters (solid line), and 39.69 for the M31 clusters (dashed line). The solid line in the face-on view is McLaughlin's fit for the outer Milky Way clusters. Symbols as in Figure 5.20.

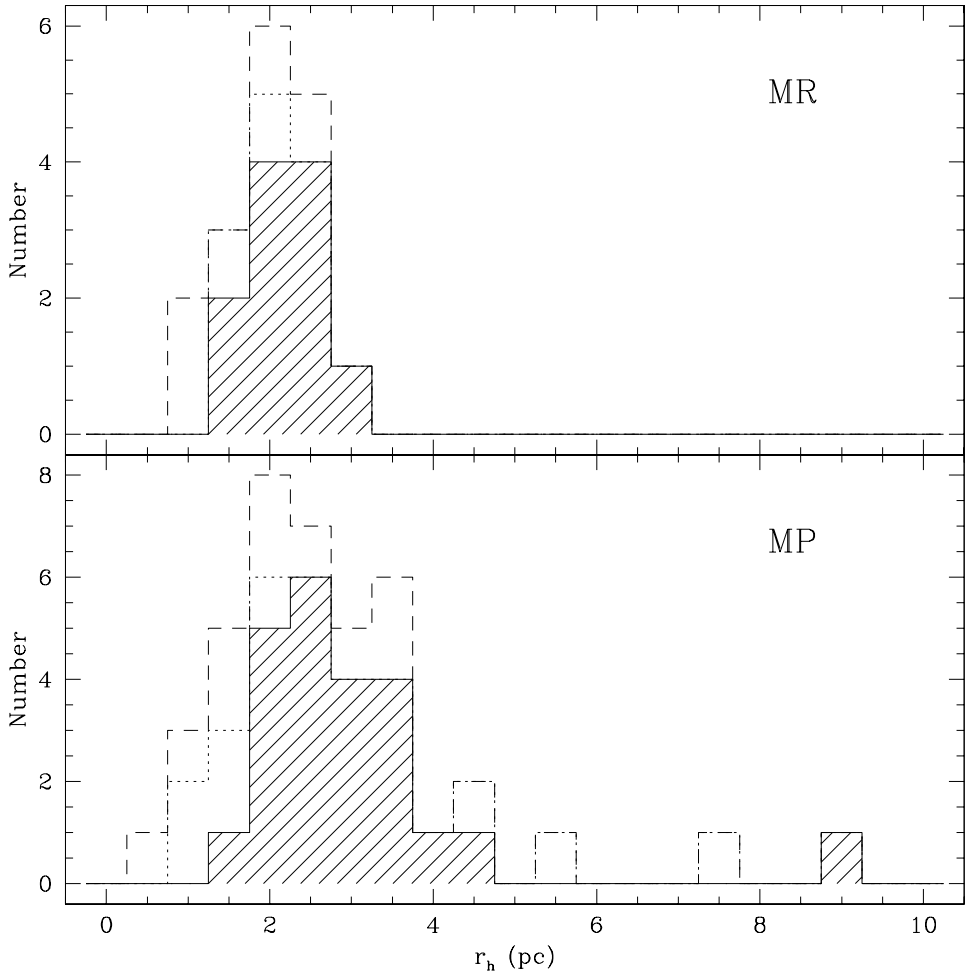

Fig. 5.27.— Size distribution of M31 globular clusters in two metallicity groups. Solid line/shaded histogram includes only clusters with spectroscopic metallicities. Dotted line histogram also includes clusters with color-derived metallicities from Chapter 2. Dashed line histogram also includes clusters with rough metallicity indicators from single colors.

5.4 Summary

Using the Hubble Space Telescope Archive to search for M31 globular clusters in WFPC2 images, we present the discovery of a number of new cluster candidates and an improved estimate of the completeness of existing cluster catalogs. As expected, the existing catalogs are least complete for faint clusters and clusters very near the center of M31. The completeness is very high to the magnitude limits usually used for computing the globular cluster luminosity function. We also report the discovery of some 20 objects which may be M31 open clusters.

We use the HST images of the good-quality candidates to measure the clusters' sizes, shape parameters, and best-fit King model parameters. Cluster departures from sphericity are consistent with being caused by rotation, although there are also indications of relations between ellipticity and luminosity and metallicity. There is great similarity between Milky Way and M31 GCs' structural parameters; both are well-described by the three-parameter family of King models. The correlations between structural parameters are very similar for Milky Way and M31 clusters, and the tightest correlation known for Milky Way GCs — binding energy with luminosity — is also followed by the M31 clusters. The M31 and Milky Way clusters have very similar fundamental planes, and this implies that the formation and evolution of GCs must have been very similar in the two galaxies. If additional galaxies' GCs have similar fundamental planes, this will strengthen the case for a 'universal' GC formation mechanism, in which GC properties are controlled by very few parameters (possibly the initial protocluster gas mass; McLaughlin 2000). Metallicity may play a small role in cluster properties: while there is no direct correlation of M31 cluster structural parameters with metallicity, our data suggest that the half-light radii of metal-rich and metal-poor sub-groups may be slightly different.

Chapter 6

Conclusions

6.1 Thesis summary

At the beginning of this thesis, I set out to (1) assemble of a catalog of modern, reliable measurements of integrated properties of M31 globular clusters; (2) compare the properties of M31 globular clusters with those of Milky Way globulars; and (3) test modern theories of galaxy and globular cluster system formation using the comprehensive picture of the M31 globular cluster system.

Chapter 2 is the main effort toward the first goal. It describes the creation of a comprehensive list of M31 globular clusters and candidates, and compilation of the best available photometric and spectroscopic data for each object. Many of the observations presented in this chapter were newly-acquired using a number of different telescopes and instruments; the remainder were compiled from the literature with careful attention paid to the reliability of the data sources. Several important results are also contained in this chapter. I confirmed the similarity of the color-metallicity relationships for the M31 and Milky Way globular clusters. This shows that the stellar populations of the two globular cluster systems are at least broadly similar and provides an important method for estimating the metallicity of extragalactic globular clusters without spectroscopy. I used the M31 globular clusters as probes of the extinction law in M31 and found it to be similar to the Galactic extinction law. This is important not only for the study of M31 globular clusters, but for all work on M31 where internal extinction is relevant, including comparative studies of the two galaxies' interstellar media. I reconfirmed that the metallicity distribution of the M31 globular clusters is bimodal, and that the two metallicity groups have different spatial distributions and kinematics. This

is an important confirmation, since M31 is one of the few spiral galaxies whose globular clusters have been well-studied enough to show a distinction between metal-rich and metal-poor cluster subsystems.

Chapter 2 also discusses discrepancies between M31 and Milky Way globular cluster colors and the predictions of population synthesis models. The standard technique of plotting data and models in a two-color diagram makes it difficult to discern exactly where the discrepancies arise. In Chapter 3, I attempted to remedy the situation by developing a new comparison technique in which individual model colors are compared to the colors of clusters with the same metallicity. The comparison showed that the $U-V$ and $B-V$ colors of the models are systematically bluer than those of clusters at all metallicities. This has been noticed before and is likely due to problems with the spectral libraries used by the models. Aside from this offset, the models fit the data quite well, with a mean offset of < 0.05 mag. A surprising result is that younger-aged models are required to fit the highest-metallicity clusters' colors. While the absolute age calibration of the models is in doubt, the relative age ordering is less so, so this result implies that the metal-rich clusters in M31 are younger than the metal-poor clusters. A slightly younger age might have been anticipated, since chemical evolution in a galaxy takes time to enrich gas from [Fe/H] $= -1.5$ to -0.5, but most chemical evolution models predict that the time needed is only a few Gyr. The question of how the metal-rich clusters could be much younger than the metal-poor clusters is addressed in more detail in Chapter 4.

Chapter 4 contains another exploration of integrated photometry of M31 GCs, this time from the perspective of their integrated luminosities. The GCLF is used as a distance indicator and often calibrated with the M31 GCs, so it is important to understand any variation in the M31 GCLF. Computing the overall and 'halo' GCLFs, I found results very similar to those of previous authors. The GCLF peak colors were not significantly different from the mean cluster colors, indicating that there is no strong color-magnitude relationship for the halo clusters. I found that the M31 clusters were, on average, brighter near the galaxy center and that this was partially due to the radial distribution of metallicities — the metal-rich clusters were brighter than the metal-poor clusters. This was a surprise, since theoretical expectations for the effects of metallicity on mass-to-light ratios predicted that metal-rich clusters with the same mass function and age as metal-poor clusters should be fainter. Several factors, including age, mass, and IMF, affect GCs' luminosities, so there is no unique interpretation of the GCLF results. However, because of the results presented in Chapter 3, it was interesting to interpret the GCLF difference between metal-rich and metal-poor clusters in terms of an age

difference. Comparison with simple stellar population models shows that the GCLF differences could be explained if the metal-poor clusters were twice as old as the metal-rich ones. The difference in GCLF with radial position, for approximately equivalent metallicity distributions, corresponds to an age difference of 45% or (our preferred interpretation) a mass difference of a factor of 1.6. Such a mass difference might be expected; theory predicts that low-mass inner clusters are more easily destroyed by dynamical interactions with the parent galaxy, and the mass difference found is within the range of theoretical predictions.

If there really is a substantial age difference between metal-rich and metal-poor clusters in M31, what might be the cause? An intriguing possibility is that the metal-rich clusters were created during a merger event, where the merging components brought the metal-poor clusters along with them. Suggestions that there are sub-groups of globular clusters in M31 (Ashman & Bird 1993; Saito & Iye 2000) would tend to support this picture; such groups might have belonged to one of the original merging galaxies. Freeman (1999) suggested that M31 might have undergone a major merger which formed its metal-rich halo stars and large bulge. Unfortunately, independent confirmation of the merger hypothesis will be difficult to find; obvious merger signatures such as tidal tails or kinematic disturbances would have long since vanished. There have been suggestions that the Milky Way thick disk is the result of a major merger (e.g., Robin et al. 1996), but detecting a thick disk in M31 would be very difficult because of the galaxy's inclination. An independent confirmation of age differences between metal-rich and metal-poor clusters in M31 would be extremely helpful, and may be possible with color-magnitude diagrams.

The GCLF differences in M31 sub-samples could be due not to true differences between the groups but to selection effects. If metal-rich and central cluster samples are missing faint clusters, their GCLFs would of course appear too bright. I tried to address this question by using archival HST data to search for previously-unknown clusters in M31. To the magnitude limit used for the GCLF study, I found no significant difference in the completeness of the existing catalogs between the inner and outer regions. I did find a number of new cluster candidates in the innermost region $R_{gc} < 5'$, which validated my decision not to use this region in the GCLF study.

During the survey of HST fields, I discovered a number of new M31 GC candidates, and many more known M31 GCs. Most of these were not deliberately targeted with HST; they appear in fields imaged for other purposes or in 'parallel' fields imaged when another HST instrument was being used. The HST images of clusters found in the survey described in Chapter 4, plus additional clusters in fields

out to 150′ from M31, formed the basis for the work described in Chapter 5. This chapter describes the newly-found clusters and includes a quantitative estimate of the incompleteness of existing catalogs. As expected, the existing catalogs are reasonably complete to $V = 18$, after which the completeness drops off rapidly. The completeness does not show any particular trends with location; as mentioned above, the completeness of existing catalogs is worst near the very center of M31.

The high spatial resolution of HST images allows the study of the detailed internal properties of M31 GCs to an extent impossible from ground-based imaging. I found that about a dozen clusters had significant color gradients; most were bluer in the center, as has been found for Milky Way core-collapsed clusters. The (weak) trends of M31 cluster ellipticity with other parameters such as concentration and R_{gc} were consistent with the idea that clusters' ellipticities are caused by rotation, and inconsistent with the notion that they are caused by tidal forces. The clusters' surface brightness profiles were in most cases well-fit by Michie-King model profiles, with indications that some clusters may have extra-tidal stars and others may have experienced core collapse. However, the possible core-collapsed clusters cannot be clearly distinguished from highly-concentrated clusters with small core radii. With the exception of a few objects which are not confirmed clusters (and the fact that the sample is missing low-surface-brightness M31 clusters because of observational selection), the M31 clusters have the same range of King model parameters as Milky Way clusters. The correlations between parameters are also very similar for Milky Way and M31 clusters, and the tightest correlation known for Milky Way GCs — binding energy E_b with luminosity — is also followed by the M31 clusters. Measuring E_b for M31 clusters requires assuming a mass-to-light ratio, since few objects have measured masses. However, this affects only the normalization of E_b vs. L and not its slope (or scatter, if M31 clusters have a constant M/L like Milky Way clusters). The M31 and Milky Way globular clusters clearly have very similar structural properties.

This thesis provided a new view of the M31 GCS, using observational data not previously available for these objects. In analyzing these data I attempted to take theories and ideas about GCS and galaxy formation and evolution into account and to test them against the observations. The most important results of the thesis are the confirmation that metal-poor and metal-rich GCs in M31 are different systems, with different metallicity distributions (by definition), spatial distributions, and luminosity and color differences. I used the luminosity and color information to infer that the populations of GCs have substantially different ages, an interpretation which, although model dependent, has interesting implications for ideas about the formation of clusters and galaxies. The other important result

in this thesis is the confirmation that the M31 clusters, like Milky Way clusters, are well-described by King models with parameters confined to a very narrow range of values. This indicates that GCs must have fairly uniform formation and evolution mechanisms which regulate their properties.

6.2 Open questions and concerns

The most serious potential problem in the results presented here is associated with the estimation of extinction. Estimating individual clusters' extinctions required the assumptions that the extinction curve and cluster color-magnitude relations in M31 were similar to those in the Milky Way. I found that these assumptions were supported by the results, but the circular reasoning required is worrisome. If the reddening and extinction were systematically overestimated for the M31 metal-rich clusters (by having too shallow a slope for the color-metallicity relations), the clusters' corrected colors and magnitudes would be too blue and too bright, respectively. Similarly, underestimating the reddening of metal-poor clusters would result in their corrected colors and magnitudes being too red and too faint. Either error would affect the results on color and luminosity differences between the two groups. It would have been preferable to estimate the M31 clusters' extinction from data which did not involve the clusters directly, possibly high-resolution dust or molecular gas maps, but I was unable to find such data covering all of M31 at high enough spatial resolution. There would also have been a problem of determining whether individual clusters are on the near or far side of the disk. For the GCLF measurements, it would have been preferable to use K-band magnitudes, for which extinction corrections are minimal and could have been ignored. This was originally planned to be part of this thesis, but poor weather and instrument problems prevented me from acquiring the necessary data.

The GCLF work also suffers from the variable incompleteness of the existing M31 GC catalogs. My HST search covered only a fraction of the total M31 area; if it did not yield a true picture of the incompleteness, or if there is a population of still-undetected highly-extinguished metal-rich GCs near the center of M31, the results on the GCLF could still be in error. Several large-area CCD surveys of M31 are currently being carried out, led by M. G. Lee and P. Massey, and hopefully the cluster population detected in these surveys will have more spatially-uniform completeness. This work should also help to fill out the census of faint, low surface brightness, and distant M31 globular clusters.

The HST study of M31 clusters suffer from the fact that clusters are not

specific targets in many images; often the HST images are unusable for any purpose except cluster identification. Studies which specifically target M31 GCs will of course improve the measurements of their structural parameters, and one such is currently underway, a STIS snapshot survey conducted by Harris, Harris & McLaughlin. Their targets include faint clusters in M31 and very bright clusters in NGC 5128, which will permit the $E_b - L$ relationship for globular clusters to be explored over a greater luminosity range than is currently possible. Having a single filter and uniform exposure times in this study will also eliminate concerns about the systematic effects of filter and exposure time on recovered structural parameters.

The age difference recovered from integrated photometry should be confirmed with more precise age-dating methods. It may be possible to do this with HST color-magnitude diagrams; about 30 M31 GCs have deep enough HST images for CMDs to be made. As an example, Sarajedini et al. (2000) have used the shape of the horizontal branch in M33 clusters' HST CMDs to infer that M33 clusters have intermediate (~ 7 Gyr) ages. However, not all workers in the field agree that the second parameter shaping the clusters' horizontal branches really is age. Ideally one would age-date extragalactic clusters with similar techniques to those used for Milky Way clusters. Such a goal is part of the Design Reference Mission for the Next Generation Space Telescope (Rich & Neill 1999), and should also be feasible with proposed extremely large ground-based telescopes (OWL, GSMT, CELT) with adaptive optics.

An open question not directly addressed by this thesis is that of chemical abundance in M31 GCs. It is now well-established that some M31 GCs are over-abundant in nitrogen compared to Milky Way GCs of the same metallicity. The physical reason for this is unknown, as are its effects on the derived properties of the clusters. Published ground-based spectra are generally of too low a quality to permit the extensive investigation of this phenomenon. Space-based UV spectra were important in establishing nitrogen as the primary cause of CN overabundance (Ponder et al. 1998), but more work could clearly be done in this area both from the ground and from space.

6.3 Future prospects

The study of the M31 GCS is far from complete; as with most topics in astronomy, new observational techniques both provide answers to old questions and open up new questions. Some future studies of the M31 GCS have been mentioned in the

previous section, including new CCD surveys of M31, completion of the near-IR survey, and additional HST observations. Other data which will hopefully become available include two new spectroscopic surveys of M31 GCs by K. Perrett and P. Seitzer, which will allow both metallicities and radial velocities (and hence kinematics) to be measured with greater precision. High-resolution spectroscopy of M31 GCs with the Keck telescope, undertaken by S. Djorgovski and our group, will allow measurement of the clusters' velocity dispersions and yield vital information on mass-to-light ratios. High-resolution imaging with ground-based adaptive optics systems may allow the construction of more M31 globular cluster CMDs and density profiles from star-count analyses.

The improved picture of the M31 GCS gained from these studies should ideally be compared with more detailed theoretical pictures of how stars, clusters, and galaxies form and evolve. The importance of clustering in star formation has long been recognized (Lada et al. 1991), and scenarios for cluster formation are beginning to emerge which recognize that globular clusters may not be a distinct phenomenon, but part of a continuum of clustered star formation (Elmegreen & Efremov 1997). The relevance of star and cluster formation to galaxy formation is only beginning to be explored, and, aside from the broad-brush pictures of Eggen et al. (1962), Searle & Zinn (1978) and Ashman & Zepf (1998), the connections of cluster properties with galaxies' histories (for example, the relationship of cluster system metallicity with galaxy stellar metallicity and galaxy mass) are not well-understood. Also lacking is a comprehensive picture of how clusters with evolving stars and a realistic IMF evolve over time in realistic galaxy potentials, although steps in this direction have certainly been made (e.g., Portegies Zwart et al. 2001).

M31 is not the only external galaxy with GCs, of course, and the answers to questions about galaxy history and evolution will not come from M31 alone. To know if spirals' globular cluster systems are truly distinct from those of elliptical galaxies (as might be expected if the two galaxy types have different histories), we need a better understanding of GCs in spirals. The reason such a study does not already exist is simple: the study of GCS in spirals is much more difficult than in ellipticals. Nevertheless, important steps toward studies of star clusters in spirals have been taken (e.g., Larsen & Richtler 1999) and will continue. Together with many other areas of astrophysics, the study of extragalactic star clusters will help to answer the questions of 'How did our galaxy get to its current state?' and indirectly, 'How is it that we are here to ask questions about the universe?' It is my intention that this thesis contribute in some way towards an answer to these fundamental questions.

References

Abraham, R. G., Tanvir, N. R., Santiago, B. X., Ellis, R. S., Glazebrook, K., & van den Bergh, S. 1996, MNRAS, 279, L47

Adams, F. & Laughlin, G. 1999, The five ages of the universe (New York: Free Press)

Ajhar, E. A., Grillmair, C. J., Lauer, T. R., Baum, W. A., Faber, S. M., Holtzman, J. A., Lynds, C. R. C., & O'Neil, E. J. 1996, AJ, 111, 1110

Akritas, M. G. & Bershady, M. A. 1996, ApJ, 470, 706

Alton, P. B. et al. 1998, A&A, 335, 807

Arimoto, N. & Yoshii, Y. 1986, A&A, 164, 260

Armandroff, T. E. 1989, AJ, 97, 375

Armandroff, T. E., Da Costa, G. S., & Zinn, R. 1992, AJ, 104, 164

Armandroff, T. E. & Zinn, R. 1988, AJ, 96, 92

Arp, H. C., Baum, W. A., & Sandage, A. R. 1952, AJ, 57, 4

Ashman, K. A. & Bird, C. M. 1993, AJ, 106, 2281

Ashman, K. A., Bird, C. M., & Zepf, S. E. 1994, AJ, 108, 2348

Ashman, K. A. & Zepf, S. E. 1992, ApJ, 384, 50

—. 1998, Globular Cluster Systems (Cambridge: Cambridge University Press)

Ashman, K. M., Conti, A., & Zepf, S. E. 1995, AJ, 110, 1164

Aurière, M., Coupinot, G., & Hecquet, J. 1992, A&A, 256, 95

Baade, W. 1944, ApJ, 100, 137

Baade, W. & Arp, H. 1964, ApJ, 139, 1027

Bajaja, E. & Gergeley, T. E. 1977, A&A, 61, 229

Battistini, P. L., Bònoli, F., Braccesi, A., Federici, L., Fusi Pecci, F., Marano, B., & Börngren, F. 1987, A&AS, 67, 447

Battistini, P. L., Bònoli, F., Braccesi, A., Fusi Pecci, F., Malagnini, M. L., & Marano, B. 1980, A&AS, 42, 357

Battistini, P. L., Bònoli, F., Buonanno, R., Corsi, C. E., & Fusi Pecci, F. 1982, A&A, 113, 39

Battistini, P. L., Bònoli, F., Casavecchi, M., Ciotti, L., Federici, L., & Fusi Pecci, F. 1993, A&A, 272, 77

Baum, W. A., Hammergren, M., Thomsen, B., Groth, E. J., Faber, S. M., Grillmair, C. J., & Ajhar, E. A. 1997, AJ, 113, 1438

Baum, W. A. et al. 1995, AJ, 110, 2537

Baumgardt, H. 1997, A&A, 330, 480

Bellazzini, M. 1998, NewA, 3, 219

Bendinelli, O., Cacciari, C., Djorgovski, S., Federici, L., Ferraro, F. R., Fusi Pecci, F., Parmeggiani, G., Weir, N., & Zavatti, F. 1993, ApJ, 409, L17

Bendinelli, O., Zavatti, F., Parmeggiani, G., & Djorgovski, S. 1990, AJ, 99, 774

Berman, B. G. & Suchkov, A. A. 1991, Ap&SS, 184, 169

Bertin, E. & Arnouts, S. 1996, A&AS, 117, 393

Binney, J. & Merrifield, M. 1998, Galactic Astronomy (Princeton, NJ: Princeton University Press)

Blakeslee, J. P. & Tonry, J. L. 1996, ApJ, 465, L19

Blakeslee, J. P., Tonry, J. L., & Metzger, M. R. 1997, AJ, 114, 482

Blumenthal, G. R., Faber, S. M., Primack, J. R., & Rees, M. J. 1984, Nature, 311, 517

Bònoli, F., Delpino, F., Federici, L., & Fusi Pecci, F. 1987, A&A, 185, 25

Bònoli, F., Delpino, F., Federici, L., Fusi Pecci, F., & Longmore, A. J. 1992, A&AS, 96, 163

Bridges, T. J., Ashman, K. M., Zepf, S. E., Carter, D., Hanes, D. A., Sharples, R. M., & Kavelaars, J. J. 1997, MNRAS, 284, 367

Bridges, T. J. & Hanes, D. A. 1992, AJ, 103, 800

Brodie, J. P. & Huchra, J. P. 1990, ApJ, 362, 503

—. 1991, ApJ, 379, 157

Bruzual, G. & Charlot, S. 1996, version of models reported in Leitherer et al. 1996, PASP, 108, 996

Buonanno, R., Corsi, C. E., Battistini, P., Bònoli, F., & Fusi Pecci, F. 1982, A&AS, 47, 451

Burgarella, D., Kissler-Patig, M., & Buat, V. 2000, in ASP. Conf Ser. 211: Massive Stellar Clusters, ed. A. Lançon & C. Boily (San Francisco: ASP), 288

Burstein, D. & Heiles, C. 1984, ApJS, 54, 33

Burstein, D., Faber, S. M., Gaskell, C. M., & Krumm, N. 1984, ApJ, 287, 586

Buzzoni, A. 1989, ApJS, 71, 817

Capaccioli, M., Ortolani, S., & Piotto, G. 1991, A&A, 244, 298

Cardelli, J. A., Clayton, G. C., & Mathis, J. S. 1989, ApJ, 345, 245

Carr, B. J. & Rees, M. J. 1984, MNRAS, 206, 315

Carretta, E. & Gratton, R. G. 1997, A&AS, 121, 95

Chaboyer, B., Demarque, P., Kernan, P. J., & Krauss, L. M. 1996a, Science, 271, 957

Chaboyer, B., Demarque, P., & Sarajedini, A. 1996b, ApJ, 459, 558

Charlot, S., Worthey, G., & Bressan, S. 1996, ApJ, 457, 625

Ciardullo, R., Jacoby, G. H., Feldmeier, J. J., & Bartlett, R. E. 1998, ApJ, 492, 62

Cohen, J. G., Blakeslee, J. P., & Ryzhov, A. 1998, ApJ, 496, 808

Cohen, J. G. & Freeman, K. C. 1991, AJ, 101, 483

Cohen, J. G. & Matthews, K. 1994, AJ, 108, 128

Côté, P. 1999, AJ, 118, 406

Côté, P., Marzke, R. O., & West, M. J. 1998, ApJ, 501, 554

Couture, J., Racine, R., Harris, W. E., & Holland, S. 1995, AJ, 109, 2050

Covino, S., Pasinetti Fracassini, L. E., Malagnini, M. L., & Buzzoni, A. 1994, A&A, 289, 775

Crampton, D., Cowley, A. P., Schade, D., & Chayer, P. 1985, ApJ, 288, 494

Da Costa, G. & Armandroff, T. E. 1995, AJ, 109, 2533

Da Costa, G. S. & Mould, J. R. 1988, ApJ, 334, 159

Davoust, E. & Prugniel, P. 1990, A&A, 230, 67

De Marchi, G. & Paresce, F. 1999, in American Astronomical Society Meeting, Vol. 195, 312

Djorgovski, S. & King, I. R. 1984, ApJ, 277, L49

Djorgovski, S. & Meylan, G. 1993, in ASP Conf. Proc. 50, Structure and Dynamics of Globular Clusters, ed. S. G. Djorgovski & G. Meylan (San Francisco: ASP), 325

Djorgovski, S. & Meylan, G. 1994, AJ, 108, 1292

Djorgovski, S., Piotto, G., & Capaccioli, M. 1993, AJ, 105, 2148

Djorgovski, S., Piotto, G., & Mallen-Ornelas, G. 1991a, in ASP Conf. Ser. 13: The Formation and Evolution of Star Clusters, ed. K. Janes (San Francisco: ASP), 262–264

Djorgovski, S., Piotto, G., Phinney, E. S., & Chernoff, D. F. 1991b, ApJ, 372, L41

Djorgovski, S. G., Gal, R. R., McCarthy, J. K., Cohen, J. G., de Carvalho, R. R., Meylan, G., Bendinelli, O., & Parmeggiani, G. 1997, ApJ, 474, L19

Dolphin, A. E. 2000, PASP, 112, 1397

D'Onofrio, M., Capaccioli, M., Wagner, S. J., & Hopp, U. 1994, Memorie della Societa Astronomica Italiana, 65, 731

Dressler, A. 1980, ApJ, 236, 351

Dubath, P. & Grillmair, C. J. 1997, A&A, 321, 379

Durrell, P. R., Harris, W. E., Geisler, D., & Pudritz, R. E. 1996, AJ, 112, 972

Eggen, O. J., Lynden-Bell, D., & Sandage, A. R. 1962, ApJ, 136, 748

Elias, J. H., Frogel, J. A., Matthews, K., & Neugebauer, G. 1982, AJ, 87, 1029

Elmegreen, B. G. & Efremov, Y. N. 1997, ApJ, 480, 235

Elson, R. A. W. & Walterbos, R. A. M. 1988, ApJ, 333, 594

Fall, S. M. & Rees, M. J. 1985, ApJ, 298, 18

Fall, S. M. & Rees, M. J. 1988, in IAU Symp. 126: The Harlow-Shapley Symposium on Globular Cluster Systems in Galaxies, ed. J. E. Grindlay & A. G. D. Philip, Vol. 126 (Dordrecht: Reidel), 323

Federici, L., Bònoli, F., Fusi Pecci, F., Marano, B., Lipovetski, V. A., Niezvestny, S. I., & Spassova, N. 1993, A&A, 274, 87

Federici, L., Marano, B., & Fusi Pecci, F. 1990, A&A, 236, 99

Ferrarese, L. et al. 2000, ApJ, 529, 745

Forbes, D. A., Brodie, J. P., & Grillmair, C. J. 1997a, AJ, 113, 1652

Forbes, D. A., Brodie, J. P., & Huchra, J. P. 1996a, AJ, 112, 2448

—. 1997b, AJ, 113, 887

Forbes, D. A. & Forte, J. C. 2001, MNRAS, 322, 257

Forbes, D. A., Franx, M., Illingworth, G. D., & Carollo, C. M. 1996b, ApJ, 467, 126

Forbes, D. A., Grillmair, C. J., & Smith, R. C. 1997c, AJ, 113, 1648

Freeman, K. 1999, in The Stellar Content of Local Group Galaxies, IAU Symposium 192, ed. P. Whitelock & R. Cannon (San Francisco: ASP), 383

Frogel, J. A., Persson, S. E., & Cohen, J. G. 1980, ApJ, 240, 785

Fusi Pecci, F., Battistini, P., Bendinelli, O., Bònoli, F., Cacciari, C., Djorgovski, S., Federici, L., Ferraro, F. R., Parmeggiani, G., Weir, N., & Zavatti, F. 1994, A&A, 284, 349

Fusi Pecci, F., Cacciari, C., Corsi, C. E., Djorgovski, S. G., Federici, F., Ferraro, F. R., Parmeggiani, G., & Rich, R. M. 1996, AJ, 112, 1461

Gebhardt, K. & Kissler-Patig, M. 1999, AJ, 118, 1526

Geisler, D., Lee, M. G., & Kim, E. 1996, AJ, 111, 1529

Giacconi, R., Murray, S., Gursky, H., Kellogg, E., Schreier, E., Matilsky, T., Koch, D., & Tananbaum, H. 1974, ApJS, 27, 37

Girardi, L., Chiosi, C., Bertelli, G., & Bressan, A. 1995, A&A, 298, 87

Glass, I. S. & Feast, M. W. 1973, MNRAS, 163, 245

Gnedin, O. 1997, ApJ, 487, 663

Grillmair, C. J., Ajhar, E. A., Faber, S. M., Baum, W. A., Holtzman, J. A., Lauer, T. R., Lynds, C. R. C., & O'Neil, E. J. 1996, AJ, 111, 2293

Grillmair, C. J., Forbes, D. A., Brodie, J. P., & Elson, R. A. W. 1999, AJ, 117, 167

Gunn, J. E. 1980, in Globular Clusters, ed. D. Hanes & B. Madore (Cambridge: Cambridge University Press), 301

Harris, W. E., Harris, G. L. H., & McLaughlin, D. E. 1998, AJ, 115, 1801

Harris, W. E. & Pudritz, R. E. 1994, ApJ, 429, 177

Harris, W. H. 1988, in ASP Conf. Ser 4: The Extrgalactic Distance Scale, ed. C. Pritchet & S. van den Bergh (San Francisco: ASP), 231

Harris, W. H. 1991, ARA&A, 29, 543

—. 1996, AJ, 112, 1487

Harris, W. H. 2000, in Saas-Fee Advanced Course 28, Stellar Evolution in Star Clusters, ed. B. Binggeli & R. Buser (New York: Springer-Verlag), 1

Harris, W. H. & Racine, R. 1979, ARA&A, 17, 241

Heald, A. J., Griffiths, W. K., Penny, A. J., & Morris, P. W. 1999, MNRAS, 307, 789

Helfer, H. L., Wallerstein, G., & Greenstein, J. L. 1959, ApJ, 129, 700

Hernquist, L. & Mihos, J. C. 1995, ApJ, 448, 41

Hilker, M., Infante, L., & Richtler, T. 1999, A&AS, 138, 55

Hilker, M. & Richtler, T. 2000, A&A, 362, 895

Hodge, P. W. 1979, AJ, 84, 744

—. 1982, Atlas of the Andromeda Galaxy (Seattle: University of Washington Press)

—. 1992, The Andromeda Galaxy (Dordrecht: Kluwer Academic Publishers)

Holland, S. 1998, AJ, 115, 1916

Holland, S., Côté, P., & Hesser, J. E. 1999, A&A, 348, 418

Holland, S., Fahlman, G. G., & Richer, H. B. 1996, AJ, 112, 1035

—. 1997, AJ, 114, 1488

Holtzman, J. A., Burrows, C. J., Casertano, S., Hester, J. J., Trauger, J. T., Watson, A. M., & Worthey, G. 1995, PASP, 107, 1065

Holtzman, J. A. et al. 1992, AJ, 103, 691

Hubble, E. P. 1929, ApJ, 69, 103

—. 1932, ApJ, 76, 44

Huchra, J., Stauffer, J., & van Speybroeck, L. 1982, ApJ, 259, L57

Huchra, J. P. 1996, in ASP Conf. Ser. 92, From Stars to Galaxies: the Impact of Stellar Physics on Galaxy Evolution, ed. C. Leitherer, U. F. von Alvensleben, & J. Huchra (San Francisco: ASP), 597

Huchra, J. P., Brodie, J. P., Caldwell, N., Christian, C., & Schommer, R. 1996, ApJS, 102, 29

Huchra, J. P., Brodie, J. P., & Kent, S. M. 1991, ApJ, 370, 495

Hurt, R. L., Jarrett, T. H., Kirkpatrick, J. D., Cutri, R. M., Schneider, S. E., Skrutskie, M., & van Driel, W. 2000, AJ, 120, 1876

Ibata, R. A., Gilmore, G., & Irwin, M. J. 1994, Nature, 370, 194

Iye, M. & Richter, O.-G. 1985, A&A, 144, 471

Jablonka, P., Bica, E., Bonatto, C., Bridges, T. J., Langlois, M., & Carter, D. 1998, A&A, 335, 867

Jedrzejewski, R. 1987, MNRAS, 226, 1747

Kavelaars, J. J. & Hanes, D. A. 1997, MNRAS, 285, L31

King, I. R. 1966, AJ, 71, 64

Kinman, T. D. 1963, ApJ, 137, 213

Kissler-Patig, M. 1997a, A&A, 319, 83

—. 1997b, PhD thesis, Sternwarte Bonn

Kissler-Patig, M. 2000, in Reviews in Modern Astronomy 13: New Astrophysical Horizons, ed. R. E. Schielicke (Hamburg: Astronomische Gesselschaft), 13

Kissler-Patig, M., Brodie, J. P., Schroder, L. L., Forbes, D. A., Grillmair, C. J., & Huchra, J. P. 1998, AJ, 115, 105

Kontizas, E., Kontizas, M., Sedmak, G., & Smareglia, R. 1989, AJ, 98, 590

Kontizas, E., Kontizas, M., Sedmak, G., Smareglia, R., & Dapergolas, A. 1990, AJ, 100, 425

Kron, G. E. & Mayall, N. U. 1960, AJ, 65, 581

Kundu, A. 1999, PhD thesis, University of Maryland

Kundu, A., Whitmore, B. C., Sparks, W. B., Macchetto, F. D., Zepf, S. E., & Ashman, K. M. 1999, ApJ, 513, 733

Kurth, O. M., Fritze-von Alvensleben, U., & Fricke, K. J. 1999, A&AS, 138, 19

Kurucz, R. 1995, private communication

Lada, E. A., Evans, N. J., Depoy, D. L., & Gatley, I. 1991, ApJ, 371, 171

Landolt, A. U. 1992, AJ, 104, 340

Larsen, S. S., Brodie, J. P., Huchra, J. P., Forbes, D. A., & Grillmair, C. J. 2001, AJ, in press (astro-ph/0102374)

Larsen, S. S. & Richtler, T. 1999, A&A, 345, 59

—. 2000, A&A, 354, 836

Larson, R. B. 1993, in ASP Conf. Ser. 48: The Globular Cluster-Galaxy Connection, ed. G. H. Smith & J. P. Brodie (San Francisco: ASP), 675

Larson, R. B. & Tinsley, B. M. 1978, ApJ, 219, 46

Lee, M. G. & Kim, E. 2000, AJ, 120, 260

Leitherer, C. et al. 1996, PASP, 108, 996

Lejeune, T. 1997, PhD thesis, Univ. Louis Pasteur, Strasbourg & Astron. Institute of Basel University, Basel

Lloyd Evans, T. 1978, MNRAS, 182, 293

Lupton, R. H. 1989, AJ, 97, 1350

Lutz, D. 1991, A&A, 245, 31

Massey, P., Armandroff, T. E., Pyke, R., Patel, K., & Wilson, C. D. 1995, AJ, 110, 2715

McLachlan, G. J. & Basford, K. E. 1988, in Mixture Models: Inference and Application to Clustering (New York: Marcel Dekker)

McLaughlin, D. E. 1999, AJ, 117, 2398

—. 2000, ApJ, 539, 618

McLaughlin, D. E. & Pudritz, R. E. 1996, ApJ, 457, 578

McLean, I. S. et al. 1994, in Instrumentation in Astronomy VIII, ed. D. Crawford (Bellingham: SPIE), 457

Meylan, G., Sarajedini, A., Jablonka, P., Djorgovski, S. G., Bridges, T., & Rich, R. M. 2000, in American Astronomical Society Meeting 197, #24.03, Vol. 197, 2403

Michie, R. W. 1963, MNRAS, 125, 127

Miller, G. E. & Scalo, J. M. 1979, ApJS, 41, 513

Minniti, D. 1995, AJ, 109, 1663

Mitchel, O. M. 1869, Stellar Worlds (Glasgow: William Collins)

Mochejska, B. J., Kaluzny, J., Krockenberger, M., Sasselov, D. D., & Stanek, K. Z. 1998, Acta Astronomica, 48, 455

Moore, B. 1996, ApJ, 461, L13

Morgan, S. & Lake, G. 1989, ApJ, 339, 171

Mostek, N., Taft, A., Elias, J., & Geisler, D. 1999, in American Astronomical Society Meeting, Vol. 195, 310

Murray, S. D. & Lin, D. N. C. 1992, ApJ, 400, 265

Nelson, A. E., Zaritsky, D., & Cutri, R. M. 1998, ApJ, 115, 2273

Norris, J. 1987, ApJ, 313, L65

Okazaki, T. & Tosa, M. 1995, MNRAS, 274, 48

Oke, J. B. et al. 1995, PASP, 107, 375

Ostriker, J. P. & Gnedin, O. 1997, ApJ, 487, 667

Ostrov, P., Geisler, D., & Forte, J. C. 1993, AJ, 105, 1762

Parmentier, G., Jehin, E., Magain, P., Neuforge, C., Noels, A., & Thoul, A. A. 1999, A&A, 352, 138

Peebles, P. J. E. 1984, ApJ, 277, 470

Peebles, P. J. E. & Dicke, R. H. 1968, ApJ, 154, 891

Perelmuter, J.-M., Brodie, J. P., & Huchra, J. P. 1995, AJ, 110, 620

Perelmuter, J.-M. & Racine, R. 1995, AJ, 109, 1055

Perrett, K. et al. 1999, in preparation

Persson, S. E., Murphy, D. C., Krzeminski, W., Roth, M., & Rieke, M. J. 1998, AJ, 116, 2475

Peterson, C. J. 1993, in ASP Conf. Proc. 50, Structure and Dynamics of Globular Clusters, ed. S. G. Djorgovski & G. Meylan (San Francisco: ASP), 337

Peterson, R. 1989, in Dynamics of Dense Stellar Systems, ed. D. Merritt (Cambridge: Cambridge University Press), 161

Ponder, J. M., Burstein, D., O'Connell, R. W., Rose, J. A., Frogel, J. A., Wu, C.-C., Crenshaw, D. M., Rieke, M. J., & Tripicco, M. 1998, ApJ, 116, 2297

Portegies Zwart, S. F., McMillan, S. L. W., Hut, P., & Makino, J. 2001, MNRAS, 321, 199

Pryor, C. & Meylan, G. 1993, in ASP Conf. Proc. 50, Structure and Dynamics of Globular Clusters, ed. S. G. Djorgovski & G. Meylan (San Francisco: ASP), 357

Puzia, T., Kissler-Patig, M., Brodie, J. P., & Huchra, J. P. 1999, AJ, 118, 2734

Racine, R. 1968, PASP, 80, 323

—. 1991, AJ, 101, 865

Racine, R. & Harris, W. E. 1992, AJ, 104, 1068

Racine, R. & Shara, M. A. 1979, AJ, 84, 1694

Ratnatunga, K., Casertano, S., & Bahcall, J. N. 1989, ApJ, 357, 435

Reed, B. C. 1996, PASP, 97, 120

Reed, B. C., Hesser, J. E., & Shawl, S. J. 1988, PASP, 100, 545

Reed, L. G., Harris, G. L. H., & Harris, W. E. 1992, AJ, 103, 824

—. 1994, AJ, 107, 555

Rich, R. M., Mighell, K. J., Freedman, W. L., & Neill, J. D. 1996, AJ, 111, 768

Rich, R. M. & Neill, J. D. 1999, in American Astronomical Society Meeting 194, #07.12, Vol. 194, 712

Richtler, T. 1992, Habilitationsschrift zur Erlangung, Sternwarte Bonn

Richtler, T. 1994, in Reviews in Modern Astronomy, ed. G. Klare, Vol. 8, 163

Robin, A. C., Haywood, M., Creze, M., Ojha, D. K., & Bienayme, O. 1996, A&A, 305, 125

Rosenberg, A., Saviane, I., Piotto, G., & Aparicio, A. 1999, AJ, 118, 2306

Rosenblatt, E. I., Faber, S. M., & Blumenthal, G. R. 1988, ApJ, 330, 191

Rutledge, G. A., Hesser, J. E., & Stetson, P. B. 1997, PASP, 109, 907

Saito, Y. & Iye, M. 2000, ApJ, 535, L95

Salpeter, E. E. 1955, ApJ, 121, 161

Sandage, A. & Tammann, G. A. 1995, ApJ, 446, 1

Sandage, A. R. & Schwarzschild, M. 1952, ApJ, 116, 463

Sarajedini, A., Chaboyer, B., & Demarque, P. 1997, PASP, 109, 1321

Sarajedini, A., Geisler, D., Schommer, R., & Harding, P. 2000, AJ, 120, 2437

Sargent, W. L. W., Kowal, C. T., Hartwick, F. D. A., & van den Bergh, S. 1977, AJ, 82, 947

Scalo, J. M. 1986, Fund. Cosmic Phys., 11, 1

Schlegel, D. J., Finkbeiner, D. P., & Davis, M. 1998, ApJ, 500, 525

Schommer, R. A. 1993, in Asp Conf. Ser. 48: The Globular Cluster-Galaxy Connection, ed. G. H. Smith & J. P. Brodie (San Francisco: ASP), 458

Schommer, R. A., Christian, C. A., Caldwell, N., Bothun, G. D., & Huchra, J. P. 1991, AJ, 101, 873

Schommer, R. A., Suntzeff, N. B., Olszewski, E. W., & Harris, H. C. 1992, AJ, 103, 447

Schweizer, F. 1979, ApJ, 233, 23

—. 1981, AJ, 86, 662

—. 1982, ApJ, 252, 455

Searle, L. & Zinn, R. 1978, ApJ, 225, 357

Secker, J. 1992, AJ, 104, 1472

—. 1995, PASP, 107, 496

—. 1997, Documentation for version 2.01 of MAXIMUM, online at `http://www.cyberus.ca/~secker`

Secker, J. & Harris, W. E. 1993, AJ, 105, 1358

Seitzer, P. et al. 1999, in preparation

Seyfert, C. K. & Nassau, J. J. 1945, ApJ, 102, 377

Shapley, H. 1918, ApJ, 48, 89

Sharov, A. S. 1977, AZh, 54, 285

Sharov, A. S. & Lyutyi, V. M. 1983, Ap&SS, 90, 371

—. 1985, PaZh, 11, 590

—. 1989, AZh, 66, 241

Sharov, A. S., Lyutyi, V. M., & Esipov, V. F. 1987, PaZh, 13, 643

—. 1995, PaZh, 21, 275

—. 1996, PaZh, 22, 456

Sharov, A. S., Lyutyi, V. M., & Ikonnikova, N. P. 1992, PaZh, 18, 99

Silk, J. 1977, ApJ, 214, 718

Sitko, M. L. 1984, ApJ, 286, 209

Skrutskie, M. et al. 1997, in The Impact of Large-Scale Near-IR Sky Surveys, ed. F. Garzon et al. (Dordecht: Kluwer Academic Publishing Company), 25

Smith, G. & McClure, R. 1987, ApJ, 316, 206

Solomon, P. M., Rivolo, A. R., Barrett, J., & Yahil, A. 1987, ApJ, 319, 730

Stanek, K. Z. & Garnavich, P. M. 1998, ApJ, 503, L131

Staneva, A., Spassova, N., & Golev, V. 1996, A&AS, 116, 447

Stetson, P. B. 1993, in ASP Conf. Proc. 48, The Globular Cluster-Galaxy Connection, ed. G. H. Smith & J. P. Brodie (San Francisco: ASP), 14

Strauss, M. A., Huchra, J. P., Davis, M., Yahil, A., Fisher, K., & Tonry, J. 1992, ApJS, 83, 29

Suntzeff, N. 1993, in ASP Conf. Proc. 48, The Globular Cluster-Galaxy Connection, ed. G. H. Smith & J. P. Brodie (San Francisco: ASP), 167

Supper, R., Hasinger, G., Pietsch, W., Trümper, J., Jain, A., Magnier, E. A., Lewin, W. H. G., & van Paradijs, J. 1997, A&A, 317, 328

Szentgyorgyi, A. et al. 1999, in preparation

Takahashi, K. 2000, in International Conference of the Astronomische Gesellschaft at Heidelberg, March 20-24, 2000, Vol. 16, 84

Tinsley, B. 1968, ApJ, 151, 547

Tollestrup, E. V. & Willner, S. P. 1998, SPIE, 3354, 502

Toomre, A. 1977, in The Evolution of Galaxies and Stellar Populations, ed. B. M. Tinsley & R. B. Larson (New Haven: Yale University Observatory), 401

van den Bergh, S. 1969, ApJS, 19, 145

—. 1985, ApJ, 297, 361

—. 1993, PASP, 95, 839

—. 1994, AJ, 108, 2145

—. 1995, AJ, 110, 1171

—. 2000, PASP, 112, 932

van den Bergh, S. & Lafontaine, A. 1984, AJ, 89, 1822

van den Bergh, S. & Morbey, C. L. 1984, ApJ, 283, 598

Vesperini, E. 1998, MNRAS, 299, 1019

—. 2000, MNRAS, 318, 841

—. 2001, MNRAS, 322, 247

Vesperini, E. & Heggie, D. C. 1997, MNRAS, 289, 898

Vetešnik, M. 1962a, Bull. Astron. Inst. Czech., 13, 180

—. 1962b, Bull. Astron. Inst. Czech., 13, 218

Walterbos, R. A. M. & Kennicutt, R. C. 1988, A&A, 198, 61

Webbink, R. F. 1985, in Dynamics of Star Clusters, IAU Symposium 113, ed. J. Goodman & P. Hut (Dordrecht: Reidel), 541

West, M. J. 1993, MNRAS, 265, 755

West, M. J., Côté, P., Jones, C., Forman, W., & Marzke, R. O. 1995, ApJ, 453, L77

White, R. E. & Shawl, S. J. 1987, ApJ, 317, 246

Whitmore, B. C. 1997, in StScI Symposium Series 10: The Extragalactic Distance Scale, ed. M. Livio, M. Donahue, & N. Panagia (Cambridge: Cambridge University Press), 254

Whitmore, B. C. & Schweizer, F. 1995, AJ, 109, 960

Wilson, C. D., Scoville, N., Madden, S. C., & Charmandaris, V. 2000, ApJ, 542

Wirth, A., Smarr, L. L., & Bruno, T. L. 1985, ApJ, 290, 140

Woolley, R. R. 1966, Royal Observatory Annals, 2, 1

Worthey, G. 1994, ApJS, 95, 107

—. 1996, version of models reported in Leitherer et al. 1996, PASP, 108, 996

Zaritsky, D., Kennicutt, R. C., & Huchra, J. P. 1994, ApJ, 420, 87

Zepf, S. E. & Ashman, K. A. 1993, MNRAS, 264, 611

Zepf, S. E., Ashman, K. M., English, J., Freeman, K. C., & Sharples, R. M. 1999, AJ, 118, 752

Zepf, S. E., Ashman, K. M., & Geisler, D. 1995, ApJ, 443, 570

Zhang, X., Zhen, Y., Chen, H., & Wang, S. 1993, A&AS, 99, 545

Zinn, R. 1985, ApJ, 293, 424

Zinn, R. 1993, in ASP Conf. Proc. 48, The Globular Cluster-Galaxy Connection, ed. G. H. Smith & J. P. Brodie (San Francisco: ASP), 38

Zinn, R. & West, M. J. 1984, ApJS, 55, 45